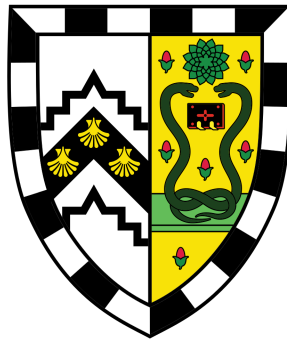


Exploring Interacting Bose Gases in and out of Equilibrium



Christoph Eigen
Gonville & Caius College

This dissertation is submitted for the degree of
Doctor of Philosophy

August 2019

Cavendish Laboratory
Department of Physics

 UNIVERSITY OF
CAMBRIDGE

To the memory of my grandfather, Manfred.

.

Contents

Declaration of Authorship	i
Abstract	iii
Acknowledgements	v
Acronyms and Global Variables	ix
1 Introduction	1
1.1 Outline	2
2 Theory of Bose Gases	5
2.1 The ideal Bose gas	6
2.2 Scattering theory	8
2.3 Theory of the condensate	9
2.4 Bogoliubov theory	13
2.5 Tan’s contact	15
3 Experimental Platform	17
3.1 Sample preparation	17
3.1.1 Bose–Einstein condensation	18
3.1.2 Quasi-uniform potential	19
3.2 Manipulating and probing samples	20
3.2.1 Tuning interactions	21
3.2.2 Imaging & measurement	22
3.2.3 Radio-frequency spectroscopy	23
3.2.4 Bragg spectroscopy	25
4 Turbulent-Cascade Fluxes	29
4.1 Introduction	29
4.2 Emergence of a turbulent cascade	32
4.3 Synthetic dissipation scale	37
4.4 Probing the turbulent cascade fluxes	39
4.4.1 Turbulent cascade atom-loss dynamics	39
4.4.2 Steady-state particle and energy flux	41
4.4.3 Pre-steady-state cascade-front dynamics	42
4.4.4 Unifying qualitative picture	43
4.5 Conclusion	45
5 Weak Collapse of a Bose–Einstein Condensate	49
5.1 Introduction	49
5.2 Qualitative picture and scaling laws	51
5.2.1 Critical interaction strength	52
5.2.2 Collapse time	53
5.2.3 Atom loss and weak collapse theory	53

5.3	Experimental studies	54
5.3.1	Critical interaction strength	54
5.3.2	Collapse dynamics	56
5.3.3	Aftermath of the collapse	59
5.4	Conclusion	70
6	Moderately Strongly Interacting Bose Gases	71
6.1	Introduction	71
6.2	Quantum depletion	73
6.2.1	Bragg filtering	74
6.2.2	Quantum depletion	78
6.2.3	Conclusion	79
6.3	Quasi-particle excitations	80
6.3.1	Beyond Bogoliubov theory	81
6.3.2	Spectroscopy of quasi-particle excitations	83
6.3.3	Exploring the limits of validity of Feynman–Tan theory	84
6.3.4	Conclusion	87
6.4	Conclusion	88
7	Boses Gases Quenched to Unitarity	89
7.1	Introduction	89
7.1.1	Advantages of an optical box potential	92
7.1.2	Atom-loss scaling-law predictions	93
7.1.3	Quench protocol	97
7.2	Degenerate Bose gases quenched to unitarity	99
7.2.1	Universal loss dynamics	102
7.2.2	Momentum distribution dynamics	104
7.2.3	Molecular correlation dynamics	107
7.3	Thermal Bose gases quenched to unitarity	110
7.3.1	Momentum redistribution dynamics	110
7.3.2	Atom-loss and correlation dynamics	116
7.4	Conclusion	119
8	Outlook	120
A	Cross-calibration of the zero-crossing of a	123
B	Atom number control & stability	124
C	Inverse-Abel transform	125
D	Field control & stability	126
D.1	Mains oscillation	126
D.2	Dynamical field control	127
D.2.1	Primary field response time	128
D.2.2	Quenches to unitarity	128

Declaration of Authorship

I certify that this thesis is the result of my own work unless declared otherwise in the text. It is not substantially the same, in whole or in part, as any that I have submitted, or, is concurrently being submitted for a degree (or other qualification) at this or any other University (or similar institution). This thesis does not exceed the world limit of sixty thousand words, excluding figure captions, acknowledgements, and bibliography, as set out by the Faculty of Physics and Chemistry.

Christoph Eigen,

August 2019

Cavendish Laboratory,
University of Cambridge,
JJ Thomson Avenue,
Cambridge CB3 0HE,
United Kingdom

Abstract

This thesis describes a collection of experiments that explore interacting ultracold Bose gases, both in and out of equilibrium. Our experiments are performed using a gas of ^{39}K or ^{87}Rb confined in the uniform potential of an optical box trap, a novel testbed for quantum many-body phenomena. Our work focuses on weakly interacting non-equilibrium systems, moderately interacting systems that are still in equilibrium, and the unitary Bose gas which is both strongly interacting and eludes equilibrium.

We begin with studies of weakly-interacting gases far from equilibrium, which feature ties to nonlinear wave phenomena. Highlights of our experiments include the direct measurement of turbulent-cascade fluxes, which (alongside realizing a tuneable dissipation scale) allow us to demonstrate the zeroth law of turbulence, and the first observation of weak collapse, a general type of nonlinear wave collapse predicted over 40 years ago.

We then turn to moderately strong interactions, confronting existing theories of interacting quantum fluids. One of our most important results is the first quantitative measurement of the quantum depletion of a Bose–Einstein condensate, confirming a 70-year-old theory first developed to describe liquid helium.

The culmination of our work explores the unitary Bose gas, where interparticle interactions are as strong as allowed by the laws of quantum mechanics. This strongly-correlated state promises tantalizing possibilities, including emergent universal behavior set solely by the gas density and novel forms of superfluidity. However, the strong interactions also lead to a complex interplay between coherent and dissipative dynamics. By disentangling these two processes, we have caught a glimpse of the promises that the unitary Bose gas holds. In particular, we observe the emergence of universal behavior, and find that the gas features a well defined quasi-equilibrium state, with a non-zero condensed fraction.

Acknowledgements

Expressing genuine gratitude to the people that one owes everything to is one of the most daunting challenges of writing a thesis, since one faces the inevitable failure of doing them justice. Nevertheless, trying matters, so here goes.

First and foremost, I would like to thank Rob, who has been the kind of supervisor any student can only dream of¹. From day one (at the start of my MPhil) he has been there to guide my steps, and his patience and unerring support have been invaluable. It is unclear what would have become of me without his inherent urge for directly confronting problems and identifying issues at their root.

On equal footing, I would like to thank Zoran, who also took on (or rather retained) the role of a supervisor. His immeasurable² enthusiasm for science, as well as his high standards (sometimes seemingly unattainable so) are outright infectious. Together Rob and Zoran formed a supervisor dream team, complimenting each other across the board but ultimately sharing their love of science. I am deeply indebted to both Rob and Zoran for investing so much of their time into not only my scientific prosperity but also my career.

Throughout the years I have had the pleasure to be mentored exclusively by brilliant post-docs, whose contributions to the work presented in this thesis are massive. Before I knew what was going on, Alex had already taken me on board, teaching me the arts of sculpting³ while on a fast-track involuntary crash-course in how to rebuild the machine⁴. His love for computers and physics (it's a tough call) paved the way for success, and in particular his pioneering box traps underpin this entire thesis. Nir offered continual advice and valuable insight at all times, and was in charge of running BEC I. While his sense of humor often kept me on my toes⁵, he brought an overall badass scientist vibe to the lab, making it a stimulating and unique environment. Raphael was unarguably one of the most (openly) passionate people around, and both his flair for science and his intrinsic drive to never stop left a profound impression. His 'hostile takeover' (in a good way), implementing the Bragg setup and subsequently putting it to use,

¹I say that even though he left me to go to the other place.

²I realize what I'm getting myself into.

³Optical boxes, that is.

⁴This incident is no longer spoken of.

⁵Passwords are useful it turns out.

was extremely fruitful in many ways, and led to a large number of nights and weekends in the lab, which were however also regularly complemented by tennis breaks. While not directly involved in any of my work, Rich (who was leading BEC II at the time) was readily available for advice, either during coffee break discussions or while enforcing key lab traits (such as looking over ones shoulder while working and asking stimulating questions). All of them have since moved on, and their departure marked a notable transition in the lab dynamics.

When Jake joined as a fellow PhD student, he swiftly transformed our early dabbles in the unitary regime with his savvy sense for electronics and problem solving. It has been a delight exploring the unitary regime with him, and I owe a great deal to him. I also want to thank Jinyi, who took over Nir's role as the BEC I postdoc, keeping its future bright. He has been central to acquiring the data that BEC I has amassed.

There were a large number of summer and Part III students that have made an appearance throughout the years; I would like to thank them all for their involvement (from small conveniences to large contributions), particularly emphasizing Adam and Sam.

I would also like to thank Timon, who as the newest BEC III postdoc has already imprinted many of the stern Munich standards onto daily lab life. While we kind of threw Lena, our new PhD student addition, in at the deep end, this seems to have paid off with significant progress. Indeed, the current BEC III team is being remarkably productive in my writing absence, making me eagerly anticipate my return.

I am particularly fond of a collaboration with Eric when he visited us for a sabbatical, instilling a refreshing and inspiring atmosphere to the lab, and providing profound insight into our studies of the unitary regime. I would also like to thank our theory collaborators, Kazuya and Makoto, who performed the numerical simulations in our studies on turbulence.

The last person associated with BEC III who I would like to thank is Aziza, who even though we never overlapped, I owe a great deal to as she orchestrated the majority of the building of the machine at the heart of this thesis.

The physical segregation⁶ of office occupations for BEC II and BEC III has slowly drifted into crisis. From back in the early days when things were still in order, I would also like to thank Jay and Konrad (who deserted to the lab next door), who were also new recruits back when I joined the group and who were central in ensuring that days spent in the lab were a delight. I would also like to thank Milan and Nathaniel (Rob's 'students in crime'), as well as Max who we unfortunately lost to Innsbruck; they all enhanced daily lab life.

Turning to the current BEC II inhabitants, I would like to thank Panos, Maciej, and Julian.

⁶Overpopulation led to division into two offices.

While faced with a bumpy start, their now operational 2D box experiment features optical potentials which are something to be jealous of. I have enjoyed their company and contributions to daily lab life throughout, as well as social activities from football games to pub nights.

I also enjoyed the numerous aperiodic encounters with Konrad and Matteo, who started their PhDs next door at the same time as I did, and with whom I share many good memories.

More generally, I would also like to thank Mete, Ulrich, Andreas, and Richard, alongside all of their students and postdocs, for making the AMOP group an awesome, scientifically stimulating environment in which to pursue a PhD. I also extend thanks to all friends and peers that have supported me or otherwise enhanced this journey.

Finally, I would like to turn to my family and those nearest my heart. First, I would like to thank my extended 'science family' from the Winter Seminar in Klosters. I have been fortunate to attend this unique conference since I was a child, and presenting our novel findings in this setting has been priceless. I am thankful to everyone that attends and keeps this special experience alive, but would like to particularly thank Michael, Markus, and Eberhard.

Finally, I cannot express enough gratitude to my parents Gerald and Andrea, as well as my brother Julian. They have supported me on all fronts, and they are directly to 'blame' for instilling my curiosity for science.

Last and quite a lot, I would like to thank Janine, without her constant support and unconditional compassion none of this would have been as enjoyable.

Acronyms and Global Variables

BEC Bose–Einstein Condensate

rf Radio Frequency

ToF Time of Flight

DF Diffracted Fraction

TF Transferred Fraction

ODT Optical Dipole Trap

SLM Spatial Light Modulator

OD Optical Density

QD Quantum Depletion

k_B - Boltzmann's constant

\hbar - reduced Plank's constant

m - atom mass

n - atomic density

n_k - momentum distribution

a - s -wave scattering length

T - temperature

E - energy per particle

L - length

R - radius

N - atom number

s.e.m. - standard error on the mean

1 Introduction

Our world is inherently transient and interactions lie at the heart of its many-body nature. While different areas of research present unique and novel problems at every stage of the fundamental ‘cascade’ linking them [1], there still exists a curious relationship between the strange simplicity governing the fundamental laws of physics and the complex familiarity that describes our everyday world [2].

Understanding quantum matter which is either far from equilibrium or strongly-interacting, lies at the heart of most fundamental problems in modern physics. Since its inception two decades ago, when the first gaseous atomic Bose–Einstein condensates were created [3,4], and following the advent of degenerate atomic Fermi gases a decade later [5], the field of ultracold atoms has established itself as an ideal setting for investigating quantum many-body phenomena, in the spirit of Feynman’s proposal of quantum simulation [6]. Key ingredients for the field’s success are the pristine control of atom-trapping geometries, the ability to coherently manipulate the atom’s internal states, the experimentally resolvable intrinsic timescales, and the unique ability to tune the interparticle interactions using molecular resonances [7].

Over the last two decades, ultracold atom research has led to myriad achievements, which are (at least in part) reviewed in [8–20]. Some of the major achievements can be attributed to the use of optical lattices to mimic the solid-state setting, freezing-out of excitations to gain access to the peculiarities of lower-dimensional physics, and artificial gauge potentials to simulate behavior of arbitrarily charged particles in electromagnetic fields.

Our focus here is on Bose gases, which tend to form Bose–Einstein condensates at low temperatures, when the thermal wavelength becomes comparable to the interparticle separation. This statistical second-order phase transition leads to a macroscopically occupied ground state, and the emergence of the wave properties of matter. Such condensates are generally well understood when they are in equilibrium and the interparticle interactions are weak. However, if the gas is driven out of equilibrium or if it is strongly-interacting, things typically escalate, swiftly becoming more complicated. Exploring these two regimes is at the heart of this thesis. We utilize ultracold Bose gases confined in a quasi-uniform box potential [21,22], sculpted from repulsive (blue-detuned) laser light. Most of our experiments are performed using ul-

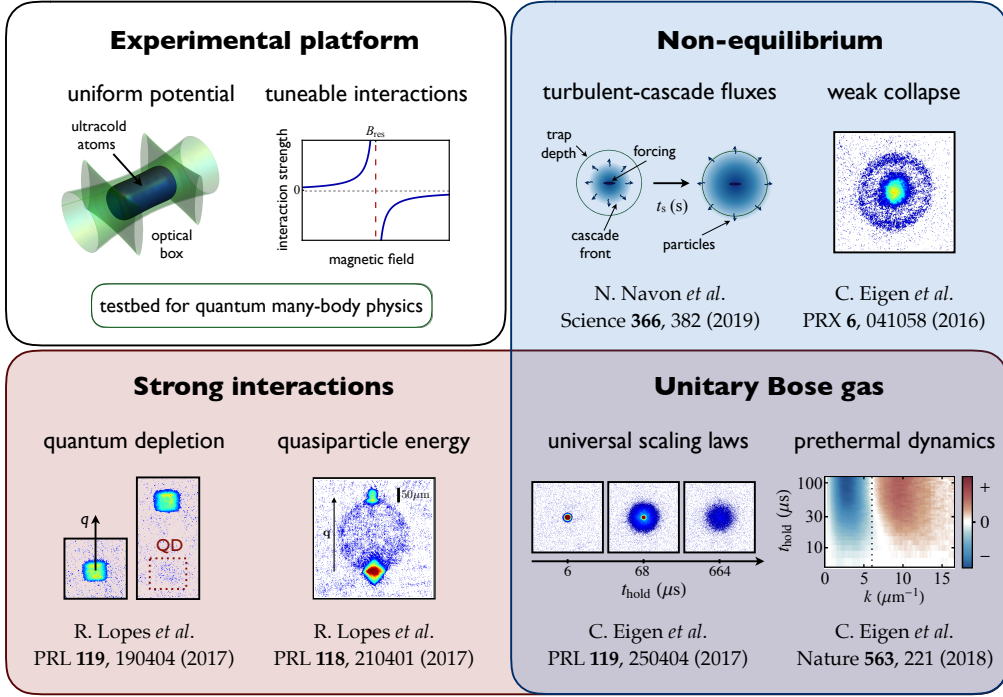


Fig. 1.1 Thesis outline. Our experimental platform, which combines a uniform potential and the ability to tune the interparticle contact interactions, establishes a novel testbed for quantum many-body physics. In the six papers that form the basis of this thesis we explore systems that are either out-of-equilibrium or strongly-interacting, or, in the case of the unitary Bose gas, both.

tracold ^{39}K gases in our second generation box-experiment [22]; this combines the benefits of a uniform trapping potential with tuneable interparticle interactions [7], establishing a novel testbed for fundamental many-body physics.

More generally, our experiments are part of a shift towards uniform box potentials [21–25]. These box-traps are an invaluable tool for extracting bulk properties of the gas, and are particularly promising in the context of non-equilibrium phenomena, where the otherwise non-uniform density imposed by more traditional harmonic traps can obscure or even alter the resulting physics¹.

1.1 Outline

As outlined in Fig. 1.1, the work presented in this thesis closely follows the six papers [26–31], which explore intricate many-body phenomena in systems that are either far-from-equilibrium or strongly-interacting, or, in the case of the resonantly interacting unitary Bose gas, both.

Following a brief introduction of the pertinent theory of Bose gases in Chapter 2, we begin in Chapter 3 by giving an overview of the experimental platform used to create and manipu-

¹Note that for experiments performed in harmonic traps it has been possible to deal with the varying density in clever ways, even in some cases exploiting it as an advantage, broadly speaking achieved by assuming the local density approximation to extract uniform system results.

late a ^{39}K Bose gas at nanokelvin temperatures. We highlight our key experimental features, including the quasi-uniform box potential [21] and the ability to tune the interparticle interactions using magnetic Feshbach resonances [7]. In Chapters 4 and 5 we present experiments that investigate nonlinear wave phenomena in weakly-interacting gases. In Chapter 4 we drive the cloud out of equilibrium and probe the fluxes underlying the emerging turbulent cascades, while in Chapter 5 we study the effect of attractive interactions in a BEC, which leads to dramatic non-equilibrium behavior as the BEC collapses. Chapter 6 focuses on ‘moderately’ strong interactions, where simple mean-field theories break and beyond-mean-field quantum correlation effects become important, but the experiments also remain tractable within the existing theories. Chapter 7 explores the unitary Bose gas, where interactions between particles become as strong as theoretically possible and a complex interplay between coherent and dissipative dynamics occurs. Finally, in Chapter 8 we briefly discuss future research avenues.

2 Theory of Bose Gases

Erst die Arbeit, dann das Spiel

Our goal in this chapter is to provide a minimal basis of the theory of Bose gases that we will rely on throughout this thesis; a comprehensive treatment can be found in several places, for example [8, 17], to which we refer the reader (and which we in part follow closely here). Instead, for the core concepts of atomic physics we recommend *e.g.* [32].

If we consider two indistinguishable particles, the corresponding wave function under particle exchange (indicated by a subscript change) generically satisfies

$$|\psi_{1,2}|^2 = |\psi_{2,1}|^2. \quad (2.1)$$

For this relation to hold, we require $\psi_{1,2} = |\psi| \exp(i\gamma)$, where γ could in theory take any real value. In practice, all known particles fall into one of two categories, either $\gamma = 0$ or $\gamma = \pi$, defining bosons and fermions respectively¹. Fermions have half-integer spin while bosons, which we consider throughout this thesis, have integer spin. In the case of fermions, Eq. (2.1) reveals the Pauli exclusion principle, while as we will see below bosons are more ‘sociable’.

As highlighted by the cartoon in Fig. 2.1, a Bose gas can typically be described by three relevant lengthscales: the interparticle spacing $n^{-1/3}$ (set by the gas density n), the thermal wavelength $\lambda = h/\sqrt{2\pi mk_B T}$ (set by the temperature T), and the s -wave scattering length a (capturing the two-body contact interactions)². In the following sections we will discover how these lengthscales (or combinations thereof) reveal themselves.

¹An active field of research constitutes attempts to create so-called ‘anyonic’ quasi-particles in lower dimensions, where γ can take values other than 0 and π .

²The finite size of the box can also play a role (*e.g.* when the interaction energy is comparable to the kinetic energy). The van der Waals length a_{vdw} (which is $\approx 60 a_0$ for ^{39}K [33]) can also play a role when $a \lesssim a_{\text{vdw}}$. Additionally, in Bose gases the Efimov effect occurs [34], which formally requires the introduction of a three-body lengthscale R_3 (see *e.g.* [35, 36]), which can also become important.

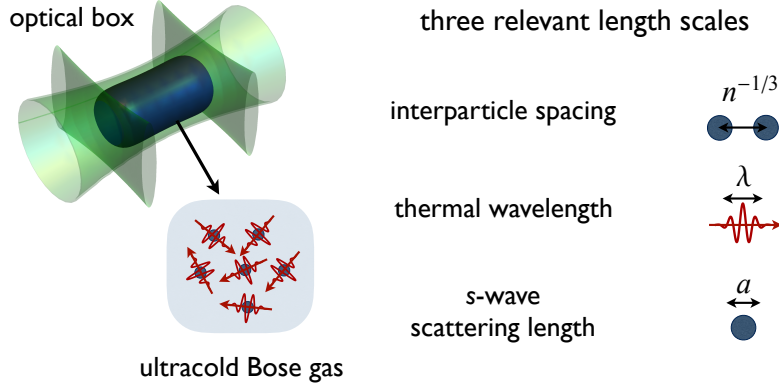


Fig. 2.1 Box-trapped Bose gases. A weakly interacting gas can typically be described by three characteristic lengthscales: the interparticle spacing $n^{-1/3}$, where n is the gas density, the thermal wavelength $\lambda = h/\sqrt{2\pi mk_B T}$, where T is the gas temperature, and the s -wave scattering length a , which characterizes the strength of the two-body contact interactions.

2.1 The ideal Bose gas

We begin our discussion entirely neglecting interactions. The equilibrium Bose distribution function is

$$f(\epsilon_i) = \left(\frac{\partial \Phi}{\partial \mu} \right)_{T,V} = \frac{1}{\exp \frac{\epsilon_i - \mu}{k_B T} - 1}, \quad (2.2)$$

where $k_B T$ is the thermal energy [37] (commonly defined by a temperature T and Boltzmann's constant k_B), ϵ_i is the energy of a single-particle state, μ is the chemical potential, V is the volume, and $\Phi = -k_B T \ln Z$ is the grand potential, where Z is the grand partition function.

In the case of non-interacting bosons, Eq. (2.2) gives the mean occupation of number of a given state, and summing over all states simply yields the total particle number

$$N = \sum_i f(\epsilon_i). \quad (2.3)$$

If the thermal energy is much larger than the energy difference between neighboring states ($k_B T \gg \Delta \epsilon_i$), we can resort to the semi-classical approximation, treating the discrete energy spectrum as a continuum, and replacing the sum over states with an integral over a density of states $g(\epsilon)$ (ignoring the quantum-mechanical ground-state energy). Within this approximation, $g(\epsilon)$ encapsulates the thermodynamic behavior, and for all cases relevant here one finds the form $g(\epsilon) = C_\alpha \epsilon^{\alpha-1}$, where C_α is a constant and α is the thermodynamic scaling parameter.

From Eq. (2.2), we see that the need for positive occupation numbers defines a critical atom number N_c ($\mu \rightarrow \epsilon_0$), at which point the number of excited states saturates and the system undergoes the *statistical* phase transition known as Bose–Einstein condensation [38, 39]. The

critical atom number is given by

$$N_c = \int_0^\infty g(\epsilon) f(\epsilon) d\epsilon = C_\alpha \zeta(\alpha) \Gamma(\alpha) (k_B T)^\alpha, \quad (2.4)$$

where $\zeta(\alpha)$ is the Riemann function and $\Gamma(\alpha) = \int_0^\infty x^{\alpha-1} e^{-x} dx$ (assuming $\Re(\alpha) > 0$). For $N > N_c$, since the excited states are saturated at N_c all of the remaining particles occupy the ground state, forming a Bose–Einstein condensate, which can be treated separately³.

We can rewrite Eq. (2.2) as an explicit function over phase space⁴

$$f(\mathbf{r}, \mathbf{p}) = \frac{1}{\exp\left[\frac{\epsilon(\mathbf{r}, \mathbf{p}) - \mu}{k_B T}\right] - 1}, \quad (2.5)$$

where

$$\epsilon(\mathbf{r}, \mathbf{p}) = \frac{p^2}{2m} + U(\mathbf{r}). \quad (2.6)$$

In addition to the free-particle dispersion relation we have included a potential energy term $U(\mathbf{r})$. We assume a general power-law form, which to simplify our discussion here we assume to be spherically symmetric, that is $U(\mathbf{r}) = U_0 r^b$. We can relate the form of this power-law trapping potential directly to the density of states (captured by the thermodynamic parameter α), which yields

$$\alpha = \frac{3}{2} + \frac{3}{b}. \quad (2.7)$$

For a uniform potential ($b \rightarrow \infty$) $\alpha = 3/2$ and for a harmonic trap ($b = 2$) $\alpha = 3$.

Finally, we obtain the momentum and density distribution by (respectively) integrating Eq. (2.5) over \mathbf{r} or \mathbf{p} :

$$f(\mathbf{p}) = \frac{4\pi}{b} \left(\frac{U_0}{k_B T}\right)^{-\frac{3}{b}} \Gamma\left(\frac{3}{b}\right) \tilde{g}_{\frac{3}{b}} \left[\frac{1}{k_B T} \left(\mu - \frac{p^2}{2m}\right) \right], \quad (2.8)$$

$$n_{\text{th}}(\mathbf{r}) = \frac{1}{\lambda^3} \tilde{g}_{\frac{3}{2}} \left(\exp \left[\frac{\mu - U(\mathbf{r})}{k_B T} \right] \right), \quad (2.9)$$

where $\tilde{g}_\ell(x)$ is the polylogarithm of order ℓ and λ is the thermal wavelength.

Around the critical point λ is comparable to $n^{-1/3}$, which is intuitive as quantum effects should become important when the wave packet size is comparable to the interparticle spacing. Indeed, in an infinite uniform non-interacting gas the critical phase space density $n_c \lambda^3 \approx 2.6$ [see Eq. (2.9)].

³In interacting systems this separation works to a first approximation.

⁴This violates the Heisenberg uncertainty principle, and highlights the fact that it is a semi-classical approximation.

2.2 Scattering theory

While the ideal gas description above lends some insight, atoms typically do interact with each other. In general, one is faced with the daunting task of developing a full microscopic description of the quantum-mechanical scattering problem. One of the most compelling aspects of ultracold atom experiments is that one can dramatically simplify this problem, and achieve conditions where the interactions between atoms can be described by a single parameter, known as the s -wave scattering length, a .

An extensive discussion of scattering theory, and the approximations required to formulate such a simple description, can be found in many places (e.g. [8, 32, 40]); below we merely provide an outline.

Solving the Schrödinger equation for the relative motion of two particles (within the Born approximation) yields the resultant scattering wave function

$$\psi(\mathbf{r}) \approx \phi_{\mathbf{k}}(\mathbf{r}) + \frac{\exp(ikr)}{r} \overbrace{\left[-\frac{m_r}{2\pi\hbar^2} \langle \phi_{\mathbf{k}'}(\mathbf{r}) | \tilde{V}(\mathbf{r}) | \phi_{\mathbf{k}}(\mathbf{r}) \rangle \right]}^{f(k)} \quad (2.10)$$

where m_r is the reduced mass, $\phi_{\mathbf{k}}(\mathbf{r}) = \exp(i\mathbf{k} \cdot \mathbf{r})$ and $\tilde{V}(\mathbf{r})$ is the scattering potential. Physically, we interpret this as the sum of an incident plane wave and a spherically scattered wave modulated by the scattering amplitude $f(k)$.

The general form of $\tilde{V}(\mathbf{r})$ can be rather complicated, however the short-range nature of the van der Waals potential (falling faster than $1/r$) facilitates progress. If we compare the range of interaction r_{int} with the gas's relevant length scales ($n^{-1/3}$ and λ), we find that for a dilute gas ($r_{\text{int}} \ll n^{-1/3}$)⁵, at degeneracy ($n^{-1/3} \sim \lambda$), the angular momentum of the interacting pair (approximated by $\sim hr_{\text{int}}/\lambda$), is small⁶. This allows us to only consider the spherically symmetric $l = 0$ (s -wave) component [so that $f(\mathbf{k}) = f(k)$], since the collisions lack the relative momentum to significantly admix states with $l > 0$ into $\psi(\mathbf{r})$.

Assuming that only elastic scattering events occur, the sole effect of the collision is to impart a phase-shift δ (bounded between $\pm\pi/2$) on the $l = 0$ component, which defines the scattering length a (in the limit $k \rightarrow 0$) as

$$k \cot \delta = -\frac{1}{a}, \quad (2.11)$$

⁵The range of interaction is typically $\sim 100 a_0 \approx 5 \text{ nm}$ [e.g. for ^{39}K the van der Waals radius $r_{\text{vdw}} \approx 60 a_0$], while for our typical densities $n^{-1/3} \sim 1 \mu\text{m}$.

⁶Here we approximated the impact parameter b_{im} of the interaction with r_{int} , which overestimates the ratio since $b_{\text{im}} < r_{\text{int}}$.

and the scattering amplitude is

$$f = \frac{e^{2i\delta} - 1}{2ik} = -\frac{a}{1 + ika}. \quad (2.12)$$

For bosons, the scattering cross-section can be obtained by integrating $|f|^2$ over the solid angle, also accounting for the bosonic factor of 2 (to ensure symmetric wave functions):

$$\sigma = \frac{8\pi}{a^{-2} + k^2}. \quad (2.13)$$

In summary, we have found that $\tilde{V}(\mathbf{r})$ (and more generally the entire scattering process), however complicated it may be, is parametrized entirely by a . Consequently, given that a ‘pseudopotential’ reproduces the same a , its exact shape is unimportant, which is particularly useful for theoretical considerations. Physically, this can be traced back to the fact that the collision does not probe the short-distance behavior, and so we can simply reduce the entire description into *e.g.* a contact interaction with a delta-function potential $\tilde{V}(\mathbf{r}) = g\delta(\mathbf{r})$, where $g = 4\pi\hbar^2 a/m$.

Finally, a remarkable feature of ultracold atom systems is that we can experimentally vary δ (and hence a) using molecular Feshbach resonances [7], by simply changing a magnetic field (see Section 3.2.1). From Eq. (2.11) we see that for $|a| \rightarrow \infty$ the phase shift becomes maximal ($|\delta| = \pi/2$), which means that the interactions are as strong as allowed by the laws of quantum mechanics; this is known as the unitary regime. As discussed in Section 3.2.1, Feshbach resonances directly give us access to this regime, as well as *any* other values of a along the way.

2.3 Theory of the condensate

In our discussion in Section 2.1 we considered a statistical description of the thermally excited states. We now turn to the Bose–Einstein condensate (BEC), a coherent macroscopic quantum object, which we can describe by a macroscopic wave function

$$\Psi(\mathbf{r}_1, \mathbf{r}_2, \dots, \mathbf{r}_N) = \prod_{i=1}^N \phi(\mathbf{r}_i), \quad (2.14)$$

where the single particle wave functions are normalized [$\langle\phi|\phi\rangle = 1$].

Taking a step further, let us consider the general Hamiltonian of a Bose gas with two-body

contact interactions, which in second-quantized form is

$$\hat{H} = \underbrace{\sum_j \varepsilon_j \hat{a}_j^\dagger \hat{a}_j}_{\hat{K}} + \underbrace{\frac{g}{2V} \sum_{ijkl} I_{ijkl}^\alpha a_i^\dagger \hat{a}_j^\dagger \hat{a}_k \hat{a}_l}_{\hat{I}}, \quad (2.15)$$

where \hat{K} and \hat{I} are the kinetic and interaction energy operators (respectively) and we have made use of an effective pseudopotential, characterized by $g = 4\pi\hbar^2 a/m$, neglecting the short range details of the two-body potential. Here \hat{a}_j^\dagger (\hat{a}_j) is the creation (annihilation) operator for the eigenstate α_j , and $I_{ijkl}^\alpha = \int \alpha_i^* \alpha_j^* \alpha_k \alpha_l d^3r$, with wave functions normalized to unit volume. The optimal basis choice for α_i depends on the specific problem (see *e.g.* [41]), though we can always rewrite the condensate wave function as a superposition of these eigenstates.

A convenient (and widely used, albeit slightly unphysical) choice is to assume periodic boundary conditions (or an infinite system) and use momentum eigenstates⁷. In this case the Hamiltonian becomes

$$\hat{H} = \sum_{\mathbf{p}} \frac{p^2}{2m} \hat{a}_{\mathbf{p}}^\dagger \hat{a}_{\mathbf{p}} + \frac{g}{2V} \sum_{\mathbf{p}_1, \mathbf{p}_2} \hat{a}_{\mathbf{p}_1}^\dagger \hat{a}_{\mathbf{p}_2}^\dagger \hat{a}_{\mathbf{p}_1} \hat{a}_{\mathbf{p}_2}, \quad (2.16)$$

where the annihilation (creation) operators $\hat{a}_{\mathbf{p}}$ ($\hat{a}_{\mathbf{p}}^\dagger$) can be used to write the field operators as plane waves

$$\hat{\Psi}(\mathbf{r}) = \sum_{\mathbf{p}} \hat{a}_{\mathbf{p}} \frac{1}{\sqrt{V}} e^{i\mathbf{p}\cdot\mathbf{r}/\hbar}. \quad (2.17)$$

In the case of weak interactions ($na^3 \ll 1$) it is insightful and often sufficient to resort to a mean-field approximation, disregarding all operators with $\mathbf{p} \neq 0$ and replacing $\hat{a}_0 = \sqrt{N_0}$; for simplicity, here we assume a pure zero-temperature gas where $N = N_0$ ⁸. Within this approximation, we can readily identify the ground-state energy

$$\mathcal{E}_0 = \frac{gN^2}{2V}, \quad (2.18)$$

and proceed along the typical lines to identify macroscopic thermodynamic quantities such as the pressure

$$P = -\frac{\partial \mathcal{E}_0}{\partial V} = gn^2/2, \quad (2.19)$$

chemical potential

$$\mu = \frac{\partial \mathcal{E}_0}{\partial N} = gn, \quad (2.20)$$

⁷While it is fundamentally unphysical, it does generally offer a good approximation assuming that kinetic energy is negligible compared to interaction energy.

⁸We turn to a description of both quantum and thermal depletion of the condensate in Section 2.4, while the more general case of interacting partially condensed gases is beyond the scope of this thesis (see *e.g.* [17] as a starting point).

and the compressibility

$$\frac{\partial n}{\partial P} = \frac{1}{gn} = \frac{1}{mc^2}, \quad (2.21)$$

where $c = \sqrt{\frac{gn}{m}}$ is the speed of sound.

Time-independent Gross–Pitaevskii equation

Starting from Eq. (2.15), as long as a state (identified as the condensate) has a macroscopic population much greater than all other states orthogonal to it, it is possible to show⁹ that the condensate wave function Ψ is described by the time-independent Gross–Pitaevskii equation

$$-\frac{\hbar^2}{2m}\nabla^2\Psi(\mathbf{r}) + U(\mathbf{r})\Psi(\mathbf{r}) + g|\Psi(\mathbf{r})|^2\Psi(\mathbf{r}) = \mu\Psi(\mathbf{r}), \quad (2.22)$$

which is a nonlinear Schrödinger equation with a cubic interaction term [and we have introduced a potential energy term $U(\mathbf{r})$]. Here $\mu = \partial\mathcal{E}/\partial N$ is the Hartree–Fock chemical potential and the condensate density is $n(\mathbf{r}) = |\Psi(\mathbf{r})|^2$. If we neglect the kinetic energy to make a connection to the infinite system results (known as the Thomas–Fermi limit), we find a density

$$n(\mathbf{r}) = \frac{\mu - U(\mathbf{r})}{g}, \quad (2.23)$$

which for a uniform box potential corresponds to a uniform condensate density inside the system volume V , gracefully decaying to zero¹⁰ at the trap edges to avoid an otherwise diverging kinetic energy.

In experiments using quasi-homogeneous trapping potentials the density is also not perfectly uniform due to the unavoidable smooth edges of the trapping potential, which can be described using a power-law potential of the form $U(\mathbf{r}) = U_0 r^b$ ¹¹. While it is typically sufficient to assume a constant volume, it can be beneficial to assess the residual dependence of the effective volume of the gas on its typical energy scale. To this end, we define an effective size r_{eff} using the condition $U_0 r_{\text{eff}}^b \propto gn$ (within the Thomas–Fermi approximation). We then self-consistently solve for r_{eff} using $n = N/V_{\text{eff}}$ with $V_{\text{eff}} \sim r_{\text{eff}}^3$, such that

$$r_{\text{eff}} \propto \left(\frac{gN}{U_0}\right)^{\frac{1}{3+b}}. \quad (2.24)$$

While this is only a rough estimate of the condensate size (as the prefactor and exact box shape matter), it is valuable in that given a measurement of the condensate size we can analytically

⁹See e.g. [8, 17, 41].

¹⁰This change occurs over a distance set by the healing length $\xi = 1/\sqrt{8\pi na}$.

¹¹Here we assume spherical symmetry only for the simplicity of the argument.

correct for slight size variations for experiments with different g , N , and U_0 . A similar correction is obtained for a thermal gas, though as the temperature is independent of V one simply has $r_{\text{eff}} \propto (k_B T/U_0)^{\frac{1}{6}}$ [22].

Time-dependent Gross–Pitaevskii equation

For investigating the dynamics of the condensate, a natural extension to Eq. (2.22) is the time-dependent Gross–Pitaevskii equation

$$i\hbar \frac{\partial \Psi}{\partial t} = -\frac{\hbar^2}{2m} \nabla^2 \Psi + U\Psi + g|\Psi|^2\Psi, \quad (2.25)$$

where under stationary conditions we require the time evolution of $\Psi(\mathbf{r}, t)$ to be set by $e^{-i\mu t/\hbar}$ [*i.e.* demanding consistency with Eq. (2.22)]. It is important to recall that the GP equation is a nonlinear Schrödinger equation with cubic nonlinearity, and above all else it is a wave equation. The GP equation is at the heart of our theoretical understanding weakly-interacting of out-of-equilibrium Bose gases, and will be of utmost importance in Chapters 4 and 5. Curiously, it is possible to use Eq. (2.25) to arrive at equations of motion which are remarkably similar to the Euler equations governing classical ideal fluid dynamics (*i.e.* in the absence of viscosity and thermal conductivity).

The condensate satisfies the continuity equation for particle density¹²

$$\frac{\partial n}{\partial t} + \nabla \cdot (n\mathbf{v}), \quad (2.26)$$

where the velocity of the condensate is given by

$$\mathbf{v} = -\frac{i\hbar}{2m} \frac{(\Psi^* \nabla \Psi - \Psi \nabla \Psi^*)}{|\Psi|^2}. \quad (2.27)$$

By writing $\Psi = \sqrt{n}e^{i\phi}$ as a complex number in terms of its amplitude and phase, we identify

$$\mathbf{v} = \frac{\hbar}{m} \nabla \phi, \quad (2.28)$$

which shows us that the condensate dynamics satisfy potential flow, with a velocity potential $\hbar\phi/m$, and consequently highlights the profound physical trait that the motion of the condensate is irrotational [$\nabla \times \mathbf{v} = 0$], apart topological defects in the form of vortex lines, which feature quantized circulation (in units \hbar/m) and a vanishing density along the vortex core (oc-

¹²This is relatively simple to show by multiplying Eq. (2.25) by $\Psi^*(\mathbf{r}, t)$ and subtracting the complex conjugate from the resultant equation, further using $n = |\Psi|^2$ and identifying \mathbf{v} . Interestingly, it is also entirely independent of the nonlinear term (as this is real and cancels).

curing in a regular manner over the healing length ξ).

Our next goal is to find an equation of motion for \mathbf{v} . By inserting $\Psi = \sqrt{n}e^{i\phi}$ into Eq. (2.25), retaining the real part (the imaginary part recovers the continuity equation), and taking the gradient, we get

$$m \frac{\partial \mathbf{v}}{\partial t} = -\nabla \left(\frac{1}{2}mv^2 + gn - \frac{\hbar^2}{2m\sqrt{n}} \nabla^2 \sqrt{n} + U \right). \quad (2.29)$$

By introducing the pressure using the Gibbs–Duhem relation $dP = nd\mu$, we finally arrive at

$$m \frac{\partial \mathbf{v}}{\partial t} + \frac{1}{n} \nabla P = \nabla \left(\frac{\hbar^2}{2m\sqrt{n}} \nabla^2 \sqrt{n} \right) - \nabla \left(\frac{mv^2}{2} \right) - \nabla U, \quad (2.30)$$

which we can now directly compare to the classical Euler equation

$$m \frac{\partial \mathbf{v}}{\partial t} + \frac{1}{n} \nabla P = m\mathbf{v} \times (\nabla \times \mathbf{v}) - \nabla \left(\frac{mv^2}{2} \right) - \nabla U. \quad (2.31)$$

Taking the restricted irrotational flow of our superfluids into account, the two equations differ only in that the GP equation has an additional term on the r.h.s., known as the quantum pressure term. Physically, this term originates from forces that arise due to spatial variations of the magnitude of the condensate wave function, and it becomes important only when spatial variations of the density occur on lengthscales shorter than the healing length.

2.4 Bogoliubov theory

In this section we give a brief overview of the pertinent aspects of Bogoliubov theory [42], which perturbatively extends our previous simple mean-field approximation to include the next order corrections from Eq. (2.16), and forms the basis of our discussion in Chapter 6.

At the heart of Bogoliubov theory is the formulation of non-interacting quasi-particle excitations, which historically matched Landau’s original heuristic picture of interacting quantum fluids. These quasi-particles feature the dispersion relation

$$\hbar\omega = \frac{\hbar^2 k^2}{2m} \sqrt{1 + \frac{2}{k^2 \xi^2}}, \quad (2.32)$$

which we plot as a function of k in Fig. 2.2 for ^{39}K at fixed $\bar{\xi} = 1 \mu\text{m}$. For large $k\xi$, Eq. (2.32) reduces to a quadratic dispersion relation and the excitations are particle-like, whereas at low $k\xi$ the dispersion is linear in k and the excitations correspond to collective sound-waves.

To obtain this quasi-particle description from Eq. (2.16), one recasts the Hamiltonian into quadratic form neglecting terms cubic and higher in $\hat{a}_{\mathbf{k}} \neq 0$, which yields a description in

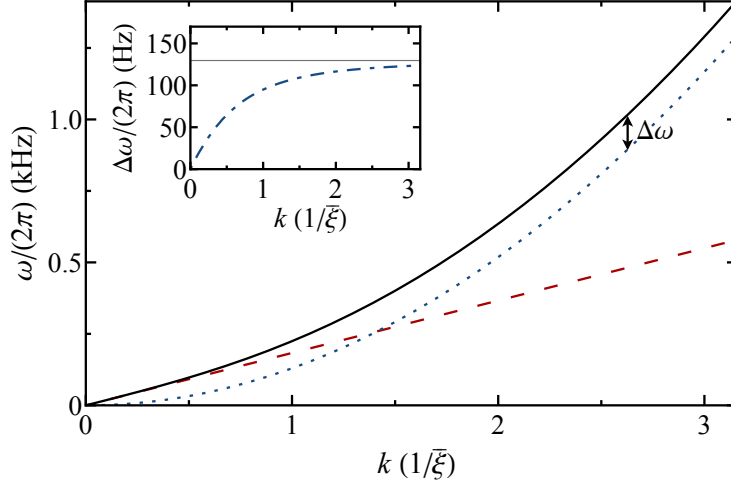


Fig. 2.2 Bogoliubov dispersion relation. The solid black line shows the Bogoliubov dispersion relation ω_B calculated for ^{39}K as a function of k [Eq. (2.32)], in units of $1/\bar{\xi}$, with fixed $\bar{\xi} = 1 \mu\text{m}$ (so as to feature typical experimental values; for example a gas with $n = 2 \mu\text{m}^{-3}$ and $a = 400 a_0$ has $\xi \approx 1 \mu\text{m}$). The dotted blue line shows the free-particle dispersion relation ω_0 , and the red dashed line corresponds to $\omega_p = ck$, where $c = \hbar/(\sqrt{2}\bar{\xi}m)$ is the speed of sound. The inset shows the frequency shift from the free-particle dispersion relation $\Delta\omega = \omega_B - \omega_0$ (dot-dashed line), which for large $k\bar{\xi}$ approaches a constant value $\Delta\omega_B = \hbar/(2m\bar{\xi}^2)$ (horizontal line).

terms of *independent* quasi-particles with energy $\epsilon = \hbar\omega$, again having replaced $\mathbf{k} = 0$ operators with \sqrt{N} and made use of particle number conservation $\hat{a}_0^\dagger \hat{a}_0 = N - \sum_{\mathbf{k} \neq 0} \hat{a}_\mathbf{k}^\dagger \hat{a}_\mathbf{k}$. These new quasi-particles are bosonic in nature and described by annihilation (creation) operators \hat{b} (\hat{b}^\dagger), so that

$$\hat{H} = \mathcal{E}_0 + \sum_{\mathbf{k} \neq 0} \epsilon(k) \hat{b}_\mathbf{k}^\dagger \hat{b}_\mathbf{k}, \quad (2.33)$$

where the ground state energy is found to be

$$\mathcal{E}_0 = \frac{gN^2}{2V} \left(1 + \frac{128}{15\sqrt{\pi}} \sqrt{na^3} + \dots \right), \quad (2.34)$$

as first theoretically demonstrated by Lee, Huang, and Yang [43,44]¹³, and recently experimentally confirmed by Navon *et al.* [45,46].

This reduction of the many-body Hamiltonian to diagonal form is achieved using the Bogoliubov transformation

$$\hat{a}_\mathbf{k} = u_\mathbf{k} \hat{b}_\mathbf{k} + v_{-\mathbf{k}}^* \hat{b}_{-\mathbf{k}}^\dagger, \quad \hat{a}_\mathbf{k}^\dagger = u_\mathbf{k}^* \hat{b}_\mathbf{k}^\dagger + v_{-\mathbf{k}} \hat{b}_{-\mathbf{k}}, \quad (2.35)$$

where $|u_\mathbf{k}|^2 - |v_{-\mathbf{k}}|^2 = 1$ (to satisfy the bosonic commutation relations) and

$$u_\mathbf{k}^2 = \frac{1}{2} \left[\frac{1 + 1/(k\xi)^2}{\sqrt{1 + 2/(k\xi)^2}} + 1 \right], \quad v_{-\mathbf{k}}^2 = \frac{1}{2} \left[\frac{1 + 1/(k\xi)^2}{\sqrt{1 + 2/(k\xi)^2}} - 1 \right]. \quad (2.36)$$

¹³This $\propto \sqrt{na^3}$ correction to the mean-field energy is known as the LHY correction.

The number of quasi-particles is not conserved ($\mu = 0$), and we assume a thermal population

$$N_{\text{quasi}} = \langle \hat{b}_{\mathbf{k}}^\dagger \hat{b}_{\mathbf{k}} \rangle = \frac{1}{\exp[\epsilon/(k_B T)] - 1}. \quad (2.37)$$

This is to be contrasted to the number of particles in the condensate

$$N_0 = N - \sum_{\mathbf{k} \neq 0} \langle \hat{a}_{\mathbf{k}}^\dagger \hat{a}_{\mathbf{k}} \rangle = N - \frac{V}{(2\pi)^3} \int \left(|v_{-\mathbf{k}}|^2 + \frac{|u_{\mathbf{k}}|^2 + |v_{-\mathbf{k}}|^2}{\exp[\epsilon/(k_B T)] - 1} \right) d\mathbf{k}. \quad (2.38)$$

Interestingly, the number of particles out of the condensate is non-zero even at $T = 0$; this is the interaction-driven quantum depletion of the condensate, which arises entirely due to quantum fluctuations. Performing the integral yields the famous prediction for the condensed fraction

$$n_0/n = 1 - \frac{8}{3\sqrt{\pi}} \sqrt{na^3}. \quad (2.39)$$

Finally, it is insightful to further resolve the momentum distribution of the quantum depleted fraction, which is given by the Bogoliubov coefficient $|v_{-\mathbf{k}}|^2$ (corresponding to pair-wise excitations out of the condensate), and reads

$$n_{\mathbf{k}}^{\text{QD}} = \frac{1}{2} \left[\frac{1 + 1/(k\xi)^2}{\sqrt{1 + 2/(k\xi)^2}} - 1 \right], \quad (2.40)$$

which is a distribution of typical width $1/\xi$, and features power-law behavior at both low and high momenta:

$$\left(n_{\mathbf{k}}^{\text{QD}} \right)_{k\xi \rightarrow 0} = \frac{1}{2\sqrt{2}k\xi}, \quad \left(n_{\mathbf{k}}^{\text{QD}} \right)_{k\xi \rightarrow \infty} = \frac{1}{4(k\xi)^4}. \quad (2.41)$$

2.5 Tan's contact

The two-body contact parameter C_2 is the central quantity amid a powerful set of universal relations that link the strength of short-range two-body correlations to the macroscopic thermodynamic behavior of a quantum many-body system. In particular, the contact connects quantities such as the ground-state energy and the high- k behavior of the momentum distribution and spectroscopic responses. It was first uncovered by Tan [47–49] in the context of ultracold Fermi gases, where it has been further explored theoretically [50–54] and verified experimentally [55,56] (see also [57–61]).

The description also extends to Bose gases [28,36,62–65], however the situation is complicated by Efimov physics which leads to three-body bound states [33,34,66] and three-body correlations that cannot be inferred from knowledge of the pairwise ones [62,63,65]. Formally,

universality is broken and requires the introduction of a second contact parameter, known as the three-body contact C_3 . However, away from unitarity coherent signs of the three-body contact are elusive, and one expects three-body physics to only slightly modify the scenario. We restrict our discussion to two-body contact interactions, governed by the two-body contact density C_2 , to briefly illustrate the power of these universal relations.

The two-body contact is related to the ground-state energy \mathcal{E}_0 via a derivative with respect to a ¹⁴, known as the adiabatic sweep theorem

$$\frac{\partial \mathcal{E}_0}{\partial a} = \frac{\hbar^2}{8\pi m a^2} C_2, \quad (2.42)$$

which upon inserting \mathcal{E}_0 [Eq. (2.34)] gives

$$C_2 = (4\pi n a)^2 \left(1 + \frac{64}{3\sqrt{\pi}} \sqrt{n a^3} + \dots \right). \quad (2.43)$$

To give one concrete example, we can now simply obtain the high- k behavior of the momentum distribution

$$n_{\mathbf{k} \rightarrow \infty} = \frac{C_2}{k^4}. \quad (2.44)$$

Indeed, this agrees with our Bogoliubov theory result [see Eq. (2.41)], which however only captures C_2 to mean-field level¹⁵ with $C_2 = (4\pi n a)^2$.

¹⁴For comparison, the three-body contact is related to the ground-state energy via a derivative with respect to the three-body parameter κ_* (which is inversely proportional to the size of the Efimov state).

¹⁵As typical for perturbation theory, the wave functions are ‘one step behind’ the energy.

3 Experimental Platform

In theory, there is no difference between theory and practice.

In practice, there is.

- anonymous -

The experimental platform at the heart of this thesis is an ultracold gas of ^{39}K confined to the quasi-uniform potential of an optical box trap. It combines key aspects of the two other machines in our group: the general design, vacuum chamber, and atomic-species-specific apparatus are inspired by ‘BEC II’ (see [67–70]), while the quasi-uniform optical box trap closely follows the set-up used in ‘BEC I’ (see [21, 71]). The aim of this chapter is to merely provide an overview of our experimental platform and the tools at our disposal for manipulating and probing ultracold samples, as the details of building and characterizing this machine are documented in two MPhil theses [22, 72]¹.

We begin in Section 3.1 with a brief overview of how we produce quasi-pure Bose–Einstein condensates in a quasi-uniform optical box potential, starting from a gas of ^{39}K at room temperature. In Section 3.2 we detail several key methods for probing and manipulating our ultracold samples, including the versatile ability to tune the effective interparticle interaction strength by changing an external magnetic field.

3.1 Sample preparation

Here we provide a brief overview of the initial stages of our experiment, describing how our ultracold ^{39}K samples are prepared; we refer the readers to [22, 72] for a more detailed account of our machine (see also [68, 69, 71]). In Section 3.1.1 we give an overview of the experimental apparatus and provide an outline of the methods used to initially cool a gas of ^{39}K from room temperature to tens of nanokelvin. Section 3.1.2 illustrates how we sculpt our optical box

¹It should be noted that in Chapter 4 our experiments are performed on BEC I (using ^{87}Rb in a box), which we omit in our discussion here as the relevant experimental concepts are the same; for a more in-depth discussion of BEC I see [71, 73–75].

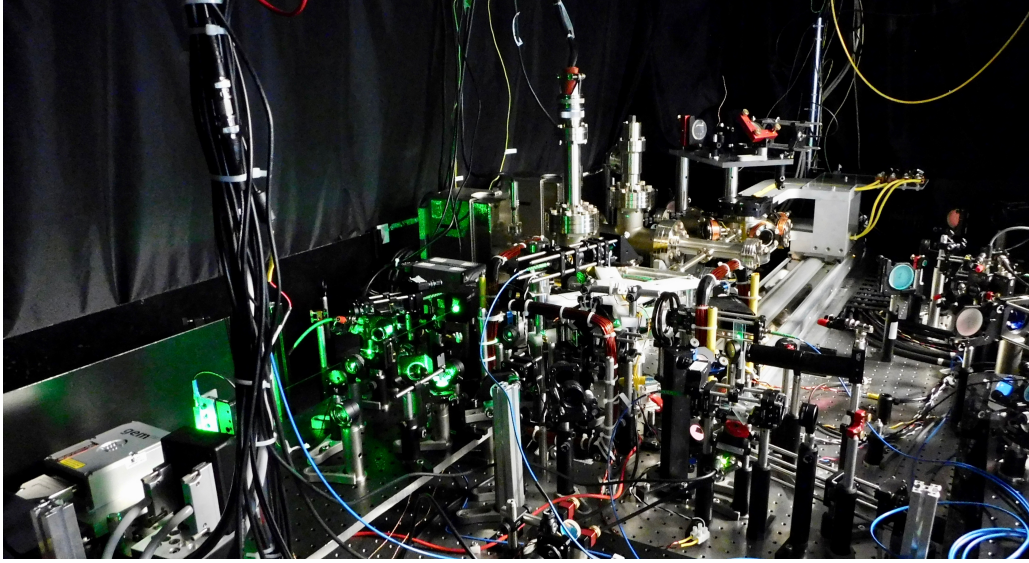


Fig. 3.1 Photograph of the main experimental apparatus. The final part of the experiment takes place within the ‘science chamber’, a glass cell surrounded by the white cross-shaped Feshbach coil holder seen in the middle of the image.

trap and describes the loading of our pre-cooled atoms into this final trapping geometry, also providing our benchmarks of its uniformity.

3.1.1 Bose–Einstein condensation

The vacuum system that comprises the backbone of our experimental apparatus consists of two chambers, connected by a narrow tube to allow for differential pumping (using two ion pumps along the tube)². Our magneto-optical trap (MOT) is situated at one end, where each experiment begins by laser-cooling a sample of ^{39}K from background vapor³. After initial trapping and cooling of the atoms in the MOT we use a gray molasses cooling protocol [76–78], which enables sub-doppler laser cooling of the atoms to $\sim 10\ \mu\text{K}$. We then optically pump (using D1 light) the atoms into the $|F, m_F\rangle = |2, 2\rangle$ hyperfine ground state before trapping them in a magnetic quadrupole trap and mechanically transporting $\sim 3 \times 10^8$ atoms to the ‘science cell’ at the other end. Figure 3.1 shows a photograph of our experimental apparatus, while Fig. 3.2 shows a detailed overview of the coils and laser beams in the region surrounding the science cell.

Once in the science cell, we proceed by ramping on an optical dipole trap (ODT), generated using a 20 W 1070 nm laser beam of $\sim 30\ \mu\text{m}$ waist crossed with a recycled beam of waist $\sim 100\ \mu\text{m}$. We subsequently switch off the magnetic trap to leave $\sim 10\%$ of the atoms trapped in a purely optical trap. We perform a radio frequency Landau-Zener (LZ) [79,80] sweep of the

²We reach a pressure of $\sim 10^{-12}$ mbar in the science cell, manifesting itself as a one-body lifetime of > 100 s.

³To maintain a steady background vapor gas of ^{39}K in the vacuum system we provide additional ^{39}K using getter material that resides inside the vacuum chamber, and which we discharge daily by applying a current of 5.5 A through the material for ≈ 80 s (see also [68]).

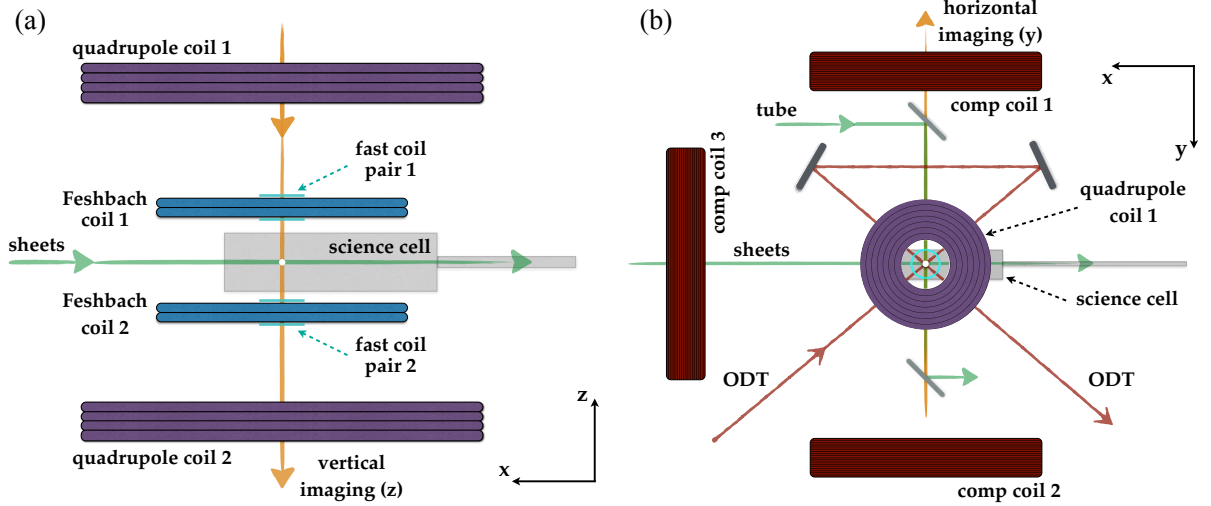


Fig. 3.2 Schematic of the science cell surroundings. We highlight the essential laser beams and current carrying coils used to trap and manipulate our atomic samples. (a) side view along $-y$ and (b) top view. The repulsive light used to form the cylindrical box potential (sheets and tube) is shown in green. The optical dipole trap used for evaporation is shown in dark red, while the imaging light is shown in orange. The location of the atoms is indicated by the white circle. The Feshbach coils (blue) are used to create the uniform magnetic field. The quadrupole coils (purple) initially trap and then mechanically transport the atoms to the science cell. Quadrupole coil 2 is used in conjunction with the three compensation coils ('comp coil', brown) to magnetically levitate the cloud. A pair of auxiliary 'fast coils' (cyan) is positioned around each Feshbach coil in order to minimize inductive coupling and allow fast switching of the magnetic field.

atoms from the $|2, 2\rangle$ state to the $|1, 1\rangle$ state, where a Feshbach resonance at a field of $402.70(3)$ G occurs (see Section 3.2.1), enabling us to vary the scattering length of the atoms during the evaporative cooling process. This allows us to optimize the evaporation procedure, which relies on scattering events to redistribute energy in order for cooling to occur. After ~ 5 s of evaporation, where the trap depth is decreased by a factor of ~ 700 , we form (harmonically trapped) BECs of up to $\sim 3 \times 10^5$ atoms, at condensed fractions of around 50%⁴.

3.1.2 Quasi-uniform potential

We then load the condensate into the cylindrical optical box potential formed by 532 nm laser light, blue-detuned to ensure that the atoms feel a repulsive potential due to the dipole force (see *e.g.* [32]). The method used to sculpt the box potential directly follows the footsteps of [21], and is described in detail for our experimental set-up in [22]. In short, we begin by controlling and stabilizing the power of a near-gaussian beam coming directly from a commercial source⁵ using an acousto-optic modulator with a proportional-integral feedback control system. The diffracted gaussian beam is then reflected off a single phase-only spatial light modulator (SLM) in order to produce three spatially separated beams at a first focal plane: One hollow ring (the

⁴Note that while lowering the trap depth further would result in more pure harmonically trapped samples, we find that these parameters maximize the final atom number in the box.

⁵We use a Laser Quantum Gem 532, which features a short coherence length (~ 1 cm) so as to minimize interference effects.

tube of the cylinder) and two thin sheets (its end caps). These beams are overlapped at a right angle and re-imaged to form a cylindrical box of light in which the atoms reside. We ensure the focus and quality of our sculpted optical box by performing a wave-front correction protocol [22], inspired by previous work [81] that exploits the tuneable nature of the SLM to implement the Shack-Hartmann procedure [82]. To further ensure a uniform potential in the dark central region of the box we cancel gravity and the effect of any magnetic field gradients to the $\sim 10^{-4} g_0$ level, where g_0 is the gravitational acceleration. Our coils are also positioned to achieve low (negligible) residual magnetic field curvatures with associated frequencies ≈ 1 Hz (trapping in a direction in the x - z plane and anti-trapping in the two orthogonal directions).

We achieve a quasi-uniform trapping potential, which is thermodynamically well described by a $r^{15(4)}$ power-law. For most purposes in this thesis our potential can be well approximated by a uniform cylindrical box of length L and radius R . The box dimensions are set by the SLM parameters and are tuneable between experimental repetitions⁶. We typically work with box dimensions in the range $(10 - 50) \mu\text{m}$, for which we are able to ensure uniformity [22].

In order to form quasi-pure condensates in our box trap, we perform a final stage of evaporation where we lower the depth of the box trap to $< k_B \times 50$ nK. This typically produces condensates of up to $(2 - 3) \times 10^5$, with condensed fractions of $> 95\%$ and a shot-to-shot standard deviation of around 3%. In order to reduce the atom number we simply increase the scattering length at the end of evaporation (before loading into the box) to make use of three-body recombination losses. This is beneficial as it is a self-normalizing process (*i.e.* one loses more when starting with more); for details of our atom number control and stability see Section B. In order to prepare thermal samples we subsequently raise the trap depth again (which sets the maximum temperature that can be reached due to evaporation) and violently oscillate a magnetic field gradient which ultimately leads to an equilibrium thermal gas at varying temperature and atom number (set by the shaking amplitude, trap depth, and initial atom number; see [22] for details)⁷.

3.2 Manipulating and probing samples

Having reviewed how we prepare initially degenerate (or thermal) Bose gases in a quasi-uniform box potential, we now turn to an overview of the tools used to manipulate and probe our gases. In Section 3.2.1 we outline how Feshbach resonances allow us to vary the interaction

⁶Our phase-only SLM (Hamamatsu X10468-04 with pixel size $20 \mu\text{m}$ and dimensions $800 \text{ pixels} \times 600 \text{ pixels}$) does not allow for reliable dynamical changes on experimentally relevant timescales.

⁷We use such a reheating protocol compared to directly loading a thermal cloud as this method avoids trapping cold atoms outside of the box potential (*e.g.* in the tube), which are subsequently difficult to remove.

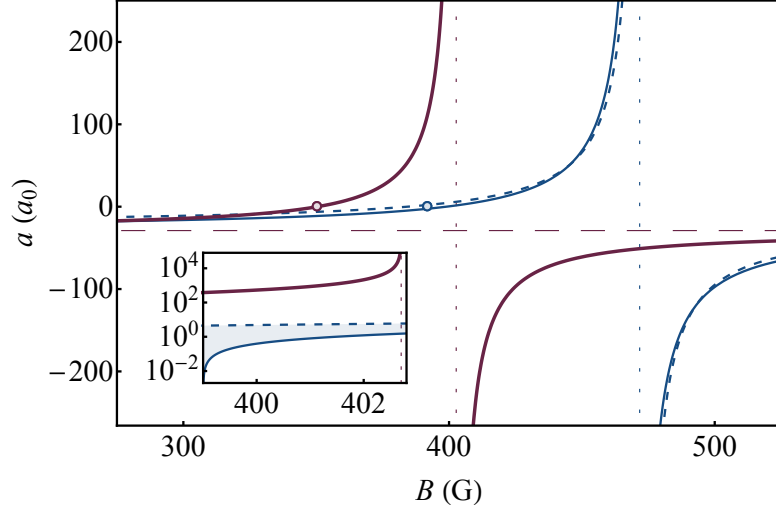


Fig. 3.3 Controlling interparticle interactions using magnetic Feshbach resonances. We plot the magnetic Feshbach resonances for ^{39}K in the $|1, 1\rangle$ (red) and $|1, 0\rangle$ (blue) hyperfine state around 400 G. The approximate resonance position is indicated by the vertical dotted lines, while the horizontal dashed line depicts the background scattering length a_{bg} for $|1, 1\rangle$. The open circles indicate the approximate zero-crossing of the two resonances. For the $|1, 1\rangle$ state $B_\infty = 402.70(3)$ G [65], $\Delta = -52.25(4)$ G [26], and $a_{\text{bg}} \approx -29 a_0$ [83,84]. For the resonance in the $|1, 0\rangle$ state high-precision measurements are elusive, and we instead plot two independent theoretical predictions: solid - [83] and dashed - [84]. In the inset, we show a zoom-in of the region around the $|1, 1\rangle$ resonance on a log plot. This reveals the remarkable feature that while the scattering length in the $|1, 1\rangle$ state varies from $\sim 400 a_0$ to ∞ , the $|1, 0\rangle$ state is essentially non-interacting ($|a| < 10 a_0$), but repulsive ($a > 0$).

strength by changing the magnetic field strength. Section 3.2.2 describes our absorption imaging protocol used to photograph (and ultimately destroy) the sample after every experimental cycle. We also include a brief summary of two invaluable spectroscopic tools: radio-frequency spectroscopy in Section 3.2.3 and Bragg spectroscopy in Section 3.2.4.

3.2.1 Tuning interactions

Owing to the existence of molecular Feshbach resonances [7], we are able to tune the effective scattering length a by varying an external magnetic field. This remarkable feature makes ultracold atom experiments unparalleled in terms of studying the effect of interactions in quantum many-body problems.

Feshbach resonances

Feshbach resonances occur due to resonant behavior when the energy of a pair of particles is similar to that of a molecular bound state, in an energetically forbidden quantum state. Since the energy depends linearly on the magnetic field strength (due to the Zeeman effect) this leads to a second-order perturbation-theory-type dependence of a on B given by

$$a(B) = a_{\text{bg}} \left(1 - \frac{\Delta}{B - B_\infty} \right), \quad (3.1)$$

where a_{bg} is the background scattering length, B_∞ the resonance position and Δ the resonance width, defined as the distance in field between B_∞ and B_0 , where $a(B_0) \equiv 0$ ⁸. In Fig. 3.3 we show a sketch of the Feshbach resonances for both $|1, 1\rangle$ and $|1, 0\rangle$ states of ^{39}K at around 400 G. We perform most of our experiments using spin-polarized samples in $|1, 1\rangle$, though the $|1, 0\rangle$ state acts as an invaluable resort.

Field control

As we have seen the problem of tuning a has been reduced to a problem of controlling the magnetic field strength. We use a set of electromagnetic coils (see Fig. 3.2) to create a tuneable magnetic field, that is essentially uniform apart from a magnetic field gradient used to cancel the gravitational force that the atoms experience (for details see [22]). To vary B we simply vary the current in the coils, while striving to maintain gravity (and other field gradient) compensation throughout. For our main coils these field variations are limited to \gtrsim ms timescales. For situations where faster field quenches are desired, we additionally utilize a set of auxiliary ‘fast coils’ that allow rapid field quenches in a few μs . A detailed characterization as well as additional technical details can be found in Section D.2 (see also [86]).

3.2.2 Imaging & measurement

Our experiments are performed in cycles, where for every experimental realization we begin with a room temperature gas of ^{39}K and subsequently produce quasi-pure condensates within ~ 20 s⁹, as described above. At the end of each cycle, we record absorption images [32] of the atomic samples, providing a glimpse of its properties (such as atom number or kinetic energy per particle), before ultimately destroying the sample.

We image the atoms at low field, first optically pumping them back into the $|F = 2\rangle$ state¹⁰ before resonantly imaging them using the $|F = 2\rangle \rightarrow |F' = 3\rangle$ transition along one of two directions [viewing either along the axis of the cylinder or in a perpendicular direction (from the top)]. Our imaging is performed using low intensity, with $I \approx 0.1 I_s$, where $I_s = 1.75 \text{ mW/cm}^2$ is the saturation intensity of the transition. The absorption imaging essentially integrates over the line-of-sight, and so we obtain the two-dimensional column density after conversion from

⁸Feshbach resonances can also occur when using other methods to shift the energy levels with respect to each other; for example optical potentials can be used to achieve similar feats (see [85] for an overview).

⁹The typical duration of an experimental cycle ranges between 30 - 40 s, depending on the experiments performed.

¹⁰Our pumping uses D1 light with σ^+ polarization, which pumps atoms to $|F' = 2, m'_F = 2\rangle$ in the $4^2P_{1/2}$ state. The atoms subsequently decay back to the $|F = 2\rangle$ manifold, but not all of the atoms end up in the $|2, 2\rangle$ state (a significant fraction also decays to $|2, 1\rangle$). We have calibrated the resulting error in the measured atom number by instead using an essentially 100% efficient LZ transfer back to the $|2, 2\rangle$ state. We find that the atom number measured this way is 1.32(1) times that measured using the optical pumping protocol.

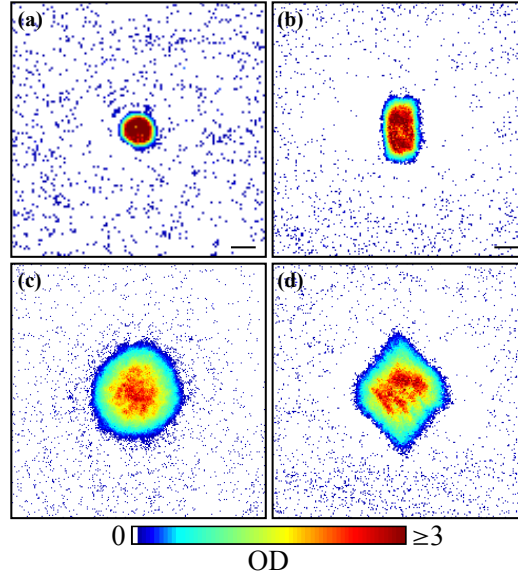


Fig. 3.4 Absorption images of homogeneous Bose–Einstein condensates trapped in a cylindrical optical box. (a,b) In-situ images for horizontal and vertical imaging, respectively (the actual in-situ optical density is > 100 however our imaging saturates at about 3). Scale bar corresponds to $30 \mu\text{m}$. (c,d) Time-of-flight absorption images, allowing the clouds to expand in the presence of interactions. Image adapted from [22].

the measured optical density (where we assume an ideal imaging cross-section, taking into account the pumping efficiency and the finite imaging intensity).

In Fig. 3.4 we show examples of typical absorption images of box-trapped quasi-pure homogeneous Bose–Einstein condensates along these two directions, both in-situ and following ToF expansion in the presence of interactions. The in-situ images highlight the cylindrical box shape, while in ToF (in the non-symmetric direction) the characteristic diamond-like shape with flattened edges clearly reveals the quantum nature of the gas [71, 87, 88].

3.2.3 Radio-frequency spectroscopy

In order to accurately tune the interparticle interaction strength we require precise control of the magnetic field that the atoms experience. Using ordinary field probes is not possible due to the fact that the atoms reside in a vacuum chamber that cannot regularly be opened. However, our atomic samples themselves are extremely sensitive to magnetic fields, and thus provide the best magnetic field probe at our disposal.

An external magnetic field leads to a hyperfine splitting between the different internal states, which can be calculated using the Breit–Rabi formula [89], and is plotted for ^{39}K in Fig. 3.5(a). Outside of the Paschen–Back regime (high- B), the energy differences between the states are field dependent, which allows for a direct probe of the magnetic field using radio-frequency (rf) photons. Here we confine our discussion to rf-driven transitions between the $|1, 1\rangle$ and the $|1, 0\rangle$ state, which are suitable for our field calibration but also have the additional advantage of

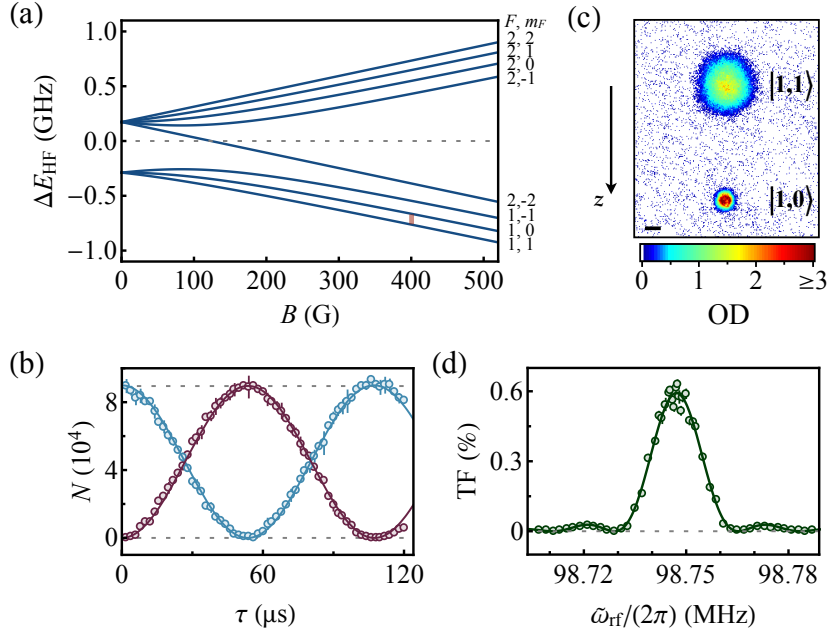


Fig. 3.5 Radio-frequency spectroscopy. (a) Hyperfine structure in the $4^2S_{1/2}$ ground state of ^{39}K as a function of B , calculated using the Breit–Rabi formula. (b) Measured evolution of N in $|1, 1\rangle$ (blue) and $|1, 0\rangle$ (red) for an on-resonance rf-pulse of variable pulse duration τ , exhibiting a coherent Rabi oscillation between the two states. (c) ToF absorption image following a $\pi/2$ pulse for a cloud at a magnetic field of 399.38(1) G [inferred from (d) and indicated as the red vertical line in (a)]. The difference in relative size of the clouds clearly highlights the dramatic difference in interaction strength between the two states, and the two states separate in space due to their slightly different magnetic moments at these intermediate field strengths (we use 45.08(3) ms ToF expansion). The scale bar corresponds to 50 μm . (d) Radio-frequency spectrum, plotting the transferred fraction (TF) versus applied rf-frequency $\tilde{\omega}_{\text{rf}}/(2\pi)$. We extract a resonance frequency $\omega_{\text{res}}/(2\pi) = 98.7471(1)$ MHz, corresponding to a 2-mG statistical uncertainty in B .

enabling a fast interaction switch (see Section 3.2.1 and [29, 65, 90]). The splitting between $|1, 1\rangle$ and $|1, 0\rangle$ grows monotonically in field, and for the range of fields of interest to us (350 - 450) G, the sensitivity of our RF spectroscopy (set by the slope of the energy-level difference) ranges between 63 and 38 kHz/G.

Throughout an rf-pulse the system evolves as a superposition of the two states, exhibiting Rabi oscillations between the two states [32]. For a system initially spin-polarized in $|1, 1\rangle$, the transition probability to $|1, 0\rangle$ takes the form

$$P_0 = \frac{\Omega^2}{\delta^2 + \Omega^2} \sin^2(\sqrt{\Omega^2 + \delta^2} \tau/2), \quad (3.2)$$

where τ is the rf-pulse duration, $\delta = \omega_{\text{res}} - \tilde{\omega}_{\text{rf}}$ is the detuning of the applied rf-frequency $\tilde{\omega}_{\text{rf}}$ with respect to the resonance frequency ω_{res} (set by the energy level splitting¹¹), and Ω is the on-resonance Rabi frequency. In Fig. 3.5(b) we show a measurement of such an on-resonance Rabi oscillation with a π -pulse time $\tau_\pi = 53.6(1)$ μs , corresponding to $\Omega/(2\pi) \approx 9.3$ kHz. From Eq. (3.2) we see that the effective Rabi frequency $\Omega_{\text{eff}} = \sqrt{\Omega^2 + \delta^2}$ slightly increases off

¹¹While rf spectroscopy is also sensitive to differences in interaction energy between the clouds in the two states, these shifts are typically $\lesssim 100$ Hz, corresponding to only a few-mG systematic shifts.

resonance, while the maximal transfer probability is suppressed. For our perturbation $\hat{H}_p = \hat{H}_p^0 \cos(\tilde{\omega}_{\text{rf}}\tau)$, the Rabi frequency is given by the matrix element between the two states $\hbar\Omega = \langle 1, 1 | \hat{H}_p^0 | 1, 0 \rangle$, which experimentally translates to a scaling $\Omega \propto \sqrt{P_{\text{rf}}}$, where P_{rf} is the rf-power supplied¹².

As illustrated by the ToF absorption image in Fig. 3.5(c), performing a ToF expansion realizes a Stern–Gerlach experiment [92], as the two spin states separate in space due to their different magnetic moments at these intermediate field strengths. We compensate gravity and any residual magnetic field gradients to within $2 \times 10^{-4} g_0$ for the $|1, 1\rangle$ state, which leaves the $|1, 0\rangle$ state with the ratio of magnetic moments as the residual acceleration. At a field of 399.38(1) G, as used in Fig. 3.5(c), this corresponds to feeling a residual 3.6% of gravity, which for our ToF of 45.08(3) ms predicts a separation of 360(1) μm , in agreement with the measured displacement of 358(4) μm ¹³. The fact that the two spin components separate in a clean manner without any apparent collisions is in line with the relatively weak inter-state scattering length, which for the range of fields explored here is positive but below $10 a_0$ [84].

In Fig. 3.5(d) we show a typical example of a high-resolution rf-spectrum, used to calibrate the magnetic fields at which we work. We achieve a precision on the single-mG level, which is smaller than typical absolute field drifts (of order ~ 10 mG) over the course of a day. Note that in order to achieve these precisions, we are required to trigger our measurements on the 50 Hz alternating-current mains cycle, which feeds into our coils and leads to a 50 Hz (and multiples thereof) modulation of the field that our coils produce, with a non-negligible amplitude of ≈ 100 mG¹⁴. A detailed characterization of this oscillation, as well as further information about our field control and stability can be found in Section D.1.

3.2.4 Bragg spectroscopy

In the context of ultracold atomic gases, Doppler-sensitive two-photon Bragg scattering [93,94] has proven to be a versatile spectroscopic probe, and it has become a standard tool in the arsenal of many modern experiments. In contrast to the historical Bragg scattering of x-rays off periodic atomic lattices [95,96], here instead the atoms scatter off a periodic light potential (obtained by interfering two laser beams), which selectively imparts momentum to the atoms. In this section we provide an overview of the experimentally relevant aspects of Bragg

¹²The rf antenna is formed by a single $\varnothing 3.5$ mm wire wound into a circular $\varnothing 70$ mm coil, designed to achieve maximal emission signals at around 100 MHz. We use a variable capacitor to achieve impedance matching; see [91] for details.

¹³We have separately calibrated the apparent pixel size s_{pix} using the mechanical transport track to controllably move the cloud in a magnetic trap (and cross-calibrated both our imaging systems this way); this could otherwise also be achieved using the measurement presented here (or generally the free fall of a cloud under gravity). For horizontal imaging we have $s_{\text{pix}} = 2.59(3)$ μm , whereas for vertical imaging $s_{\text{pix}} = 1.60(4)$ μm .

¹⁴This issue could be readily overcome by running the power supplies on batteries.

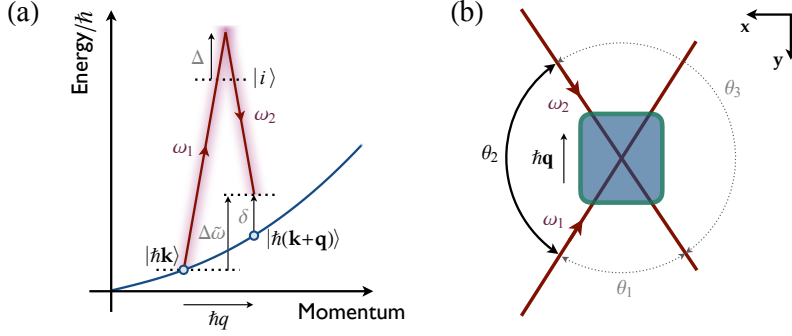


Fig. 3.6 Bragg spectroscopy concepts. (a) Sketch of laser arrangement for performing Bragg spectroscopy (not to scale). The two Bragg beams couple the atomic states $|\hbar\mathbf{k}\rangle$ and $|\hbar(\mathbf{k} + \mathbf{q})\rangle$ via an intermediate state $|i\rangle$. The resonance condition is given by $\delta = 0$, and depends on both the initial momentum and the dispersion relation. (b) Top-view cartoon of the orientation of the two laser beams intersecting on our atomic sample (blue) confined in the cylindrical box trap (green). The cartoon is not to scale: in reality the box dimensions are $\lesssim 50 \mu\text{m}$ and the beam widths are $\approx 1 \text{ mm}$. The beams form a moving optical lattice of period $2\pi/q$ and speed $\Delta\tilde{\omega}/q$ (not shown). We highlight our most used laser configuration with $\theta_2 = 133.6(1)^\circ$, which approximately achieves an axial momentum kick. We make use of a third counter-propagating beam overlapped with ω_2 (so that $\theta_3 = \pi$), to easily obtain access to three distinct \mathbf{q} .

spectroscopy; a detailed description of the theory of two-photon atom-light interactions can be found in many places (*e.g.* [32]), and the more technical aspects of our Bragg spectroscopy set up are detailed in [91, 97].

The essence of Bragg scattering can be understood by simple means of energy and momentum conservation. As depicted in Fig. 3.6(a), let us consider an artificial three-level system consisting of two momentum states (from the continuum) that are coupled by two laser beams of frequency ω_1 and ω_2 via an intermediate state $|i\rangle$ (from which we are detuned by Δ). The two beams essentially have the same wavelength (and corresponding recoil momentum k_{rec}) apart from a small frequency difference $\Delta\tilde{\omega} = \omega_1 - \omega_2$. The beams are intersected on the atoms at an angle θ , so that the corresponding wave vector is $\mathbf{q} = \mathbf{k}_1 - \mathbf{k}_2$ with its magnitude given by

$$q = 2 \sin\left(\frac{\theta}{2}\right) k_{\text{rec}}. \quad (3.3)$$

In a stimulated process the atom initially in momentum state $|\hbar\mathbf{k}\rangle$ can absorb a photon from ω_1 and coherently re-emit into ω_2 , which imparts a momentum $\hbar\mathbf{q}$ to the atom. This process is resonant ($\delta = 0$ so that $\Delta\omega = \Delta\tilde{\omega}$) when energy is conserved

$$\hbar\Delta\omega = \frac{\hbar^2 q^2}{2m} + \Delta E_{\text{int}} + \frac{\hbar^2}{m} \mathbf{k} \cdot \mathbf{q}, \quad (3.4)$$

where the three terms correspond (left to right) to: the recoil energy acquired by a diffracted atom, the difference in per-particle interaction energy between the two states (see *e.g.* Section 2.4), and the energy shift arising from the Doppler effect when the atom's initial velocity

has a component along \mathbf{q} .

During a Bragg pulse the two atomic states $|\mathbf{k}\rangle$ and $|\mathbf{k} + \mathbf{q}\rangle$ in our artificial three-level system are coherently coupled by the Bragg beams and thus undergo Rabi oscillations as a function of the pulse duration τ , where the probability to be diffracted to $|\mathbf{k} + \mathbf{q}\rangle$ is

$$P_{\text{B}} = \frac{\Omega^2}{\Omega^2 + \delta^2} \sin^2 \left[\sqrt{\Omega^2 + \delta^2} \frac{\tau}{2} \right]. \quad (3.5)$$

Here Ω is the two-photon Rabi frequency, which is related to the single-photon Rabi-frequencies of the two individual transitions via $\Omega \simeq \Omega_1 \Omega_2 / (2\Delta)$ (provided $|\Delta| \gg \Omega_i$, with $i \in \{1, 2\}$, which is satisfied throughout).

Experimentally, we use D2 laser light with a wavelength $\lambda_{\text{D2}} = 766.7$ nm, so that $k_{\text{rec}} = 2\pi/\lambda_{\text{D2}} \approx 8.2/\mu\text{m}$. The intensity of the two beams is kept roughly equal (to within $\lesssim 5\%$), the beams are ≈ 1 GHz red-detuned from the D2 transition, and have $\hat{\pi}$ polarization. These parameters ensure that losses due to spontaneous emission are minimal; the expected fraction lost per π -pulse is $\pi\Gamma/|\Delta| \approx 2\%$, where $\Gamma/(2\pi) \approx 6$ MHz is the line width of the intermediate state. In our experiments in Chapter 6 we make use of three angles $\{\theta_1, \theta_2, \theta_3\} = \{66.4^\circ, 113.6^\circ, 180^\circ\}$ [see Fig. 3.6(b)], which gives us access to three different \mathbf{q} with $q \in \{1.1, 1.7, 2.0\} k_{\text{rec}}$, and corresponding recoil velocities $|\mathbf{v}_{\text{r}}| = \hbar|\mathbf{q}|/m \in \{14.6, 22.3, 26.7\} \mu\text{m}/\text{ms}$. In the absence of any interaction shifts the free-particle resonance frequencies are $\Delta\omega/(2\pi) \in \{10.43, 24.37, 34.81\}$ kHz. The two-photon Rabi frequency Ω is linked to the experimental parameters via

$$\Omega = \frac{\Gamma^2 I}{4\Delta I_{\text{s}}}, \quad (3.6)$$

which crucially is proportional to the beam intensity.

Equipped with our three-level system analysis let us now consider the full continuum of momentum states that we experimentally probe. For the purposes here we restrict our discussion to the use of \mathbf{q}_2 , which is aligned with the axial length of our cylindrical box, so we effectively probe the integrated one-dimensional momentum distribution of the cloud along $\hat{\mathbf{y}}$. For a homogeneous pure BEC the distribution is sinc²-like with a Heisenberg-limited momentum width $\sim \pm\hbar/L$, corresponding to a spectral full-width-half-maximum (FWHM) $0.44 \times 4\pi v_{\text{r}}/L$ [87]. Our spectroscopic resolution is set by Ω , corresponding to a momentum resolution of $\Omega m/q$. To perform high-resolution Bragg spectroscopy we thus want to minimize Ω and maximize τ , while keeping the diffracted fraction $\lesssim 10\%$ so that our experiments can be interpreted within linear-response theory [17].

In Fig. 3.7(a) we show an example of a typical Bragg spectrum of a weakly-interacting sam-

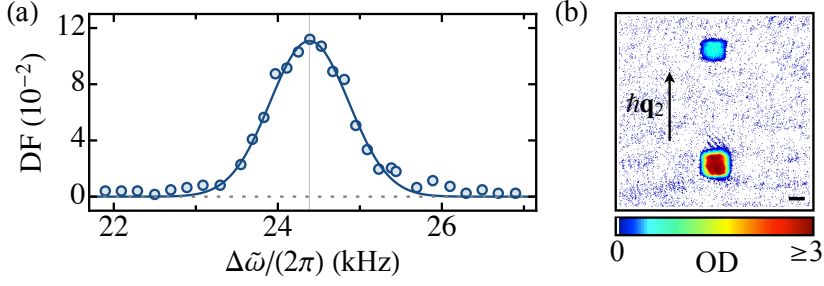


Fig. 3.7 Bragg spectroscopy. (a) Bragg spectrum showing the recorded diffracted fraction (DF) as a function of the frequency difference between the beams $\Delta\tilde{\omega}/(2\pi)$. The spectroscopy is performed with a 1-ms Bragg pulse with wave vector \mathbf{q}_2 on a weakly-interacting cloud with $a \approx 70 a_0$ and $n \approx 2.0 \mu\text{m}^{-3}$, in a box of length $L \approx 50 \mu\text{m}$. We use a gaussian fit to extract the resonance position $\Delta\omega/(2\pi) = 24.39(2)$ kHz and full-width-half-maximum $\sigma_{\text{FWHM}} = 1.13(4)$ kHz. (b) Absorption image of the Bragg diffraction of an essentially non-interacting homogeneous sample after 15 ms time-of-flight showing the stationary (bottom) and diffracted (top) clouds. The cloud is prepared as in (a) but for aesthetic purposes we perform a $64 \mu\text{s}$ π -pulse to the $|1, 0\rangle$ state, before applying the Bragg pulse. Scale bar corresponds to $50 \mu\text{m}$.

ple, where we are still sufficiently deep in the Thomas–Fermi regime so as to keep the density quasi-uniform, but where interaction shifts are essentially negligible. We obtain a resonance frequency $\Delta\omega/(2\pi) = 24.39(2)$ kHz (extracted using a gaussian fit), which demonstrates the fact that the interaction energy is near-negligible (indeed we expect only a 20 Hz shift), and the displacement following ToF is in line with v_r . To obtain a Heisenberg-limited width (which in this case would correspond to $\sigma_{\text{FWHM}} \approx 400$ Hz) we would also need to avoid any Fourier broadening and use pulse times $\tau \gtrsim L/v_r \approx 2.2$ ms, which equivalently ensures that a recoiling atom can traverse the box during the pulse (and leave assuming that the recoil energy is larger than the trap depth, as is the case here)¹⁵.

¹⁵While measurements with $\tau \gtrsim 4$ ms do recover Heisenberg-limited widths to within $< 10\%$ (see also [87]), we empirically found the best signal-to-noise (for fixed ≈ 100 images), and ultimately precision on $\Delta\omega$, by allowing for slightly larger Ω but accepting slight Fourier broadening by using τ between 1-2 ms (see also Fig. 6.7).

4 Turbulent-Cascade Fluxes

Big whirls have little whirls
that feed on their velocity,
And little whirls have lesser whirls
and so on to viscosity
- Lewis F. Richardson [98] -

4.1 Introduction

A continuously driven fluid can become turbulent, exhibiting irregular fluctuations. This familiar yet complex phenomenon is observed in a myriad of physical systems ranging from biology to astrophysics; examples include arterial blood [99], surface water waves [100–104], clear air [105], optical beams [106–109], supernovae [110], and interplanetary media [111, 112]. While turbulence is truly ubiquitous, its multifaceted nature also makes it difficult to define concisely. Turbulence generally describes a field that is in a state far from equilibrium, which involves many interacting degrees of freedom, spans vastly different lengthscales, displays chaotic properties, involves drive and dissipation, is statistically steady, and displays local restoration of symmetries (isotropy and homogeneity)¹.

The study of turbulence is a long-standing endeavor, with early observations dating back to da Vinci in the early 16th century [114] and first quantitative experiments being performed by Reynolds in the late 19th century [115]. Throughout the years it has attracted considerable cross-disciplinary attention, however even today it remains a somewhat mysterious phenomenon.

A foundational breakthrough occurred in 1941, when Kolmogorov and Obukhov discovered a universal law describing the transfer of energy from large to small lengthscales in turbulent flows [116–118]². In contrast to their extremely complex real-space dynamics, turbu-

¹Note that all of these properties are not necessarily fulfilled, a particularly famous example being intermittency bursts, breaking the statistically time-invariant nature of the state (see *e.g.* [113]).

²Note that in certain cases inverse cascades can also occur, where energy flows from small to large lengthscales instead; two-dimensional fluids are a famous example in which this is the case [119–122].

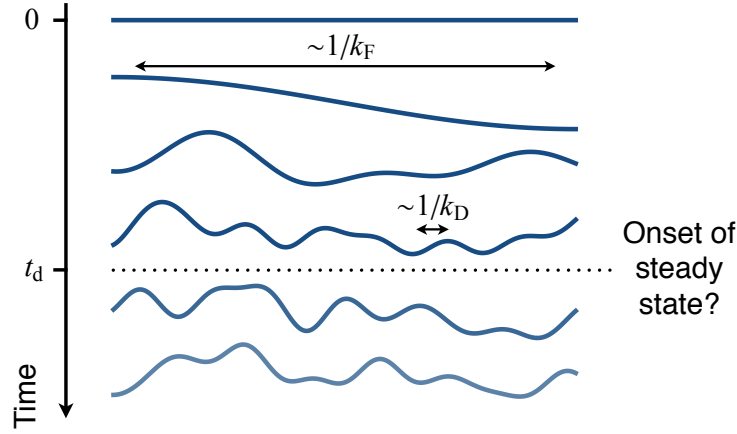


Fig. 4.1 Cartoon of turbulent cascade dynamics. For illustration, we consider a compressible field in real space, where from time $t_s = 0$ onwards energy is injected at a large lengthscale ($1/k_F$). The nonlinear interactions then propagate the energy to ever smaller lengthscales (larger k), and once the excitations reach the dissipation lengthscale ($1/k_D$) at time t_d , a steady-state can be established. Figure from [27].

lent flows often feature comparatively simple Fourier-space dynamics, where scale-invariant cascade-fluxes transport energy across very different lengthscales, sustaining scale-free steady-state behavior across the propagation lengthscales.

A typical scheme for generating turbulence is by injecting a disturbance into a field at a specific length scale. As shown in Fig. 4.1, the (in this case compressible) field initially at rest is continuously forced (at times $t > 0$) at large lengthscale $1/k_F$. Nonlinear interactions then promote the excitations to ever smaller lengthscales (larger k) in relay fashion until they reach the dissipation lengthscale $1/k_D$ (at time t_d), at which point the field is fluctuating on all lengthscales between $1/k_F$ to $1/k_D$ ³. The interplay between driving and dissipation can, rather miraculously, lead to steady-state properties on these intermediate lengthscales known as the inertial range. If such a steady-state is achieved, conservation of energy simply dictates that energy is dissipated at k_D at the same rate at which it is injected at k_F . Crucially, within the inertial range universal transport laws emerge, responsible for turbulent cascades in which conserved quantities such as the energy or wave density obey k -space power-law distributions.

Even though not always understood from first principles, this simple picture has proven to be remarkably universal, and such turbulent cascades have been observed in a plethora of different systems, including tidal channels [123], solar wind [124], interplanetary plasma [112], liquid helium [125], dwarf galaxies [126], financial markets [127], and the hippocampus [128], just to name a few. In comparison, the underlying scale-invariant cascade-fluxes are harder to measure as their extraction typically relies on non-trivial assumptions [129–132].

³As a familiar classical example, consider water flowing around a pillar. The velocity field is perturbed on the scale of the pillar’s diameter. Now, further down the flow, large eddies interact with each other forming ever smaller eddies. This transfer of energy to smaller scales happens until the energy is ultimately dissipated at very small scales, where inertial forces are overcome by viscous ones.

Turbulence in quantum (superfluid) systems features two profound differences as compared to classical fluids. First, superfluids have no intrinsic dissipation scale, which alters the conventional picture of how dissipation can occur [133]. Secondly, superfluids exhibit highly restricted flow properties, as the flow is irrotational apart from vortex lines with quantized circulation (in units \hbar/m), in which the density must vanish along the core in a well-defined manner featuring a regular core structure (see Section 2.3 and *e.g.* [8, 17]). It is thus natural to decompose the kinetic energy of the fluid into two parts [134]: a compressible but irrotational one associated with wave-like excitations, and an incompressible one associated with the vortex dynamics. The vortices present in quantum systems are topological defects; they cannot terminate within the fluid and must either form loops or terminate on the walls of the container, and they cannot simply decay⁴. Vortex structures are responsible for peculiar dynamics at the heart of so-called quantum turbulence [140–144]⁵, and more generally the absence of intrinsic dissipation and the highly restricted flow raise fundamental questions about the character of turbulent cascades in quantum fluids (see *e.g.* [142, 147]).

Over the last few decades in the emerging field of turbulence in quantum (superfluid) systems many experiments were performed on liquid helium, exploring both vortex [125, 142, 148–150] and wave turbulence [151–153]. A particularly exciting observation was the existence of a Kolmogorov energy spectrum $\propto k^{-5/3}$ [125] in incompressible-flow-dominated superfluid helium, highlighting universal parallels to classical-fluid turbulence [118]. Steady progress in the field has been ensured by inventive techniques, such as the addition of tracer particles to visualize quantum vortices directly [154] and the ability to probe the vortex line length with second sound attenuation [155]. However, unfortunately, liquid helium is a strongly-interacting fluid, for which only approximate theoretical descriptions exist, rendering a first-principles understanding of the experiments intractable.

More recently, there has been a fast-growing interest in the possibility to study turbulence in the highly controllable setting of ultracold atomic gases [27, 156–168], which are more suitable for a fruitful interplay between experiment and theory. Experimentally, first qualitative evidence for turbulence in ultracold atomic gases was observed in dramatically perturbed harmonic traps [156], but quantitative comparisons with theory were hindered by the inhomogeneous density imposed by the harmonic trap. The advent of uniform-density quantum gases [21–25] has proven to be a considerable advance in establishing quantum gases as plat-

⁴Vortex lines can sustain helical deformations (known as Kelvin waves) [135], and interact with each other via vortex reconnections [136, 137]. In both cases this leads to sound-wave emission and thus provide an energy transfer mechanism between incompressible and compressible flows [138, 139].

⁵Onsager uncovered the first theoretical links between turbulence and point vortex dynamics in 2D fluids [145], and later Feynman envisioned tangles of vortices at the heart of quantum turbulence in 3D [146].

forms for elaborate studies of quantum-fluid turbulence [27, 162, 166, 167]. A major reason for this is that weakly-interacting zero-temperature Bose gases are well described by the classical-field Gross–Pitaevskii (GP) equation, a nonlinear Schrödinger equation with cubic nonlinearity. This nonlinear wave equation is frequently used to model turbulence in quantum fluids [134, 169–173] and more generally constitutes a universal model of turbulence [169], with striking similarities to the classical Euler equation (see Section 2.3).

In this chapter we present studies of a turbulent cascade in a box-trapped quantum gas [27, 162], where we exploit unique features of ultracold atom systems to measure properties that are otherwise not easily accessible. In Section 4.2 we provide the experimental context of earlier work observing the emergence of a turbulent cascade in our box-trapped quantum gas [162], which provides the starting point for our work studying the underlying cascade fluxes [27]. In Section 4.3 we outline the pertinent theoretical framework in order to directly link dissipation in the gas to the cascade fluxes. Exploiting the synthetic dissipation scale in our gas, we study the cascade-induced atom-loss dynamics in Section 4.4, which reveals both particle and energy fluxes in steady state and provides insight as to how the cascade front propagates in momentum space before a steady-state has been established. Throughout we confront all our findings with *ab-initio* simulations of the GP equation. While the complex far-from-equilibrium quantum dynamics that occurs in our system are not necessarily captured by this simple model, our experiments directly probe its regime of validity. Finally, we conclude in Section 4.5, outlining avenues for future research.

4.2 Emergence of a turbulent cascade

We begin by reviewing our procedure for initiating a turbulent cascade in our box-trapped quantum gas (following [162]), which sets the scene for our more recent studies on the underlying turbulent cascade fluxes [27]. Our experiments start with a quasi-pure Bose–Einstein condensate of ^{87}Rb atoms in the uniform potential of a cylindrical optical box trap of radius $R \approx 16 \mu\text{m}$ and length $L \approx 27 \mu\text{m}$ ⁶. We prepare the atoms in the $|F, m_F\rangle = |2, 2\rangle$ hyperfine ground state, where they are weakly-interacting with an *s*-wave scattering length $a \approx 100 a_0$. For our typical atom numbers of $N \sim 10^5$ the healing length is $\xi \sim 1 \mu\text{m}$ and so the condensate density is quasi-homogeneous⁷. The corresponding chemical potential is $\mu \sim k_B \times 2 \text{ nK}$, which sets the gas’s natural energy scale.

⁶The experiments in this chapter were performed using the first-generation box experiment [21], which uses ^{87}Rb as opposed to ^{39}K (see [71, 73–75] for experimental details).

⁷The homogeneity is also limited by the imaging resolution of our optical setup used to create the optical box trap; for a characterization of the trapping potential see [21, 71].

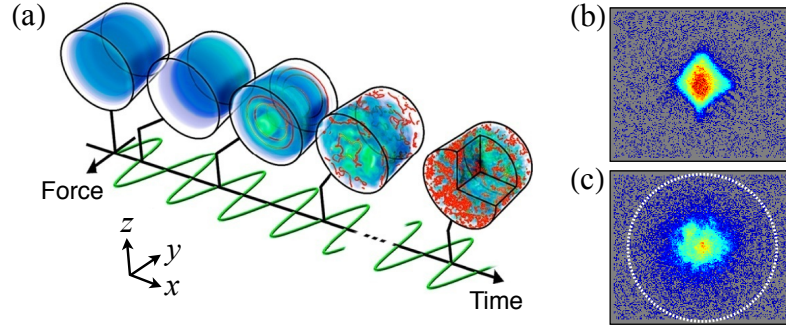


Fig. 4.2 Initiating the turbulent cascade. (a) Gross–Pitaevskii equation simulations of the shaking protocol used to initiate a turbulent cascade in our box-trapped Bose gas. As one continuously drives the lowest-lying axial mode, the system transitions from unidirectional sloshing to an isotropic turbulent state. The blue shading indicates the gas density and the red lines indicate vortices. (b,c) Experimental absorption images taken along x after 100 ms ToF expansion, with $N \approx 8 \times 10^4$ atoms. (b) Initial quasi-pure Bose–Einstein condensate and (c) after shaking for 2 s at 8 Hz with amplitude $F_0 L / \mu \approx 1.2$. The white dashed circle in (c) shows the size that would constitute an expansion energy of $k_B T_c / 2$, highlighting that $E \ll k_B T_c$. Figure adapted from [162] © Nature Publishing Group.

As illustrated by the simulations shown in Fig. 4.2, the turbulent cascade is initiated by resonantly driving the lowest-lying axial Bogoliubov sound mode of wavelength $2L$ (so $k_F = \pi/L$) using a spatially uniform force $\mathbf{F}_s(\mathbf{r}, t) = F_0 \sin(\omega_s t) \hat{\mathbf{y}}$, where $\hat{\mathbf{y}}$ is the axial unit vector⁸. These simulations reveal that as one continuously excites the gas, the initially unidirectional sloshing transforms into irregular, statistically isotropic motion over many ever smaller lengthscales⁹. Experimentally, electromagnetic coils provide the magnetic field gradient that creates a potential $V_s(\mathbf{r}) = F_0 y$ and after resonantly [$\omega_s / (2\pi) \sim 10$ Hz] exciting the condensate for several seconds with an amplitude $F_0 \sim \mu/L$ the initially anisotropic, diamond-shaped ToF absorption images [Fig. 4.2(b)] also become statistically isotropic [Fig. 4.2(c)]. This provided the first qualitative indication of a kinetic-energy-dominated turbulent state where phase coherence is destroyed. It is important to distinguish this far-from-equilibrium state from an equilibrium thermal state, which is also isotropic and would be achieved if the gas was heating to temperatures $T > T_c$. From the second-moment of the ToF images the total (mostly kinetic) energy per particle was found to be $E \approx 0.12 k_B T_c$ (here $T_c \approx 50$ nK), and so an equilibrium gas with the same E would still be deeply degenerate (with a condensed fraction $\eta \approx 0.7$). Moreover, as a proof, if the forcing is stopped the phase coherence of the gas gradually re-establishes itself and a BEC with $\eta \approx 0.7$ reforms [162]. These relaxation dynamics constitute a fascinating problem in their own right, but here we will restrict ourselves to the establishment and the steady-state properties of the turbulent state.

⁸The fact that the excitation spectrum is discrete constrains how the excitations can propagate to larger k , and the full microscopic picture of how this initially occurs is still an open problem.

⁹Note that the cylindrical symmetry of the (time-dependent) Hamiltonian is broken. In any real physical system imperfections would always lead to such symmetry breaking. In the simulations the position of the numerical grid provides the symmetry breaking instead.

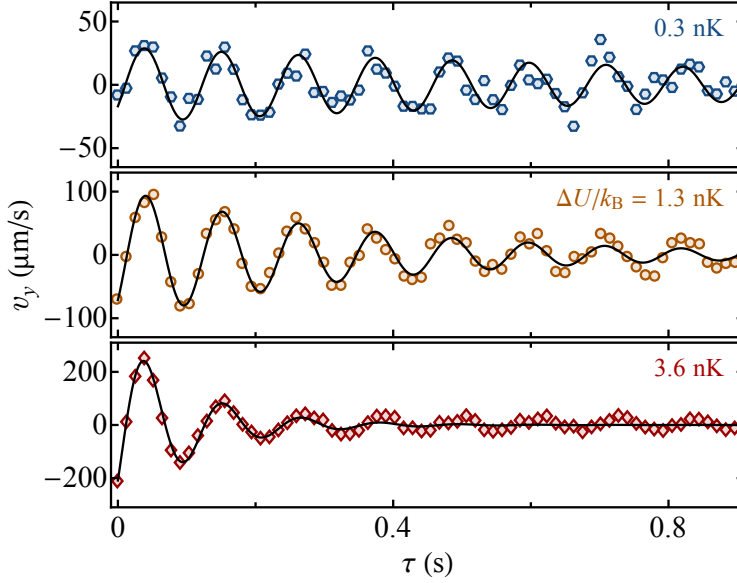


Fig. 4.3 Nonlinear damping of the Bogoliubov sound mode. Axial velocity oscillations $v_y(\tau)$, following pulsed ($\Delta t = 20$ ms) excitations with three different amplitudes ΔU (see top right corner of the panels); here $N = 1.2(1) \times 10^5$. We infer $v_y(\tau)$ from the center-of-mass displacement after ToF. The solid black lines are exponentially decaying sinusoidal fits to the early-time data ($\tau < 0.25$ s). With increasing ΔU the extracted frequency $\omega_{\text{res}}/(2\pi) \approx 9.0$ Hz remains essentially unchanged (to within $\approx 2\%$), while the initial damping increases dramatically (mind the varying y -axis scale). At large ΔU the decay exhibits clear non-exponential behavior. Figure adapted from [41].

Spectroscopic measurements elucidate how resonantly exciting the lowest-lying axial mode eventually leads to a turbulent state [162]. For weak driving amplitudes ($F_0 L/\mu \ll 1$) one probes the linear response of the collective mode, allowing for precise measurements of the resonance frequency, which are found to be in good agreement with Bogoliubov theory (see also [41]). Instead, for stronger drive amplitudes ($F_0 L/\mu \gtrsim 1$) nonlinear behavior is observed, where the response curves broaden, indicating that energy is leaking out of the mode. A particularly striking example of such nonlinear behavior can be directly observed in complementary ‘kick’ measurements, where instead of driving the mode a potential difference ΔU is pulsed across the box for a time $\Delta t = 20$ ms (shorted compared to the period of the mode). The ensuing dynamics of the excited cloud are then observed as a function of the subsequent in-trap hold time τ . As shown in Fig. 4.3 for three different ΔU , the cloud’s axial velocity $v_y(\tau)$ exhibits oscillations with τ . The extracted oscillation frequency $\omega_{\text{res}}/(2\pi) \approx 9.0$ Hz is the same (to within $\approx 2\%$) for all three ΔU , and matches the expected frequency from Bogoliubov theory [41], in line with complementary stroboscopic measurements [162]. The weak kick measurement ($\Delta U = k_B \times 0.3$ nK = 0.15μ) only features a subtle damping, which is well described for all τ by an exponentially decaying sine fit to the early-time data, $\tau < 0.25$ s (solid line). Instead, for larger ΔU the initial damping is increasingly rapid, but a long-lived oscillation persists. This nonlinear decay is further accentuated by the same early-time fitting procedure, which fails to

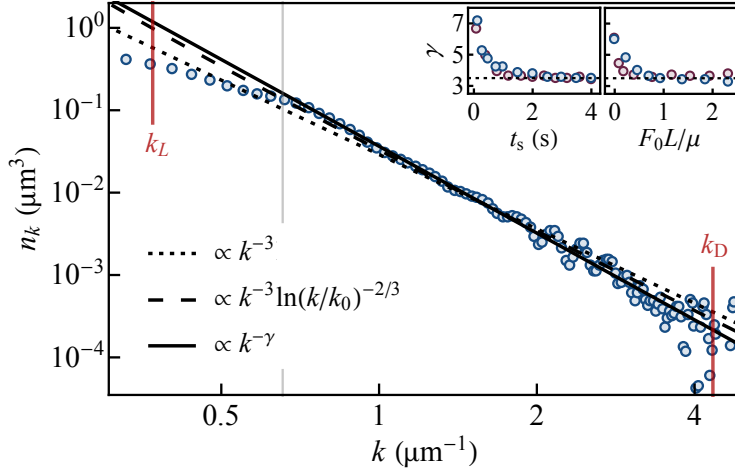


Fig. 4.4 Emergence of a turbulent cascade. Momentum distribution $n_k(k)$ of a turbulent gas (on log-log scale); here $N = 7(1) \times 10^4$, $\Delta U/\mu = 1.1(1)$, $t_s = 4$ s, $\omega_s/(2\pi) = 9$ Hz, and $t_{\text{ToF}} = 100$ ms. To obtain n_k we average over 20 experimental repetitions and perform an azimuthal average, before finally performing an inverse-Abel transform. The red vertical lines indicate our k -space resolution k_L and the momentum cut-off introduced by the finite trap depth k_D . In between k_L and k_D the momentum distribution is well characterized by a power-law $n_k \propto k^{-\gamma}$ with $\gamma \approx 3.5$ (solid line). We also plot the weak-wave turbulence prediction [169]; the dotted line shows the simple $n_k \propto k^{-3}$, whereas the dashed line includes expected logarithmic corrections from a forcing scale k_0 , which we assume to be equal to k_F (see text). The vertical gray line corresponds to $1/\xi$. The normalization is such that $\int 4\pi k^2 n_k dk = 1$. The insets show the extracted γ as a function of shaking time t_s (left, with fixed $F_0 L/\mu \approx 1$) and amplitude $F_0 L/\mu$ (right, with fixed $t_s = 4$ s) in both experiments (blue) and simulations of the GPE (red), highlighting the robust steady-state nature of the cascade, characterized by $\gamma_0 \approx 3.5$ (dotted horizontal line). Data from [162] © Nature Publishing Group.

capture the data at long times ($\tau \gtrsim 0.4$ s). Our observations hint at a nonlinear many-body decay mechanism, and understanding the microscopic origin of this decay is an important task, however here our focus is to simply exploit this feature as a route to turbulence.

In Fig. 4.4 we present an example of the turbulent state momentum distribution n_k which our gas attains. The isotropic ToF images correspond to the convolution of the in-trap momentum distribution with the initial trap size, integrated along the line of sight. We assume the momentum-space mapping $\hbar k_r = mr/t_{\text{ToF}}$, where r is the radial distance to the cloud's center, which is a good approximation between k_L and k_D for our kinetic-energy-dominated gas¹⁰; here $k_L = mL/(2\hbar t_{\text{ToF}})$ is our momentum-space resolution set by the initial size of the box and $k_D = \sqrt{2mU_D}/\hbar$ is the high- k sink introduced by the finite trap depth U_D .

To reconstruct n_k from the line-of-sight integrated distribution presented in [162], we perform an inverse-Abel transform (see Section C). The distribution n_k is well described by a power-law $\langle n_{\mathbf{k}} \rangle \approx n_k \propto k^{-\gamma}$ at intermediate k (between k_L and k_D), where n_k decreases by over two orders of magnitude. A fit to the data (solid line), which we use to characterize the distribution, yields $\gamma \approx 3.5$ ¹¹. In the inset we map out the dependence of γ on t_s and $F_0 L/\mu$,

¹⁰The validity of this mapping relies on the fact that the energy per particle $E \approx k_B \times 10$ nK is significantly larger than the interaction energy $E_{\text{int}} \approx k_B \times 1$ nK. However, we do expect some contamination at lower k where atoms are propelled to slightly larger k due to the conversion of interaction energy to kinetic energy in ToF.

¹¹For details concerning the extraction of γ see [162].

at fixed $F_0 L/\mu = 1$ and $t_s = 4$ s respectively, which shows that the gas indeed reaches a robust steady-state power-law distribution ($\gamma_0 \approx 3.5$) under continuous forcing. These measurements are complemented with numerical simulations of the GP equation, which give a consistent steady-state $\gamma_0 \approx 3.5$ (see [27, 162] and Section 4.4.4 for additional details). It is not a given that the classical field approximation of the GP equation should hold in this far-from-equilibrium scenario, especially at high k where the occupations become small, however the fact that it succeeds at describing the experiments suggests its validity. Finally, we also compare our results to the analytical predictions of weak-wave turbulence theory of the 3D GP equation with particle-like excitations, 4-wave interactions, and a direct energy cascade [169]. A dimensional estimate in this regime predicts $n_k \propto k^{-\gamma_w}$, with $\gamma_w = 3$ (dotted line). It is however expected that due to a weak non-locality of the interactions, the form of n_k slightly deviates from this prediction by a logarithmic factor. Such a logarithmic deviation has so far not been experimentally or numerically validated, though it is analytically expected to be of the form $n_k \propto k^{-3}[\ln(k/k_0)]^{-2/3}$, where k_0 is a low- k cut off associated with the pumping scale [106, 169, 174].

The dashed line in Fig. 4.4 shows this prediction, fixing $k_0 = k_F$, which is barely distinguishable from a power-law with $\gamma_0 \approx 3.5$ across our k -range. However, it should be noted that the choice of $k_0 = k_F$ is somewhat arbitrary (especially as k_F is not isotropic [175]) as well as the fact that the theory assumes an infinite system. A free fit to the data yields $k_0 \approx 0.3/\mu\text{m}$. Instead, performing the same analysis on the n_k obtained from our GP equation simulations (Section 4.4.4) yields an optimal $k_0 \approx 0.7/\mu\text{m}$. The analytical logarithmic correction to the naive γ_w is also qualitatively in line with recent theoretical work which links the deviation from γ_w to finite size effects, employing an approach based on the kinetic theory of non-thermal fixed points [176].

While the data seem to support this logarithmic correction, we note that the analytical weak-wave-turbulence theory neglects the role of vortices which are expected to be present in our turbulent gas, and while in our simulations the compressible flow contribution to the energy dominates over the incompressible one, vortices could have a residual effect [162]. Other inter-linked factors that may play a role and which cannot be ruled out are the not necessarily weak interactions [153, 169] and the increasing importance of quantum pressure in GP equation with increasing k ¹². Finally, our GP equation simulations in Section 4.4.4 reveal self-similar behavior, which is at odds with such a logarithmic correction (albeit probing only a rather limited k -range where one may be insensitive to this).

¹²As described in Section 2.3, the GP equation reduces to the classical Euler equation when the quantum pressure term $\frac{1}{m}\nabla[\hbar^2/(2m\sqrt{n})\nabla^2\sqrt{n}]$ is negligible, which is the case in the absence of spatial variations of the wave function on the order of the healing length [8].

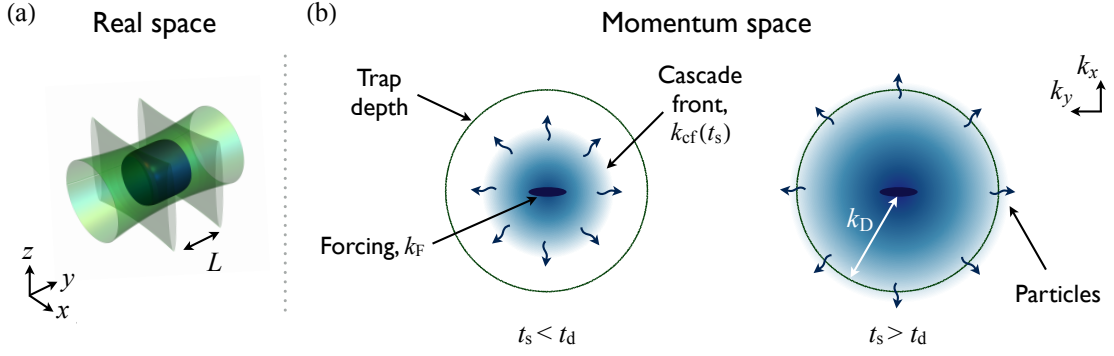


Fig. 4.5 Synthetic dissipation scale. (a) Our optical box trap (green) confines atoms (blue) in a cylindrical trap with a readily tuneable energy-depth U_D . (b) In momentum space U_D corresponds to $k_D = \sqrt{2mU_D}/\hbar$ (green circle). At $t_s = 0$ the anisotropic forcing is initiated (dark blue disk elongated along k_y), which quickly becomes isotropic as nonlinear interactions establish a cascade front k_{cf} , which propagates to larger k . The cascades front k_{cf} reaches k_D at $t_s = t_d$ and subsequently particles are continuously lost from the trap. Figure adapted from [27].

4.3 Synthetic dissipation scale

Dissipation in turbulent flows is fundamental to the existence of a steady state under continuous energy injection. The emergence of a steady-state n_k in our quantum gas suggests that both energy and particle fluxes through the inertial range are k -independent, however, it does not directly reveal the fluxes. Here we study the role of dissipation in our gas, which offers a wealth of information about the cascade dynamics, including direct access to the particle flux.

In conventional fluids the hydrodynamic (macroscopic) degrees of freedom are accessible, but there are also 'hidden' degrees of freedom (microscopic motion). Dissipation, which is governed by the viscosity ν of the fluid, occurs in the form of heating on lengthscales set by the viscosity, where energy is transferred from the hydrodynamic degrees of freedom into the microscopic ones. Conventional fluids are also typically thermally coupled to their surroundings, making it difficult to measure this (often minute) heating [177]. Moreover, ν is generally not tuneable in an independent manner.

Our quantum gas offers direct access to the atomic momentum distribution, and hence all microscopic degrees of freedom, and it is thermally isolated from its surroundings. When a specific mode is damped it just means that energy is transferred to other modes, which we also observe. Even though our superfluid lacks an intrinsic dissipation scale, the optical box [Fig. 4.5 (a)] has a finite trap depth U_D which realizes a synthetic dissipation scale and acts as a particle and energy sink. Atoms can simply escape from the trap when they attain sufficiently high energies, and such atom loss is experimentally measurable to high precision ($\sim 1\%$).

In momentum space [see Fig. 4.5 (b)], U_D corresponds to a spherical shell of radius $k_D = \sqrt{2mU_D}/\hbar$, which is readily tuneable by simply varying the trapping laser power. The initially

anisotropic forcing, that injects energy into the system at k_F (indicated by the dark blue area elongated along k_y), quickly becomes isotropic and establishes a cascade front which propagates through momentum space (at times $t_s < t_d$). When it reaches the dissipation scale k_D at time t_d , atom loss occurs and a steady-state can be established as atoms are transported from the source to the sink.

To explore the experimental possibilities arising from this tuneable dissipation scale we turn to wave-turbulence theory. Within its framework, it is possible to derive a continuity equation from the equations of motion, including a source and a sink, that is local in momentum space [169]:

$$\frac{\partial \tilde{n}_{\mathbf{k}}(\mathbf{k}, t)}{\partial t} = F(\mathbf{k}, t) - D(\mathbf{k}, t) - \nabla_{\mathbf{k}} \cdot \mathbf{\Pi}_n(\mathbf{k}, t). \quad (4.1)$$

Here $F(\mathbf{k}, t)$ and $D(\mathbf{k}, t)$ respectively correspond to the forcing and dissipation, $\tilde{n}_{\mathbf{k}}$ is normalized so that $\int \tilde{n}_{\mathbf{k}} d\mathbf{k} = N$, and $\nabla_{\mathbf{k}} \cdot \mathbf{\Pi}_n$ describes the nonlinear interactions, where $\mathbf{\Pi}_n$ is the particle flux. In the absence of forcing and dissipation ($F = D = 0$) the steady-state solutions are thermodynamic equilibrium states with $\mathbf{\Pi}_n = 0$. Now, if F and D are nonzero but localized in momentum space, then non-equilibrium steady-state solutions also exist, where a scale-independent particle flux is sustained between the source F and the sink D .

Assuming that the outflow is isotropic, we can integrate out all angular dependencies and consider the total radial particle flux $\Pi_n(k) = 4\pi k^2 |\mathbf{\Pi}_n(\mathbf{k})|$. Applying Eq. (4.1) in the inertial range then yields $4\pi k^2 \partial \tilde{n}_k / \partial t = -\partial \Pi_n / \partial k$, and after integrating over k (up to k_D) we have

$$\frac{\partial N}{\partial t} \equiv -\Pi_n(k_D, t). \quad (4.2)$$

As one may intuitively expect, in steady-state the particle flux through the momentum shell at k_D is simply given by the rate at which atoms are lost from the trap. Moreover, as the momentum distribution in the inertial range is also stationary (see Fig. 4.4) this means that the radial particle flux is both k - and t -independent, such that $\Pi_n(k_D, t) = \Pi_n(k, t) = \Pi_n$.

The corresponding total radial energy flux $\Pi_{\mathcal{E}}(k, t)$, is also k - and t -independent in the inertial range, and it reflects the rate of energy dissipation. To formulate a relationship between $\Pi_{\mathcal{E}}(k, t)$ and Π_n , let us consider the general case of weakly-interacting particles with the dispersion relation $\omega(k)$, where the energy spectrum is $\mathcal{E}(k, t) = \hbar\omega(k)n_k(k, t)$; in our case the excitations approach particle-like¹³ behavior $\omega(k) \propto k^2$.

One may naively expect that $\Pi_{\mathcal{E}}(k) = \hbar\omega(k)\Pi_n(k)$, but this cannot be true as both $\Pi_{\mathcal{E}}$ and Π_n are independent of k in steady state, while $\omega(k)$ is not. This nontrivial relationship between

¹³The Bogoliubov dispersion relation $\omega = \hbar k^2 / (2m) \sqrt{1 + 2/(k^2 \xi^2)}$, where $\xi = 1/\sqrt{8\pi n a}$ is the healing length, becomes particle-like at large $k\xi$ (see Section 2.4).

the energy and particle fluxes stems from the fact that they are *net* fluxes, and the microscopic interactions drive particles to both smaller and larger k , for $k < k_D$. However, at k_D there is no ‘back-flow’ from the sink into the inertial range and the particles only flow one way, allowing us to write

$$\Pi_{\mathcal{E}}(k_D) = \hbar\omega(k_D) \Pi_n(k_D). \quad (4.3)$$

Furthermore, the existence of a steady state requires that $\Pi_{\mathcal{E}} = \hbar\omega(k_D) \Pi_n$ throughout the inertial range. For our dispersion relation $\omega(k) \propto k^2$ we have that $\Pi_{\mathcal{E}} \propto k_D^2 \Pi_n$.

A more formal approach to deriving Eq. (4.3) consists of multiplying Eq. (4.1) by $\hbar\omega(k)$ and invoking the energy continuity equation to obtain

$$\frac{\partial \Pi_{\mathcal{E}}(k, t)}{\partial k} = \hbar\omega(k) \frac{\partial \Pi_n(k, t)}{\partial k} \quad (4.4)$$

in the inertial range. This equation is trivially satisfied for $k < k_D$ as the particle and energy fluxes are k -independent in the inertial range and so both sides are zero, and no relation between $\Pi_{\mathcal{E}}(k)$ and $\Pi_n(k)$ is imposed. However, by integrating across the momentum-space shell k_D , and assuming that \tilde{n}_k and all fluxes are zero for $k > k_D$, one recovers Eq. (4.3).

In summary, we have shown that both the particle and energy fluxes underlying the turbulent cascade can be extracted from a simple time-resolved measurement of $N(t_s)$ at different k_D (keeping F_0 fixed).

4.4 Probing the turbulent cascade fluxes

4.4.1 Turbulent cascade atom-loss dynamics

We now turn to our measurements of the atom-loss dynamics arising from the turbulent cascade. At $t_s = 0$ we initiate the turbulent cascade using a fixed forcing amplitude $F_0 L = k_B \times 2.5$ nK tuned to resonance [$\omega_s / (2\pi) \approx 9$ Hz]¹⁴. Our initial quasi-pure BEC has $N \approx 1.2 \times 10^5$, and we map out the cascade-induced loss N_{loss} as a function of t_s for different trap depths¹⁵ $U_D \propto k_D^2$. To accurately determine N_{loss} we perform differential measurements in which we subtract each measurement from a reference measurement with $F_0 = 0$ but otherwise identical parameters. This allows us to mitigate the effects of few-percent drifts in the initial N as well

¹⁴A weak dependence of ω_{res} on U_D exists due to imperfections in the trapping potential, and so for each U_D we tune ω_s to resonance [27].

¹⁵The radial and axial trapping potentials are independently controlled, and we have performed several calibration measurements to make them as equal as possible (including Bragg diffraction to give the atoms a direction-specific velocity and see if they leave the trap). Overall, these tests have suggested that various directions are equal to better than $\sim 20\%$, which is smaller than the range of U_D that we explore and is no larger than the systematic uncertainty in the average U_D , averaged over directions.

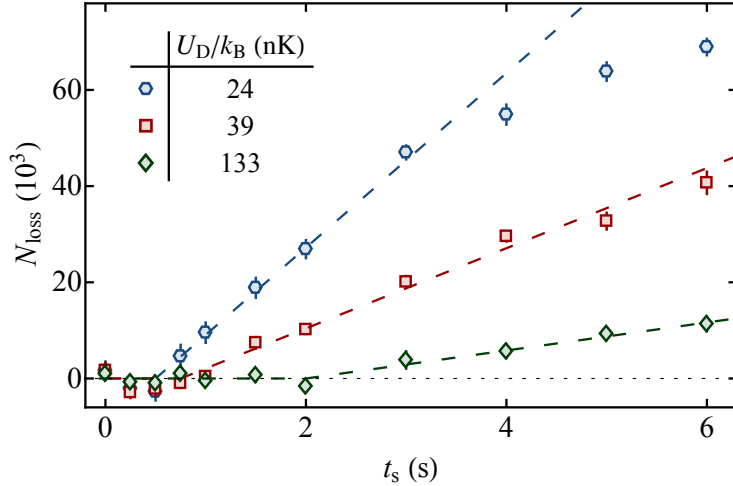


Fig. 4.6 Turbulent cascade atom-loss dynamics. Measured atom loss N_{loss} due to the turbulent dynamics as a function of shaking time t_s , for three different trap depths U_D (see legend). The initial atom number at $t_s = 0$ is $N \approx 1.2 \times 10^5$. The error bars arise from averages over typically 50 repetitions, and they indicate the error on the mean. The dashed lines show piece-wise linear fits that we use to extract the delay time t_d and the subsequent initial loss rate (see text). The systematic error in U_D values is 20%. Figure from [27].

as the additional one-body loss from collisions with the background gas¹⁶.

In Fig. 4.6 we plot N_{loss} versus t_s for three different U_D , which reveals the expected qualitative behavior. We find that the loss at short times is consistent with zero for all U_D , in line with our expectations that it takes time for the excitations to cascade through k -space and reach k_D at t_d . For $t > t_d$ and relatively small total loss ($< 30\%$ of the initial $N \approx 1.2 \times 10^5$) N_{loss} is linear in t_s and so $\partial N_{\text{loss}}/\partial t$ is constant in time. Following Eq. (4.2), we identify this loss rate as the steady-state particle flux $\Pi_n(k_D) = \Pi_n$ in the inertial range (see Section 4.3). Instead, when the fractional loss is large and the low- k source of atoms is significantly depleted the loss rate is no longer constant and the steady-state assumption also breaks down¹⁷.

In order to extract both the loss onset delay time t_d and the particle flux Π_n we perform piecewise linear fits (dashed lines). Qualitatively, we see that for increasing U_D the delay time t_d increases while the particle flux Π_n decreases. In the following two subsections we will quantitatively study these two dependencies and compare our experiments to numerical simulations of the GP equation as well as analytical predictions of turbulent cascades. Finally, in Section 4.4.4 we present a unifying picture of the cascade dynamics, which we further validate using our simulations.

¹⁶We assume that this additional loss (the one-body lifetime in this experiment is ≈ 14 s) does not substantially affect the turbulent loss dynamics, which we have confirmed in GPE simulations.

¹⁷Note that $\omega_{\text{res}} \propto \sqrt{N}$, and while the response curves are significantly broadened (see e.g. [162]) the system does eventually shift out of resonance when N is significantly reduced.

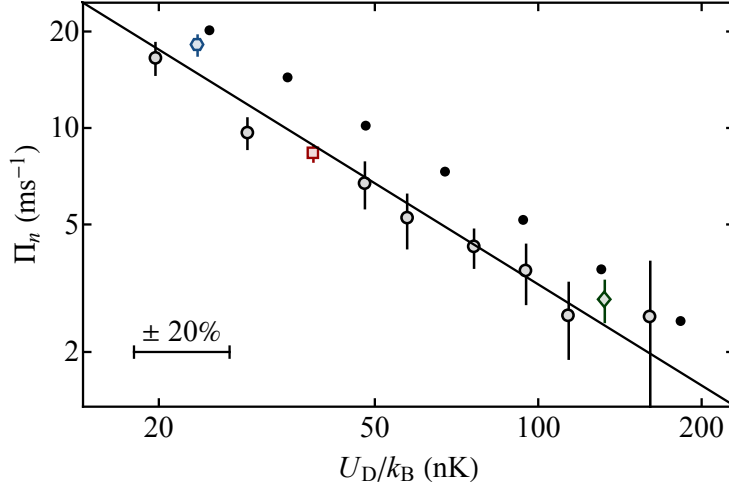


Fig. 4.7 Steady-state particle flux. Log-log plot of the particle flux Π_n versus trap depth $U_D \propto k_D^2$ for both experiment (open symbols) and simulation (solid circles). The colored points correspond to the values extracted from the data shown in Fig. 4.7 and the horizontal error bar shows the systematic uncertainty in experimental values of U_D . The solid line shows a power-law fit to the experimental data, which yields $\Pi_n \propto U_D^{-1.05(8)} \propto k_D^{-2.10(16)}$, providing a demonstration of the zeroth law of turbulence. Figure from [27].

4.4.2 Steady-state particle and energy flux

We begin by studying the steady-state particle flux, and in Fig. 4.7 we plot Π_n versus U_D on log-log scale. The linear dependence of the experimental data (open symbols) indicates power-law behavior of Π_n with U_D , and a fit yields $\Pi_n \propto U_D^{-1.05(8)} \propto k_D^{-2.10(16)}$. Our experimental data are in agreement with numerical simulations based on the Gross–Pitaevskii equation (solid circles), in which we mimic the experimental protocol and Π_n extraction without any free parameters (details are provided in [27]); a fit to the numerical data (omitted for visual clarity) yields a consistent $\Pi_n \propto U_D^{-1.04(1)}$, although the numerical values lie systematically slightly above the experimental ones.

Our results indicate that for our experimentally fixed F_0 , in the limit $k_D \rightarrow \infty$ (vanishingly small dissipation lengthscale) the particle flux vanishes while the energy flux $\Pi_\mathcal{E} \propto k_D^2 \Pi_n$ remains approximately constant, which is a hallmark of a direct energy cascade. This rather counter-intuitive feature is a demonstration of the zeroth law of turbulence, which was first formulated in the context of classical incompressible fluids, where in the limit of vanishing viscosity (analogous to our $1/k_D \rightarrow 0$) it stipulates that for constant energy input the steady-state rate of energy dissipation tends to a non-zero constant [118,178]¹⁸. Note that while energy conservation requires that in steady-state the energy input rate ϵ must be equal to $\Pi_\mathcal{E}$, this alone is not sufficient to predict a constant $\Pi_\mathcal{E}$ for fixed F_0 , as it is not a given that the rate at which

¹⁸In classical fluids the dissipation lengthscale generally depends on the viscosity ν of the fluid; as an example, for incompressible turbulence the Kolmogorov dissipation lengthscale depends on the viscosity of the fluid as $\nu^{3/4}$ [118,169].

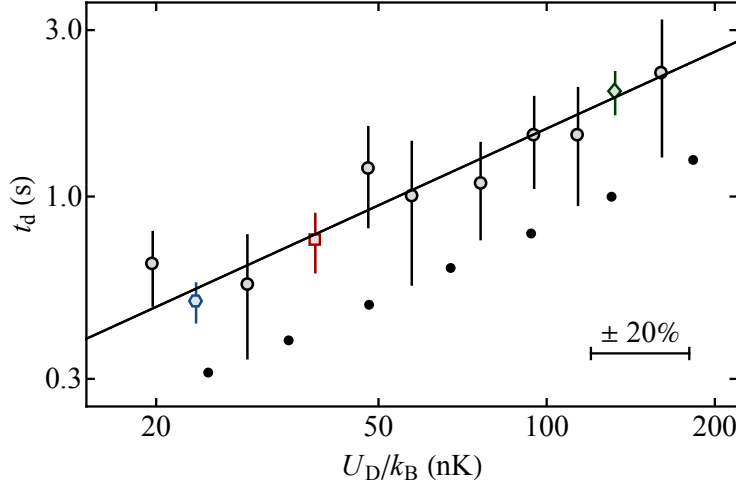


Fig. 4.8 Cascade front dynamics. Onset time for dissipation t_d versus U_D on log-log scale for both experiment (open symbols) and simulation (solid circles). The colored points correspond to the data from Fig. 4.7 and the horizontal error bar shows the systematic uncertainty in experimental values of U_D . A power-law fit, $t_d \propto U_D^\beta$, to the experimental data (solid line) gives $\beta = 0.73(6)$. The numerical data shows the same dependence with a slight systematic offset; a power-law fit to the numerical data yields a consistent $\beta = 0.71(1)$. Figure from [27].

the system absorbs energy is k_D -independent¹⁹. It is the constancy of $\Pi_\mathcal{E}$ inferred from Fig. 4.7 (alongside energy conservation) that shows that the steady-state ϵ is independent of k_D across our experimentally accessible k -range.

4.4.3 Pre-steady-state cascade-front dynamics

We now turn to a time-resolved study of the initial stage of turbulence [179–181], where the cascade front is propagating through k -space and dissipation has not yet occurred. Our ability to access this regime is rather unique, and in almost all past experimental studies of turbulence, turbulent cascade spectra in k -space were obtained with single-point probes by translating time variations into the spatial fluctuations required for k -space spectra measurements (through the so-called Taylor frozen turbulence hypothesis [182]). It has thus been difficult to experimentally extract real-time information on the cascade-establishing dynamics²⁰. The fact that we observe the initial dissipationless stage of turbulence ($t_s < t_d$, see Fig. 4.6) together with our ability to study the dependence of t_d on U_D provides direct access to the dynamics of the cascade front. In Fig. 4.8 we explore the dependence of t_d on U_D , which we find to be well described by a power-law $t_d \propto U_D^\beta$, with $\beta = 0.73(6)$ (solid line). Consequently, the dynamics of the cascade front are described by $k_{cf}(t_s) \propto t_s^{1/(2\beta)}$. The results of our numerical simulations (solid circles) exhibit a similar trend with U_D but feature a small systematic offset. A fit to the numerical data

¹⁹For example, in the familiar case of the damped harmonic oscillator, the steady-state energy-absorption rate depends on both forcing and dissipation.

²⁰While our time-resolved measurements of n_k yield qualitative insight into the pre-steady-state dynamics [162], the low- k region (of interest at early times) is sufficiently contaminated by interactions in ToF to hinder a quantitative study.

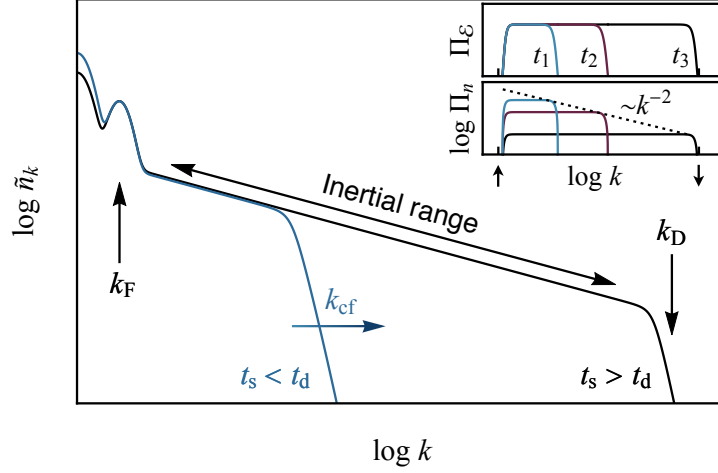


Fig. 4.9 Momentum-space turbulent dynamics. Energy is continuously injected into the system at k_F from $t_s = 0$ onwards. The steady-state turbulent cascade distribution \tilde{n}_k is established in the wake of the cascade front $k_{cf}(t_s)$ as it propagates towards k_D (for $t_s < t_d$), reaching it at t_d . For the sake of our qualitative message, we show an idealized sketch with an exaggerated ratio of k_D/k_F ; numerical simulations with our experimental parameters, which support this qualitative picture, are shown in Fig. 4.10. The inset shows our consistent picture for the evolution of both energy and particle fluxes, for three different times t_1 (blue) $< t_2$ (purple) $< t_3$ (black), with $t_2 < t_d < t_3$. The vertical arrows indicate the forcing and dissipation scales, as in the main panel. Figure from [27].

(omitted for visual clarity) yields a consistent $\beta = 0.71(1)$.

In Section 4.4.4 we present a unifying picture of both pre-steady-state and steady-state turbulent dynamics, which offers insight into how the cascade forms as well as the value of β . We furthermore verify this picture using the time evolution of the momentum distributions extracted from our numerical simulations.

4.4.4 Unifying qualitative picture

In Fig. 4.9 we present our consistent picture of the Fourier-space dynamics. At $t_s = 0$ we initiate the shaking, which continuously generates a surplus of atoms at k_F in anisotropic fashion. The nonlinear interactions establish an isotropic cascade front $k_{cf}(t_s)$ which subsequently propagates to larger k . As the cascade front propagates it forms the steady-state turbulent cascade $\tilde{n}_k \propto k^{-\gamma_0}$ in its wake. Once k_{cf} reaches k_D (at time t_d) dissipation occurs, and a steady-state is established where the energy input rate ϵ is equal to the energy flux $\Pi_E(k_D)$. As the cascade front propagates ($t_s < t_d$), the instantaneous particle flux, which is k -independent for $k < k_{cf}(t_s)$ and zero for $k > k_{cf}(t_s)$, must equal the rate at which the population increases in the inertial range (to ensure atom number conservation), so that $\tilde{n}_k(k_{cf}) 4\pi k_{cf}^2 dk_{cf} = \Pi_n(k_{cf}) dt_s$, where $\tilde{n}_k(k_{cf}) \propto k_{cf}^{-\gamma_0}$. Moreover, to ensure energy conservation, the instantaneous energy-injection rate ϵ must equal the energy flux $\Pi_E(k_{cf})$ in the inertial range, so we analogously have $k_{cf}^{4-\gamma_0} dk_{cf} \propto \Pi_E(k_{cf}) dt_s$.

We found experimentally that ϵ does not depend on k_D for $t_s > t_d$ (see Section 4.4.2). If we

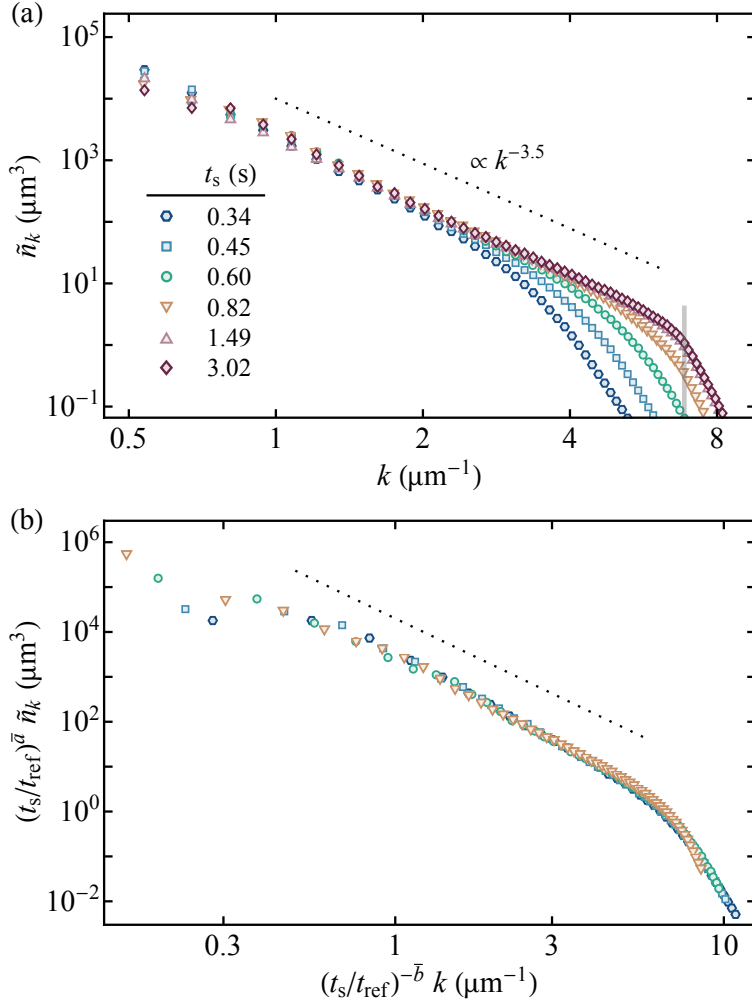


Fig. 4.10 Momentum-space dynamics in numerical simulations. (a) Log-log plot of the calculated \tilde{n}_k versus k for $U_D = k_B \times 130$ nK and several t_s (see legend), revealing how the power-law $\tilde{n}_k \sim k^{-\gamma_0}$, with $\gamma_0 \approx 3.5$, develops in the wake of the cascade front. Once the cascade front reaches k_D (indicated by the vertical gray line) a steady-state is established over the inertial range. The profiles are normalized such that $\sum_k 4\pi k^2 \tilde{n}_k \delta k = N$, where $\delta k = \pi/(20\xi)$ is the grid resolution in \mathbf{k} space. (b) To highlight the self-similar nature of the pre-steady-state dynamics, we rescale the curves from (a) with $t_s \lesssim t_d \approx 1.0$ s, using $\bar{a} = \gamma_0/(5 - \gamma_0) = 2.33$, $\bar{b} = \bar{a}/\gamma_0 = 0.67$, and $t_{\text{ref}} = 1$ s (see text), collapsing our data onto a single curve. Figure from [27].

extend this to the pre-steady-state dynamics and assume that ϵ is also independent of k_{cf} for $t_s < t_d$, we find that for $k < k_{\text{cf}}(t_s)$ the instantaneous particle flux $\Pi_n(t_s) \propto k_{\text{cf}}^{-2}$. As shown in the inset of Fig. 4.9, this elegantly unifies our description of the fluxes for $t_s < t_d$ and $t_s > t_d$; the k -independent Π_n is the same function of the high- k cutoff up to which the steady-state n_k has been established (above which there is no back-flow), whether this is the instantaneous $k_{\text{cf}}(t_s) < k_D$ (for $t_s < t_d$) or k_D (for $t_s > t_d$). Crucially, this picture also makes a concrete prediction for β , which we can compare to our measured value $\beta = 0.73(6)$ (see Fig. 4.8). With a time-independent ϵ , we have $k_{\text{cf}}^{4-\gamma_0} dk_{\text{cf}} \propto dt_s$, which for $\gamma_0 < 5$ and $k_D \gg k_F$ yields the power-law prediction $t_d \propto U_D^\beta$, with $\beta = (5 - \gamma_0)/2 \approx 0.75(5)$, in good agreement with the measured value.

To further test this qualitative picture we compute the evolution of \tilde{n}_k during shaking using GP simulations including dissipation (see [27] for details). In Fig. 4.10(a) we show snapshots of $\tilde{n}_k(t_s)$ for $U_D = k_B \times 130$ nK, which support the qualitative picture put forward in Fig. 4.9; the cascade front is more rounded here due to the moderate ratio of $k_D/k_F \approx 60$ ²¹. In order to highlight that \tilde{n}_k evolves in a self-similar way as the cascade front propagates through k -space with $k_{cf}(t_s) \propto t_s^{1/(2\beta)}$, we rescale the data from Fig. 4.10(a) for $t \lesssim t_d$ such that $(t_s/t_{ref})^{\bar{a}} \tilde{n}_k[(t_s/t_{ref})^{-\bar{b}} k, t_s]$, with $\bar{b} = 1/(2\beta) = 1/(5 - \gamma) = 0.67$, $\bar{a} = \bar{b}\gamma = 2.33$, and setting arbitrarily $t_{ref} = 1$ s. This successfully collapses all the curves onto a single one, providing strong support for this picture. Moreover, the particular values of \bar{a} and \bar{b} confirm our assumption that ϵ is time-independent.

Interestingly, the condition for t_d to exhibit scaling behavior ($\gamma < 5$ and hence $\beta > 0$) is closely linked to whether the steady-state \tilde{n}_k has infinite energy capacity, which also occurs for $\gamma < 5$ and means that the cascade carries infinite energy for $k_D \rightarrow \infty$. In general it is expected that in infinite-capacity systems the cascade front propagates at a finite speed and that a Kolmogorov–Zakharov turbulence spectrum forms behind it [183], in line with our observations.

4.5 Conclusion

In this chapter we provided a consistent unifying picture of the wave-turbulent dynamics in our box-trapped quantum gas, finding good agreement with ab-initio simulations of the GP equation throughout. More generally, our quantum gas provides an example of an essentially stationary non-thermal state, and is of interest in the broader context of far-from-equilibrium many-body quantum systems [31, 184, 185]. Our experimental platform is an excellent testbed for future studies of turbulence, with many intriguing possibilities in sight. Below we present several of these, starting with those that are more immediate (**A**) before turning to more general tasks (**B**).

A₁ - It would be interesting to perform dynamical experiments in which one suddenly varies k_D , further exploiting the tuneable nature of the dissipation in our gas. Such experiments could be interesting in two different ways. First, they could provide a complementary way to measure the atom number in a particular k -space shell, which one could use to cross-validate the n_k measurements [162]. Secondly, one could study quenches between different turbulent states, offering a glimpse at how the system transitions from one turbulent state to another with a

²¹For the lowest k_D that we explore $k_D/k_F \approx 23$.

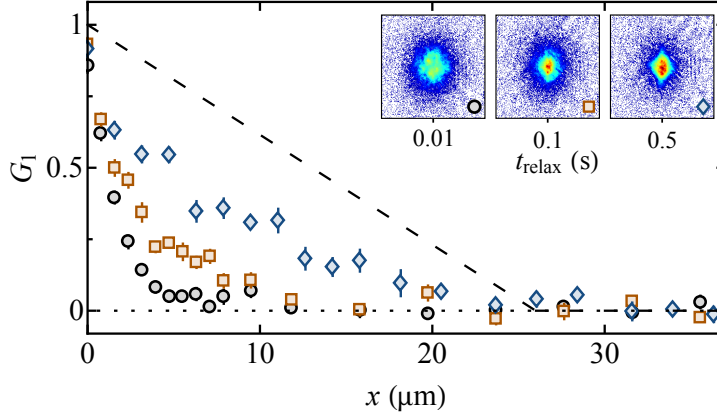


Fig. 4.11 Relaxation of the turbulent state. Following the preparation of a turbulent state, we halt the forcing at $t_{\text{relax}} = 0$ and study the relaxation dynamics. Here we show preliminary results of the extracted correlation function $G_1(x) = g_1(x)(1 - x/L)$ using a homodyne detection scheme [186], where L is the box length and $g_1(x) \equiv \Re[g_1(\mathbf{r}, \mathbf{r} + x\hat{\mathbf{x}})]$ is first-order two-point correlation normalized so that $g_1(0) = 1$; see [71, 186] for additional details of the experimental protocol. The main panel shows $G_1(x)$ for three different t_{relax} , where the coherence length increases as a function of t_{relax} , from initially highly-suppressed long-range order towards that of a pure BEC (dashed line). The inset shows the corresponding absorption images, which qualitatively show how a BEC with the characteristic diamond-shape reforms.

new k_D . In particular, such a new steady-state would require Π_n to adjust across the entire inertial range ($k_F < k < k_D$), so that Π_n is both k_D -dependent, to obey the zeroth law, and k -independent for a given k_D .

A₂ - In nature energy injection always eventually stops, which inevitably leads to the decay turbulence - its final stage. Experiments where we carefully study the relaxation of our turbulent gas back to a quasi-pure condensate are under way, and a glimpse of these are shown in Fig. 4.11. We use a homodyne detection protocol [186] to measure the two-point correlation function for different relaxation times, as phase coherence is re-established and a BEC reforms. These experiments will pose as fundamental tests of both the decay of turbulence in quantum gases [143, 187] and more generally the phase-ordering kinetics of Bose gases (see *e.g.* [188]).

A₃ - Extending our studies on turbulence using our box-trapped ^{39}K gas will allow us to explore the role of interactions in all three stages of turbulence: its establishment, steady-state properties, and eventual decay.

B₁ - An important future task is exploring the relationship between incompressible and compressible turbulent dynamics. A integral part of this endeavor is benchmarking different excitation protocols to find regimes where the gas reaches turbulent states in which incompressible flow dominates and vortex tangles form. This is also coupled with designing probes that provide access to the quantities of interest from a theory perspective, such as the incompressible

energy spectrum or the average vortex line length [142, 144, 159, 160, 168].

B₂ - An exciting prospect is to study turbulence in homogeneous two-dimensional quantum gases, where an inverse-energy cascade propagating from large to small scales is expected to occur (see *e.g.* [122, 160]). Indeed, recent experiments have already detected signatures of such dynamics [166, 167].

B₃ - It would also be interesting to explore the long time behavior for different forcing amplitudes, to see how (or even if) the gas eventually does become thermal. Alternatively, for weak enough forcing relaxation processes could dominate the dynamics and prohibit ever reaching a turbulent state.

5 Weak Collapse of a Bose–Einstein Condensate

Not so fatal attraction

- Zoran Hadzibabic -

5.1 Introduction

Even weak attractive interactions can lead to dramatic far-from-equilibrium behavior in BECs. In the presence of attractive interactions, BECs are prone to collapse. Such an implosion is however opposed by the cloud's kinetic energy, which stabilizes it. A metastable state is formed for sufficiently small interaction energies, however if the attractive forces overwhelm the dispersive ones, then collapse occurs. The collapse of a BEC is an example of wave collapse, a phenomenon ubiquitous in nature. Examples include white-caps on choppy water [189, 190], self-focusing light beams propagating in nonlinear optical media [191–193], the collapse of Langmuir waves in plasmas [194–199], and discontinuities formed in gas-dynamics [200]. It is also thought to share parallels with the collapse and subsequent supernova explosion of stars at the end of their lifetime [201, 202]. Wave collapse entails the formation of a singularity in a finite amount of time. However, in real physical systems, dissipative effects necessarily intervene before this singularity is reached.

The unifying theoretical framework for understanding wave collapse is provided by the nonlinear Schrödinger equation. Theoretically, general forms of the nonlinearity are considered [190, 193], however the case of a cubic nonlinearity is of particular physical interest. It describes both atomic BECs with s -wave two-body interactions, and nonlinear optical media with a Kerr nonlinearity, and thus has been a theoretical focus [190, 193, 203–205]. In this case, the nature of the collapse is governed by the dimensionality of the system, which has impor-

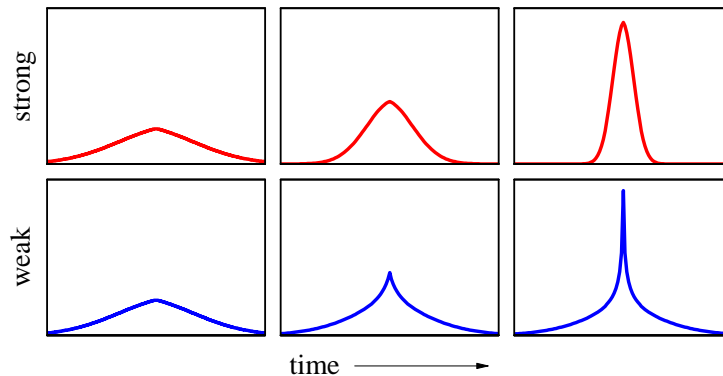


Fig. 5.1 Cartoon comparing strong and weak collapse. In the case of strong collapse, a finite part of the wave (100% for simplicity) collapses into the singularity, whereas for weak collapse this fraction diminishes as time progresses and the singularity is approached. Figure from [26].

tant consequences for how effective collapse is as a nonlinear energy dissipation mechanism. In 2D the collapse is classified as *strong*, while in 3D it is *weak*, the difference being that in strong collapse the weight of the collapsing part of the wave function¹ is constant and a finite amount of energy is trapped in the singularity, whereas for weak collapse the weight of the wave function that collapses into the singularity tends to zero as the collapse proceeds [203,204] (see also Fig. 5.1). This has the counter-intuitive consequence that in weak collapse less dissipation occurs for stronger attraction, as the collapse proceeds further before dissipative forces intervene. Collapse does not occur in 1D for a cubic nonlinearity. Instead, stable solitons are formed, where the dispersion (kinetic energy) exactly balances the nonlinear attraction (interaction energy).

The collapse of a BEC was first observed during the evaporative cooling of an ultracold gas of ^7Li [206,207]. More detailed studies were enabled by the use of a Feshbach resonance in ^{85}Rb , where the interaction strength could be tuned to initiate the collapse [208,209]. This confirmed the expected condition for collapse $N|a_c| = k_h a_{\text{osc}}$, arising from the balance of kinetic and interaction energy. Here a_c is the critical interaction strength, N the condensate atom number, a_{osc} the harmonic oscillator length and k_h a constant. Moreover, these quench experiments allowed a detailed study of the collapse dynamics, which in turn led to the observation of a rich phenomenology, including the formation of solitary waves in the aftermath of the collapse [210] and ‘jets’ of atoms emanating from the BEC during the collapse [209]. All previous experiments studying the collapse of atomic BECs with contact interactions were performed in harmonic traps [206–212]. While the critical point and the collapse dynamics were in general agreement with theory [213–220], the observed atom loss was only seen to grow with $|a|$ [210], and no evidence for the theoretically expected weak collapse was found.

¹For example, in the case of BECs the weight is the number of atoms in the collapsing wave function, whereas for optical beams it is the power of the self-focusing beam.

Since then, collapse has also been studied in cases where the initial density distribution is roughly uniform locally, and a modulation instability seeds the collapse [221]. More exotic collapse phenomena have also been studied in BECs. Collapse was found to occur in Bose–Fermi mixtures [222–224], and the collapse of condensates with dipolar interactions has shown clear signs of the d -wave nature of the interactions in the collapse remnants [225–227]. More recently, the beyond-mean-field quantum-fluctuations in such dipolar gases were used to oppose the attraction, forming so-called quantum droplets [228–230], and transient regimes where supersolid properties emerge were observed [231–233]. Similar quantum droplets were later also observed following the original proposal by Petrov [234], using a mixture of two Bose–Einstein condensates [235–237].

In this chapter we study the collapse of a ^{39}K BEC confined in an optical box potential (see also [26]). Our discussion is guided by three principal questions:

- (i) *What is the condition for collapse?*
- (ii) *What is the time to collapse?*
- (iii) *What is aftermath of the collapse?*

In Section 5.2 we introduce the relevant theoretical background and motivate a qualitative picture to guide our discussion. Dimensional analysis allows us to hint at the universal scaling laws that should govern the collapse process. In Section 5.3 we present our experiments, starting with equilibrium studies aimed at answering (i) before turning to quench experiments to tackle (ii, iii); in our quench experiments we prepare a gas close to the critical point where it is still stable, before rapidly tuning the interaction strength beyond the critical point and observing the ensuing dynamics.

5.2 Qualitative picture and scaling laws

As a starting point for our discussion we consider the generalized Gross–Pitaevskii (GP) equation², modified to include three-body recombination events (a nonlinear dissipative loss mechanism). In a uniform potential, this is given by

$$i\hbar\frac{\partial\psi}{\partial t} = -\frac{\hbar^2}{2m}\nabla^2\psi + g|\psi|^2\psi - i\frac{\hbar K_3}{2}|\psi|^4\psi, \quad (5.1)$$

²The Gross–Pitaevskii equation is the nonlinear Schrödinger equation with a cubic nonlinearity.

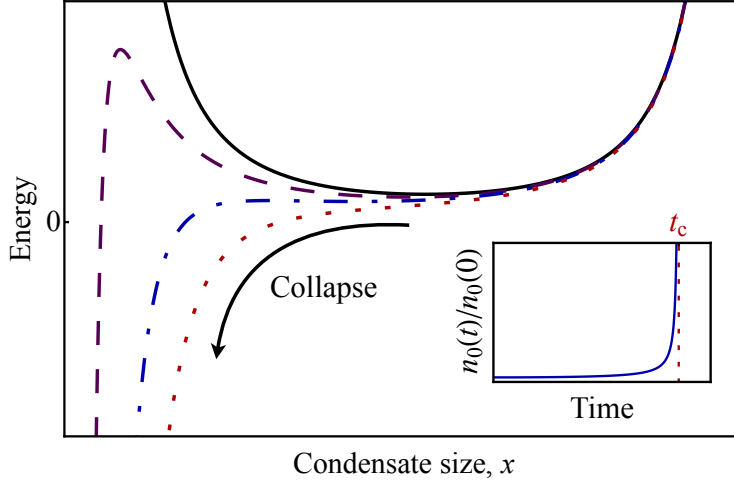


Fig. 5.2 Simple collapse model. The main panel shows the energy landscape as a function the condensate size x , for different values of the interaction parameter α . For $\alpha \geq 0$ (black solid line) only one minimum exists, and the BEC is stable. For any negative α , a new minimum at $x = 0$ appears, and the non-zero x solution is metastable. For small negative $|\alpha|$ the condensate is protected from collapse ($x \rightarrow 0$) by a kinetic energy barrier (purple dashed line). At the critical interaction strength ($\alpha = \alpha_c$, blue dot-dashed line) the energy barrier disappears, rendering the condensate unstable. If α is suddenly quenched below α_c (red dotted line) the condensate collapses ($x \rightarrow 0$) in a time t_c . The inset shows a sketch of how the central density varies after such a collapse is initiated.

where \hbar is Planck's constant, m is the atomic mass, and $g = 4\pi\hbar^2 a/m$ the nonlinear coupling strength (describes the contact interactions in a mean-field picture with an s -wave scattering length, a). K_3 is the three-body loss coefficient, which controls the importance of the dissipative loss mechanism and is crucial for the aftermath of the collapse. Even though the potential energy term does not feature, the walls of the box potential impose the boundary condition that $\psi \rightarrow 0$ at the edges. We proceed by re-writing Eq. (5.1) using the dimensionless variables $\tilde{\mathbf{r}} = \mathbf{r}/L$ and $\tilde{t} = t/\tau_0$ with $\tau_0 = 2mL^2/\hbar$, where the L is the characteristic size of the box, yielding

$$i\frac{\partial\tilde{\psi}}{\partial\tilde{t}} = -\nabla^2\tilde{\psi} + \alpha|\tilde{\psi}|^2\tilde{\psi} - i\eta|\tilde{\psi}|^4\tilde{\psi}, \quad (5.2)$$

where

$$\alpha = \frac{8\pi aN}{L} \quad \text{and} \quad \eta = \frac{N^2 m K_3}{\hbar L^4}, \quad (5.3)$$

and $\tilde{\psi}^2$ is now normalized to unity rather than N . With Eq. (5.2) in hand, we turn to our three principal questions.

5.2.1 Critical interaction strength

We begin with question (i) What is the condition for collapse? Collapse occurs due to the competition between kinetic energy ($\propto 1/x^2$) and interaction energy ($\propto \alpha/x^3$), for a state of characteristic size x . In Fig. 5.2 we show a sketch of the total energy as a function of x for different representative values of α . In the case where the interactions are repulsive or zero

($\alpha \geq 0$), only one energy minimum exists and the BEC is stable. For attractive interactions ($\alpha < 0$) a new global minimum emerges at $x = 0$. While the minimum at $x = 0$ represents the singularity to which the BEC can collapse, we see that for small negative α a kinetic energy barrier leads to a metastable solution at non-zero x . At α_c this barrier disappears, leaving nothing to stop the BEC from collapsing towards $x = 0$. This stability criterion is a static parameter, and only depends on α and *not* on η ³. The critical interaction strength a_c thus scales with atom number N and box size L as $a_c \propto L/N$ [c.f. Eq. (5.3); $a_c = \alpha_c L / (8\pi N)$].

5.2.2 Collapse time

Here we elaborate on the second question (ii) What is the time to collapse? After performing a quench of α to below α_c , the condensate is free to collapse towards the singularity ($x = 0$). In the absence of losses ($\eta = 0$) this occurs in a time t_c , where the central density asymptotically diverges, as shown in the inset of Fig. 5.2. Such an increase in density however eventually results in atom loss. As the losses are a higher-order nonlinear phenomenon, for relatively small η their stabilizing effect is only encountered close to t_c and the collapse time remains essentially unchanged compared to the lossless ($\eta = 0$) case. Within this approximation, the dimensionless collapse time t_c/τ_0 is expected to only depend on α .

5.2.3 Atom loss and weak collapse theory

The answer to (iii) What is the aftermath of the collapse?, should be contained in Eq. (5.2), and hence it depends on both α and η . Moreover, the fraction of atoms lost, $\Delta N/N$, should also just be a function of α and η . The nature of the collapse event (*i.e.* whether it is *strong* or *weak*) will dictate the dynamics around t_c and determine how many atoms are lost in a collapse event. Collapse has been extensively studied theoretically for $\eta = 0$, where it has been shown that the wave function adopts a self-similar form close to t_c [203, 204]. The most pertinent prediction of weak collapse, which is expected in 3D, is that the collapsing self-similar solution contains a decreasing number (and fraction) of atoms as the singularity is approached. As atom loss only occurs once the central density reaches $\sim |\alpha|/\eta$, this means that the stronger the attractive interactions, the further the collapse progresses towards t_c and the higher the maximum density reached. Combining these insights, counter-intuitively predicts that the *stronger* the attractive interactions, the *fewer* atoms will be lost in a single collapse event⁴.

³This still relies on the implicit assumption that $\eta \ll 1$, so that three-body loss is negligible in the metastable condensates and only becomes important if the BEC collapses.

⁴It has been theoretically shown that when considering $\eta \neq 0$ for a cubic self-focusing term and a quintic non-linearity the collapse is a critical case between weak collapse and the formation of a hotspot, where atom loss occurs for an extended amount of time once the singularity is reached [238–240].

5.3 Experimental studies

5.3.1 Critical interaction strength

In order to measure the critical interaction strength we initially prepare a quasi-pure BEC with N atoms, confined in a three-dimensional cylindrical box trap of linear size $L \approx 2R$, at a scattering length of $4 a_0$. Note that for the range of scattering lengths that we explore K_3 is essentially constant [241, 242], with the value $1.3(5) \times 10^{-41} \text{m}^6 \text{s}^{-1}$ [243]⁵. For the range of L and N explored throughout, this corresponds to small values of η ($< 6 \times 10^{-4}$), which ensures that three-body loss is negligible in our (meta)stable condensates. However, if collapse occurs, then significant loss occurs, providing the primary experimental signature of a collapse.

We slowly (over ≈ 1 s) ramp the scattering length to a final value a and hold in trap for an additional ≈ 3 s before taking an absorption image after 80 ms time-of-flight (ToF) expansion at $20 a_0$. In Fig. 5.3(a) we show the number of atoms remaining, denoted by N_f , as a function of a for a fixed $N = 18.7(5) \times 10^4$ and $L = 30(1) \mu\text{m}$. A sharp drop in N_f is observed at a well defined a , clearly signifying a_c . This is also accompanied by a dramatic deformation of our clouds, as shown in Fig. 5.3(b). Fig. 5.3(c) shows the measurements of a_c for $L = 30(1) \mu\text{m}$, spanning over a factor of 20 in N . A striking linear dependence of a_c on $1/N$ is observed, with the gradient of a linear fit giving $Na_c = -4.88(5) \mu\text{m}^6$.

Furthermore, as shown in Fig. 5.3(d), by plotting Na_c versus L , we extract $|\alpha_c| = 4.0(1)$ ($\alpha_c = 8\pi Na_c/L$). Numerically solving the GP equation for our cylindrical box using imaginary time evolution to determine the ground state yields the critical point $|\alpha_c| = 4.3$. While this discrepancy is larger than our statistical error bar, it can be readily explained by considering our two main sources of systematic errors. Our calibration of the absolute atom number presents a lower bound, and it could reasonably underestimate the actual atom number by up to 10%. Our simulations also assume an ideal cylindrical box potential, whereas any imperfections in the trapping potential could lead to small deviations of α_c . In particular, we cancel gravity and any other stray magnetic field gradients so that the atoms experience a residual acceleration (in all directions) on the $10^{-4}g_0$ level [22], where $g_0 \approx 9.84 \text{m s}^{-2}$ is the local gravitational acceleration. This leads to a gravitational potential energy of $L \times 4 k_B \text{pK} (\mu\text{m})^{-1}$ across the box, which is equal to the ground state energy in a cylindrical box (with $L = 2R$) when $L \approx 40 \mu\text{m}$.

⁵The indistinguishability of atoms in a BEC leads to a reduction of K_3 by a factor of $3!$ compared to thermal gases.

⁶By extrapolating a_c to the $1/N \rightarrow 0$ limit, we are able to slightly refine the location in magnetic field at which the scattering length vanishes in the $|1, 1\rangle$ state. We refine the previously determined value of $B_0 = 350.4(1) \text{G}$ [244] to $B_0 = 350.45(3) \text{G}$ [26]. A third, independent measurement of the zero crossing (see Section A), based on the failure of evaporation in a thermal Bose gas, is also consistent with this value of B_0 . The remaining 30-mG uncertainty in B_0 corresponds to a systematic uncertainty in our a values of $\approx 0.02 a_0$.

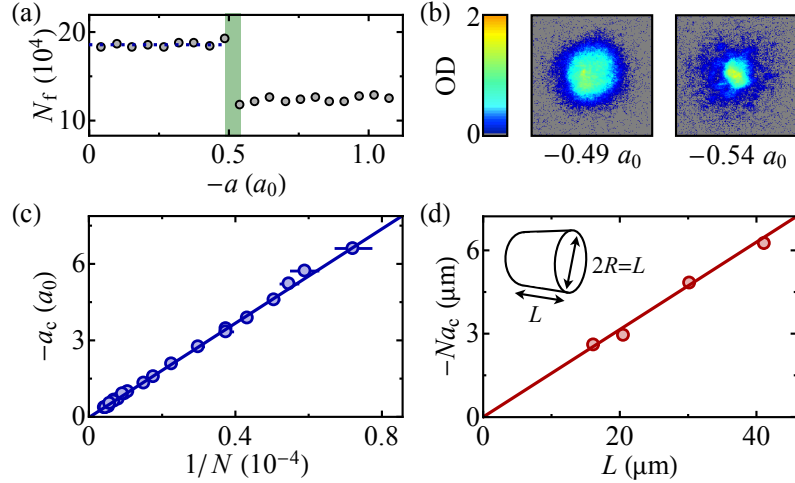


Fig. 5.3 Critical interaction strength. (a) Atom number, N_f , after a ramp to a final scattering length, a . The critical interaction strength a_c is clearly visible by a sharp drop in N_f . (b) Absorption images of clouds produced under identical conditions apart from a small $0.05 a_0$ change in a , clearly indicating the collapse event. (c) Variation of a_c with N for a cylindrical box with $L \approx 2R \approx 30 \mu\text{m}$. The linear fit confirms $a_c \propto 1/N$. (d) Variation of Na_c with L , where the aspect ratio is fixed such that $L = 2R$ (within experimental uncertainties). The linear fit (whose intercept is consistent with zero) confirms the expected $Na_c \propto L$ scaling and its gradient gives the critical parameter $\alpha_c = -4.0(1)$. Figure from [26].

However, the linear dependence of $-Na_c$ on L in Fig. 5.3(d) suggests that the condensate size is only weakly perturbed by these not-so-small gradients, and that the uniform potential remains a good approximation for describing our optical box trap.

To further investigate these effects experimentally, we explore how the critical condition for collapse is altered in a tilted cylindrical box potential, which we achieve by purposefully applying a magnetic field gradient along the axis of the cylinder. To supply the field gradient, we use the pair of compensation coils along the experimental y -axis (see Fig. 3.2). The atoms experience a force given by the Zeeman interaction, which leads to an axial linear potential, resulting in a ‘wedge’-like trapping potential as shown in Fig. 5.4(a). We use an axial field gradient corresponding to an acceleration $g_y = 4.5(2) \times 10^{-3} g_0$ along y ⁷. For our $L \approx 30 \mu\text{m}$ box the resultant gravitational potential energy $\approx k_B \times 6.2 \text{ nK}$ dwarfs the ground-state energy of only $\approx k_B \times 0.2 \text{ nK}$ and so it dominates the non-interacting Hamiltonian.

We now repeat the measurements presented in Fig. 5.3 for the tilted box potential. In Fig. 5.4(b) we show a dataset taken for fixed $N = 9.2(4) \times 10^4$. A sharp drop in N at well defined a_c is also observed here, exhibiting the same qualitative behavior as for the uniform box potential. There is however a qualitative difference in the absorption images recorded [see Fig. 5.4(b)]. The uncollapsed metastable BEC is already significantly perturbed as compared to the uniform case [c.f. Fig. 5.3(c)]. Once the collapse has occurred, the absorption images now also feature

⁷We calibrate the field gradient by measuring the acceleration felt by the atoms as the current in the coil is varied. We use both 70 ms and 100 ms ToF to guard against any initial position or velocity effects, which we find to be negligible. We obtain $g_y = 1.70(1) I \times 10^{-3} g_0$, where I is the current in the coils (in ampere).

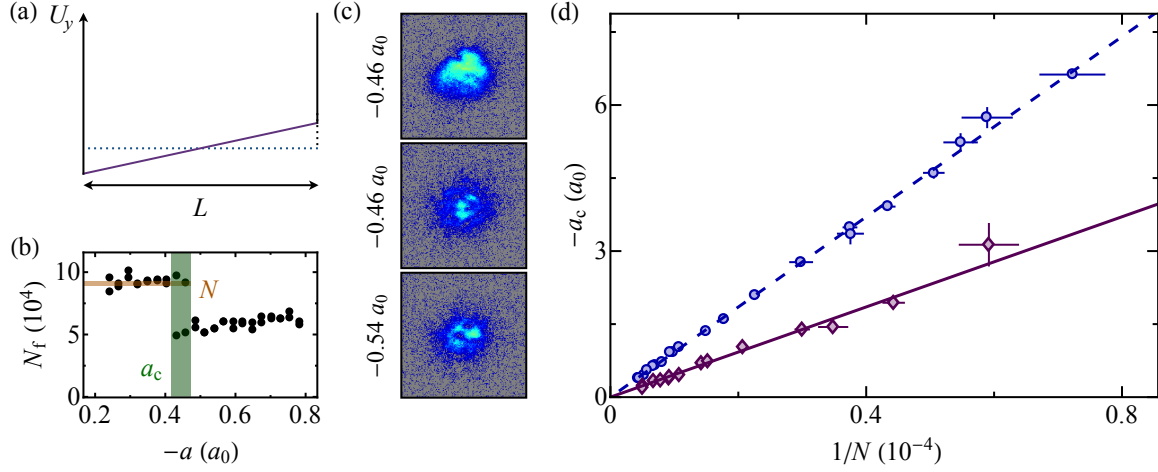


Fig. 5.4 Critical condition for collapse in a tilted box. (a) Sketch of both the tilted box potential (purple solid line) and the uniform box potential (blue dotted line). (b) Typical measurement of N_f as a function of a for the tilted box potential; a sharp drop in N_f occurs at a_c . (c) Absorption images of the clouds before (top) and after (middle and bottom) collapse, taken with 100 ms ToF at $a_{\text{ToF}} = 20 a_0$. The clouds before collapse already look perturbed, and once collapse has occurred they feature a myriad of density perturbations and high-contrast dips. (d) Extracted a_c values versus $1/N$, comparing wedge (purple) and uniform (blue) box data under otherwise identical conditions.

myriad high contrast holes and perturbations.

In Fig. 5.4(c) we plot the measured a_c for various different $1/N$ in our tilted box, and for convenient comparison we also include the data from our quasi-uniform box experiments. In both cases we see linear behavior in $1/N$, however the gradient of the tilted box potential is reduced by $\approx 50\%$ compared to the quasi-uniform case. This change is to be expected as the gradient introduces another term in the Hamiltonian, which reduces the effective condensate size. On dimensional grounds one can predict that $Na_c \propto \ell$ holds true for any dominant lengthscale ℓ involved. It would be interesting to test these scalings, however due to the anisotropic nature of the gradient it would also require an understanding of the dependence of α_c on the aspect ratio of the box, which we have fixed to $2R \approx L$ throughout.

5.3.2 Collapse dynamics

Here we explore the dynamics of collapsing BECs and our experiments aim to answer the second question posed in Section 5.1: (ii) What is the time to collapse? To this end we perform quench experiments. We begin by preparing a metastable BEC with N atoms in a box of linear size $L \approx 2R$, at a scattering length $a_i < 0$, a small distance ($\approx 0.3 a_0$) above a_c ⁸. We then quench the interaction strength to a final value $a < a_c$, before waiting for a variable hold time t . The

⁸This allows us to indiscriminately quench to final values of $a > a_c$, providing a simultaneous measurement of a_c for every set of N and L ; this acts as a cross-check against magnetic field drifts that could otherwise compromise our calibration of a . We checked that our results do not appreciably depend on the exact choice of a_i .

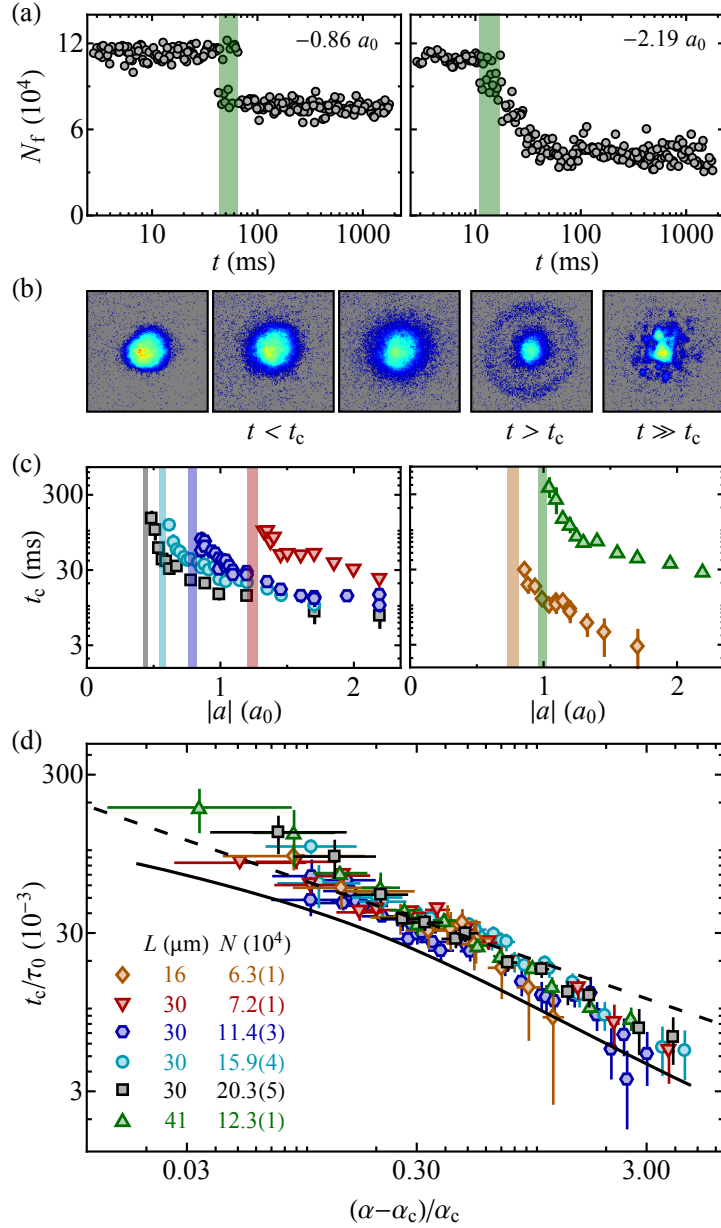


Fig. 5.5 Collapse dynamics. (a) Final atom number N_f versus t , for two different a , where $N = 11.4(3) \times 10^4$ and $L = 30(1) \mu\text{m}$. We extract the collapse time t_c (green vertical bands) as the onset of atom loss. For small $|a|$ (left) N_f suddenly jumps to a lower value at t_c . For much larger $|a|$ (right) the loss occurs gradually in time until a final value is reached. (b) Example images at various hold times after a quench to below a_c ; here $a = -1.02 a_0$ and $a_{\text{ToF}} \approx 20 a_0$. (c) The extracted collapse time t_c versus $|a|$ for six series with different N and L [see legend in (d)]. The shaded vertical bands correspond to a shift in a_c . The difference in N predominantly leads to an x -axis shift, related to a shift in a_c . By changing L , drastically different collapse times are observed, varying between 3 ms and 300 ms. (d) Universal collapse dynamics. Dimensionless collapse time t_c/τ_0 versus the dimensionless log-distance of α from α_c . A striking coalescence of all the six data series is seen. The solid line shows the results of lossless GP simulations without any free parameters and the dashed line shows $t_c/\tau_0 \propto [\alpha_c/(\alpha - \alpha_c)]^{1/2}$, which is predicted from a simplistic classical model (see text). Figure adapted from [26].

starting point for measuring t is defined as the half-way point between a_i and a ⁹. The collapse process is finally halted by a jump in scattering length to $a_{\text{ToF}} \geq 0$, before switching off the box trap letting the cloud expand in 80 - 100 ms ToF.

In Fig. 5.5(a) we show typical time traces of N_f in two qualitatively different regimes. For quenches just beyond the critical point (small $|a - a_c|$) the atom number exhibits a sudden drop to a stable lower value at t_c . We interpret this as a single collapse event. Instead, for quenches far beyond the critical point (large $|a - a_c|$) N_f decays in a seemingly continuous manner before it ultimately stabilizes. This behavior, also seen in previous measurements of collapse in harmonically trapped BECs [209, 217], is understood to arise from a series of multiple, experimental unresolved, collapse events [214, 215, 245–251]. In this multiple-collapse regime we associate t_c with the onset of atom loss, which coincides with the time when the atom loss-rate is maximal.

Fig. 5.5(b) shows a series of representative images observed throughout the collapse process. For these measurements we use $a_{\text{ToF}} \approx 20 a_0$, which leads to an additional expansion of the clouds by adding repulsive interaction energy at the start of ToF, which is then converted to kinetic energy during ToF. This avoids saturation of the images to allow for accurate counting of the remaining atoms. Moreover, as the interaction energy increases quadratically with density, this procedure also indirectly provides a measure of the in-situ density. The atom number remains constant up to the collapse time, t_c , but during the approach we see a clear swelling of the clouds. This increase in expansion energy is interpreted as the shrinking of the BEC wave function on route to collapse. Shortly after t_c (within ≈ 10 ms), we observe collapse remnants consisting of two parts: a lower-energy central part, and a higher-energy shell, reminiscent of the atom bursts generated in [209]. Similar shells are observed when imaging the samples from a perpendicular direction, indicating that they are spherical. From the size of these shells in ToF we infer that they expand at a rate of $\approx 2 \mu\text{m}/\text{ms}$. At longer times, more irregular patterns are observed, which is consistent with the shell reflecting off the trap walls and interfering with the central part of the cloud after ≈ 10 ms¹⁰.

It is already evident in the two examples shown in Fig. 5.5(a) that the time it takes for collapse to occur decreases as the scattering length becomes more negative. We have repeated such measurements for a range of different a , N , and L . In Fig. 5.5(c) we plot the extracted collapse times t_c for each series (fixed N and L) as a function of $|a|$. We see divergent behavior of t_c as a approaches a_c (the vertical shaded bands indicate a_c for each series). The predominant

⁹We define $t_q = t + \delta t$ as time when the quench is initiated. For the quenches used here we have measured $\delta t = 5(2)$ ms using RF spectroscopy, approximating the smooth change of a (varying from 20% to 80% in ≈ 4 ms) as an instantaneous jump centered at the half-way point, which is only meaningful when $\delta t/t$ is small.

¹⁰A more in-depth discussion of the collapse remnants can be found in Section 5.3.3.

effect of increasing N is a negative x -axis shift, accompanied by a shift in a_c . By changing L for series with similar a_c instead, we observe a drastic change in the observed collapse times, which vary by over two orders of magnitude. Due to the divergent behavior around a_c and from the expected scaling laws (see Section 5.2.2) predicted by the dimensionless generalized GP equation [Eq. (5.2)] for small values of η (for our six data series η varies between 4×10^{-5} and 4×10^{-4}), we plot t_c/τ_0 versus $(a - a_c)/a_c \equiv (\alpha - \alpha_c)/\alpha_c$ in Fig. 5.5(d) on log-log scale. A remarkable coalescence of all six series is observed, supporting the universal scaling laws that Eq. (5.2) predicts for small η where the losses only occur very close to the critical point and thus do not appreciably alter t_c . The solid line in Fig. 5.5 shows t_c extracted from numerical simulations of the lossless GP equation, without any free parameters. This reproduces a similar dependence of t_c on α , although the numerical values lie systematically slightly below the experimental ones.

To provide some additional qualitative insight, we turn to the simple model from Section 5.2. We consider the classical dynamics of a ball on the energy landscape shown in Fig. 5.2. The acceleration of the ball is proportional to the gradient dE/dx . Since the ball is moving slowly at the start, it is reasonable to assume that the initial change in x will dominate the time it takes to reach $x = 0$ (collapse to occur). This yields a simple over-estimation of t_c , where we assume that the acceleration remains constant at its initial value. As E depends linearly on α , the initial acceleration is proportional to $\alpha_c - \alpha$, and hence under these assumptions we predict $t_c \propto 1/\sqrt{\alpha - \alpha_c}$. This power-law prediction is shown by the dashed line in Fig. 5.5(d), and is in relatively good agreement with the data (in particular for small $\alpha - \alpha_c$) for such a simplistic picture.

5.3.3 Aftermath of the collapse

To address question (iii) What is the aftermath of the collapse?, we further consider the quench experiments from Section 5.3.2, now focusing on $t > t_c$. The remnant atom number N_f provides our primary experimental signature of the aftermath of the collapse, but we also examine the structure of the collapse remnants.

Observation of weak collapse

We begin by considering the loss dynamics in a single quench experiment series with fixed N and L . In Fig. 5.6(a) we plot the fractional atom loss $\Delta N/N$ versus t for four different a . Here $\Delta N = N - N_f$, where N is the initial pre-collapse atom number, and N_f the final time-dependent one. For small $|a - a_c|$ (left panel), in the regime of single-collapse events where the

atom loss occurs abruptly, we observe the surprising result that increasing $|a|$ leads to less atom loss, indicating weak collapse. Instead, for quenches to much larger $|a - a_c|$ (right panel), in the multiple-collapse regime where the atom loss occurs gradually once t_c has been reached, the opposite trend is observed in the long-time limit, in line with previous experiments [209–211].

In order to understand the non-monotonic behavior between these two regimes, we plot the fractional atom loss $\Delta N/N$ versus $a_c/|a|$ for all hold times in Fig. 5.6(b). Our choice of x axis captures the full range of $a < a_c$, from $a/a_c \approx 1$ to $a/a_c \rightarrow \infty$. For $t < t_c$, collapse has not yet occurred, and thus our data is scattered around $\Delta N = 0$. When collapse occurs ($t > t_c$), outcomes at non-zero $\Delta N/N$ are observed. As $a_c/|a|$ increases, ΔN smoothly decreases, in line with weak collapse theory. For $a_c/|a| < -0.6$, in the regime of single-collapse events, we clearly see that the atom loss decreases with increasing $a_c/|a|$, and extrapolates to zero as $a_c/|a|$ vanishes. This is the hallmark signature of weak collapse.

A linear extrapolation of $\Delta N/N(a_c/|a|)$ gives a y -intercept of $\Delta N/N = -0.02(2)$ (dot-dashed

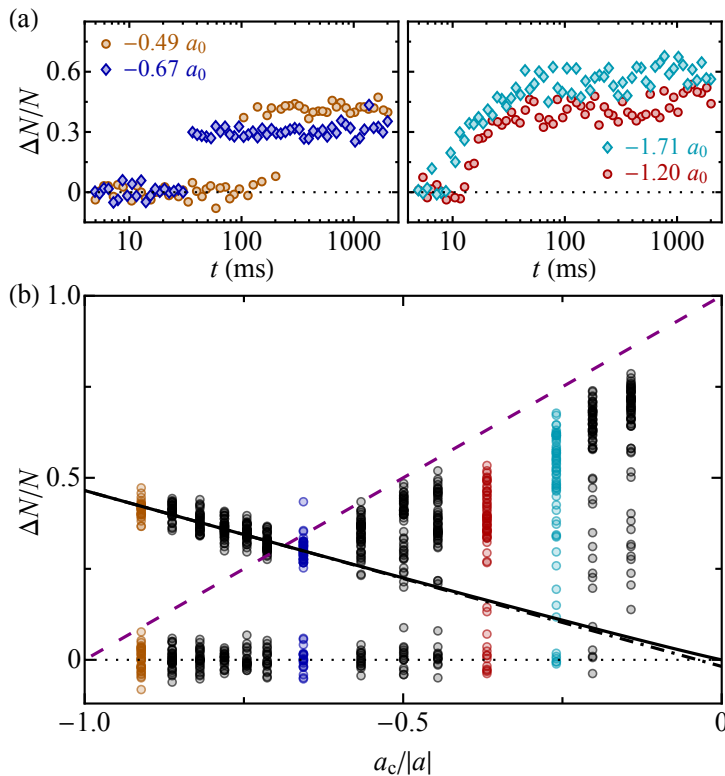


Fig. 5.6 Observation of weak collapse. (a) Fractional atom loss $\Delta N/N$ versus t for four different a with $N = 20.3(5) \times 10^4$ and $L = 30(1) \mu\text{m}$. For a close to a_c (left panel) the fractional loss decreases for increasing $|a|$, whereas for much larger $|a|$ (right panel) the opposite trend is seen in the long-time limit. (b) $\Delta N/N$ versus $a_c/|a|$ for the entire data series from (a) (including all $a < a_c$ and t); the colors indicate the respective series from (a). The points around $\Delta N/N = 0$ show BECs that have not yet collapsed ($t < t_c$). For a close to a_c , in the regime of single-collapse events, we see $\Delta N/N$ monotonically decrease with increasing $|a|$. Moreover, extrapolating to $a_c/|a| \rightarrow 0$ shows how $\Delta N/N$ vanishes (solid and dot-dashed black lines), which is the unambiguous signature of weak-collapse. When $a_c/|a| > -0.6$ the single-collapse atom loss fails to stabilize the clouds (as too few atoms have been lost), and multiple collapse events occur; the purple dashed line indicates the equilibrium stability requirement, $\Delta N/N = 1 - a_c/a$. Figure from [26].

black line in Fig. 5.6). Instead, fitting a power-law we obtain $\Delta N/N \propto |a|^{-1.05(7)}$, which is shown by the (almost indistinguishable) solid black line.

For $a_c/|a| > -0.6$, a deviation from the weak-collapse trend is observed, where the dwindling single-collapse atom loss can no longer stabilize the remnant, and additional collapse events occur. The purple dashed line shows the equilibrium post-quench stability criterion $\Delta N/N = 1 - a_c/a$, which defines (assuming equilibrium) the required atom loss in order to stabilize the cloud after the quench [$N_c(a) = \alpha_c L / (8\pi a) = N a_c/a$]. The validity of this condition is not a given in the far-from-equilibrium setting following the first collapse event [210]. Nevertheless, we find that it gives a decent estimate for both the crossover between single- and multiple-collapse regimes ($a_c/|a| \approx -0.6$), and the long-time loss for large $|a|$. Note that the slight underestimation of the long-time loss at large $|a|$ is consistent with the fact that any added kinetic energy from the first collapse event will help stabilize the clouds.

Weak collapse scaling laws

We now turn to unravelling the scaling laws that describe the weak-collapse atom loss. We perform a similar analysis as above for our five other quench experiment series with different N and L (from Section 5.3.2). We restrict ourselves to only include those values of a for which the first collapse event is clearly resolved. This predominantly includes cases where only a single collapse event occurs, but also some where both single and double collapse events are resolved.

For our six series, we follow the same procedure as in Fig. 5.6(b) and perform power-law fits of the form $\Delta N/N \propto |a|^{-\gamma}$ to extract γ . As shown in Fig. 5.7(a), we always obtain values consistent with $\gamma = 1$; a weighted average over all six series gives $\bar{\gamma} = 1.02(2)$.

Having experimentally uncovered the form $\Delta N/N = C/|a|$, we now turn to the N and L dependence of C . Plotting C versus N on a log-log plot [see Fig. 5.7(b)] reveals power-law behavior with $C \propto N^{-0.51(2)}$, and no experimentally resolvable dependence on L ; our two data series with $L \approx 16 \mu\text{m}$ and $L \approx 41 \mu\text{m}$ lie on the same curve as the four with $L \approx 30 \mu\text{m}$. Hence we have experimentally deduced that the weak-collapse atom-loss scales as $\Delta N/N \propto 1/(\sqrt{N}|a|)$. Re-writing this in terms of α and η [see Eq. (5.3)] yields $\Delta N/N \propto \eta^{1/4}/|\alpha|$. While the determined weak-collapse scaling laws are independent of the linear size of the box L , note that they may depend on its aspect ratio (we fix $L \approx 2R$ throughout); this could be interesting to study in the future.

In Fig. 5.7(c) we show the fractional single-collapse atom loss for all our series versus $\eta^{1/4}/|\alpha|$, where each point in a series corresponds to a specific a , averaged over all $t > t_c$. We find that

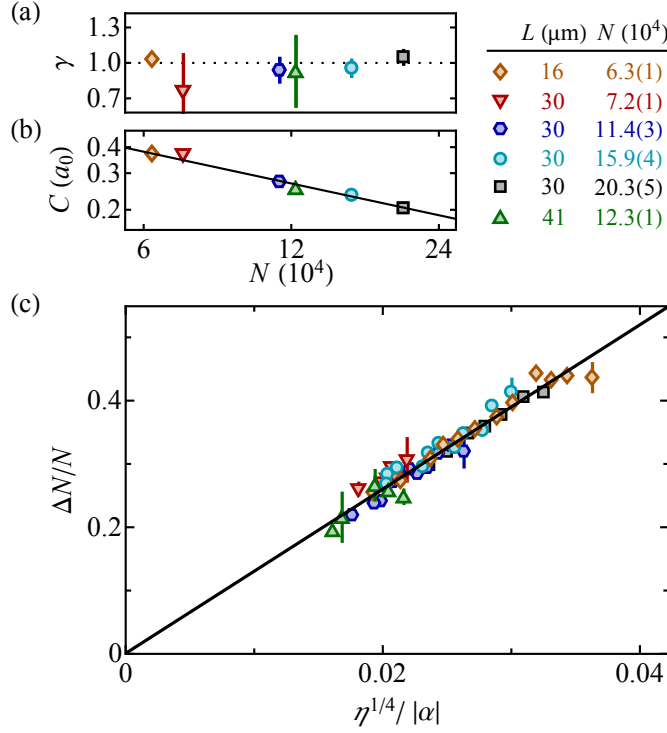


Fig. 5.7 Weak collapse scaling laws. (a) We fit a power-law of the form $\Delta N/N \propto |a|^{-\gamma}$ to the single-collapse atom loss data for our six series (see legend). A weighted average yields $\bar{\gamma} = 1.02(2)$. (b) Assuming the functional form $\Delta N/N = C/|a|$, we get $C \propto N^{-0.51(2)}$ (solid black line), without any dependence on L . (c) Universal weak-collapse atom loss behavior. By plotting the single-collapse data for different a , N and L versus $\eta^{1/4}/|\alpha|$, we find that all our data lie on a single universal curve. Moreover, this clearly highlights how the single weak-collapse atom loss vanishes in the limit of infinitely strong attractive interactions, $|\alpha| \rightarrow \infty$. We obtain $\Delta N/N \approx 13\eta^{1/4}/\alpha$ from a linear fit. Figure from [26].

all our data can be described by a single universal function $\Delta N/N \approx 13\eta^{1/4}/|\alpha|$. Theoretically understanding this scaling law remains an open problem; our measured scaling differs from a simple prediction based on scaling arguments within weak-collapse theory, which predicts $\eta^{1/2}/|\alpha|^2$ [204]. Moreover, as $\Delta N/N$ cannot exceed 100%, its linear dependence necessarily breaks down for larger values of $\eta^{1/4}/|\alpha|$. In future it would be compelling to experimentally explore the regime of strong dissipation by, for example, using a different Feshbach resonance or atomic species.

In the same spirit, it is interesting to ask what experimental parameters maximize the range over which single weak-collapse events are observable. The critical scattering length is given by $a_c = \alpha_c L/(8\pi N)$, and the equilibrium post-quench stability criterion reads $N_{\text{safe}} = \alpha_c L/(8\pi a)$. Moreover, the experimentally extracted scaling of ΔN implies $N_f = N - \Delta N = N - c_1 N^{1/2}/a$, where c_1 is a constant. We expect that for more negative a single weak-collapse events occur only until N_f exceeds N_{safe} , as then not enough atoms are lost in the single collapse event, owing to the diminishing weak-collapse atom loss for stronger attractive interactions. We denote the

scattering length at which $N_f = N_{\text{safe}}$ as $a = a^*$; solving for a^* yields

$$a^* = a_c + \frac{c_1}{N^{1/2}}. \quad (5.4)$$

Now, the relevant distance between a^* and a_c in log-space is given by

$$\frac{a^* - a_c}{a_c} = \frac{8\pi c_1 N^{1/2}}{\alpha_c L}, \quad (5.5)$$

which suggests that range over which single-weak collapse events are resolvable in our experiments increases for increasing N and decreasing L ¹¹. This conclusion is also supported experimentally, where the range over which clearly resolvable single collapse events occur is the largest for series with large N and small L , as evidenced in Fig. 5.7(c) where these series span the largest portion of the graph.

Crossover between single and double collapse

Having elucidated the scaling laws for single weak-collapse events, we now present experimental evidence for a gradual crossover between single- and double-collapse events as $|a|$ is increased. We start by considering a single series with $L \approx 30 \mu\text{m}$ and $N = 11.4(3) \times 10^4$. In Fig. 5.8(a) we show the time evolution of N_f following a quench to various closely spaced a between a_c and a^* (defined as $N_f = N_{\text{safe}}$), which reveals a striking bifurcation of the collapse outcome. We observe two clearly resolved branches, which we interpret as the result of either one (upper branch) or two (lower branch) collapse events; the accompanying histograms of N_f values accentuate this.

The existence of such a crossover regime, where the system moves between preferentially collapsing one or two times, strongly supports our interpretation that an increasing number of sequential collapse events occur as $|a|$ is increased, until for large $|a - a_c|$, in the regime of multiple collapse, the different discrete branches become experimentally unresolved and the loss is seemingly continuous.

In Fig 5.8(b), we show the corresponding $\Delta N/N$ versus $|a|$ on a log-log plot, from a_c to a^* . Importantly, in the regime where double-collapse occurs, the single collapse branch still clearly follows the weak-collapse scaling $\Delta N/N \propto 1/|a|$. Interestingly, the bifurcation regime does not have the same extent in a for all our data series; it seems to occur more prevalently for small N and large L . In these cases we also see hints at higher order bifurcation branches (though not statistically unambiguous).

¹¹Note that $a^* - a$ increases for decreasing N .

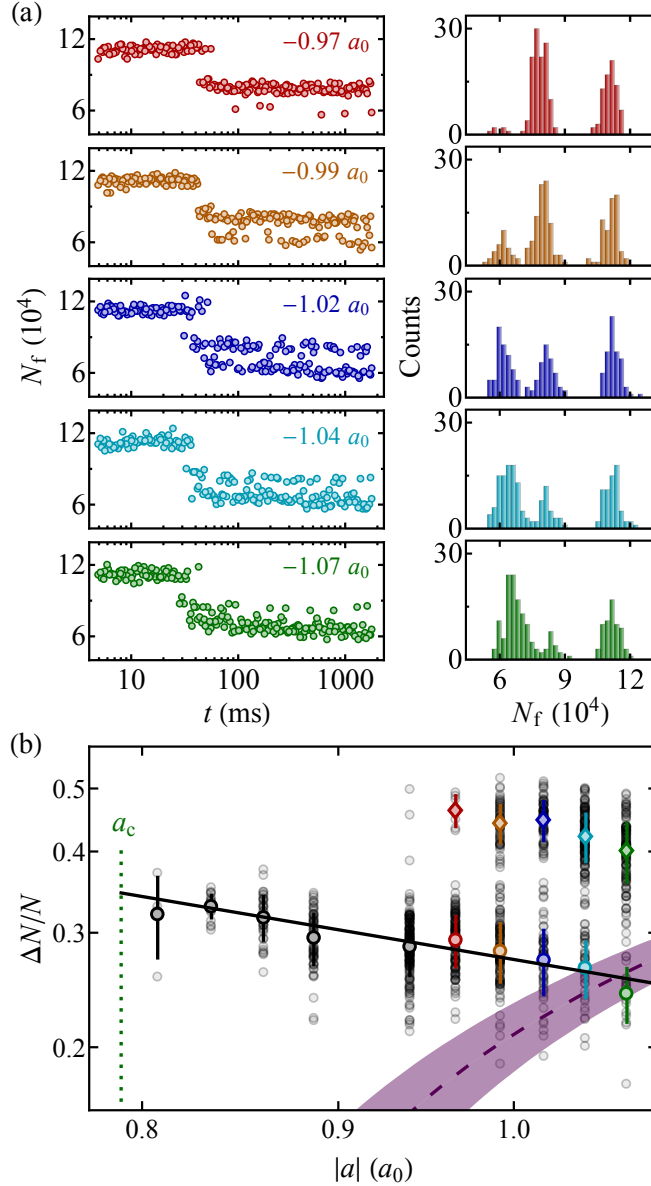


Fig. 5.8 Transition from one to two collapse events. (a) $N_f(t)$ for $L \approx 30 \mu\text{m}$, $N = 11.4(3) \times 10^4$, and finely spaced a in the range between a_c and a^* , accompanied by histograms of N_f values on the right. For $t > t_c$, as we increase $|a|$ and the weak-collapse atom loss decreases, a second outcome branch in N_f emerges. The two clearly resolved N_f branches correspond to one (upper branch) and two (lower branch) collapse events. The double-collapse probability gradually increases with $|a|$. (b) $\Delta N/N$ versus $|a|$ on a log-log plot. The raw data are shown as transparent black circles, while the colored circles and diamonds, respectively, show the average values for single- and double-collapse events. The error bars indicate the standard deviation. The purple dashed line shows the equilibrium post-quench stability criterion, and the band indicates its uncertainty. The solid black line shows the single-event weak collapse scaling law, $\Delta N/N \propto 1/|a|$, fit to the data. Figure from [26].

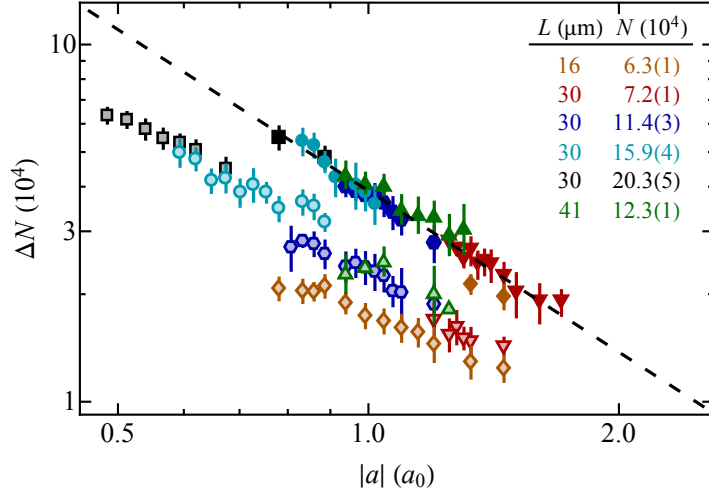


Fig. 5.9 Double-collapse scaling laws. We show ΔN versus $|a|$ on a log-log plot for both single (open symbols) and double (solid symbols) collapse events. Plotting the data this way predictably fails to align the single, weak collapse data. However, a striking coalescence of the double-collapse branch is observed. A weighted power-law fit to the double-collapse data for fixed L yields $\Delta N \propto a^{-1.50(4)}$ (black dashed line). The data do suggest a weak dependence on L ($\sim L^{0.25(10)}$) as evidenced by the larger (smaller) box data lying slightly above (below) the fit.

Double-collapse scaling laws

We proceed by repeating the above analysis for all our six data series, empirically distinguishing both single- and double-collapse branches¹². In Fig. 5.9 we show the time-averaged ΔN versus $|a|$ on a log-log plot for both single- and double-collapse branches (open and solid symbols, respectively). Plotted this way, the single-collapse data [from Fig. 5.7(c)] *do not* fall onto a universal curve, as expected since this form is not equivalent to the weak-collapse scaling law $\Delta N/N \propto 1/(\sqrt{N}a)$. On the contrary, and rather surprisingly, the data for the double-collapse branch does fall onto a single curve. From a power-law fit to the double-collapse data with fixed L (dashed black line) we obtain $\Delta N \propto a^{-1.50(4)}$. Note that the data do suggest a weak dependence on L , and optimal coalescence is achieved with $\Delta N/N \propto L^{0.25(10)}/(Na^{3/2})$. It should be noted that this scaling is no longer dimensionless (or solely captured by η and α), implying that our dimensional analysis from Eq. (5.2) is no longer adequate.

The mere existence of such a simple scaling for the double-collapse atom loss is already surprising when one considers the far-from-equilibrium dynamics that occurs in a double-collapse¹³. In general, a particularly important problem is that the initial condition for the second collapse event (if truly sequential in nature) is relatively unclear, and numerical continuations of the GP equation beyond the singularity are difficult, demanding adaptive grids and other subtle assumptions on continuation through a singularity (see *e.g.* [193]). Fully under-

¹²Cases where this distinction is ambiguous are rare, and disregarding them does not affect the results.

¹³As an example, there is numerical evidence that Eq. (5.2) presents a critical case between weak collapse and the formation of a hotspot [238–240], which could be related to the curious dynamics that we observe.

standing these scaling laws presents an exciting task for future work.

Structure of the collapse remnants

In the preceding sections we focused on the atom number of the collapse remnant, N_f , as our primary experimental signature. Here we extend our analysis to include the momentum distribution of the collapse remnants, which offers insight into the rich post-collapse dynamics. To this end, we perform quench experiments with $a_{\text{ToF}} \approx 0$ for otherwise identical parameters as in Fig. 5.5(a) [where $a_{\text{ToF}} \approx 20 a_0$]. This avoids adding expansion energy in flight, allowing a more accurate measurement of the shape of the momentum distribution, but remains complimentary to the $a_{\text{ToF}} \approx 20 a_0$ measurement as it does not faithfully measure N_f ¹⁴.

We start by considering the single-collapse regime, and in Fig. 5.10 we show typical $a_{\text{ToF}} \approx 0$ images of the collapse dynamics [see Fig. 5.5(b) for the $a_{\text{ToF}} \approx 20 a_0$ counterpart]. As t_c is approached, we observe a less-pronounced swelling of the clouds compared to the $a_{\text{ToF}} \approx 20 a_0$ case, as we are not as sensitive to the diverging central density as the cloud shrinks. For times directly after t_c , such that $t_c < t < t_r$, we again observe isotropic shell-like structures (here t_r is the time it takes for the shell to reflect off the trap walls)¹⁵. Interestingly, the central lower-energy part of the collapse remnant is seemingly unperturbed initially [see also 5.5(b)].

For $t > t_r$ [Fig. 5.10(c)] we see structured anisotropic patterns, indicating intricate post-collapse dynamics¹⁶. However, the general structure and orientation of the ordered structures that we observe is surprisingly reproducible. At later times ($t \gg t_r$, about 100 ms after t_r), isotropic disordered structures are predominantly observed [Fig. 5.10(d)].

We propose the following qualitative picture that is consistent with the observed dynamics. Following the first collapse event, a spherically symmetric shell of atoms is initially traveling outwards. As the system has stabilized ($N_f < N_{\text{safe}}$), this shell simply propagates outwards and eventually reaches the walls of the box, where it is reflected, as its energy (≈ 2 nK) is still significantly lower than the trap depth (≈ 30 nK)¹⁷. Experimental imperfections in the homogeneity of trap depth, which we expect to be around 20%, then cause path-differences between different parts of the shell as it is reflected, which in turn leads to a failure to refocus,

¹⁴Our imaging is insensitive to high optical density ($\text{OD} \gtrsim 3$) regions, where it underdetermines the occupations.

¹⁵While the shell-like structures are most spectacularly observed in the single-collapse regime, they are also observed for much larger $|a|$ close to (but above) t_c .

¹⁶Experimental variability in the initial conditions leads to scatter in t_c from shot to shot, and as we only know the average value of t_c the exact time since collapse has occurred is unknown in each realization. Consequently, the trends described here are based on empirically assessing the occurrence probability of specific types of images. Implementing a weak measurement imaging technique (*e.g.* phase contrast imaging [252]) would allow quantitative time-resolved measurements of the same cloud as it collapses.

¹⁷We have checked that if the box trap is turned off 15 ms before t_c , the collapse still occurs and shell-like structures are observed predominantly (also for $t > t_r$).

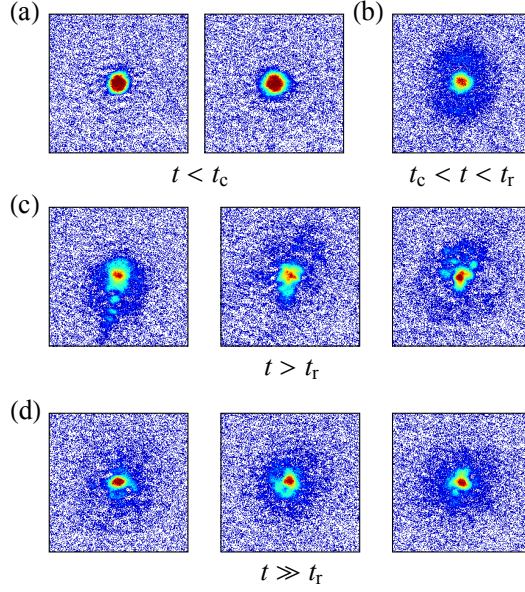


Fig. 5.10 Single-collapse remnants. Typical absorption images taken with $a_{\text{ToF}} \approx 0$ for clouds in the single-collapse regime (low $|a|$) at different times t (a-d); see text. The images highlight the rich collapse dynamics before, at long times, isotropic disordered structures eventually emerge.

generating ‘tail-like’ structures. Subsequently, additional reflections occur, leading to peculiar ordered structures, which only at long times, after numerous reflections, form an isotropic disordered final state.

We now turn to the question: What is the nature of this final state? To address this question, we proceed by extracting the final-state momentum distribution of the remnants. The distribution measured in ToF is the convolution of the in-trap momentum distribution with the initial size of the trap, integrated along the line of sight. The mapping to momentum space is given by $\hbar k_r = mr/t_{\text{ToF}}$, where r is the radial distance from the center of the cloud. The initial size of the box defines $k_L = mL/(2\hbar t_{\text{ToF}})$, the smallest momentum which can be meaningfully measured, and the trap depth U_D introduces a high- k cut-off, and defines the maximum $k_D = \sqrt{2mU_D}/\hbar$. In between these two limits, we can safely posit that $k_r \approx k$. In order to reconstruct the 3D momentum distribution \tilde{n}_k , we first azimuthally average the images (assuming isotropy and $k = k_r$), before performing inverse-Abel transforms (see Section C) and finally averaging over time (for $t \gg t_c$). In this final step we assume that any relaxation is slow on this ~ 1 s timescale, which we will scrutinize experimentally in the following.

In Fig. 5.11 we show \tilde{n}_k averaged for $0.2 \text{ s} < t < 1.8 \text{ s}$ on a log-log plot (solid blue line) in the single-collapse regime ($a = -0.86 a_0$) for $N = 11.4(3) \times 10^4$ and $L = 30(1) \mu\text{m}$. The blue band shows the standard deviation of the time average, and the thin dotted orange and green lines show, respectively, \tilde{n}_k at $\approx 0.2 \text{ s}$ and $\approx 1.7 \text{ s}$, confirming our assumption that the final state momentum distribution is stationary on these timescales. The inset shows the time-averaged

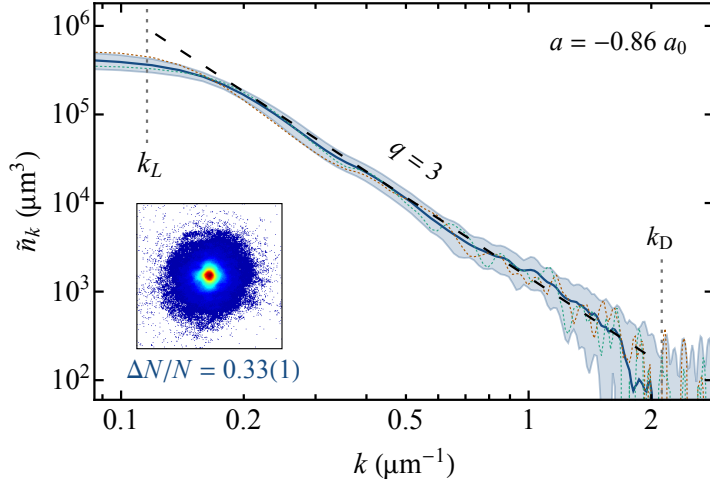


Fig. 5.11 Remnant momentum distribution in the single-collapse regime. We show a log-log plot of \tilde{n}_k for $a = -0.86 a_0$, $N = 11.4(3) \times 10^4$, and $L = 30(1) \mu\text{m}$. The blue solid line shows the time average for $0.2 \text{ s} < t < 1.8 \text{ s}$. The shaded band shows the standard deviation of the time average, while the dotted orange and green lines show \tilde{n}_k at $\approx 0.2 \text{ s}$ and $\approx 1.7 \text{ s}$, respectively. The vertical dotted lines indicate k_L and k_D , corresponding to $L = 30 \mu\text{m}$ and $U_D/k_B = 30 \text{ nK}$. The black dashed line shows a decaying power-law with exponent $q = 3$, which \tilde{n}_k follows over a decade in k . The inset shows the time average of the absorption images, revealing an isotropic distribution.

absorption image, further highlighting the isotropy of the collapse remnants. The momentum distribution \tilde{n}_k exhibits a striking power-law dependence $\tilde{n}_k \propto k^{-q}$, with $q \approx 3$ (black dashed line). It is curious that this power-law coincides with that expected for a turbulent cascade in the weak-wave turbulence regime [169] (see also Section 4.2).

So far we only considered collapse remnants in the single-collapse regime, and we now turn to the remnants in the regimes of multiple collapse. We start by considering the bifurcation regime, where both single- and double-collapse events can occur (see also Fig. 5.8). In Fig. 5.12(a) we present typical $a_{\text{ToF}} \approx 0$ images for $t \gg t_r$ at $a = -1.04 a_0$ with $N = 11.4(3) \times 10^4$ and $L = 30(1) \mu\text{m}$. The two collapse outcome branches, which feature different $\Delta N/N$, are also clearly resolved by a dramatic difference in the central low-energy part of the cloud. The images from the double-collapse branch (left), where more atoms are lost, are visually similar to the remnants in the single-collapse regime at lower $|a|$ (see Fig. 5.11). Instead, for the single-collapse branch (right), where only one collapse event occurs and less atoms are lost, the images now look strikingly different, with a completely disturbed central core.

In Fig. 5.12(b) we show \tilde{n}_k in the bifurcation regime ($a = -1.04 a_0$), where we separately average the single- and double-collapse branches for $t > 0.2 \text{ s}$. A clear difference in \tilde{n}_k is also observed between the two branches, where the single-collapse branch features a significant increase in occupation of momentum states at around $0.5(2)/\mu\text{m}$. In both cases the distribution for $k \gtrsim 1/\mu\text{m}$ still remains consistent with the decaying $q = 3$ power-law dependence (dashed black line). The insets, showing time-averaged images, reiterate the striking difference between

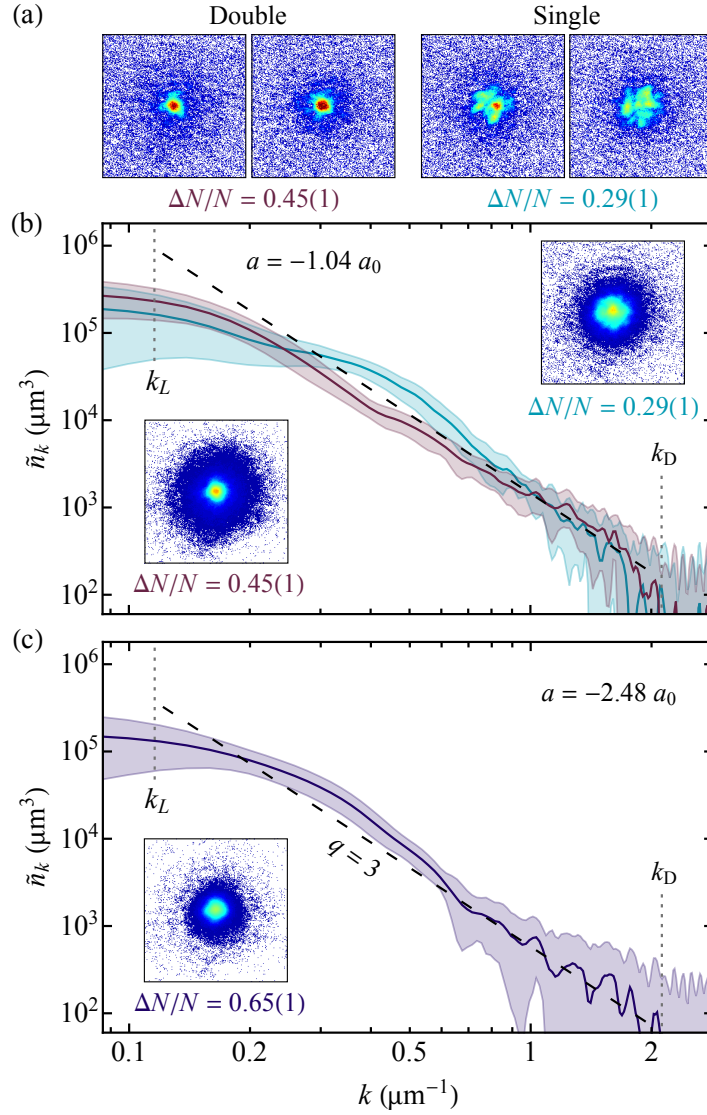


Fig. 5.12 Remnant momentum distributions in the regimes of multiple collapse. Here $N = 11.4(3) \times 10^4$ and $L = 30(1) \mu\text{m}$. (a) In the bifurcation regime ($a = -1.04 a_0$) where either single- or double-collapse events can occur, the absorption images also clearly exhibit a dramatic visual difference between single- and double-collapse events. (b-c) Momentum distribution \tilde{n}_k for (a) $a = -1.04 a_0$ in the bifurcation regime (separately averaging single and double collapse outcomes) and (b) $a = -2.48 a_0$ in the multiple collapse regime. The solid curves are the long-time ($t > 0.2$ s) averaged \tilde{n}_k and the bands show the standard deviation. The black dashed line shows the power-law $\tilde{n}_k \propto k^{-q}$, with $q = 3$, and the vertical dotted lines indicate k_L and k_D (see text). The insets show the corresponding averaged images, highlighting dramatic visual differences between regimes.

the two outcome branches. Physically, in cases where a second collapse occurs, the situation is similar to the single-collapse regime, but with a non-equilibrium initial condition. However, the fact that being prone to collapse a second time profoundly affects the post-collapse dynamics, even if the second collapse event does not occur, is strong evidence that the two collapse events are sequential in time.

In Fig. 5.12(c) we show the long-time averaged \tilde{n}_k for the same N and L , but at large $|a|$ ($a = -2.48 a_0$) in the multiple-collapse regime, where atom loss has occurred in seemingly continuous fashion through multiple (experimentally unresolvable) collapse events. Here the distribution resembles that from the single-collapse branch in the bifurcation regime of Fig. 5.12(b), and it remains consistent with a power-law distribution $\tilde{n}_k \propto k^{-q}$, with $q = 3$ for $0.7 < k < k_D$.

5.4 Conclusion

In summary, we performed a detailed study of the collapse of a box-trapped BEC. We have successfully answered the three questions that we set out to explore. Most importantly, we provided first experimental evidence of weak collapse in any physical system, demonstrating the associated scaling laws that dictate the weak-collapse atom loss. While our experiments provide concrete benchmarks for the theory, they also pose many new questions and puzzles for future research.

A specific, particularly intriguing example is the loss of phase information following a collapse event [193, 253], which is thought to be a general property of collapse. After a singularity occurs, the solution of the nonlinear Schrödinger equation is only determined up to a phase factor of $\exp(i\theta)$. In real physical systems, where the singularity is only approached and not entirely reached due to dissipative loss mechanisms that enter, this is thought to translate to the fact that the phase is ‘almost’ lost, in the sense that the final phase becomes highly sensitive to small changes in the initial conditions. It is therefore thought that interactions between separate post-collapse components result in a chaotic final state [193] (see also [254]). This property was recently tested in the collapse of optical beams [255], where wave function phase scrambling is presented as an explanation for the chaotic and turbulent behavior that is observed in the aftermath of collapse events.

However, in their case the collapse is strong, and it is unclear how these notions extend to weak collapse theory, where the collapse is only partial in that only a part of the wave collapses towards the singularity (see Section 5.2.3). Nevertheless, turbulence at low nonlinearity levels is generally thought to correspond to a set of waves whose phases are close to random [169], which is consistent with the notion of phase loss and our observations.

6 Moderately Strongly Interacting Bose Gases

Therefore love moderately: long love doth so;

Too swift arrives as tardy as too slow.

Romeo & Juliet

- William Shakespeare -

6.1 Introduction

Superfluidity is one of the most dramatic manifestations of coherent quantum many-body phenomena. Following its monumental discovery in liquid ^4He in 1937 [256–258], London [259] had the intuition to conceptually link this fascinating behavior to Bose–Einstein condensation, which to fair accuracy allowed him to predict the lambda temperature of liquid ^4He . Tisza shortly afterwards followed suit when using the notion of Bose–Einstein condensation to formulate his two-fluid model [260], which qualitatively explained the superfluid fountain effect and predicted the existence of two sound velocities. However, these early links did not go uncontested, and most prominently include Landau’s criticism that an ideal-gas picture of the strongly-interacting liquid ^4He state is fundamentally inadequate. Landau had formulated a phenomenological description of superfluids based on mixtures of weakly interacting elementary excitations (phonons and rotons) [261], which even though not rooted in microscopic theory, did correspond to the later measured excitation spectrum of superfluid ^4He .

In 1947 Bogoliubov developed a microscopic theory of the interacting Bose gas based on a perturbative treatment of excitations above a macroscopically occupied condensate [42], arriving at an effective quadratic Hamiltonian valid for contact interactions governed by an interaction parameter $na^3 \ll 1$ (see Section 2.4). This constituted a breakthrough in the understanding of Landau’s excitation spectrum, providing a direct link between Bose–Einstein condensation and superfluid behavior, while also reproducing the linear dispersion at low momenta. However any comparison to liquid helium remained only qualitative, owing to the inherently strong

and poorly understood interactions in superfluid ^4He , which bring it far out of the theory's regime of validity¹.

Bogoliubov theory has become a cornerstone of our modern understanding of interacting quantum fluids. The advent of laboratory synthesized gaseous atomic Bose–Einstein condensates [3, 4] which offer truly weak interactions ($na^3 \ll 1$) brought experiments directly into Bogoliubov theory's regime of validity, and allowed many of its aspects to be directly experimentally tested (see *e.g.* [8, 17, 267, 268] and references therein). By exploiting magnetic Feshbach resonances [7] (see Section 3.2.1), gaseous atomic BECs offer readily tuneable contact interactions characterized by an s -wave scattering length a , providing a flexible setting for pushing towards the strongly interacting regime $na^3 \sim 1$, where such experiments have started to probe the richer physics of interacting Bose fluids [10, 18]. However, increasing a also dramatically enhances inelastic three-body collisions, which makes experiments on strongly interacting bulk BECs [28–31, 46, 64, 269–271] difficult and still scarce².

More generally, the connection between condensation and superfluidity, as well as superconductivity (a superfluid of electrons), remains an active research topic; see *e.g.* [12, 272].

In this chapter we present our first studies of strongly-interacting homogeneous Bose gases. Here we focus on 'moderately' strong interactions, where simple mean-field theories break down and one can observe beyond-mean-field quantum correlation effects, but the gas remains in equilibrium and the experiments remain tractable within the existing theories. Our experiments provide steps towards the long-term goal of bridging the gap between weakly-interacting BECs and the richer phenomena observed in liquid helium, in a regime where the interaction parameter na^3 is no longer $\ll 1$.

We divide our discussion into two sections focusing on the ground state (Section 6.2, see also [29]) and the elementary excitations (Section 6.3, see also [28]). We note that many of the pertinent aspects of Bogoliubov theory, alongside our primary experimental tool for probing moderately strongly interacting samples, Bragg diffraction, have already been introduced in Chapter 3, to which we refer the reader as we will assume knowledge of these throughout.

¹Bogoliubov's theory was later extended by Lee, Haung, and Yang to hard-sphere bosons [44], and field theoretical formulations extended the predictions to the regime of strong interactions, showing that the linear low- k dispersion was a robust general feature [262, 263]. A vast amount of theoretical effort has been dedicated to the understanding of liquid ^4He (see *e.g.* [264–266] and references therein).

²In both mass-balanced Fermi gases near Feshbach resonances, and Bose and Fermi gases in optical lattices, the regime of strong correlations is readily reached experimentally owing to the suppression of three-body losses.

6.2 Quantum depletion

The central goal of this section is to experimentally address the 80-year old question - *How much of a superfluid is really a Bose–Einstein condensate?* Bogoliubov’s 1947 theory [42] describing the zero-temperature properties of weakly-interacting ($na^3 \ll 1$) Bose gases provides a tentative answer to this question. Within this theory, the condensate excitations are expressed as a superposition of pairs of counter-propagating single-particle states, and quantum fluctuations ensure that even at zero temperature there exists a non-zero occupation of such excitations (see Section 2.4). This leads to the coherent interaction-driven depletion of the condensate, and predicts the remaining condensed fraction

$$n_{\text{BEC}}/n = 1 - \gamma\sqrt{na^3}, \quad (6.1)$$

with $\gamma = 8/(3\sqrt{\pi}) \approx 1.5$.

While Bogoliubov first developed this theory in order to describe the superfluid state of ^4He , it was never directly applicable to it. Indeed, due to inherently strong interparticle interactions in superfluid ^4He , while 100% of the system is superfluid only about 10% of the atoms are actually in the condensate [264, 273]. The remaining atoms are coherently expelled from the condensate and spread over a large range of momenta.

Numerically, diffusion Monte Carlo simulations have rigorously tested the regime of validity of Eq. (6.1), and found it to be quantitatively valid for $na^3 \lesssim 10^{-3}$ [274]. The advent of gaseous atomic BECs offered new hope in experimentally confirming Eq. (6.1), as the interparticle interactions are well described by s -wave contact interactions and the achievable values of na^3 fall directly into the theory’s regime of validity.

Experimentally, however, an orthogonal challenge presented itself: the predicted depleted fraction n_{QD}/n is typically below³ 1%, making it rather difficult to measure. In harmonically trapped ultracold atomic gases, characteristic signs of quantum depletion were observed by either enhancing the role of interactions using optical lattices [275] (see also [276, 277]), or by performing high-resolution studies of the expansion of a weakly-interacting gas [278]. Nevertheless, only semiquantitative comparison to theory has been possible, due to complications associated with the addition of the lattice, the inhomogeneous gas densities involved, and the interpretation of the expansion experiments [279]. Recent experiments in the non-equilibrium driven-dissipative setting of polariton condensates [280] have also observed characteristic sig-

³For typical parameters $a = 100 a_0$ and $n = 10^{19} \text{ m}^{-3}$, we have $na^3 \approx 1.5 \times 10^{-6}$ and Eq. (6.1) predicts a depleted fraction of 0.2%.

natures of quantum depletion [281].

Here we experimentally create a textbook setting in order to quantitatively test and verify Bogoliubov's theory of quantum depletion. Using our experimental platform, outlined in Chapter 3, we produce homogeneous ^{39}K condensates with a readily tuneable scattering length a . We prepare our clouds in relatively large cylindrical boxes, with $R \approx 32 \mu\text{m}$, $L \approx 50 \mu\text{m}$ in order to achieve low-density quasi-uniform condensates with $n = 3.5 \times 10^{17} \text{ m}^{-3}$, as this allows us to reach larger values of $\sqrt{na^3}$ while enduring the same three-body loss rate $\dot{N}/N \propto n^2 a^4$ (ignoring the modulation due to Efimov physics [33, 34, 66]).

We turn to Bragg spectroscopy [93, 94], a coherent momentum-selective two-photon process, in order to access the underlying momentum distribution in spectroscopic fashion (see Section 3.2.4 for an overview of this technique and details of our experimental setup).

As we show below, the large separation of momentum scales between the Bose–Einstein condensate and the quantum depletion allows us to employ a BEC filtering technique [282], which in turn allows us to spatially separate the BEC from the high-momentum components of the gas. This significantly simplifies the experiments and, to within a good approximation, conceptually reveals the condensed fraction of the cloud in a single experimental run.

6.2.1 Bragg filtering

Our goal is to spatially separate the BEC from its depleted counterpart, in order to directly measure the condensed fraction and test Eq. (6.1). As Bragg spectroscopy probes the one-dimensional momentum distribution of the cloud $\check{n}_k^{1\text{D}}$, we begin by taking a closer look at the theoretically expected zero-temperature 1D momentum distribution of both the BEC, \check{n}_{BEC} , and the quantum depletion, \check{n}_{QD} , for realistic experimental parameters.

The BEC distribution $\check{n}_{\text{BEC}}(k)$ features a Heisenberg-limited width $\propto 1/L$ [87] and exponentially suppressed tails. A top-hat BEC wave function $\psi(y)$, of extent L , would give $\check{n}_{\text{BEC}} \propto \text{sinc}^2(kL/2)$, however the unphysical sharp edges in real space give unphysical high- k momentum tails $\propto 1/k^2$. In reality, the wave function is rounded off (over the healing length ξ) near the walls and so the momentum distribution has exponentially suppressed high- k tails. In the limit $\xi \ll L$, we have $\psi(y) \propto \tanh\left(\frac{L/2-|y|}{\sqrt{2}\xi}\right)$ for $|y| < L/2$ [8], which we use to compute $\check{n}_{\text{BEC}}(k)$ numerically.

On the other hand, the quantum depletion $\check{n}_{\text{QD}}(k)$ has a width $\propto 1/\xi$ and polynomial tails [8, 64, 270, 278]. In order to compute $\check{n}_{\text{QD}}(k)$ we assume that any finite-size effects are negligible and use the standard textbook prediction [8, 17] for the three-dimensional QD in an infinite system (see Section 2.4 for additional details). Integrating Eq. (2.40) over the two orthogonal

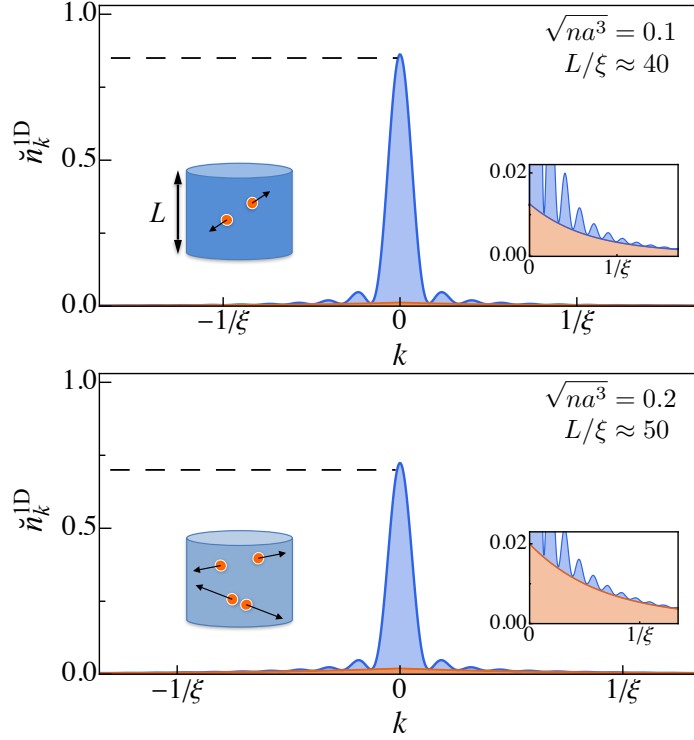


Fig. 6.1 Momentum distribution of a zero-temperature homogeneous Bose gas. Integrated 1D momentum distributions \check{n}_k^{1D} for a gas of density n and size L at two different interaction strengths a . We normalize the distributions such that $\check{n}_k^{1D}(0) = 1$ [setting $\gamma = 0$ in Eq. (6.1)]. The total $\check{n}_k^{1D}(k)$ consists of two parts: the low- k BEC (blue) with a Heisenberg-limited width $\propto 1/L$, and a broad quantum-depletion pedestal (orange) with characteristic width set by the inverse healing length $1/\xi$ (see text). The low- k distribution is (to good approximation) the same as for a pure BEC just rescaled by a factor $\sim 1 - \gamma\sqrt{na^3}$ (see dashed lines). The insets on the right accentuate that $\check{n}_{QD}(k) \gg \check{n}_{BEC}(k)$ at large k . The cartoons on the left depict the underlying microscopic picture of the coherent excitations out of the condensate (blue), which occur as a superposition of pairs of counter-propagating particles. Note that while we use experimentally relevant values of L/ξ , we do use slightly exaggerated values of $\sqrt{na^3}$ for visual clarity. Figure from [29].

directions gives

$$\check{n}_{QD}(k) \propto a \left(1 + \xi^2 k^2 - \sqrt{\xi^2 k^2 (\xi^2 k^2 + 2)} \right). \quad (6.2)$$

We normalize the r.h.s. of Eq. (6.2) to $\gamma\sqrt{na^3}$, and the numerical BEC momentum distribution to $1 - \gamma\sqrt{na^3}$. In Fig. 6.1 we show examples of the expected $\check{n}_k^{1D}(k) = \check{n}_{BEC}(k) + \check{n}_{QD}(k)$, where we scale both distributions so that in the absence of quantum depletion $\check{n}_k^{1D}(0) = 1$.

As long as $L/\xi \gg 1$, separation of scales is ensured and $\check{n}_{QD}(k)$ extends over a much wider range of momenta than $\check{n}_{BEC}(k)$. This in turn allows a Bragg pulse with two-photon Rabi frequency Ω to be tuned to resonance with $k = 0$ to selectively diffract the BEC, leaving most of the high- k QD tails behind. However, for a non-infinite L/ξ the choice of Ω is non-trivial, as both the imperfect diffraction of the BEC and the partial diffraction of the QD introduce opposite systematic effects⁴. As shown in Fig. 6.2, we find satisfactory results with $\Omega = 2\pi \times$

⁴Naively one might choose Ω so that a π -pulse has a Fourier width equivalent to the central (zero-to-zero) width of the BEC spectral line [set by $4\pi\hbar q/(mL) \approx 2\pi \times 900$ Hz for our $q = 1.7k_{\text{rec}} \approx 13.7/\mu\text{m}$ considered here]. However, it is beneficial to capture more of the sinc^2 -tails to avoid leaving behind a significant fraction of the BEC (see [29] for a detailed discussion).

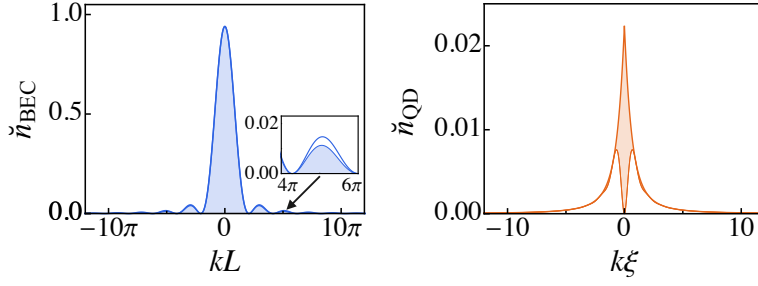


Fig. 6.2 Bragg filtering efficiency. Expected zero-temperature 1D momentum distributions of both \tilde{n}_{BEC} (left) and \tilde{n}_{QD} (right) for typical experimental parameters: $n = 3.5 \times 10^{17} \text{ m}^{-3}$, $L = 50 \text{ }\mu\text{m}$, and $\sqrt{na^3} \approx 0.04$. The shaded regions indicate the fraction of the distribution that a Bragg π -pulse centered on $k = 0$ with $\Omega = 1.8 \text{ kHz}$ diffracts (see Section 3.2.4). Integrating yields a predicted 96% diffraction of the BEC, while leaving behind 71% of the QD, and to a relatively good approximation achieves the desired filtering. Note the difference in x -axis between the two panels; here $L/\xi \approx 60$. Figure from [29].

1.8 kHz for representative experimental parameters. In the following, we will first assume that the filtering works perfectly, before later assessing the impact of this systematic effect, as well as those arising from the small non-zero temperature of our samples.

Finally, using $q\xi \gg 1$ permits the separation of diffracted and non-diffracted portions of the cloud in time-of-flight expansion, as it ensures that the momentum kick received by a diffracted atom, $\hbar q$, is much larger than the QD momentum spread. Combining the above requirements, we arrive at the necessary separation of scales $1/L \ll 1/\xi \ll q$. For our experiments we achieve $L/\xi > 30$ and $q\xi > 12$, allowing us to directly employ this filtering technique.

Our experimental protocol is as follows. We start by preparing a weakly interacting BEC at $a \approx 200 a_0$, such that $\sqrt{na^3} < 10^{-3}$. The condensate is quasi-pure, supported by the fact that we do not discern a thermal fraction in time-of-flight expansion. Our clouds are initially prepared in a trap of depth $U_0 \approx k_B \times 20 \text{ nK}$, but before tuning a we adiabatically increase U_0 by a factor of 5 in order to ensure that the interaction energy is smaller than the trap depth [$U_0 \gg \hbar^2/(2m\xi^2)$].

We then adiabatically (in 150 – 250 ms) increase a to a value between 700 – 3000 a_0 , and measure the diffracted fraction (DF) as a function of τ . We limit ourselves to values of a which fulfill two requirements: (i) three-body losses are kept to below 10%, and (ii) when reducing a back to 200 a_0 no signs of heating are apparent.

In order to avoid scattering between atoms as they are diffracted out of the cloud, which would jeopardize our filtering protocol, before the Bragg pulse we rapidly turn off the interactions (in $\approx 60 \text{ }\mu\text{s}$), using an RF π -pulse to transfer the atoms to the essentially non-interacting $|F = 1, m_F = 0\rangle$ state (see Section 3.2.1). This sudden turn off of the interactions before probing the gas greatly simplifies the interpretation as it eliminates any final-state interaction effects, ensures that the diffracted and non-diffracted components separate without undergoing

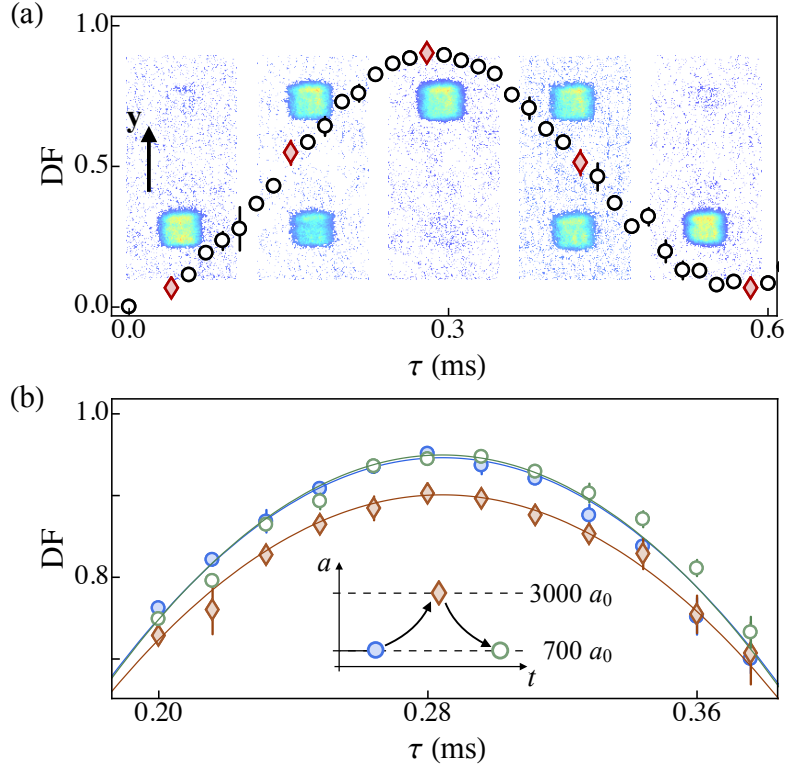


Fig. 6.3 Bragg filtering and reversible interaction tuning of the condensed fraction. (a) Diffracted fraction (DF) as a function of the Bragg pulse duration, τ , for Rabi frequency $\Omega = 2\pi \times 1.8$ kHz and $a \approx 3000 a_0$. The red diamonds correspond to data extracted from the absorption images in the background, which comprise of the spatially separated stationary (bottom) and diffracted (top) parts of the cloud. (b) Zooming in around the maximum diffracted fraction η (where τ is close to π/Ω), at three points in a round-trip protocol (see inset): at $700 a_0$ (blue circles), after increasing a from $700 a_0$ to $3000 a_0$ in 80 ms (orange diamonds), and after returning to $700 a_0$ in another 80 ms (open green circles). Each data point corresponds to the average of typically 10 repetitions (error bars indicate s.e.m.). The solid lines show the quadratic fits $[\eta - c_1(\tau - \tau_0)^2]$ used to extract η . Figure from [29].

collisions, and suddenly freezes the momentum distribution before we probe it using Bragg diffraction [283].

Following the Bragg pulse of duration τ , we wait for 10 ms, which allows the diffracted and non-diffracted portions of the gas to separate by $\approx 220 \mu\text{m}$, and ensures that the individual clouds do not significantly expand beyond the initial size of the box. Finally, we observe the gas by taking an absorption image along the z -axis (perpendicular to y).

In Fig. 6.3(a) we show an example of the measured diffracted fraction (DF) as a function of the Bragg pulse duration τ at $a \approx 3000 a_0$, for our chosen $\Omega = 2\pi \times 1.8$ kHz (see also [29]). Representative absorption images at various stages throughout this Rabi oscillation (red diamonds) are shown in the background. The images depict the clearly separated stationary (bottom) and diffracted (top) clouds.

We will initially assume that our Bragg pulse perfectly filters out the condensate from the high- k components of the gas, and that the condensed fraction of the cloud is simply given by the maximal diffracted fraction, η (which is observed for $\tau = \pi/\Omega \approx 0.28$ ms). The measured η

is slightly below unity, with a small portion of the cloud visibly left behind (see central image). While this is expected from quantum depletion, it could in practice also occur due to other reasons, including experimental imperfections or an inevitably nonzero gas temperature (which leads to thermal depletion).

To demonstrate that we are in fact observing quantum depletion, our experiments are performed in differential fashion - that is, we study how η varies with a , while keeping the other experimental parameters the same. Moreover, we verify that the initial tuning of η with a is adiabatically reversible, which excludes the possibility that the gas' condensed fraction is reduced due to non-adiabatic heating or losses. In Fig. 6.3(b), where we focus on DF at $\tau \approx \pi/\Omega$, we exemplify such adiabatic reversible tuning by performing three (sequential) protocols, as depicted in the inset: for a cloud initially prepared at $700 a_0$, following a ramp of a to $3000 a_0$, and after reducing a back to $700 a_0$ (completing the round-trip). We find that η indeed is reduced as a is increased, and crucially that this effect is fully reversible (within statistical uncertainties). We have verified such reversible tuning for our entire experimental range of a values.

6.2.2 Quantum depletion

We explore the variation of η with the interaction parameter $\sqrt{na^3}$ in Fig. 6.4. Within our assumptions, this directly tests Eq. (6.1). We observe the expected linear dependence of η on $\sqrt{na^3}$, and from a linear fit to the data, of the form $\eta_0(1 - \gamma\sqrt{na^3})$, we obtain an offset η_0 close to unity and a slope $\gamma = 1.5(2)$, in good overall agreement with Eq. (6.1).

Our next step consists of scrutinizing our assumptions. In the inset of Fig. 6.4 we summarize our numerical assessment of the systematic effects arising from imperfections of the filtering protocol both due to the non-infinite L/ξ (see Fig. 6.2), and due to a small nonzero initial temperature T . The magnitude of both of the systematic effects is of order $\lesssim 20\%$ and they partially cancel; note that here we only provide a brief account of these calculations, whereas they can be found in full detail in the supplementary information of [29].

The dashed line in the inset of Fig. 6.4 shows the simulated dependence of η on $\sqrt{na^3}$ for $T = 0$ and our experimental parameters (n , L , and Ω). As already indicated in Fig. 6.2, any non-infinite Ω slightly reduces η_0 as the tails of the BEC are not fully captured, which is in part why η_0 deviates from unity. Moreover, while the quantum depletion is spread over a large range of momenta, for non-infinite L/ξ we inevitably also diffract a portion of the quantum depletion, which has the effect of reducing the apparent γ ; a linear fit to the dashed line (omitted for clarity) gives $\gamma_0 \approx 1.2$.

The small systematic difference between our data and this $T = 0$ simulation can be explained

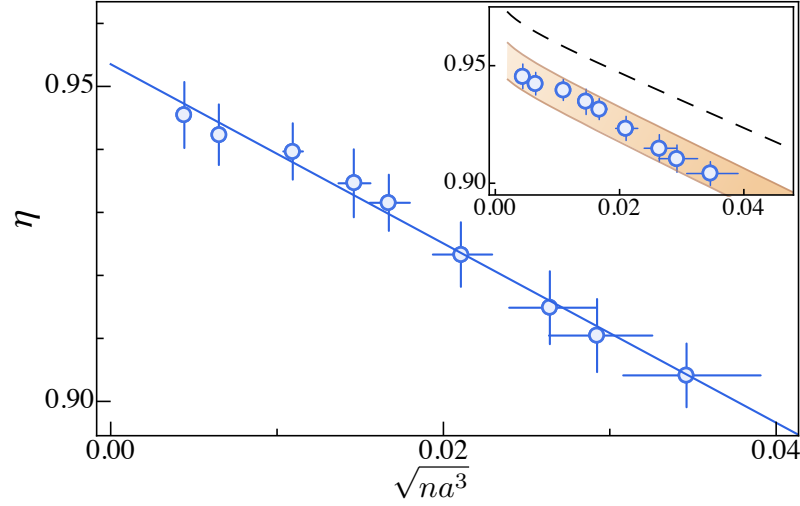


Fig. 6.4 Measurement of the quantum depletion of an interacting BEC. Plot of the maximal diffracted fraction η , which we associate with the condensed fraction, versus the interaction parameter $\sqrt{na^3}$. The solid line is a linear fit to the data, from which we obtain the offset $\eta_0 = 0.954(5)$ and slope $\gamma = 1.5(2)$. The vertical error bars show fitting errors (see Fig. 6.3), while the horizontal ones reflect both the $\approx 10\%$ uncertainty in n and the uncertainty in the Feshbach resonance position at 402.70(3) G [65]. The inset presents a detailed analysis of the systematic effects, including the non-infinite L/ξ and a small finite T . The dashed line shows numerical simulations of the expected η based on our Bragg filtering protocol for $T = 0$. The orange shaded region extends the simulations to include the effect of initial temperatures (at $a = 200 a_0$) between 3.5 to 5 nK (top to bottom). Figure from [29].

by assuming a small nonzero initial temperature. At a finite temperature, thermal depletion occurs, arising from the presence of thermal excitations (phonons); this generally reduces η as the majority of the participating atoms are also not diffracted by the Bragg pulse tuned to $k = 0$. Moreover, even if a is increased adiabatically, the amount of thermal depletion increases, because changing a modifies both the dispersion relation and the particle content of the thermally populated low- k excitations [8, 29]. If we consider our experimental protocol in which we initially prepare a gas at $200 a_0$ and small $T > 0$ before adiabatically increasing a , then due to this adiabatic heating the finite initial temperature would not only lead to a reduction of η by a constant offset (independent of $\sqrt{na^3}$) but it would also slightly increase the apparent γ . Indeed, by taking this into account in our numerical simulations we obtain the orange shaded band for an initial T between 3.5 and 5 nK, which is in quantitative agreement with our data. This low initial T is also in line with the fact that we do not discern the corresponding thermal fractions of $\lesssim 10\%$ in ToF at $200 a_0$, and it is reasonable for our trap depth $U_0 \approx 20$ nK. It is worth noting that due to these effects $\eta(\sqrt{na^3})$ is also not expected to be perfectly linear, however this is negligible on the scale of our experimental errors.

6.2.3 Conclusion

In conclusion, our experiments quantitatively confirm Bogoliubov's theory of the quantum depletion of a Bose–Einstein condensate. This theory forms the backbone of our understanding

of interacting quantum fluids. In the future, it would be interesting to perform experiments which access even larger values of $\sqrt{na^3}$, while also maintaining the stringent requirements on adiabaticity, heating, and losses. Deviations from Bogoliubov theory are expected to be observable at our level of statistical precision already for values of $\sqrt{na^3}$ about twice larger [274]⁵. Our measurements also reveal a remarkable sensitivity to the temperature of the clouds, and we envision that the Bragg filtering protocol, as originally conceived [282], could be used to achieve high precision thermometry in cases where the thermal fraction is too low to be discernible in ToF. Finally, it would also be interesting to use Bragg spectroscopy to measure the full 1D momentum distribution, and thus experimentally study the form of $\check{n}_{\text{QD}}(k)$.

6.3 Quasi-particle excitations

Elementary excitations of a many-body system provide a window into the system's ground state, and they determine how the system responds to external perturbations. They are consequently at the heart of a range of macroscopic many-body phenomena, such as superfluidity [256–258]. A powerful tool for probing elementary excitations is Bragg spectroscopy, a coherent two-photon process which provides direct access to the excitation energy $\hbar\omega$ at a well defined wavenumber q [55, 87, 93, 269, 284–286] (see Section 3.2.4). Previous experiments on weakly-interacting Bose gases have used Bragg spectroscopy to broadly confirm Bogoliubov theory, both in harmonically trapped gases relying on the local density approximation [284, 285], and more directly in homogeneous box-trapped condensates [87].

In strongly interacting atomic BECs much richer physics is expected (see [18] for a recent review), including phenomena traditionally associated with superfluid ^4He , such as the roton minimum in the excitation spectrum [287–289] (see also [264–266] and references therein). A deviation from the Bogoliubov spectrum was observed in Bragg spectroscopy of large- q excitations in a harmonically trapped ^{85}Rb BEC [269], and has inspired various theoretical interpretations [18, 269, 290–294], with no consensus or complete quantitative agreement with the experiments being reached so far⁶.

In this section we present our results of the Bragg spectroscopy of a moderately strongly

⁵Additional measurements that explore up to $\sqrt{na^3} \approx 0.08$ by abandoning our stringent adiabaticity criteria can be found in [29]. While having to be taken with a pinch of salt, they do tentatively suggest a deviation from Bogoliubov theory of the same sign and roughly the same magnitude as predicted by the Monte Carlo simulations [274].

⁶An inflection point in the dispersion relation has been observed in the one-dimensional regime in harmonically trapped gases [295], however arising purely from confinement-induced effects. Recent experiments using dipolar quantum gases have also observed a roton minimum in the excitation spectrum using oblate trap geometries [296], though here the origin of the minimum links back to the attraction between dipoles that reduce the energy cost for out-of-plane excitations.

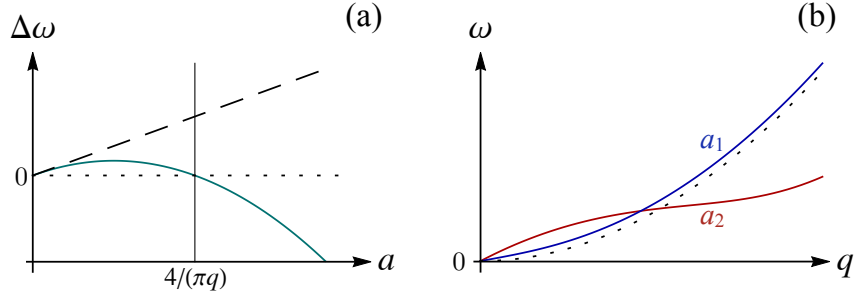


Fig. 6.5 Predictions for the excitation resonances. (a) Interaction shift $\Delta\omega$ for particle-like excitations with fixed q . The dashed line shows the Bogoliubov prediction (valid only for small qa), while the solid one shows the Feynman–Tan prediction. (b) Sketches of the dispersion relation $\omega(q)$. The solid lines correspond to two distinctly different scattering lengths ($a_2 > a_1$), following [297]. The dotted line corresponds to the free-particle dispersion relation ω_0 . Figure from [28].

interacting homogeneous BEC, focusing on large- q excitations. We significantly extend previously achieved values of a , thus confronting modern theories of interacting Bose gases.

6.3.1 Beyond Bogoliubov theory

Following Bogoliubov’s quasi-particle description (see Section 2.4), for $q\xi \gg 1$ the excitations are particle-like and the predicted interaction shift from the free-particle dispersion relation $\Delta\omega = \omega - \omega_0$, where $\omega_0 = \hbar q^2/(2m)$ is $\Delta\omega_B = 4\pi\hbar na/m$, which is q -independent and linear in na [see Fig. 6.5]. For a more qualitative understanding of this shift, consider that the atoms in the condensate feel a chemical potential $\mu = 4\pi\hbar^2 na/m$, while the diffracted (high- k) atoms have equal direct and exchange interactions with the condensate, amounting to 2μ , the difference of which recovers $\hbar\Delta\omega_B$.

In order for the prediction $\Delta\omega_B$ to be valid, one requires that: (i) the excitations are particle-like ($q\xi \gg 1$), (ii) the gas is weakly-interacting ($\sqrt{na^3} \ll 1$), and (iii) the two-body scattering amplitude is k -independent ($q \ll 1/a$), for which one can neglect the short-range two-particle correlations at distances $r \lesssim a$.

Assuming condition (ii) holds and $\sqrt{na^3} \ll 1$, the Feynman energy relation [298, 299] relates ω_0 to the excitation resonance via the static structure factor S_q , i.e. $\omega = \omega_0/S_q$. For short-range correlations and assuming $q\xi \gg 1$, S_q is given by

$$S_q = 1 + \frac{C_2}{8n} \left(\frac{1}{q} - \frac{4}{\pi a q^2} \right), \quad (6.3)$$

where term in the brackets arises from two-body correlations at short-distances, and C_2 is the two-body contact density (see Section 2.5), which captures the effects of many-body correlations [17, 294] and can be seen as a measure of the probability of finding two particles at the same point. Note that in general the possibility of such ‘factorization’ of two-body and many-

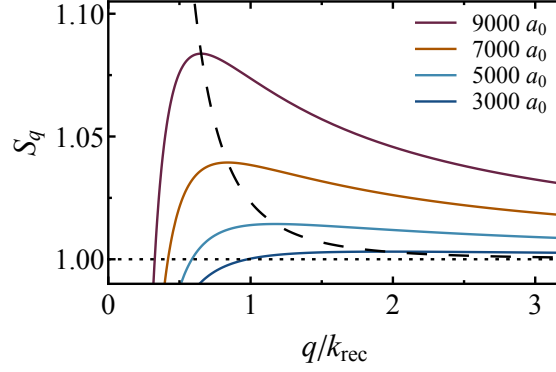


Fig. 6.6 Emergence of a peak in the structure factor. We plot the predicted S_q within the FT formalism for a gas density $n = 0.2 \times 10^{18} \text{ m}^{-3}$ at various a (see legend), with $\sqrt{na^3}$ ranging between 0.03 and 0.15, revealing the emergence of a clear peak structure as $\sqrt{na^3}$ increases. For all plotted values $q\xi \gtrsim 2$. The dashed line indicates the peak position for continuously varying a [see Eq. (6.3)].

body physics was first highlighted by Tan [47], and so we coin this the ‘Feynman–Tan’ (FT) formalism. By noting that for our experimental parameters $|S_q - 1| < 0.03$, where we have used the contact density $C_2 \approx (4\pi na)^2$ valid for low $\sqrt{na^3}$, we can approximate $1/S_q - 1 \approx 1 - S_q$. Within this approach the prediction for the interaction shift from ω_0 is then given by

$$\Delta\omega_{\text{FT}} = \frac{4\pi\hbar na}{m} \left(1 - \frac{\pi qa}{4}\right). \quad (6.4)$$

In the limit of small qa , $\Delta\omega_{\text{FT}}$ approaches the expected Bogoliubov result $\Delta\omega_{\text{B}}$ [dashed line in Fig. 6.5(a)], however for increasing a at fixed q it back-bends, changing sign at $a = 4/(\pi q)$ [solid line in Fig. 6.5(a)]. In contrast, for phonon-like excitations ($q\xi \ll 1$) $\Delta\omega$ remains positive for all a [297]. As depicted in Fig. 6.5(b), this implies an inflection point in the dispersion relation $[\omega(q)$ at fixed $a]$. Such an inflection point is a precursor of the roton minimum, which fully develops only for very strong interactions ($\sqrt{na^3} \sim 1$) [294, 297]. The static structure factor S_q (at fixed n and a) reaches a maximum at $q = 8/(\pi a)$ [see Eq.(6.3)], independent of n , as plotted for relevant experimental parameters in Fig. 6.6. While this maximum has been linked to the roton minimum [294, 300], the liquid helium scaling $q_{\text{roton}} \sim n^{1/3}$ is only recovered for $\sqrt{na^3} \sim 1$.

It is useful to define a dimensionless interaction frequency shift

$$\alpha \equiv \frac{mq}{4\pi\hbar n} \Delta\omega, \quad (6.5)$$

in order to recast the FT prediction [Eq. (6.4)] as

$$\alpha_{\text{FT}} = qa \left(1 - \frac{\pi}{4} qa\right), \quad (6.6)$$

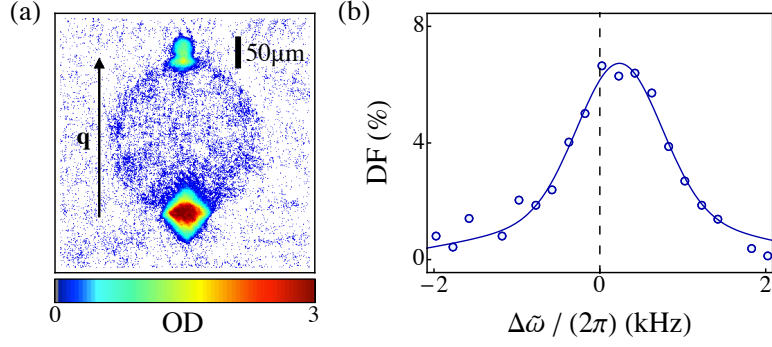


Fig. 6.7 Bragg spectroscopy of an interacting BEC. Here $n \approx 2.0 \times 10^{12} \text{ cm}^{-3}$, $q = 1.7 k_{\text{rec}}$ (along the \hat{y} axis), and $a \approx 1000 a_0$. (a) Typical absorption image (taken along \hat{z}) following a 2-ms Bragg pulse, and subsequent 15 ms ToF. It should be noted that the scattering halo, which occurs due to collisions between the stationary and diffracted cloud, does not alter the centre-of-mass of the atomic distribution. (b) Bragg spectrum for an interacting cloud, obtained by the varying frequency difference between the two Bragg beams (referenced to ω_0 , which we calibrated using a non-interacting cloud) and recording the diffracted fraction for each (obtained from the centre-of-mass). We extract the resonance position $\Delta\omega$ from a gaussian fit to the data (solid line). The typical statistical error on each data point is $\sim 1\%$. Figure from [28].

which is a universal function of qa . Within this formulation the Bogoliubov result reads $\alpha_B = qa$. In addition to its aesthetic qualities, this form is experimentally useful as it allows plotting the results with different n on the same universal curve.

6.3.2 Spectroscopy of quasi-particle excitations

We now turn to our experiments performing Bragg spectroscopy of interacting homogeneous Bose–Einstein condensates. As described in Section 3.1, we produce ^{39}K BECs in the lowest hyperfine state in order to access the Feshbach resonance at 402.70(3) G. For our purposes here, we prepare quasi-pure homogeneous BECs of $N = (50 - 160) \times 10^3$ atoms, in a cylindrical box of variable length $L = (30 - 50) \mu\text{m}$ and radius $R = (15 - 30) \mu\text{m}$; the corresponding gas densities n range between 0.2 and $2.0 \times 10^{18} \text{ m}^{-3}$. It is again beneficial to work at low densities, as one can reach larger values of qa and $\sqrt{na^3}$ for the same three-body loss rate $\dot{N}/N \propto n^2 a^4$ (ignoring the modulation due to Efimov physics [33, 34, 66]). Throughout we use a trap depth $U_0 \approx k_B \times 20 \text{ nK}$, and the condensed fraction is $> 90\%$ (see Section 6.2).

We always start by preparing the BEC at $200 a_0$, before ramping (in 50 ms⁷) the scattering length to its final value a at which we perform high-resolution Bragg spectroscopy⁸. We limit the maximal a that we explore for each n so that the total particle loss during the experiment is $< 10\%$. A significant advantage of using a homogeneous sample is that three-body loss does not intrinsically lead to significant heating [301]; this is in stark contrast to harmonic traps where ‘anti-evaporative’ heating occurs as atoms with below-average potential energy (at the

⁷We have checked that the Bragg spectra are not broadened for these ramp speeds, whereas for faster ramps we do observe significant broadening.

⁸Our Bragg pulses are 2-ms in duration, which minimizes any Fourier broadening and ensures a near-Heisenberg-limited width [87] when the sample is non-interacting.

trap center) are preferentially lost [302].

We choose three different Bragg angles θ to achieve three different values of q/k_{rec} : 1.1, 1.7, and 2.0, where $k_{\text{rec}} = 2\pi/\lambda$ and $\lambda = 766.7$ nm (see Section 3.2.4 for an overview of our Bragg set-up). For our experimental range of parameters we always stay in the regime of particle-like excitations: $q\xi$ varies between 5 and 40.

In Fig. 6.7(a) we present a typical absorption image following a 2-ms Bragg pulse and subsequent 20 ms ToF. At moderately strong interactions, the images feature a clear halo, which is spherical in shape and occurs due to collisions between the diffracted cloud as it leaves passing through the stationary BEC (see also [303, 304]). Importantly, these collisions do not alter the centre of mass of the atomic distribution, which we use to infer the diffracted fraction (DF) [269, 286]. We keep the maximum DF $\lesssim 10\%$ in order to keep the experiments within the linear response regime⁹.

We map out DF as a function of the frequency difference between the two Bragg beams $\tilde{\omega}$; in Fig. 6.7(b) we show a typical example of such a Bragg spectrum, with $\tilde{\omega}$ referenced to ω_0 ¹⁰. We extract the resonance shift from the free-particle dispersion $\Delta\omega$ using a gaussian fit to the data.

In Fig. 6.8 we plot the measured $\Delta\omega$, recast as the dimensionless α [see Eq. (6.5)], as a function of qa for three different combinations of density n and excitation wavenumber q ¹¹, which all fall onto a single universal curve. For $qa \gtrsim 0.5$ we observe back-bending and a clear deviation from the Bogoliubov theory prediction (dashed line)¹². Increasing qa further shows how α becomes clearly negative. We find excellent agreement with the Feynman–Tan (FT) prediction [solid line, see Eq. (6.6)], without any free parameters.

6.3.3 Exploring the limits of validity of Feynman–Tan theory

While we observe good agreement between our experiments and the FT prediction for $qa \lesssim 2.5$, we note that around $qa = 2.5$ the validity of this theory is questionable, and the apparent agreement could be fortuitous. For these data the interaction parameter is already sizeable; the Lee-Huang-Yang (LHY) prediction for the next-order correction to C_2 is of the order 50% [43, 44, 62] and beyond-LHY corrections [305, 306] could even be significant. The Feynman relation is also expected to be quantitatively reliable only for $\sqrt{na^3} \ll 0.1$ [297, 307].

We now consider even larger values of qa and $\sqrt{na^3}$ in order to test the limits of validity of the

⁹The measured shift $\Delta\omega$ reduces for larger DF, approaching 0 ($\omega = \omega_0$) for a π -pulse. The requirement DF $\lesssim 10\%$ should keep the resulting systematic relative suppression of $\Delta\omega$ to $\lesssim 10\%$ [285].

¹⁰We separately measure ω_0 using a non-interacting sample (see Section 3.2.4).

¹¹Note that the normalization of Eq. (6.5) allows us to take into account small $\pm 10\%$ variations in density for the data taken with the same nominal n and varying a .

¹²Previous Bragg spectroscopy experiments on harmonically trapped strongly interacting ⁸⁵Rb samples [269] achieved maximal values of a that correspond to $0.8/q$, and while back-bending was observed $\Delta\omega$ remained positive, consistent with FT theory.

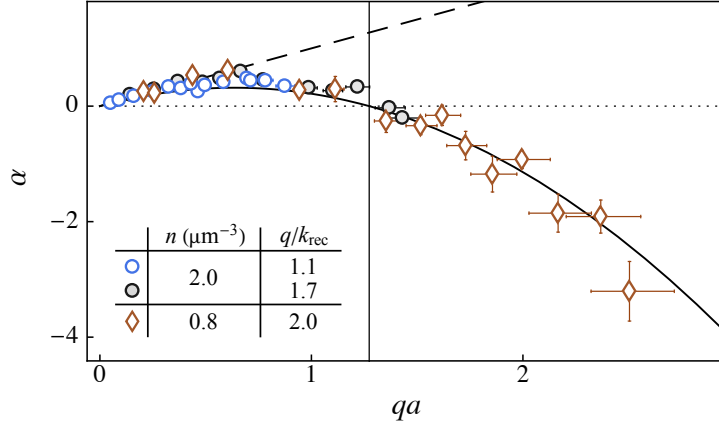


Fig. 6.8 Breakdown of the Bogoliubov approximation and observation of negative frequency shifts. Dimensionless frequency shift α versus qa for three different combinations of n and q (see legend). The solid line shows the FT prediction α_{FT} [see Eq. (6.6)] with no adjustable parameters, whereas the dashed line shows the Bogoliubov prediction $\alpha_{\text{B}} = qa$ valid for small qa . The vertical error bars show statistical fitting errors and the horizontal error bars reflect the uncertainty in a arising from uncertainty in the position of the Feshbach resonance. Figure adapted from [28].

FT prediction. In Fig. 6.8 we saw that, as anticipated, by decreasing the density (from $2.0 \mu\text{m}^{-3}$ to $0.8 \mu\text{m}^{-3}$) we were able to reach significantly larger values of a (up to $\approx 3 \times 10^3 a_0$) while adhering to our loss-requirement of $\lesssim 10\%$. Here we use even lower densities $n = 0.2 \mu\text{m}^{-3}$ (while also ensuring that our cloud remains quasi-homogeneous) to allow even larger values of $a \approx 8 \times 10^3 a_0$, corresponding to $\sqrt{na^3} \approx 0.1$, and with $q = 2k_{\text{rec}}$ we have $qa \approx 7$.

To explore deviations from FT theory we combine data taken using many different combinations of $\{n, q, a\}$, grouping them into sets with (roughly) equal $\sqrt{na^3}$, but varying values of qa . This allows us to attempt to disentangle the ‘culprit’ responsible any deviations, since if one simply increases a at fixed q and n then one simultaneously increases both qa and $\sqrt{na^3}$, thus making it difficult to identify which of the two dimensionless parameters is (primarily) responsible for any deviation¹³.

In Fig. 6.9 we plot the deviation of the dimensionless frequency shift from FT theory $\alpha - \alpha_{\text{FT}}$ versus qa , where the different symbols (see legend) correspond to different $\sqrt{na^3}$. For our values of $qa \gtrsim 3$ we see a clear deviation from the FT prediction, which overestimates the (negative) shift. As we always observe comparable shifts at the same qa and varying $\sqrt{na^3}$, we conclude that (at least for the parameter range explored here) the breakdown of FT theory occurs for $qa \gtrsim 3$, independent of $\sqrt{na^3}$.

The deviation from FT theory that we observe for $qa \gtrsim 3$ can be explained by turning to a recent calculation based on the Wilson operator product expansion (OPE) [294] (see also [262]),

¹³While increasing a at fixed q and n also reduces $q\xi$ (which could lead to the breakdown of our assumption of particle-like excitations), we still have $q\xi \approx 11$ for our largest qa and $\sqrt{na^3}$, which is larger than our lowest $q\xi \approx 5$ from Fig. 6.8, which we found to display universal behavior, and so we rule this out.

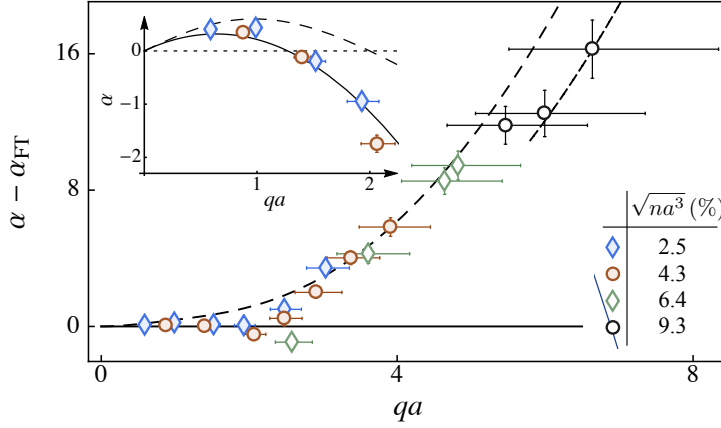


Fig. 6.9 Deviation from the Feynman–Tan prediction. We plot the deviation of the dimensionless frequency shift α from the FT theory versus qa , for four different values of $\sqrt{na^3}$, reaching up to 9.3% (see legend). As described in the text, the dashed line shows the OPE prediction with $C_2 = (4\pi na)^2$ and no adjustable parameters. The dot-dashed line shows the OPE prediction, self-consistently including LHY corrections to C_2 . The inset shows a comparison of the FT (solid) and OPE (dashed) predictions at low qa . Figure from [28].

which predicts a frequency shift

$$\Delta\omega_{\text{OPE}} = \frac{\hbar C_2}{4\pi mna} \left(\frac{2}{1 + (qa/2)^2} - 1 \right), \quad (6.7)$$

which assuming the low- na^3 result $C_2 = (4\pi na)^2$, and after being recast into dimensionless form [see Eq. (6.5)] becomes

$$\alpha_{\text{OPE}} = qa \left(\frac{2}{1 + (qa/2)^2} - 1 \right). \quad (6.8)$$

In Fig. 6.9 the dashed black line depicts $\alpha_{\text{OPE}} - \alpha_{\text{FT}}$, and we find that this prediction captures the data well for $qa \gtrsim 3$. While Eq. (6.8) is also a universal function of qa , the theory allows for the self-consistent inclusion of beyond-mean-field corrections to C_2 . To test this we write the two-body contact density including the Lee-Huang-Yang (LHY) correction [43,44,62]:

$$C_2 = (4\pi na)^2 \left(1 + \frac{64}{3\sqrt{\pi}} \sqrt{na^3} + \dots \right), \quad (6.9)$$

and calculate the LHY-corrected $\tilde{\alpha}_{\text{OPE}}$ for our largest $\sqrt{na^3} = 0.093$ ($\tilde{\alpha}_{\text{OPE}}$ now depends on both qa and $\sqrt{na^3}$). The dot-dashed line in Fig. 6.9 shows this prediction, upon subtracting the universal α_{FT} . Interestingly, this does appear to provide slightly better agreement with the data, but this observation is not statistically conclusive (see also [64]). It should be noted however that the LHY correction changes C_2 by about a factor of 2, and so at this stage beyond-LHY corrections, which also depend on the van der Waals length, could be significant [305,306].

In the inset of Fig. 6.9 we highlight that while we find success for the OPE prediction at large

qa , it is experimentally excluded for $qa \lesssim 3$, where it predicts a zero crossing of the frequency shift at $qa = 2$ instead of $qa = 4/\pi$. As observed experimentally, and also as theoretically described in [294], the two theories are complementary. In fact, while both FT and OPE theories address the short-distance behavior of the density response function, the main difference between the two lies in the type of excitation: FT theory assumes a single particle excitation, while OPE assumes high-momentum pair excitations. Theoretically, while OPE theory is predicted to be exact at $q \rightarrow \infty$, for any finite q instead there exists a regime at small values of $|S_q - 1|$ at which FT theory still holds.

Finally, it is curious to note that if α_{OPE} were valid below $qa = 1.57 > \pi/4$, then the magnitude of the frequency shift would be larger than the FT prediction, which formally gives an upper bound to the frequency shift due to the sum rules on which it is based [17].

6.3.4 Conclusion

In conclusion, we have studied the quasiparticle excitations in a moderately strongly interacting homogeneous BEC. Our experiments push far beyond the regime of validity of Bogoliubov theory. For a range of interaction strengths $qa \lesssim 3$ (and small $\sqrt{na^3}$) our experiments are quantitatively captured in the framework of the Feynman energy relation, taking into account short-range two-particle correlations, in the spirit first introduced by Tan [47]. As predicted by this theory, we observe that the shift of the excitation resonance from the free-particle energy changes sign from positive to negative, and confirm that this sign change occurs at $qa \approx 4/\pi$.

For $qa \gtrsim 3$ we find that this theory also breaks down, suggesting the need for more sophisticated theoretical approaches. In particular, a recent such approach, based on the Wilson operator product expansion, shows good agreement with our data for $qa \gtrsim 3$, however fails to capture the low- qa behavior. Unifying the different theoretical descriptions of quasiparticle resonances in all interaction regimes remains an open theoretical challenge.

Our experiments focus on the regime of particle-like excitations ($q\xi \gg 1$), however in the future it would be interesting to map out the full dispersion relation by experimentally probing lower values of $q\xi$. This can be achieved by reducing the angle between the Bragg beams θ , or through parametric excitation via the modulation of the scattering length [308] or density [309]. This should allow the experimental observation of the expected inflection point in the dispersion relation at large a , a precursor to the roton excitation.

In the opposite limit, we already exhaust the maximal $q = 2k_{\text{rec}}$ achieved with a maximum angle of $\theta = \pi$. However, it would be interesting to perform high-precision Bragg spectroscopy using a higher-order Bragg process: a four-photon process could effectively give access to twice

the maximum q , thus significantly extending our accessible range of qa .

Finally, a high precision study of the shape of the Bragg spectra (to first order characterized by their width) would provide additional valuable information [294], and is anticipated as a fruitful study for the future. Indeed, here box-traps are particularly suitable as they avoid additional broadening due to the inhomogeneous density present in harmonic traps and allow for Heisenberg-limited spectrum widths [87].

6.4 Conclusion

In conclusion, in our first studies of ‘moderately’ strongly-interacting gases we explored regimes where simple mean-field theories break down and one can observe beyond-mean-field quantum correlation effects, but the experiments also remain tractable within the existing theories. In Section 6.2 we presented the first quantitative measurement of the quantum depletion of a Bose–Einstein condensate, confirming Bogoliubov’s 70-year-old theory that describes the microscopic origin of how atoms are expelled from the condensate due to interactions. In Section 6.3 we mapped out the energy of particle-like excitations using two-photon Bragg spectroscopy, observing dramatic deviations from Bogoliubov theory and confronting modern theories of interacting quantum fluids.

We already provided detailed summaries and outlined future goals within each section, and so here we will constrain ourselves to a few general remarks. In the current state of affairs, we have more or less reached an impasse in terms of the maximal na^3 that we can explore while adhering to our stringent loss, heating, and adiabaticity requirements. In Chapter 7 we will venture down the same path as taken in the pioneering experiment [270], where the solution is to forsake any hope of preparing an equilibrium state adiabatically, and instead turn to quench experiments, allowing access to the unitary regime ($na^3 \gg 1$) though also finding oneself far from equilibrium.

7 Boses Gases Quenched to Unitarity

When you come to a fork in the road, take it.

- Yogi Berra -

7.1 Introduction

Strongly-correlated states of matter, from novel superconductors to the quark-gluon plasma, exhibit some of the most fascinating phenomena in nature. Understanding such systems, and especially their dynamics far from equilibrium, poses a fundamental challenge in modern physics.

Ultracold atomic gases act as remarkable quantum simulators for these problems, due to their tuneable interparticle interactions and experimentally resolvable intrinsic timescales. In particular, the ability to exploit magnetic Feshbach resonances [7] and tune $a \rightarrow \infty$ offers access to the unitary regime, where the interactions between particles are as strong as theoretically possible. In this strongly-correlated regime the microscopic details of a particular system are thought to become less important, so that connections between seemingly disparate quantum many-body systems can be drawn. In particular, in unitary ultracold atomic gases the underlying physical processes inevitably no longer depend on the diverging a , and instead are thought to display new types of universal behavior [11, 12, 16, 18, 310, 311].

Studies of the unitary Fermi gas (see *e.g.* [11, 12, 16] and references therein), which most famously allowed the exploration of the crossover between Bose–Einstein condensation and Bardeen–Cooper–Schrieffer superconductivity [5, 312–316], have been among the highlights of ultracold-atom research for the past 15 years.

The unitary Bose gas holds as many and as tantalizing promises as its Fermi counterpart, including novel forms of superfluidity [317–319] and emergent universal behavior set solely by the gas density [310, 311]. However, in Bose gases the strong interactions also lead to dramatically enhanced particle loss and associated heating; this establishes a complex inter-

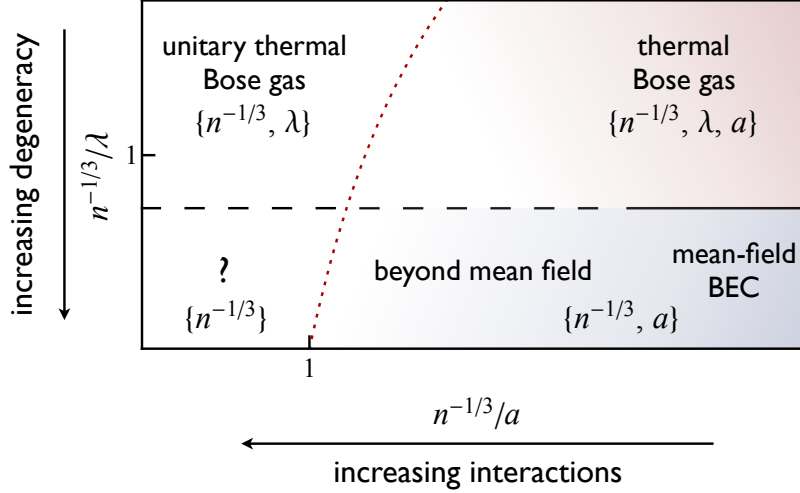


Fig. 7.1 Sketch of the equilibrium phase diagram for strongly-interacting Bose gases. We are not able to adiabatically prepare unitary gases to directly explore bottom left corner of this phase diagram. Instead, we perform quench experiments to enter the unitary regime, starting with equilibrium degenerate (blue region) or thermal (red region) Bose gases at large $n^{-1/3}/a$.

play between the coherent and the dissipative dynamics, and makes the study of the unitary Bose gas an inherently dynamical, non-equilibrium problem. Experimental studies of unitary Bose gases are only recently emerging [46, 65, 90, 270, 271, 320–322], with steady theoretical progress [18, 319, 323–354], establishing an exciting research frontier.

While our principal aim is uncovering the nature of the unitary Bose gas, this strongly-interacting far-from-equilibrium scenario also fits into recently emerging theoretical paradigm concerning general properties of equilibration and thermalization in quantum many-body systems far from equilibrium (see *e.g.* [176, 355–358]). These theories, aimed at unravelling the organizing principles of non-equilibrium quantum systems, have predicted elegant universal scaling behavior, akin to the quasi-equilibrium behavior near phase transitions between different states of matter.

As a starting point for our discussion, it is insightful to consider a cartoon sketch of the equilibrium phase diagram of strongly interacting Bose gases (Fig. 7.1) within the universality hypothesis. A weakly interacting thermal Bose has three relevant lengthscales: the interparticle spacing $n^{-1/3}$, the thermal wavelength $\lambda \propto 1/\sqrt{T}$ and the s -wave scattering length a . At low temperatures, when our gas forms a quasi-pure Bose–Einstein condensate, λ drops out of the problem we are left with just $n^{-1/3}$ and a . Here the gas is described well by mean-field theory assuming a single macroscopic wave function, as long as the interactions are relatively weak. As one starts tuning to stronger interactions, one begins to explore beyond-mean-field effects, such as those discussed in Chapter 6; for a sense of scale there we reached $n^{-1/3}/a \approx 70$ with $n^{-1/3}/\lambda \lesssim 0.4$.

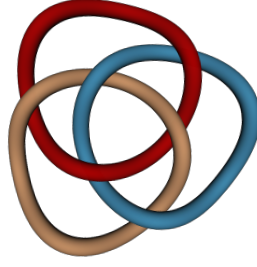


Fig. 7.2 Borromean rings act as a symbolic representation of three-body Efimov states. In this picture the three rings are bound together, but if one of them is removed the other two separate as well. The quantum mechanical analogue occurs when three bosons interact, in a situation where two-body interactions do not support a two-body bound state (as is the case at unitarity). In this case Efimov predicted a spectrum of bound three-body states [34].

In thermal unitary gases the diverging a is capped by λ . While one still has two lengthscales, in many cases their dynamics are coupled, and one can still predict universal behavior; for example, one expects essentially universal behavior of the loss dynamics, as experimentally confirmed using harmonically trapped gases [320–322].

In interaction-dominated degenerate gases, we are left with only a single lengthscales, the interparticle spacing $n^{-1/3}$, which sets the natural momentum, energy, and time scales:

$$\hbar k_n = \hbar (6\pi^2 n)^{1/3}, \quad E_n = \frac{\hbar^2 k_n^2}{2m}, \quad \text{and} \quad t_n = \frac{\hbar}{E_n}. \quad (7.1)$$

While these ‘Fermi’ scales are relevant to both Fermi and Bose gases, in Bose gases the implied universal behavior can be broken by Efimov physics [33–35, 64–66, 271, 348, 359–365]; the Efimov effect [34], a quantum few-body effect first discussed in nuclear physics in 1970, is a quantum-mechanical analogue of the Borromean rings (see Fig. 7.2), where even though there is no two-body bound state, novel three-body bound states, known as Efimov states, still exist. The Feshbach dimer molecular state, which is responsible for the resonance, is of size a with a binding energy $E_b \approx \hbar^2/(ma^2)$, and so becomes unbound as $a \rightarrow \infty$. The infinite series of excited Efimov trimer states, each of a size 22.7 times larger than the previous one, can introduce new lengthscales into the problem, and are thought to profoundly affect the many-body behavior (see *e.g.* [319, 341, 346, 366]).

First experimental forays into the unitary regime date back to [46], where the authors obtained a lower bound for the equation of state $\mu = 0.44(8)E_n$, in line with theoretical estimates [310, 323–325, 327, 332, 334, 343, 367, 368] that predict a ground state energy ranging from 0.39 to 1.75 E_n (though note that some are variational upper bounds). Indeed, it is natural to expect the ground state to have an energy $\sim E_n$.

In the pioneering experiment [270], the authors embraced the non-equilibrium nature of the

problem, and performed quench experiments to reach the unitary regime, entirely forsaking equilibrium. The gas was allowed to then evolve at unitarity for a variable time, before quenching back to low a to observe the samples. Rather remarkably, this revealed that the absolute post-quench occupation of high-momentum components reached a steady-state, while the total atom number decayed continuously. This provided first experimental evidence that the lossless processes are somewhat faster than the recombination induced ones, and raised fundamental questions about the extent to which the gas has well-defined equilibrium properties. Overall, these degenerate-gas dynamics displayed universal behavior, consistent with t_n as the only characteristic timescale [270,271].

However, many-body interferometry of a thermal unitary Bose gas has revealed novel three-body correlations [65], and Efimov trimers have been observed following a ramp out of the unitary regime [271].

In this chapter we study the dynamics of homogeneous Bose gases quenched to unitarity, focusing on initially degenerate gases in Section 7.2 and thermal gases in Section 7.3; note that core parts of our discussion closely follow [30,31].

Before turning to our experiments we first highlight the advantages of performing unitary-gas experiments using *homogeneous* Bose gases (Section 7.1.1), detail the pertinent atom-loss scaling law predictions (Section 7.1.2), and outline our quench protocol used to probe the unitary regime (Section 7.1.3).

7.1.1 Advantages of an optical box potential

All previous unitary Bose gas experiments were performed with harmonically trapped gases, and their interpretation relies on knowledge of the inhomogeneous density profiles. For degenerate gases, the density profile is known prior to the quench to unitarity, and therefore also just after it, but the subsequent evolution is complicated by strong interactions and inhomogeneous losses.

Here we prepare our gases in the quasi-uniform potential provided by a cylindrical optical box trap [21], and so they are essentially homogeneous (see Section 3.1.2). Crucially, the density in our gas is always closely related to the total atom number, which sets quantities such as E_n and t_n , which are *global* variables¹. We can therefore assume that (to a good approximation) the volume remains constant throughout an experiment, which allows us to quantitatively study the full evolution of a cloud as it decays and heats.

For the experiments in this chapter we always use the same optics (spatial light modulator

¹In experiments the density is never perfectly uniform due to edge effects, but for our box trap we assess that for more than 80% of the atoms the local E_n is within 10% of the trap average value.

parameters) to create the quasi-uniform trapping potential, which has an aspect ratio is $2R/L \approx 0.63$ and a volume $V \approx 3 \times 10^{-14} \text{ m}^3$. While it is reasonable to assume the same constant V for all our data, varying the laser power (to vary the trap depth U_0) and the typical energy scale of the gas ($k_B T$ for thermal gases and $\mu \propto Na$ for condensates) does lead to variations in the effective initial sample volumes for different experiments, which we can readily account for. In order to assess these initial volume differences we first measure a nominal volume², and then correct the volumes of other samples assuming a power-law potential of the form $\sim r^{15(4)}$ [22] (see also Section 2.3).

Another valuable benefit of using a homogeneous trap is that it eliminates ‘anti-evaporative’ heating present in harmonic traps, where atoms at the trap center with below-average energy are preferentially lost [301,302,369]. However, to avoid heating from the loss processes one still has to ensure that the loss products leave the box without undergoing secondary collisions³.

7.1.2 Atom-loss scaling-law predictions

Here we present theoretical predictions of the atom-loss scaling laws across the different interaction and temperature regimes (see Fig. 7.1). In our experiments three-body recombination is the leading order loss process, as one-body loss⁴ is usually negligible (with a lifetime $> 10^2 \text{ s}$) and two-body inelastic collisions are absent as our gas is prepared in the lowest hyperfine state. The per-particle three-body loss rate generally takes the form

$$\dot{N}/N = -g_3 L_3 \langle n^2 \rangle, \quad (7.2)$$

where g_3 is the zero-distance three-body correlation function, L_3 is the three-body loss coefficient, and $\langle \dots \rangle$ denotes a trap average. For a thermal gas boson bunching gives $g_3 = 3!$, which is suppressed in a weakly-interacting zero-temperature Bose–Einstein condensate [370–373]. While for $na^3 \rightarrow 0$ we have $g_3 = 1$, the beyond-mean-field LHY correction to g_3 (which arises from the depletion of the condensate) is

$$g_3 \approx 1 + \frac{64}{\sqrt{\pi}} \sqrt{na^3}. \quad (7.3)$$

²Our in-situ analysis used to extract V is described in detail in [22]. In short, we perform partial re-pump absorption imaging to measure the in-situ cloud shape. To extract the effective trap dimensions we convolve the expected line density distributions with a gaussian point spread function to account for both finite imaging resolution and edge effects. For our thermal gases we measure $V \approx 2.7 \times 10^{-14} \text{ m}^3$ for a cloud at $T \approx 140 \text{ nK}$ in a trap of depth $U_0/k_B \approx 3 \text{ } \mu\text{K}$. For our degenerate gases we measure $V \approx 3.7 \times 10^{-14} \text{ m}^3$ for $N \approx 1.2 \times 10^5$ at $a \approx 400 a_0$ in a trap of depth $U_0/k_B \approx 50 \text{ nK}$.

³To fulfill this requirement one requires a mean-free path $1/(8\pi na^2)$ large compared to the box dimensions (to avoid secondary collisions) and a trap depth $U_0 \ll E_b$ [assuming that three-body recombination results in the formation of an atom and a weakly bound dimer, which (respectively) gain $2/3$ and $1/3$ of E_b .]

⁴Some one-body loss is always present due to *e.g.* collisions with the background gas in the vacuum chamber.

Interestingly, this correction has a rather large prefactor ($64/\sqrt{\pi} \approx 36$) and so for $na^3 = 10^{-5}$ we already expect a $\approx 10\%$ increase of g_3 ⁵.

For a *homogeneous* gas, the density is constant across the trap and the size (set by the trap volume V) is independent of time (*i.e.* while losses occur and N decreases), which dramatically simplifies matters. In particular, we simply have $\langle n^2 \rangle = n^2 = N^2/V^2$. Equation (7.2) then generally takes the power-law form

$$\dot{N}/N = -c_0 N^\gamma, \quad (7.4)$$

where c_0 is a constant. Integration explicitly yields the atom-loss dynamics

$$N(t) = \left[c_0 \gamma t + N_0^{-\gamma} \right]^{-1/\gamma}, \quad (7.5)$$

where N_0 is the initial ($t = 0$) atom number and at long times we expect power-law behavior

$$N(t \rightarrow \infty) = (c_0 \gamma t)^{-1/\gamma}. \quad (7.6)$$

In the following we consider the different temperature and interaction regimes to deduce the explicit form of Eq. (7.4) expected in each regime (*i.e.* finding γ).

Weakly interacting regime

In degenerate gases away from unitarity⁶, on average (ignoring the additional log-periodic variation with a that arises from Efimov physics [33,35,360]) we have $L_3 \propto \hbar a^4/m$ [302,374], so that $\gamma = 2$. More generally, for a loss process involving i particles, one expects (on dimensional grounds, neglecting Efimov physics)

$$\dot{N}/N \propto \hbar/m a^{3i-5} n^{i-1}, \quad (7.7)$$

where $\gamma = i - 1$ is an integer [375,376].

In the following we will consider how these atom-loss scaling laws are modified in the unitary regime, when $a \rightarrow \infty$.

⁵The large prefactor makes studies of g_3 a promising candidate for exploring beyond-LHY corrections. In particular, for realistic experimental parameters $a = 3000 a_0$ and $n = 5 \mu\text{m}^{-3}$ the prediction from Eq. (7.3) exceeds 6 (the thermal gas g_3), which is impossible, and one would already expect strong deviations when the correction is of order 1.

⁶Here we assume that we are still in the regime where a is large compared to $a_{\text{vdw}} \approx 60 a_0$ (for ³⁹K).

Thermal unitary regime

In the thermal unitary regime the diverging a is capped by the thermal wavelength λ , which is a statistical measure of the inverse relative atomic momenta. We therefore have that (averaging over a thermal distribution) $L_3 \propto \hbar\lambda^4/m$, and generally $\dot{N}/N \propto -\langle n^2 \rangle/T^2$. More quantitatively (up to negligible corrections), the loss coefficient is

$$L_3 = \zeta_3 \frac{3\sqrt{3}\hbar}{2m} \lambda^4 = \zeta_3 \frac{6\sqrt{3}\pi^2 \hbar^5}{m^3 (k_B T)^2}, \quad (7.8)$$

where $\zeta_3 = (1 - e^{-4\eta^*})$ is a non-universal prefactor set by Efimov physics [320–322, 376–378], and we have omitted the theoretically expected weak modulation log-periodic in T ⁷. The Efimov width parameter η^* defines the lifetime of a deeply bound Efimov trimer $\hbar/(\eta^* E_T)$, where E_T is the energy of the trimer state. The physical origin of ζ_3 is that a fraction $e^{-4\eta^*}$ of three-body collisions do not result in atom loss but instead form a transient trimer that decays back into free atoms which are not lost from the trap. This form of L_3 for thermal unitary Bose gases was verified experimentally using thermal unitary Bose gases prepared in harmonic traps [320–322].

In our homogeneous gases the fractional loss rate simplifies to

$$\frac{\dot{N}}{N} = -\zeta_3 \frac{36\sqrt{3}\pi^2 \hbar^5}{m^3 k_B^2 V^2} \frac{N^2}{T^2}. \quad (7.9)$$

In contrast to the weakly-interacting case, a thermal unitary gas intrinsically heats while undergoing three-body loss because of the unitarity limited scattering cross-section $\sigma = 8\pi/(k^2 + a^{-2}) \approx 8\pi/k^2$, which leads to atoms with lower relative momenta having a higher unitarity limited loss rate and being preferentially lost [320, 322, 379]. While we now have two lengthscales, $n^{-1/3}$ and λ , their dynamics are coupled and we can consider the heating caused by loss and hence reduce Eq. (7.9) into the form of Eq. (7.4) to obtain the relevant γ . Following [322, 379], we write out the total energy before (l.h.s.) and after (r.h.s.) a loss event

$$\alpha N k_B T = \alpha(N + dN)(T + dT) - (\alpha - \delta_3) T dN, \quad (7.10)$$

separating the terms corresponding to atoms that remain in the trap (first r.h.s. term) and those that are lost (second r.h.s. term). Here $\alpha = E/(k_B T) = 3/2$ is the thermodynamic parameter (assuming $n\lambda^3 \ll 1$) and $\delta_3 = 2/3$ corresponds to the excess energy per parti-

⁷While theoretically expected, such a log-periodic modulation in T has not been resolved experimentally. Both the rather weak relative oscillation amplitude $\approx 0.022e^{-2\eta^*}$ (a few % for typical η^*) and extremely slow variation with T [a period corresponds to a factor of $e^{4\pi/s_0} \approx 3 \times 10^5$ ($s_0 = 1.00624$ for identical bosons)] make this a particularly challenging pursuit for identical bosons [322, 379].

cle from the three-body loss event, associated with the k -dependence of the recombination events [320,322,379]⁸. Simplifying and rearranging Eq. (7.10) yields

$$\frac{dT}{T} = -\frac{\delta_3}{\alpha} \frac{dN}{N} = -\frac{4}{9} \frac{dN}{N} = \frac{dE}{E}, \quad (7.11)$$

which upon integration gives $T \propto N^{-4/9}$. Putting the ingredients together, we predict the loss rate scaling law $\gamma = 2 + 2 \times 4/9 = 26/9$. We also obtain the energy dynamics by simply replacing $N(E)$ in Eq. (7.9), which retains the power-law form and reads $\dot{E}/E \propto E^{-13/2}$, resulting in the same general form as Eq. (7.5) after integration. We thus find the expected long-time power-law behavior $E(t \rightarrow \infty) \propto t^{2/13}$.

Degenerate unitary regime

In the degenerate unitary regime, within the universality hypothesis [311], there is only one lengthscale so we expect that a is limited at unitarity by $n^{-1/3} = (V/N)^{1/3}$, which directly predicts the scaling law $\gamma = 2/3$. Equivalently, one can simply argue that since t_n is the only timescale in the problem we require

$$\dot{N}/N = -A/t_n, \quad (7.12)$$

where A is a constant. Such a scaling was recently observed in the initial loss rate of a harmonically trapped ⁸⁵Rb gas quenched to unitarity [271] over two orders of magnitude in average initial density $\langle n_0 \rangle$, with $A \approx 0.18$. We however do expect that A depends on non-universal Efimov physics through ζ_3 (as in the thermal unitary regime), and an additional log-periodic modulation as function of n is also expected [366,380]⁹.

While our derivation of Eq. (7.12) was based on a 3-body loss process, we note that in a degenerate gas higher-order loss processes cannot be ruled out. However, by considering any i -body loss event [see Eq. (7.7)] one actually recovers the same scaling law (as $na^3 \sim 1$), and so all loss processes scale in the same way (set by $\sim t_n$). This recapitulates our key message in that this is a *many-body* loss rate, set by the only timescale in the problem $\sim t_n$.

This universality reveals a more serious issue, as it raises the question whether such a gas can ever exist in equilibrium. Indeed, if one considers the ‘quality factor’ of the system, that is

⁸Here we assume that the trap depth $U_0 \gg k_B T$, so that evaporation is negligible. In [320,322] the authors tuned $U_0 \gtrsim k_B T$ in order to use evaporative cooling to compensate the loss-induced heating and achieve an essentially constant T .

⁹The expected oscillation period corresponds to a change of density by a factor of $e^{3\pi/s_0} \approx 10^4$ ($s_0 = 1.00624$ for identical bosons). The expected relative amplitude for ⁸⁵Rb is $\sim 20\%$ [366], and the data from [271,380], spanning about half of the expected log-period, do show a suppression at the predicted minimum position. However, the results are inconclusive owing to systematic uncertainties in the calibration of $\langle n_0 \rangle$ [380].

the product of the energy of the many-body state ($\sim E_n$) and its lifetime ($\sim t_n$) then we are left with just a number, which is a priori unknown and not necessarily larger than 1 (required for a well-defined state to exist).

We can make some quantitative progress by taking a step back and asking whether a thermal unitary Bose gas can remain in equilibrium under three-body loss [321]. We need to compare the per-particle loss rate [Eq. (7.9)] to the two-body elastic collision rate $n\sigma v$, where on average $\sigma = 8\pi\lambda^2$ and v is the relative velocity between two thermal atoms $4\sqrt{k_B T/(\pi m)}$. The ratio of the two rates is then

$$\frac{16\sqrt{2}}{9\zeta_3\sqrt{3}} \frac{1}{n\lambda^3}, \quad (7.13)$$

which is a function of η^* and phase space density $n\lambda^3$. Using $\eta^* \approx 0.09$ measured for our ^{39}K state [321] this reduces to $\approx 5/(n\lambda^3)$, which shows us that we do not expect to be able to adiabatically prepare an equilibrium unitary state for deeply degenerate gases. Our experiments confirm this in a sobering manner. If we use our normal field ramps to tune $a \rightarrow \infty$ on ~ 10 ms timescales then initially pure BECs become thermal, losing a large fraction of atoms during the ramp, with the degenerate unitary regime eluding us.

To overcome this problem, we forsake our dreams of adiabatically preparing a degenerate unitary Bose gas, and instead turn to quench experiments, where we rapidly tune $a \rightarrow \infty$ to observe the ensuing dynamics.

7.1.3 Quench protocol

Here we outline our experimental protocol used to quench both initially degenerate and thermal Bose gases into the unitary regime. We prepare homogeneous Bose gases in the quasi-uniform potential of a cylindrical optical box trap with volume $V \approx 3 \times 10^{-14} \text{ m}^3$ and aspect ratio $2R/L \approx 0.63$ (see Section 7.1.1).

We begin our experiments in the weakly interacting regime, with initial gas parameters $n_0 a_i^3 < 10^{-3}$. In Fig. 7.4 we introduce our quench protocol, which we illustrate for an initially degenerate gas, while highlighting differences to our thermal gas experiments which enjoy several simplifications. In our degenerate gas experiments we use initial atom numbers N_0 in the range $(1-22) \times 10^4$, with corresponding initial densities n_0 in the range $(0.4-5.2) \mu\text{m}^{-3}$, so that t_{n_0} varies between $(150-27) \mu\text{s}$. However, most of our experiments are performed with four initial $N_0 = \{48, 98, 143, 214\} \times 10^3$, with s.e.m. $< 1\%$ ¹⁰. In order to reach interaction param-

¹⁰While our statistical uncertainty in N is small (which allows us to detect relative differences in N to high precision) do note that there is an overall systematic uncertainty in N of $\approx 10\%$.

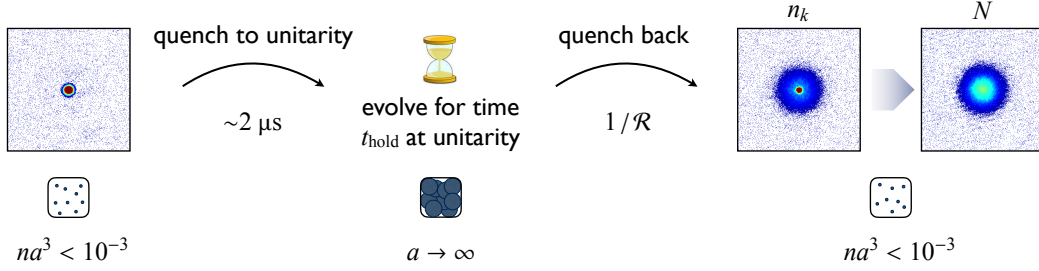


Fig. 7.3 Quench Protocol. A quasi-pure BEC is rapidly quenched to unitarity, the gas evolves under unitary interactions for a time t_{hold} , before ramping back to low a at a variable ramp-out rate $\mathcal{R} = -dB/dt$. Immediately allowing the atoms to expand in ToF at $a_{\text{ToF}} \sim 0$ gives us access to post-quench momentum distribution n_k . Instead, by holding the cloud at low a in an essentially closed environment for 40 ms and subsequently performing ToF at $a_{\text{ToF}} \approx 10^3 a_0$ we are able to spread out the optically dense low- k atoms sufficiently to faithfully measure the atom number N (see text). The circles in the cartoons depict atoms, and their sizes the interaction strength, limited at unitarity by the interparticle spacing.

eters $n_0|a|^3 > 1$ (entering the unitary degenerate regime) for our full range of n_0 , we need to tune B to within $\delta B \sim 60$ mG of the Feshbach resonance at $B_\infty = 402.70(3)$ G (see Section D for details of our field calibration at unitarity). The requirement for reaching the thermal unitary regime ($a/\lambda > 1$) is somewhat relaxed, since as $\lambda < n_0^{-1/3}$ we automatically satisfy $a/\lambda > 1$ if $n_0|a|^3 > 1$.

To enter the unitary regime, we rapidly (within $2 \mu\text{s} \ll t_{n_0}$) quench the magnetic field to B_∞ using fast auxiliary coils strategically placed to avoid coupling to the Feshbach coils. We are able to perform field quenches of up to $\Delta B \approx 3.6$ G $\approx 60 \delta B$, corresponding to a minimum $a_i = 390 a_0$.

Our quasi-pure condensates are prepared in a $U_0/k_B \approx 50$ nK deep trap, however to avoid the loss of atoms due to spilling or evaporation in the unitary regime (as $E_{n_0} \gg U_0$) we raise the trap depth to $U_h/k_B \approx 2 \mu\text{K} \gg E_{n_0}$ at unitarity¹¹. We hold the gas at unitarity as it evolves for a variable time t_{hold} , before returning to low a in order to observe the samples; we use 6 – 32 ms time-of-flight (ToF) expansion and our imaging protocol detects only free atoms.

The functional form of our B field ramp out of the unitary regime is exponential (see Section D), and since we always ramp B to more than $10 \delta B$ away from B_∞ the ramp is essentially linear in and near the unitary regime, where its form is most relevant [381]. We therefore characterize different ramps by their initial ramp-out rate $\mathcal{R} = -dB/dt = \Delta B/\tau_Q$, where ΔB is the change in field from B_∞ ¹² and τ_Q is the ramp's exponential time constant, which we can vary between (1 – 10) μs .

Conceptually, an infinitely fast ramp-out should project the resonantly interacting cloud onto free atom states. This avoids the formation of an atom-molecule mixture [271] and allows a

¹¹This occurs rapidly ($\lesssim 10 \mu\text{s}$) alongside the quench of B . We have studied the consequences of such a trap-depth quench at low a (without quenching $a \rightarrow \infty$), and find that the dynamics it induces occur on $> 100 \mu\text{s}$ timescales, leading to an increase in E which at all times is $< 10\%$ of that due to a quench to unitarity.

¹²The initial and final distance from B_∞ are the same as our current electronics do not offer separate control.

study of the gas's post-quench properties, including the atom number N , energy per particle E , and momentum distribution n_k . Instead, ramping away from unitarity slowly and creating an atom-molecule mixture allows us to study the dynamics of correlations in the unitary Bose gas¹³.

If following the quench protocol we immediately release the cloud in ToF¹⁴, then our absorption images give the post-quench line-of-sight integrated momentum distribution (convolved with the initial size). This allows us to obtain rich momentum- and time-resolved information, which is at the heart of Section 7.2.2. However, alone, these measurements have a shortcoming in that the low- k region of the cloud, which at short t_{hold} contains the majority of the atoms, is optically dense and so does not permit an accurate measure of N (see Fig. 7.3).

Our solution to this is that following the quench back to low a we introduce a 40 ms wait time at $\approx 200 a_0$, which allows the gas to rethermalize, spreading the BEC to larger momenta while maintaining an essentially closed system¹⁵. Note that for these measurements we also increase the scattering length for ToF (to $a_{\text{ToF}} \approx 10^3 a_0$) to aid the expansion¹⁶.

Our thermal gas measurements are simpler in several regards. Here we keep the trap depth fixed throughout, and prepare all gases in the same deep trap with $U_0 = U_h \approx k_B \times 3 \mu\text{K}$. There is also no dramatic separation of momentum scales following the quench, so the immediate-release n_k measurements also faithfully reveal N and the energy per particle E .

7.2 Degenerate Bose gases quenched to unitarity

Here we present an overview of the typical atom-loss, correlation, and energy dynamics that we observe using our quench protocol.

We begin by investigating the role of the sweep out of the unitary regime (see Fig. 7.4). Our goal here is to disentangle the two reasons that the observed atom number N_{obs} can decrease with t_{hold} : (i) due to losses that occur at unitarity, and (ii) because the ramp-out creates a mixture of atoms and (Feshbach and/or Efimov) molecules [271], while we only observe the free atoms. The molecular fraction of the gas following the ramp-out is governed by both the correlations that have developed at unitarity, and the ramp-out rate $\mathcal{R} = -dB/dt$ [271, 353, 366, 381–383]. In the limit of an infinitely fast ramp-out we expect that we are no longer sensitive to the many-body state at unitarity and that we essentially project the

¹³As we will see in Section 7.2, these measurements also show that our technically limited fastest ramp-out rate $1/\mathcal{R} = 0.3 \mu\text{s}/\text{G}$ underestimates the actual atom number by $\lesssim 10\%$.

¹⁴Upon releasing the gas we simultaneously (within about 3 ms) also turn off the interactions ($a \rightarrow 0$).

¹⁵If we vary U_h by $\pm 20\%$ and repeat our experiments at various t_{hold} (up to 2 ms) we obtain the same N_{obs} within error bars, and in cases where the BEC is small (or absent) both measurements give consistent N_{obs} .

¹⁶We checked that this does not cause (detectable) atom loss using quasi-pure BECs prepared at low a .

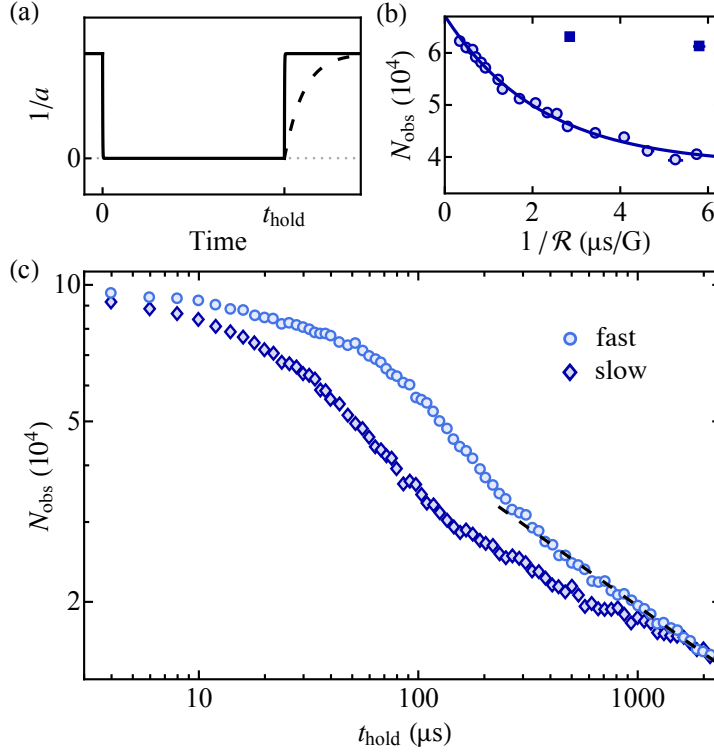


Fig. 7.4 Atom-loss and correlation dynamics of a degenerate Bose gas quenched to unitarity. (a) Quench protocol. A quasi-pure BEC is quenched to unitarity, held there for a variable time t_{hold} , and finally ramped back to the weakly-interacting regime at a variable ramp-out rate $\mathcal{R} = -dB/dt$. An infinitely fast ramp ($1/\mathcal{R} \rightarrow 0$) would project the resonantly interacting cloud onto free-atom states, while a finite-rate ramp-out creates a mixture of atoms and molecules. (b) The open circles show the observed atom number N_{obs} as a function of inverse ramp-out rate $1/\mathcal{R}$, for $N_0 = 98 \times 10^3$ and $t_{\text{hold}} = 80 \mu\text{s}$. An exponential fit to the data (solid line) gives an exponential constant $2.2(3) \mu\text{s}/\text{G}$. The solid squares show N_{obs} if we perform a second magnetic-field pulse to dissociate the molecules. (c) The evolution of N_{obs} as a function of t_{hold} on a log-log plot for our fastest ramp-out ($0.3 \mu\text{s}/\text{G}$, circles) and a much slower one ($5.8 \mu\text{s}/\text{G}$, diamonds). The fast ramp-out reveals the on-resonance atom loss, while the difference between the two curves unveils the correlation dynamics in the unitary gas. At long times we observe power-law behavior $N_{\text{obs}} \propto t_{\text{hold}}^{-9/26}$ (dashed line), corresponding to the loss expected for a *thermal* unitary Bose gas (see Section 7.1.2). The statistical error bars are smaller than the point sizes. Figure adapted from [30].

resonantly interacting cloud onto free-atom states, such that $N_{\text{obs}} = N$.

We study the dependence of N_{obs} on $1/\mathcal{R}$ for $N_0 = 98 \times 10^3$ and a fixed $t_{\text{hold}} = 80 \mu\text{s}$ [open circles in Fig. 7.4(b)], where we have varied $1/\mathcal{R}$ by varying both τ_Q between $(1-10) \mu\text{s}$ and ΔB between $(3.6-1.8) \text{G}$. We find that the data are well captured by an exponential fit, characteristic of a Landau-Zener process [382, 383]. We extract an exponential constant $2.2(3) \mu\text{s}/\text{G}$, and by extrapolating $1/\mathcal{R} \rightarrow 0$ we assess that our technically-limited fastest ramp-out $1/\mathcal{R} = 0.3 \mu\text{s}/\text{G}$ measures the true N to within $\lesssim 10\%$; we corroborate this with additional measurements for our full range of N_0 at several t_{hold} (see Section 7.2.3). For the N_0 and t_{hold} considered here we see that our slowest ramp-outs reduce N_{obs} dramatically, by up to 40%. To experimentally verify that this reduction is due to the creation of an atom-molecule mixture, we apply a second brief ($8 \mu\text{s}$) pulse back to B_∞ after the first trip to resonance (with slow ramp-out), in order to break up the molecules, finding that we can make most of the missing atoms reappear [see

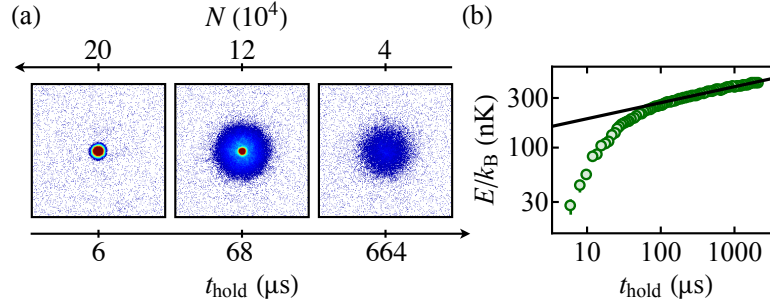


Fig. 7.5 Energy dynamics of a degenerate Bose gas quenched to unitarity. We use a BEC with $N_0 = 214 \times 10^3$ and probe the gas using our fastest ramp-out ($1/\mathcal{R} = 0.3 \mu\text{s}/\text{G}$), where $N_{\text{obs}} \approx N$. (a) Representative absorption images taken along the cylinder axis, after 12 ms ToF expansion at weak interactions for different on-resonance hold times t_{hold} . (b) Extracted kinetic energy per particle E as a function of t_{hold} . For comparison, the interaction energy per particle after the ramp-out is $< k_B \times 20$ nK. The solid line shows a power-law with exponent $2/13$, as predicted for the long-time behavior of a thermal unitary Bose gas, where $E \propto T$ (see Section 7.1.2). Figure from [30].

solid squares in Fig. 7.4(b)]¹⁷.

In Fig. 7.4(c) we plot N_{obs} versus t_{hold} on log-log scale for both our fastest ramp-out ($0.3 \mu\text{s}/\text{G}$) and a much slower one ($5.8 \mu\text{s}/\text{G}$). We see that at short t_{hold} the difference between the two curves is small, highlighting that it takes time for the system to develop the correlations that allow us to create an atom-molecule mixture. We also see that the two curves overlap again at long times, indicating that the gas eventually becomes uncorrelated. Indeed, at long times ($t_{\text{hold}} \gtrsim 1$ ms) we observe power-law behavior with $N_{\text{obs}} \propto t_{\text{hold}}^{-3.0(2)}$, which is in agreement with the scaling predicted for a *thermal* unitary Bose gas $N \propto t^{-9/26}$ (see Section 7.1.2), indicating that degeneracy is ultimately lost.

In Fig. 7.5(a) we show typical absorption images at different t_{hold} , which illustrate how initially there is a dramatic population of high- k momentum states with the central low- k region still present, before at much longer times the central low- k population disappears, in line with the fact that as the samples decay and heat, they ultimately become thermal. In Fig. 7.5(b) we show a log-log plot of evolution of the extracted kinetic energy per particle $E(t_{\text{hold}})$ ¹⁸. We see that E monotonically increases with time, and at long times we find excellent agreement with the predicted recombination heating in the thermal unitary regime $E \propto t^{2/13}$, assuming that $E \propto T$ (see Section 7.1.2).

As we have seen above, eventually, the condensate inevitably vanishes, but does the gas attain a strongly-correlated quasi-equilibrium steady state before degeneracy is lost? If so, what is the nature of this state? In the following we will explore the post-quench dynamics

¹⁷Reminiscent of the experiments in [384], we observe an oscillation of N_{obs} as a function of the time spent at low a between the two magnetic field pulses, and we tweak this time to maximize N_{obs} . As in [384], we find that the frequency of the oscillation is set by the binding energy of the Feshbach dimer state at the intermediate low a (to within our uncertainty in a). We found no discernible dependencies of ν on n or t_{hold} (varying n by more than a factor of 3 and exploring up to $\sim 4 t_{n_0}$). We also observe an oscillation of E at the same frequency.

¹⁸In extracting E we empirically suppress noise at very high- k using a gaussian fit.

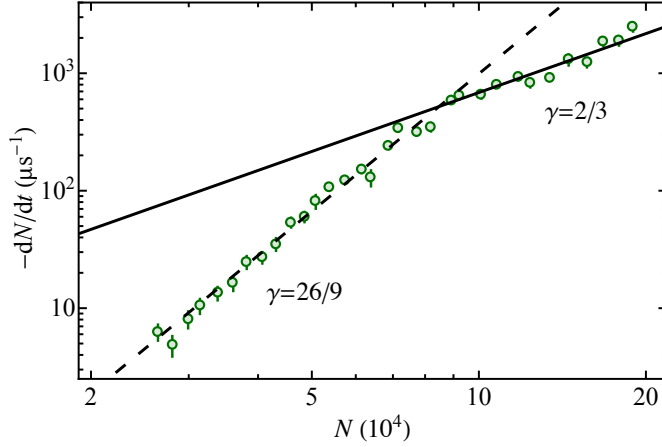


Fig. 7.6 Atom-loss scaling laws. We show the numerically differentiated loss curve $N_{\text{obs}}(t_{\text{hold}})$ for $N_0 = 214 \times 10^3$ (t_{hold} monotonically decreases from right to left, as losses reduce N). We observe both the degenerate ($\gamma = 2/3$, solid line) and thermal ($\gamma = 26/9$, dashed line) scaling laws predicted for the decay of unitary Bose gases in the two temperature regimes. The crossover between the two regimes occurs at a well defined atom number which we denote N_c (where the lines cross). Figure from [30].

in further detail, seeking answers to these questions. To study the atom-loss dynamics (and associated energy and momentum distribution dynamics) [Sections 7.2.1 and 7.2.2] we use our fastest ramp-out and assume that this faithfully measures N (*i.e.* defining $N = N_{\text{obs}}$ for our largest \mathcal{R}). Instead, in order to map out the correlation dynamics [Section 7.2.3] we consider ΔN , defined as the difference between N and N_{obs} measured using a much slower ramp-out [*e.g.* the difference between the two curves in Fig 7.4(c)].

7.2.1 Universal loss dynamics

To determine the instantaneous loss rate we numerically differentiate the atom-loss curves $N(t_{\text{hold}})$ ¹⁹, providing an elegant way to directly test Eq. (7.4). In Fig. 7.6 we show the extracted \dot{N} versus N on log-log scale for $N_0 = 214 \times 10^3$, corresponding to $n_0 = 5.1 \mu\text{m}^{-3}$. For large N (short t_{hold}) we clearly observe degenerate-gas behavior with $\gamma = 2/3$, while for small N (long t_{hold}) we instead observe the thermal-gas scaling $\gamma = 26/9$ (see Section 7.1.2). The crossover between these two regimes occurs at a well-defined N_c and corresponding t_c .

We now extend our analysis to include two additional data series with different initial n_0 ²⁰. In Fig. 7.7(a) we show a log-log plot of the relative loss rate \dot{N}/N versus n for our three different n_0 . We see that for large n/n_0 (short t_{hold}) all curves follow the same $\gamma = 2/3$ degenerate gas scaling law (solid line). As n reduces, each data series individually bends away in similar

¹⁹To numerically compute the derivative, for each experimental repetition of the full $N(t_{\text{hold}})$ curve (of which typically 30 are measured), we select the i^{th} and $(i + \delta i)^{\text{th}}$ point to calculate the instantaneous loss rate and average N for each pair [typically $\delta i = 3$]. Note that we rely on the dense logarithmic spacing of our data in t_{hold} . We repeat this procedure for all i and all our repetitions before logarithmically binning our data in the relevant x -axis (*e.g.* N in this case).

²⁰In contrast to [30], here we do take into account slight variations in the initial volume (see Section 7.1.3).

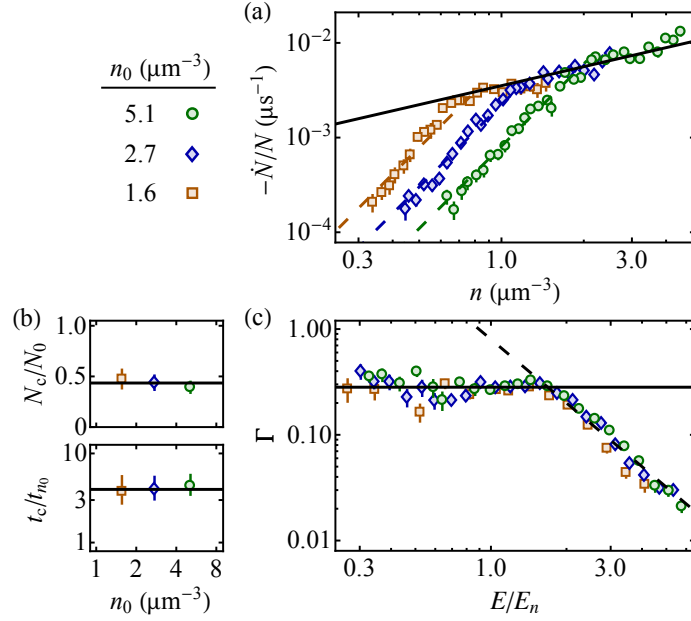


Fig. 7.7 Universal crossover from a degenerate to a thermal unitary gas. (a) Log-log plot of $-\dot{N}/N$ versus n for three different n_0 (see legend). The same $\gamma = 2/3$ law, $\dot{N}/N = -0.28/t_n$ (solid line), captures the degenerate gas data (large n/n_0) for all n_0 . The dashed lines show the expected thermal unitary scaling law $\gamma = 26/9$. (b) For our three n_0 the crossover between the two regimes occurs at almost the same N/N_0 and t_{hold}/t_{n_0} ; averaging we get $N_c = 0.43(4)N_0$ and $t_c = 4.0(3)t_{n_0}$. (c) Log-log plot of the dimensionless per-particle loss rate Γ versus E/E_n , which collapses our data onto a single universal curve. The solid line corresponds to the degenerate unitary gas $\Gamma = 0.28$, and the dashed one shows $\Gamma \propto (E_n/E)^2$, expected for a thermal unitary gas. The crossover between the two regimes occurs at $E_c = 1.7(2)E_n$. Figure adapted from [30].

fashion, separately following the thermal unitary scaling law $\gamma = 26/9$ (dashed lines).

Focusing on the degenerate gas regime, we extract the degenerate gas scaling law coefficient $A = 0.28(3)$ [defining $\dot{N}/N = -A/t_n$, see Section 7.1.2]. We assess that due to the $< 10\%$ difference between N_{obs} and the actual N , we may overestimate A by up to 0.04. It is interesting to compare our results to the ^{85}Rb data [271], from which we extract a slightly lower $A \approx 0.18$. This difference is consistent [328] with the difference in the Efimov width parameters: $\eta^* = 0.09(4)$ for our $|1, 1\rangle$ ^{39}K state [321] and $\eta^* \approx 0.057(2)$ for the $|2, -2\rangle$ ^{85}Rb state [64], though a quantitative comparison will require more precise and accurate measurements of η^* .

We now set out to answer the question: When does the crossover from degenerate gas ($\gamma = 2/3$) to thermal-gas ($\gamma = 26/9$) behavior occur? In Fig. 7.7(b) we map out the atom number N_c and time t_c at which the crossover occurs for the different n_0 . We find that, within errors, the crossover always occurs at the same fraction of N_0 and the same t_{hold} expressed in units of t_{n_0} . Averaging our data gives $N_c = 0.43(4)N_0$ and $t_c = 4.0(3)t_{n_0}$.

To understand why this crossover occurs, we proceed by relating the change in γ to the growth of the dimensionless E/E_n . We define the dimensionless per-particle loss rate

$$\Gamma = -t_n \dot{N}/N, \quad (7.14)$$

so that in the degenerate regime we simply have $\Gamma = A$, and in the thermal regime $\Gamma \propto N^{4/3}/T^2 \propto (E_n/E)^2$ [using $\dot{N}/N \propto -N^2/T^2$ and assuming $E \propto T$, see Section 7.1.2].

As shown in Fig. 7.7(c), we find that plotting Γ versus E/E_n collapses all our data onto a single universal curve, with the crossover between degenerate and thermal gas behavior at $E_c = 1.7(2) E_n$. In comparison, for an ideal Bose gas in equilibrium this energy would be rather high, corresponding to $T \approx 3 T_c$, where T_c is the BEC critical temperature. However, in a unitary gas we expect the energy to be of order E_n even at zero temperature [324, 329, 332]. We note that these measurements do not disentangle the contributions to the initial growth of E/E_n (at $t_{\text{hold}} < t_c$) due to heating and due to the development of the interaction-induced correlations that coherently broaden the momentum distribution [270, 324, 333, 341, 342].

7.2.2 Momentum distribution dynamics

Having established a comprehensive picture of the loss dynamics, we now turn to a momentum- and time-resolved analysis of the post-quench dynamics, which allows us to isolate the effects of the initial coherent dynamics. We use our fast ramp-outs that minimize molecule production [see Fig. 7.8(a)] to measure the momentum distribution n_k . To reconstruct n_k from our absorption images (which measure the line-of-sight integrated momentum distribution) we first average each image azimuthally and then average over the experimental repetitions (of which typically about 20 are taken). We then perform an inverse Abel transform (see Section C), before finally normalizing by the total atom number N , such that $\int 4\pi k^2 n_k dk = 1$ within experimental errors. Note that due to the initial cloud size and the non-infinite ToF, our measurements of n_k are not quantitatively reliable for $k < 2 \mu\text{m}^{-1}$.

In Fig. 7.8(b) we show the full $n_k(k)$ for fixed $n_0 = 5.1 \mu\text{m}^{-3}$ at several values of t_{hold} . Our key experimental observation is illustrated in Fig. 7.8(c), where we finely resolve the time-evolution of n_k for individual k states²¹. Plotted this way, we discern separate stages in their evolution: following a rapid initial growth, n_k approaches an intermediate (quasi-)steady-state, before heating takes over at long times (mind the logarithmic x -axis). While the timescales for the different processes are all of order t_{n_0} , they remain distinguishable. We determine such time separation for $k/k_{n_0} \gtrsim 0.8$, and for each k in this range we identify the plateau occupation $\overline{n_k}$ (dashed lines). We then use sigmoidal fits (solid lines) to extract the characteristic time $\tau(k)$ for the rapid initial growth, which we define as the half-way rise time, *i.e.* $n_k(k, \tau(k)) = \overline{n_k}(k)/2$. A crucial feature of Fig. 7.8(c) is that the curves are not aligned in time and the dynamics are

²¹To provide a better sense of scale we have plotted these dynamics in dimensionless form: $n_k k_{n_0}^3$ versus t_{hold}/t_{n_0} , but note that this scaling affects all curves in the same way as n_0 is fixed here, while it will become important later when we compare different n_0 .

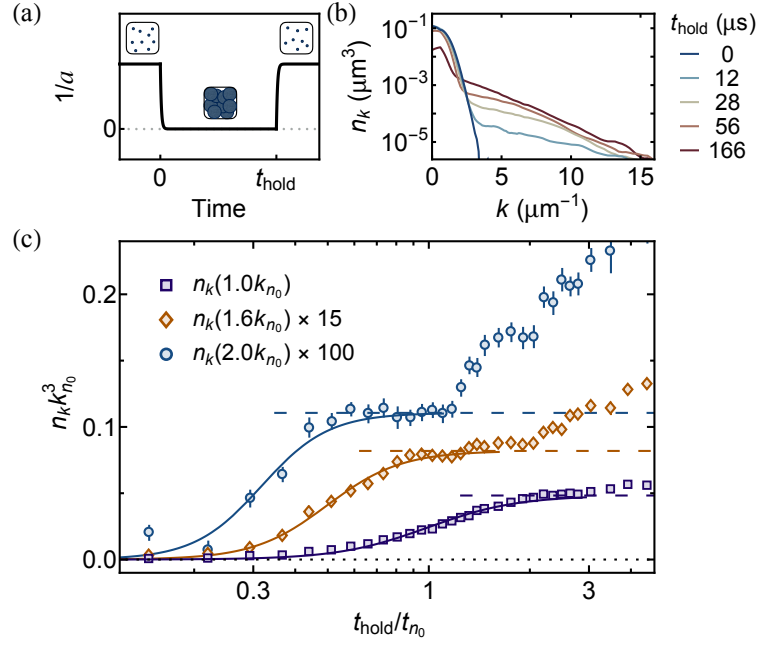


Fig. 7.8 Momentum-resolved dynamics of a degenerate Bose gas quenched to unitarity. (a) Quench protocol, highlighting that we use our fastest ramp-out ($1/\mathcal{R} = 0.3 \mu\text{s}/\text{G}$) to minimize the conversion of atoms into molecules. (b) Momentum distributions for various t_{hold} (see legend); here $n_0 = 5.1 \mu\text{m}^{-3}$, corresponding to $k_{n_0} = 6.7 \mu\text{m}^{-1}$ and $t_{n_0} = 27 \mu\text{s}$. (c) Populations of individual k states exhibit a fast initial growth, saturation at (quasi-)steady-state values \bar{n}_k (dashed lines), and long-time heating. We use sigmoidal (in log-space) fits of the form $\bar{n}_k(1 - 1/[1 + (t_{\text{hold}}/\tau)^{1/\delta\tau}])$ (solid lines) to extract the half-way rise times $\tau(k)$. Figure from [31].

clearly k -dependent. In particular, $n_k(k_{n_0})$ reaches its steady-state value only after $n_k(2k_{n_0})$ already shows signs of heating. This observation explains why previous measurements could not quantitatively separate lossless and recombination dynamics by considering all momentum states at the same t_{hold} . As a concrete example, if one considers the kinetic energy per particle $E = \int \varepsilon dk$, where $\varepsilon = \hbar^2/(2m) \times 4\pi k^4 n_k$, then these rich momentum-dependent dynamics are washed out by the sum over k [see *e.g.* Fig. 7.5(b)].

We proceed by separately extracting \bar{n}_k for different k and piecing together the function $\bar{n}_k(k)$. This *does not* reveal the momentum distribution for any specific t_{hold} , but instead allows us to infer what the steady-state $n_k(k)$ would be in the absence of losses and heating. Our curves now include information arising from different t_{hold} , and so we just use t_{n_0} and k_{n_0} set by the initial density n_0 ; note that for our longest τ we do observe $\approx 20\%$ particle loss. It should also be noted that we assume that at early times ($t_{\text{hold}} \sim t_{n_0}$) all nonzero- k states are primarily fed from the macroscopically occupied condensate [see Fig. 7.8(b)].

In Fig. 7.9 we plot the dimensionless τ/t_{n_0} and $\bar{n}_k k_{n_0}^3$ as a function of the dimensionless k/k_{n_0} , for three different n_0 . By expressing all quantities in such dimensionless form we find that within experimental errors our data points fall onto universal curves.

Across our experimentally accessible range of momenta the universal τ/t_{n_0} is consistent with

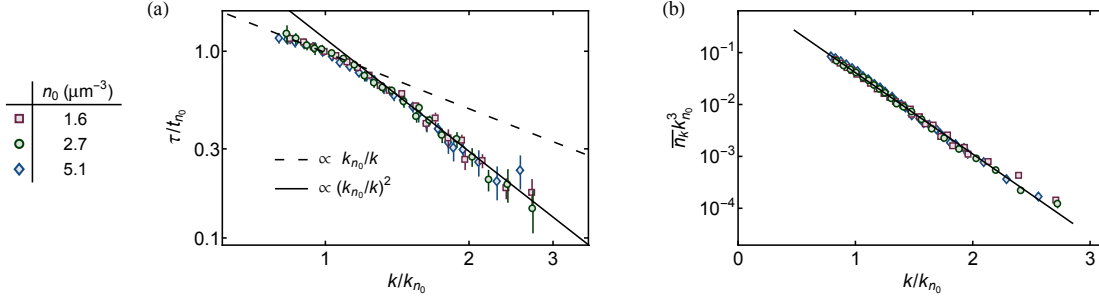


Fig. 7.9 Universal post-quench dynamics and steady-state momentum distribution in the degenerate Bose gas.

We show (a) $\tau(k)$, and (b) the steady-state $\overline{n}_k(k)$, for three different n_0 (see legend). By expressing all quantities in dimensionless form, using the natural Fermi scales t_{n_0} and k_{n_0} , we find that all our data fall onto universal curves. The solid line in (b) is an exponential fit to the data, $\overline{n}_k k_n^3 = 1.53 \exp[-3.62 k/k_n]$. Figure from [31].

the scaling $\propto k_{n_0}/k$ at low k and $\propto (k_{n_0}/k)^2$ at high k [see Fig. 7.9(a)]. Such scaling was qualitatively predicted for the emergence of a prethermal steady state [327, 328, 330, 335, 342] (see also [354]). Within this picture, immediately after the quench the excitations resemble Bogoliubov modes in a weakly interacting BEC, with phonon- and particle-like character at respectively low and high momenta, but with the usual mean-field energy replaced by an energy $\sim E_n$. Consequently, the speed of sound is $\sim \hbar k_n/m$ and the crossover between phonon- and particle-like regimes is at $k \sim k_n$. The predicted $\tau(k)$ is determined by the dephasing time, which is approximately equal to the inverse of the excitation energy.

The universal \overline{n}_k curve is more of a surprise, and presents a new theoretical challenge. Empirically, we find that over three orders of magnitude in $\overline{n}_k k_n^3$ our data are well described by an exponential $A \exp[-Bk/k_n]$, with $A = 1.53(5)$ and $B = 3.62(2)$. Interestingly, if we take this functional form at face value it implies a finite condensed fraction of $\eta = 1 - \int 4\pi k^2 \overline{n}_k dk = 19(4)\%$. Our experiments do not feature the asymptotic form $n_k \sim 1/k^4$ expected at very high k [47]²², but even if n_k were to change to this slower-decaying function right outside of our experimental range this would change η by less than 3%. While our estimate of η is close to the predictions for a prethermal state in [335, 342], we note that this functional form was not predicted so far, and it could require explicit consideration of our final quench back to low a . That been said, qualitative similarities (up to $\approx k_n$) to theoretical calculations are present [331, 341, 352].

It is also interesting to use the exponential \overline{n}_k to compute the kinetic energy per particle $\overline{E} = \int \overline{\varepsilon} dk$, defining the prethermal state spectral energy density $\overline{\varepsilon} = \hbar^2/(2m) \times 4\pi k^4 \overline{n}_k$. We obtain $\overline{E} = 0.74(4)E_{n_0}$, which highlights that the prethermal state is strongly correlated, but

²²Efimov physics is thought to modify the $1/k^4$ tail with log-periodic modulations, and several theoretical interpretations (e.g. [333, 336]) of the pioneering ⁸⁵Rb experiment [270] compared such equilibrium unitary predictions to the data. However, it is not clear that such a tail would survive a quench back to low a , and generally it has been numerically observed that the contact parameter (characterizing the high- k momentum tail) can exhibit large oscillations following a quench [385], and more generally that low momenta remain frozen while high momenta evolve adiabatically [283].

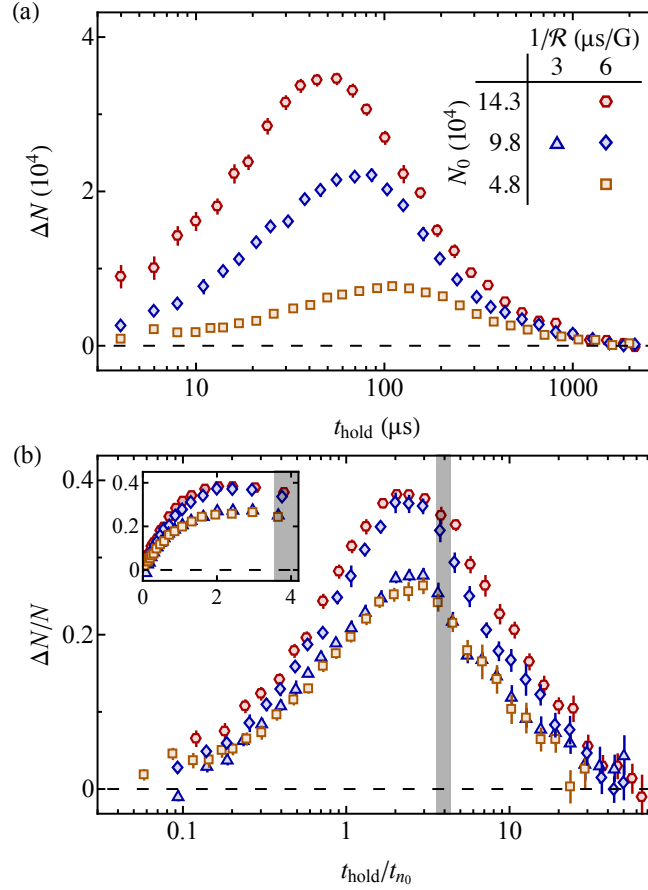


Fig. 7.10 Correlation dynamics of a degenerate Bose gas quenched to unitarity. (a) We plot ΔN versus t_{hold} for three different N_0 and the same slow ramp-out $1/\mathcal{R} = 5.8 \mu\text{s}/\text{G}$ [note the logarithmic x axis]. (b) $\Delta N/N$ versus the dimensionless time t_{hold}/t_{n_0} , for different N_0 and $1/\mathcal{R}$; see legend in (a). The shaded region indicates the crossover to the thermal regime at $t_c = 4.0(3) t_{n_0}$. The inset shows a zoom-in on the degenerate regime on linear scale, highlighting that the correlations reach a (quasi-)steady state well before t_c . Figure from [30].

for quantitative purposes one should bear in mind the caveat that we do not observe the very-high- k tails experimentally.

7.2.3 Molecular correlation dynamics

We now turn to the dynamics of correlations at unitarity, which are indirectly revealed by slowly ramping the magnetic field away from resonance and creating an atom-molecule mixture. We study ΔN , the reduction in N_{obs} due to the slow ramp-out, assuming that $N = N_{\text{obs}}$ for our fastest ramp-out with $1/\mathcal{R} = 0.3 \mu\text{s}/\text{G}$.

In Fig. 7.10(a) we plot ΔN versus t_{hold} for three different N_0 , using the same slow ramp-out with $1/\mathcal{R} = 5.8 \mu\text{s}/\text{G}$. In Fig. 7.10(b) we show a rescaled version, where we plot the fractional conversion efficiency $\Delta N/N$ versus the dimensionless t_{hold}/t_{n_0} ²³, where we have also included

²³We use the initial t_{n_0} to normalize t_{hold} , as the relevance of t_n is not clear in the thermal regime. In the degenerate regime, one can readily relate t_{n_0} to t_n , by simply rewriting the degenerate-gas loss rate [Eq. (7.12)] as $\dot{t}_n = 2A/3$, so that $t_n/t_{n_0} = 1 + 2A/3 \times t_{\text{hold}}/t_{n_0}$.

an additional data series with twice the ramp-out speed. Plotting the data this way achieves horizontal alignment of all our curves, and apart from their heights they all look essentially the same. This shows us that correlation dynamics are universally set by the initial gas density.

We can qualitatively understand the non-monotonic shape of the curves as arising from the competition of two effects. At short times following the quench to unitarity, the gas is uncorrelated as it takes time for the correlations to develop (on a timescale set by t_{n_0}). Instead, at long times the system becomes uncorrelated again as it heats up and the phase space density drops dramatically (see also [36, 383]).

We highlight the early-time dynamics (on linear timescale) in the inset of Fig. 7.10(b), which shows how $\Delta N/N$ becomes essentially constant well before t_c (where the crossover to the thermal unitary regime occurs, see Section 7.2.1). This suggests that the correlations in the system reach a quasi-equilibrium state while the gas is still degenerate, which in our homogeneous system implies a *global* (quasi-)equilibrium.

In the following we present an attempt at experimentally disentangling how the steady-state conversion efficiency $\overline{\Delta N/N}$ depends on \mathcal{R} and N_0 . Based on recent experiments with ^{85}Rb [271], which observed that the post-quench molecular gas contains Efimov trimers in the first excited state, it is likely that our atom-molecule mixture also includes such Efimov trimers (instead of simply consisting of Feshbach dimers). The presence of these trimers could break universality and lead to a nontrivial dependence of $\overline{\Delta N/N}$ on N_0 , as the on-resonance size of this state is of order $1\ \mu\text{m}$ [33, 35, 348, 362, 363, 386], which could set a scale that separates ‘small’ and ‘large’ densities [346, 347, 349, 366].

To provide a baseline for our expectations, we begin by considering the theoretically expected dependencies of the Feshbach dimer production efficiency. Following [381] (see also [353, 380]), we introduce a simple model to describe the ramp-out from the unitary regime, which as we will see predicts that the Feshbach dimer conversion efficiency is a universal function of N_0/\mathcal{R} (see also [383]). We split the ramp into two regimes, a initial sudden diabatic one and subsequent slower adiabatic one. To estimate the scattering length a_* at which the crossover between the two regimes occurs, we assume that the ramp-out remains diabatic up to the point when $E_b/\hbar = \dot{E}_b/E_b$, after which the process is assumed to become fully adiabatic, molecular conversion is halted, and one simply follows the final energy states. Assuming that we are close to the Feshbach resonance ($B - B_\infty \ll \Delta$), we substitute the Feshbach dimer binding energy $E_b \approx -\hbar^2/(ma^2)$ and solve $\dot{E}_b = E_b^2/\hbar$ to obtain

$$a_* = \left(\frac{\hbar a_{\text{bg}} \Delta}{2m\mathcal{R}} \right)^{1/3}. \quad (7.15)$$

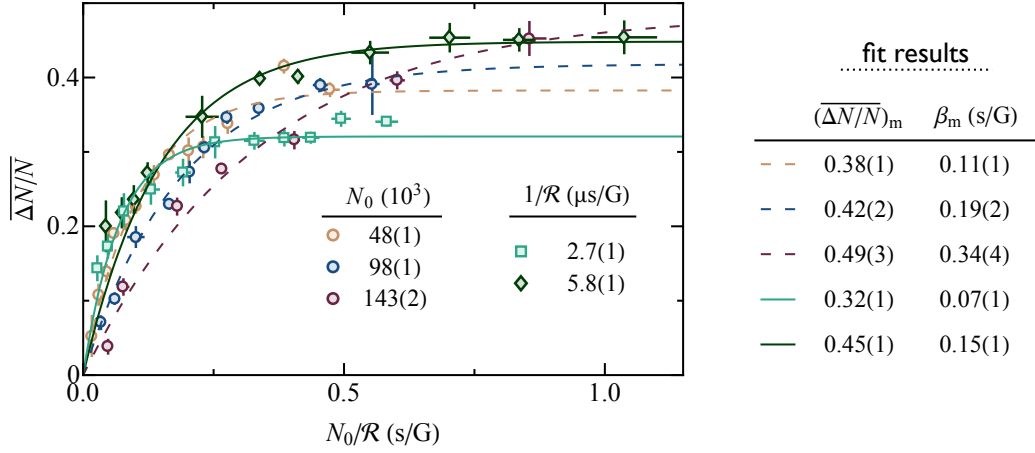


Fig. 7.11 Molecular conversion efficiency in the degenerate post-quench quasi-equilibrium state. We study the molecular correlation dynamics in the quasi-steady state (using $t_{\text{hold}} = 2.7(1)t_{n_0}$), and plot $\overline{\Delta N/N}$ versus N_0/\mathcal{R} for three fixed N_0 varying \mathcal{R} and two fixed \mathcal{R} varying N_0 (see legend). Plotted this way, we would expect our data to collapse onto a single universal curve if we were producing only Feshbach dimers (see text). To determine $\overline{\Delta N/N}$ we measure the reduced N_{obs} due to the slower ramp-outs but compute N from N_0 using the adjusted $A = 0.24$, which ensures that an extrapolation to $1/\mathcal{R} \rightarrow 0$ recovers $\overline{\Delta N/N} = 0$. We fit the data with a saturating exponential $(\overline{\Delta N/N})_m (1 - \exp[-N_0/(\mathcal{R}\beta_m)])$ (see table), finding evidence that universality is broken.

Within this picture, our ramp projects the initial many-body state onto the molecular state at scattering length a_* . For larger \mathcal{R} one achieves smaller a_* , and consequently a more localized molecular state. Assuming that universality holds, the original many-body state at unitarity has a size set by the interparticle spacing $n_0^{-1/3}$. To assess the conversion efficiency, the next step would be to compute the overlap integral between these two states. However, for our purposes here we simply resort to dimensional arguments and posit that the conversion efficiency is a function of the ratio of sizes $a_*/n_0^{-1/3}$, *i.e.* a function of N_0/\mathcal{R} .

In Fig. 7.11 we present a summary of all our measurements of $\overline{\Delta N/N}$, which we always extract at the same fixed $t_{\text{hold}}/t_{n_0} = 2.7(1)$. As outlined in the internal legend, we vary N_0/\mathcal{R} in two different ways. For three of our data series (circles) we keep N_0 fixed and vary $1/\mathcal{R}$ by varying both τ_Q and ΔB [as in Fig. 7.4(b)]. For the other two series, we instead fix $1/\mathcal{R}$ and vary N_0 . We find that a saturating exponential of height $(\overline{\Delta N/N})_m$ and $1/e$ rise-constant β_m fits all series well individually. However, we find that our data do not collapse onto a universal curve when plotted in this way. This is perhaps most clearly revealed by the individual exponential fits to the different series, which give inconsistent values of $(\overline{\Delta N/N})_m$ and β_m .

Our data thus indicates that there is more to the story than just Feshbach dimer formation, in line with [271] and the expectation that our atom-molecule mixture contains Efimov trimers. Quantitatively understanding the composition of the atom-molecule mixtures, as well as the full $\Delta N/N$ curves, remain interesting problems for future work, which have already attracted significant theoretical attention [353,366]. Experimentally, a clear limitation is that we currently

cannot achieve large values of N_0/\mathcal{R} for which $\overline{\Delta N/N}$ truly saturates (as our maximal τ_Q is limited to 10 μs). Additionally, gaining a better understanding of the expected few-body physics for ^{39}K will be beneficial to pin-point the expected densities at which deviations to universal behavior are expected (see *e.g.* [366]).

A more general remark is that our measurements currently infer the presence of molecules by the absence of atoms, and in the future we intend on moving towards the direct observation of the molecules, which following [271] also offers the possibility of distinguishing trimers from dimers by studying the decay dynamics of the molecular gas at low a .

7.3 Thermal Bose gases quenched to unitarity

In this section we explore the dynamics of thermal Bose gases quenched to unitarity, and while these experiments do offer some significant simplifications compared to their degenerate counterparts, they also come with additional surprises. We begin in Section 7.3.1 by studying the early-time post-quench redistribution dynamics in a momentum-resolved manner. The dynamic and thermodynamic properties generically depend on both n and T , but we find that they can still be expressed in terms of universal dimensionless functions. In Section 7.3.2 we turn to atom-loss and correlation dynamics, where we primarily focus on longer times after the quench, when three-body recombination dominates the gas dynamics.

7.3.1 Momentum redistribution dynamics

A simplification for studying unitary thermal gases compared to their degenerate counterparts comes from the fact that in a thermal gas three-body recombination is slowed down more than the lossless dynamics [320, 321, 326]. As shown in Fig. 7.12(a) for a thermal gas with $n_0 = 5.6 \mu\text{m}^{-3}$ and $T = 150 \text{ nK}$ ²⁴, simply looking at the energy per particle $E(t_{\text{hold}})$ on log-log scale now reveals two separate stages in the post-quench evolution: a rapid initial growth where E more than doubles, followed by heating on a significantly longer timescale.

The behavior at long times agrees with the expected energy-growth due to recombination heating in a thermal unitary Bose gas [320] (see Section 7.1.2), while the shape of the curve resembles those obtained for the evolution of individual k states in our measurements using initially degenerate samples [see Fig. 7.8(c)]. All the above reinforces our general interpretation of the two-step post-quench dynamics, for both degenerate and thermal gases. Here we will focus on the early-time dynamics [*e.g.* corresponding to $t_{\text{hold}} \lesssim 100 \mu\text{s}$ in Fig. 7.12(a)]. In Fig. 7.12(b) we show how the momentum distribution n_k is essentially identical for 60 and

²⁴Here, and throughout this section, T is the initial temperature (before the quench to unitarity).

126 μs , which demonstrates how on this timescale a true steady-state is established for all k (as opposed to the prethermal (quasi-)steady-state that we observe for degenerate gases).

In thermal gases it is natural to look at the redistribution of particles in k -space, as even prior to the quench to unitarity n_k is significant for $k \lesssim 1/\lambda$, where $\lambda = h/\sqrt{2\pi m k_B T}$ is the initial thermal wavelength. We thus consider the change $\delta n_k(k)$ with respect to our initial distribution measured at $t_{\text{hold}} = 0$, and the corresponding change in the spectral energy density $\varepsilon = \hbar^2/(2m) 4\pi k^4 n_k$. A complication arising in thermal unitary Bose gases is that they feature both $n^{-1/3}$ and λ as potentially relevant lengthscales (and any combination of the two), and it is *a priori* unknown whether the dynamic and thermodynamic properties can be expressed in terms of dimensionless universal functions.

In Fig. 7.12(c) we show a plot of the time-resolved population changes in different spherical k -space shells, $4\pi k^2 \delta n_k$. We find a special momentum k_0 (dashed line) at which the population remains essentially constant, separating the momenta that are depleted (blue) from those that grow (red). In Fig. 7.12(d) we plot vertical cuts through Fig. 7.12(c), for $k < k_0$, $k = k_0$, and $k > k_0$. We use sigmoidal fits (solid lines) to extract $\tau(k)$ away from k_0 where the populations either diminish ($k < k_0$) or grow ($k > k_0$). Close to k_0 , where the population changes are small, we find that n_k initially slightly decreases before subsequently increasing again, behavior to which we cannot assign a single timescale.

In Fig. 7.12(e,f) we (respectively) plot the extracted $\tau(k)$ and steady-state $\overline{\delta\varepsilon}(k)$, for two different combinations of n_0 and T . The $\overline{\delta\varepsilon}(k)$ curve resolves the energy growth $\overline{\Delta E} = \int \overline{\delta\varepsilon} dk$, arising from the redistribution of particles from $k < k_0$ to $k > k_0$. The dispersive shape of $\tau(k)$ was not anticipated, and invites further theoretical work. We do note a qualitative similarity to our degenerate gas data for $k > k_0$ when $\overline{\delta\varepsilon}$ is positive, where we find that τ smoothly decreases for increasing k .

Universal laws dictating the early-time momentum redistribution dynamics

We proceed by empirically investigating whether the $\tau(k)$ and $\overline{\delta\varepsilon}(k)$ curves (see Fig. 7.12) can be scaled into universal dimensionless functions. We have taken such curves for 15 combinations of n_0 and T , with corresponding initial phase-space densities $n_0 \lambda^3$ between 0.2 and 2.

In order to rescale the data horizontally, and thus find the natural scale of k we use k_0 [defined by the zero-crossing of $\overline{\delta\varepsilon}(k)$] for guidance. In Fig. 7.13 we plot k_0 versus T on log-log scale for all our 15 series (see legend), observing power-law behavior; a fit yields $k_0 \propto T^{0.53(2)}$ (dashed line). We thus deduce that the natural scale of k_0 is $1/\lambda$, independent of n_0 . Indeed, as shown in the inset, if we consider series at similar fixed $T \approx 0.2 \mu\text{K}$ but varying n_0 we see that k_0 remains

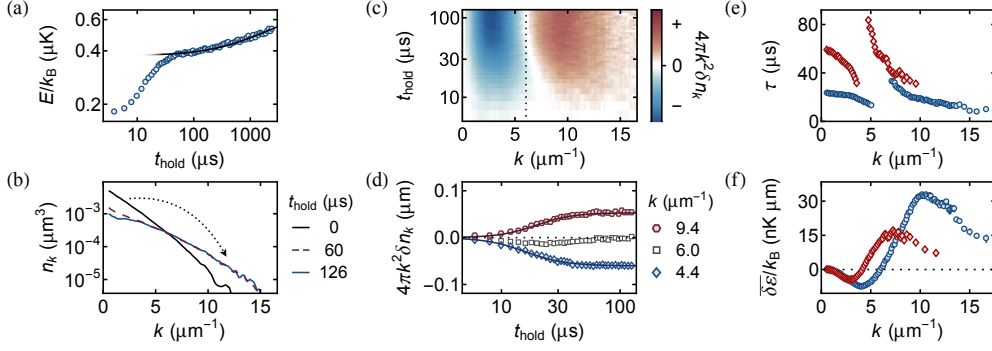


Fig. 7.12 Momentum-resolved dynamics of a thermal Bose gas quenched to unitarity. (a) Log-log plot of the kinetic energy per particle E versus t_{hold} , exhibiting a rapid initial growth at $t_{\text{hold}} \lesssim 100 \mu\text{s}$, and significant heating only for $t_{\text{hold}} \gg 100 \mu\text{s}$; the black line shows the prediction for recombination heating. Here, and in (b-d), the initial density and gas temperature are $n_0 = 5.6 \mu\text{m}^{-3}$ and $T = 150 \text{ nK}$. (b) Momentum distributions $n_k(k)$ for different hold times t_{hold} at unitarity. The initial redistribution of particles from low to high momenta (indicated by the dotted arrow) essentially occurs within $60 \mu\text{s}$, and n_k is almost identical at $126 \mu\text{s}$. (c) Time-resolved population changes in different k -space shells, $4\pi k^2 \delta n_k$; the population in $k_0 = 6.0 \mu\text{m}^{-1}$ (dashed line) remains essentially unchanged. (d) Vertical cuts through (c), above, at, and below k_0 . The solid lines show the sigmoidal (in log-space) fits of the form $\delta n_k (1 - 1/[1 + (t_{\text{hold}}/\tau)^{1/\delta\tau}])$ used to extract the half-way time τ at each k . (e,f) Here we map out the momentum dependence of the extracted parameters for our data series with $n_0 = 5.6 \mu\text{m}^{-3}$ and $T = 150 \text{ nK}$ (blue circles), and an additional one with $n_0 = 1.3 \mu\text{m}^{-3}$ and $T = 70 \text{ nK}$ (red diamonds). (e) Half-way time τ as a function of k . (f) Change in spectral-energy density (between the initial, pre-quench state, and the post-quench steady state), $\overline{\delta\varepsilon}(k) \propto k^4 \overline{\delta n_k}(k)$. Figure from [31].

essentially constant. We proceed by fitting the data with a fixed $k_0 \propto T^{1/2} \propto 1/\lambda$ scaling, and obtain $k_0 = 4.40(2)/\lambda$ (solid line). Rather curiously, we find that rewriting $\hbar^2 k_0^2 / (2m) = 1.54(1) k_B T$ yields an energy associated with k_0 which is very close to the average kinetic energy of a monatomic ideal gas ($3/2 k_B T$).

We now turn to the full $\tau(k)$ and $\overline{\delta\varepsilon}(k)$ curves for our 15 combinations of n and T , introducing $1/\lambda$ as the natural scale for k . In Fig. 7.14(a) we plot $\tau(k)$ as a function of $k\lambda$ on log-log scale, and in Fig. 7.14(d) we plot $\overline{\delta\varepsilon}(k)/\lambda$ versus $k\lambda$, ensuring that the area under each curve remains unchanged [*i.e.* conserving $\overline{\Delta E}(n_0, T)$]. In both cases we find successful horizontal alignment of the curves, further establishing that the natural scale of k is $1/\lambda$.

Our next question, which poses more of a challenge, is whether these two families of curves can be vertically scaled to each collapse onto a single universal curve. To address this we take a heuristic approach, introducing a scaling time $t_s(n_0, T)$ and energy $E_s(n_0, T)$. Our conjecture is that both t_s and E_s take power-law form, namely that $t_s \sim t_{n_0}^\alpha t_\lambda^{\beta_t}$, where $t_\lambda = \hbar / (k_B T)$, and similarly $E_s \sim E_{n_0}^{\alpha_E} (k_B T)^{\beta_E}$. We then simply search for the values of α and β that yield the best data collapse. In our analysis we treat α and β as independent, however in the absence of any other relevant scales one expects $\alpha_t + \beta_t = \alpha_E + \beta_E = 1$ for dimensional reasons. To assess the degree of data collapse we use a single figure of merit σ , which is obtained by calculating the standard deviation of our data for all n_0 and T at fixed $k\lambda$, before summing over $k\lambda$. We normalize by σ_0 , corresponding to the value obtained for no scaling ($\alpha = \beta = 0$).

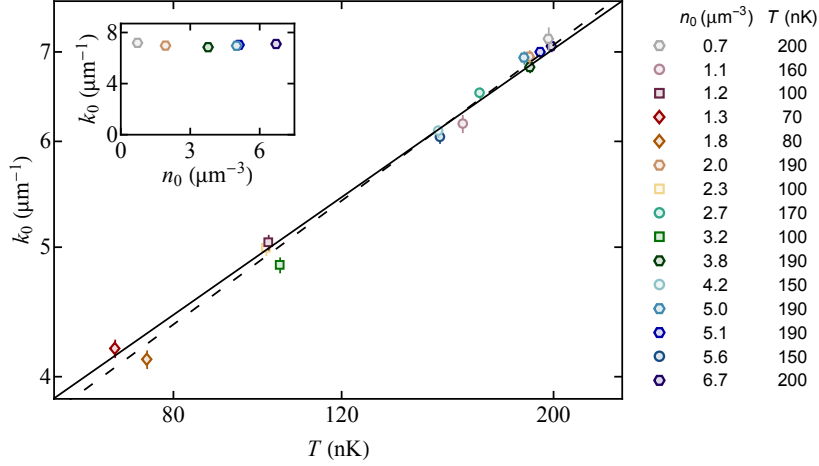


Fig. 7.13 Momentum-scale governing the redistribution dynamics. We show a log-log plot of the extracted k_0 [defined such that $\delta\bar{\varepsilon}(k_0) \equiv 0$, see Fig. 7.12(f)] as a function of the initial gas temperature T , showcasing our 15 different combinations of n_0 and T (see legend). We find power-law behavior, and a fit to the data gives $k_0 \propto T^{0.53(3)}$ (dashed line), suggesting that $k_0 \propto 1/\lambda$, independent of the initial gas density n_0 . Fixing the power-law dependence and refitting gives $k_0 = 4.40(2)/\lambda$ (solid line), which defines the natural momentum scale of the redistribution dynamics. The inset shows k_0 versus n_0 for a subset of the data for which n_0 varies but $T \approx 0.2 \mu\text{K}$ is approximately constant, highlighting the lack of n_0 dependence.

In Figs. 7.14(b) and (e), respectively, we plot σ/σ_0 for τ and $\bar{\delta\varepsilon}/\lambda$. Focusing on the temporal scaling first [Fig. 7.14(b)], we find the minimum in σ around $\alpha_t = \beta_t = 1/2$, which suggests that $t_s = \sqrt{t_{n_0} t_\lambda}$. In Fig. 7.14(c) we plot $\tau/\sqrt{t_{n_0} t_\lambda}$ versus $k\lambda$ and observe that, within experimental scatter, all our data fall onto a single universal curve. Our intuitive interpretation of this scaling is that because the particles in a thermal gas do not overlap, they must first meet in order to start feeling the unitarity interactions after the quench. Their ‘meeting time’, up to a numerical factor, is $\sqrt{t_{n_0} t_\lambda} \sim n_0^{-1/3} \lambda m/\hbar$ [*i.e.* the ratio of initial interparticle distance $n_0^{-1/3}$ and characteristic thermal speed $\propto \hbar/(m\lambda)$].

A final tentative remark regarding Fig. 7.14(c), is that it seems that at large k we approach power-law behavior $\tau/(t_{n_0} t_\lambda)^{1/2} = \tilde{c}/(k\lambda)$ (dashed line), where \tilde{c} is a constant. Curiously, one can simply rewrite this scaling as $\tau/t_{n_0} = \tilde{c}/(2\sqrt{\pi}) k_{n_0}/k$, where λ fully drops out. Moreover, this scaling is the same as observed for low- k in our degenerate gas data, where we had $\tau/t_{n_0} \approx 0.98 k_{n_0}/k$ [see dashed line in Fig. 7.9(a)]. Indeed, the dashed line shown in Fig. 7.14(c) corresponds to setting $\tilde{c} = 0.98 \times 2\sqrt{\pi}$, extracted from the degenerate gas data. Surprisingly, we find that this quantitatively captures the thermal data at high k (within experimental scatter). We currently do not understand why these two different momentum regimes in thermal and degenerate gases would behave in the same way, however we also cannot rule out that it is just a coincidence.

Turning to the spectral energy density [Fig. 7.14(e)], we instead find the optimal $\alpha_E \approx 1$ and $\beta_E \approx 0$, which rather surprisingly implies that $E_s = E_{n_0}$. In Fig. 7.14(f) we set out to test this scaling, plotting $\bar{\delta\varepsilon}/(\lambda E_{n_0})$ versus $k\lambda$, and find that it indeed collapses all our data onto a

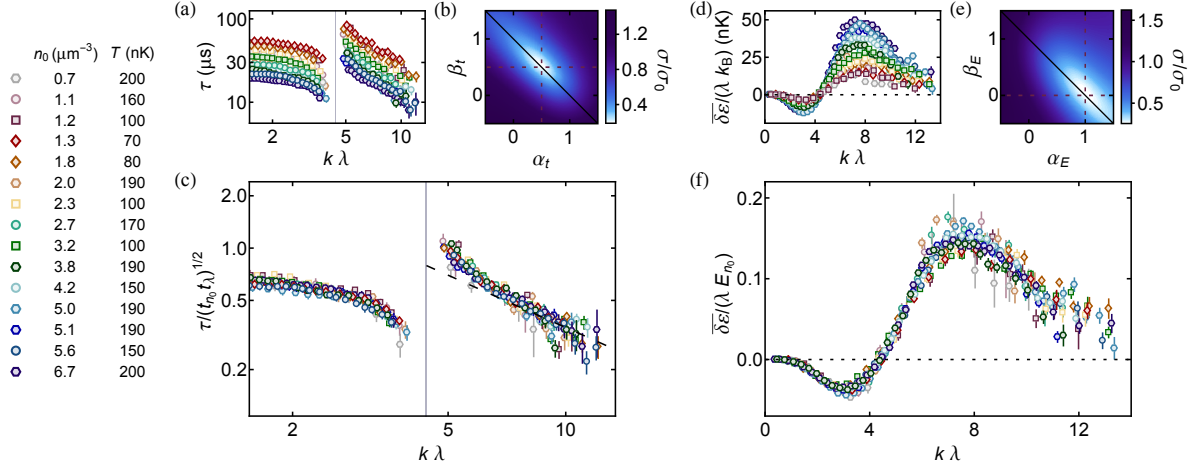


Fig. 7.14 Universal dynamic and thermodynamic functions dictating the evolution of thermal Bose gases quenched to unitarity. (a, d) By plotting τ and $\overline{\delta\varepsilon}/\lambda$ as a function $k\lambda$ we horizontally align our curves for 15 different combinations of n_0 and T (see legend). (b, e) Supposing that the characteristic timescale for the dynamics takes the form $t_s \sim t_{n_0}^{\alpha_t} t_\lambda^{\beta_t}$, we find the best data collapse (captured by small σ/σ_0) for $\alpha_t \approx \beta_t \approx 1/2$, implying that $t_s = \sqrt{t_{n_0} t_\lambda}$ (see text for details). Similarly, for the energy scale $E_s \sim E_{n_0}^{\alpha_E} (k_B T)^{\beta_E}$ we obtain $\alpha_E \approx 1$ and $\beta_E \approx 0$, suggesting that $E_s = E_{n_0}$. (c, f) To within experimental scatter, we find that the dimensionless $\tau/\sqrt{t_{n_0} t_\lambda}$ and $\overline{\delta\varepsilon}/(\lambda E_{n_0})$ are universal functions of the dimensionless $k\lambda$. Figure from [31].

universal curve. It is quite remarkable that while $\overline{\delta\varepsilon}(k)$ depends on both n_0 and T , its integral $\overline{\Delta E}$ ends up being independent of T .

Due to the lack of T dependence, in order for both thermal and degenerate gas regimes to connect gracefully we would require that $\overline{\Delta E}/E_{n_0}$ is the same in both cases, inviting a comparison to our degenerate gas data from Section 7.2.2. Bearing the caveat in mind that we only observe the distributions up to $k\lambda \approx 12$ and in general do not observe their very high- k tails, from our thermal-gas data in Fig. 7.14(f) we estimate $\overline{\Delta E}/E_{n_0} = 0.7(1)$. In comparison, taking the exponential $\overline{n_k} k_n^3$ from our degenerate gas data in Fig. 7.9(b) gives a consistent $\overline{E}/E_{n_0} = 0.74(4)$.

It is insightful to compare the universal $\overline{\delta\varepsilon}$ to the expected very-high- k equilibrium behavior of $\epsilon(k)$ at unitarity, which is expected to be governed by the unitarity limited two- and three-body contact densities $C_2 = 32\pi n^2 \lambda^3$ and $C_3 \approx 3\sqrt{3} s_0 n^3 \lambda^4$ [65, 333]; in this case we would expect the very-high k behavior to be given by

$$\frac{\epsilon}{\lambda E_n} = \frac{16}{\pi^{7/3} 6^{2/3}} n^{1/3} \lambda \left(1 + \frac{\omega_3(k)}{k\lambda} \frac{3\sqrt{3} s_0}{32\pi} n \lambda^3 \right), \quad (7.16)$$

where the log-periodic function $\omega_3(k) \approx 89.3 \sin[2s_0 \ln(k/\kappa_*) - 1.34]$ with $s_0 = 1.00624$ and κ_* is the three-body parameter. We see that this is not a universal function of $k\lambda$, but rather depends on the phase-space density of the gas. Looking past the log-periodic modulation (and safely neglecting the initial low- a contact density in a thermal gas), we find that for our range of

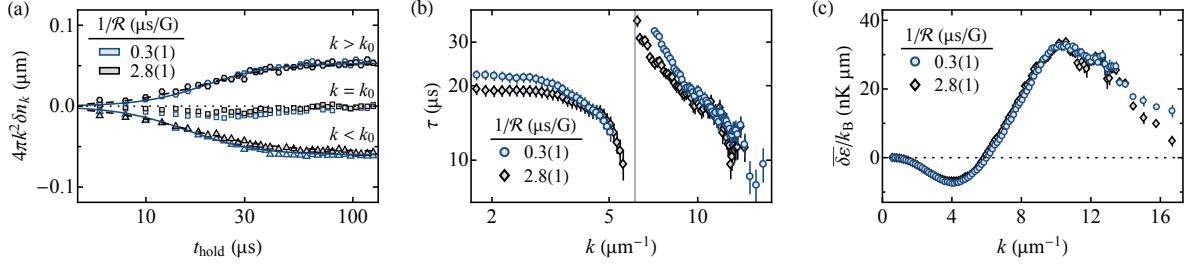


Fig. 7.15 Effects of the ramp-out rate on the initial redistribution dynamics. We compare two different \mathcal{R} for our momentum- and time-resolved measurements of the initial redistribution dynamics of a thermal Bose gas quenched to unitarity. In both cases we prepare the cloud with the same $n_0 = 5.6 \mu\text{m}^{-3}$ and $T = 150$ nK. We show a direct comparison of the results for the two different \mathcal{R} , for (a) the population dynamics of three characteristic k -space shells, and (b,c) the extracted half-way rise time $\tau(k)$ and change in spectral density $\delta \bar{\epsilon}$, respectively.

phase-space densities this prediction sits far above our data (the prefactor evaluates to ≈ 0.34). This suggests that our quench protocol is not sensitive to the contact at unitarity, most probably due to the final quench back to low a (though we also do not resolve very large values of $k\lambda$).

Do the redistribution dynamics depend on \mathcal{R} ?

In the discussion above we solely focused on data taken with our largest \mathcal{R} , which should approximately project the many-body wave function onto free-particle states and faithfully measure n_k . However, as discussed for degenerate gases in Section 7.2.3, we expect that the a_* one reaches before the system can adiabatically follow the ramp-out does depend (albeit nontrivially) on properties of the sample. This suggests that while we did keep \mathcal{R} fixed, the physically relevant parameter may vary between the different series. It is therefore a worthwhile question to ask how our measurements depend on \mathcal{R} .

To investigate this, we focus on a single data series; we use $n_0 = 5.6 \mu\text{m}^{-3}$ and $T = 150$ nK, as this is the series with the largest phase-space density and so most conducive to creating a significant fraction of molecules [383]. We repeat our full momentum- and time-resolved measurement with identical initial conditions (within 1 s.e.m.) apart from the use of a 10 times slower ramp-out, achieved by increasing the time-constant of our ramp-out τ_Q . A comparison between the two measurements is shown in Fig. 7.15, where we note that to normalize n_k we use the individually observed atom number N_{obs} , which as we will see in Section 7.3.2 is reduced by up to $\sim 20\%$ for our slow ramp-out.

In Fig. 7.15(a) we study the population dynamics for three characteristic k -space shells, plotting $4\pi k^2 \delta n_k$ versus t_{hold} for our two \mathcal{R} . We see that data for the two different \mathcal{R} essentially lie on top of each other, with only small deviations.

In Figs. 7.15(b,c) we compare the extracted τ and $\delta \bar{\epsilon}$ versus k , respectively. For $\tau(k)$ [Fig. 7.15(b)] we observe small but statistically significant differences of the extracted τ for $k < k_0$ and

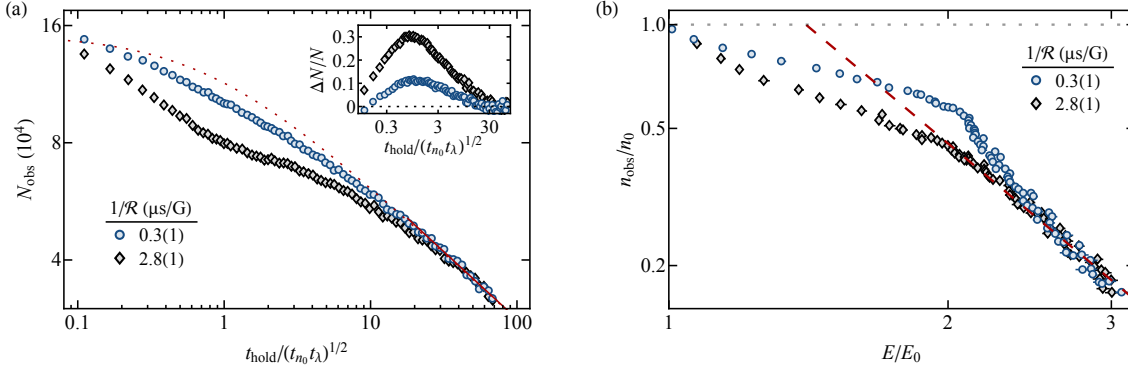


Fig. 7.16 Atom-loss, correlation, and energy dynamics of a thermal Bose gas quenched to unitarity. (a) Log-log plot of N_{obs} as a function of t_{hold} (normalized by $\sqrt{t_{n_0} t_\lambda}$) for our fastest ramp-out ($0.3 \mu\text{s/G}$) and a much slower one ($2.8 \mu\text{s/G}$). In the inset we show the molecular conversion efficiency $\Delta N/N$, where we use the long-time behavior (which agrees with the expected recombination heating loss rate) to calculate $N(t_{\text{hold}})$ (dotted line in the main panel). (b) We plot n_{obs}/n_0 versus E/E_0 on log-log scale for our two \mathcal{R} . The dashed line corresponds to the prediction for three-body recombination heating, which matches our data at long times (large E/E_0).

around k_0 , while the two agree well for $k > 1.5k_0$. For the slow ramp-out we are able to extract τ for values significantly closer to k_0 , as the region in k -space where the population shows a non-monotonic (first decreasing before subsequently increasing) time dependence, is smaller. Instead looking at $\overline{\delta\varepsilon}$ [Fig. 7.15(c)], we see that the two curves are essentially identical apart from at very large k , where we observe a suppression of $\overline{\delta\varepsilon}$ for the slow ramp-out.

7.3.2 Atom-loss and correlation dynamics

We now turn to the atom-loss, correlation, and energy dynamics of a thermal Bose gas quenched to unitarity. We consider the same data series as in Section 7.3.1, with $n_0 = 5.6 \mu\text{m}^{-3}$ and $T = 150 \text{ nK}$, comparing the two \mathcal{R} that differ by a factor of 10.

In Fig. 7.16(a) we plot the evolution of N_{obs} for our two different \mathcal{R} , where we have normalized t_{hold} by the characteristic initial meeting time $\sqrt{t_{n_0} t_\lambda} \approx 36 \mu\text{s}$ [see Fig. 7.14(c)]. Similar to our degenerate gas data, we see that the two curves converge at both short and long times, suggesting that it takes some time for correlations to develop before ultimately the phase-space density drops sufficiently for molecule formation to become negligible [383]. At long times, we observe the expected power-law behavior $N_{\text{obs}} \propto t_{\text{hold}}^{-9/26}$ [solid red line in Fig. 7.16(a), see also Section 7.1.2]. Assuming that the same three-body loss extends to short times we can use Eq. (7.5) to compute the expected loss dynamics (dotted red line) given our N_0 . Interestingly, for both our \mathcal{R} we observe more loss than expected from our calculation²⁵. For our slow ramp-

²⁵Note that recent interferometric measurements of the three-body contact density C_3 in a thermal unitary Bose gas [65] observed a relatively slow evolution of C_3 following the quench to unitarity, approaching its expected theoretical equilibrium value [333] in $100 \mu\text{s} \sim 5t_\lambda$. Since it is expected that $C_3 \propto L_3$ [36, 333], it is not clear whether we expect any traditional three-body loss immediately after the quench.

out we observe a dramatic suppression of N_{obs} , compared to both the fast-ramp data and our calculation based on the long-time behavior. This is further highlighted in the inset, where we study the evolution of $\Delta N/N$, which we compute using the calculated loss curve to define N ²⁶. The conversion efficiency reaches a broad maximum at $t_{\text{hold}}/\sqrt{t_{n_0}t_\lambda} \approx 1$. We note that the significant molecule production can be attributed to the rather large phase-space density of the gas ($n_0\lambda^3 \approx 2$) [383], and $\Delta N/N$ is significantly suppressed for samples with lower $n_0\lambda^3$.

At this point it is insightful to recall the two-step dynamics of E , and the associated redistribution dynamics that we presented in Section 7.3.1. We found that the change in energy was set solely by E_n , while the timescale for the changes was set by the ‘meeting time’ ($\sqrt{t_{n_0}t_\lambda}$), with all dynamics essentially saturating after $t_{\text{hold}}/\sqrt{t_{n_0}t_\lambda} \approx 2$. We also found that these redistribution dynamics are remarkably insensitive to \mathcal{R} , while the observed early-time atom loss depends sensitively on \mathcal{R} .

In Fig. 7.16(b) we compare the decrease in n_{obs}/n_0 to the increase in E/E_0 ²⁷. While we do observe loss at early times, visually extrapolating our fast ramp-out data to early times suggests that the loss that we observe does not lead to traditional three-body recombination heating, and in the limit of $1/\mathcal{R} \rightarrow 0$ it looks as if we are approaching an essentially lossless increase in E . Instead, at long times we observe the anticipated $n \propto E^{-9/4}$ [see Eq. (7.11) in Section 7.1.2] for recombination heating.

Attaining a full understanding of the loss dynamics at early times is an important endeavor for the future, which will require meticulously disentangling the effects of $\{n_0^{-1/3}, \lambda, \mathcal{R}, \text{ and } t_{\text{hold}}\}$. It should be noted that while for reference we consider the dynamics to be a function of $\sqrt{t_{n_0}t_\lambda}$, it is not necessarily true that the peak position of $\Delta N/N$ is set by $\sqrt{t_{n_0}t_\lambda}$; indeed it has been theoretically shown that the dynamics of the two-body contact density C_2 are set by t_λ in a thermal unitary Bose gas [65].

From here on we will focus only on our fast ramp-out ($1/\mathcal{R} = 0.3 \mu\text{s}/\text{G}$) data (which minimizes molecular conversion) and examine the observed atom-loss dynamics for different initial conditions (recall that we took data for 15 different n_0 and T). To study the loss dynamics we compute the dimensionless loss rate

$$\Gamma = -t_n \frac{\dot{N}}{N} = \zeta_3 \frac{18\sqrt{3}}{\pi^2} \left(\frac{E_n}{E} \right)^2, \quad (7.17)$$

²⁶This assumption is not necessarily correct, but plotting the data this way allows us to compare curves of $\Delta N/N$ for both our \mathcal{R} , and our previous definition (setting $N_{\text{obs}} = N$ for our largest R) simply consists of subtracting the two (aligned) curves from each other.

²⁷Here we have applied a dynamical correction to the volume as the gas heats, assuming the power-law shape of our trap (see also Section 7.1.1). For a sense of scale, within this model a change of E by a factor of 3 leads to a change in volume by $3^{3/15} \approx 24\%$.

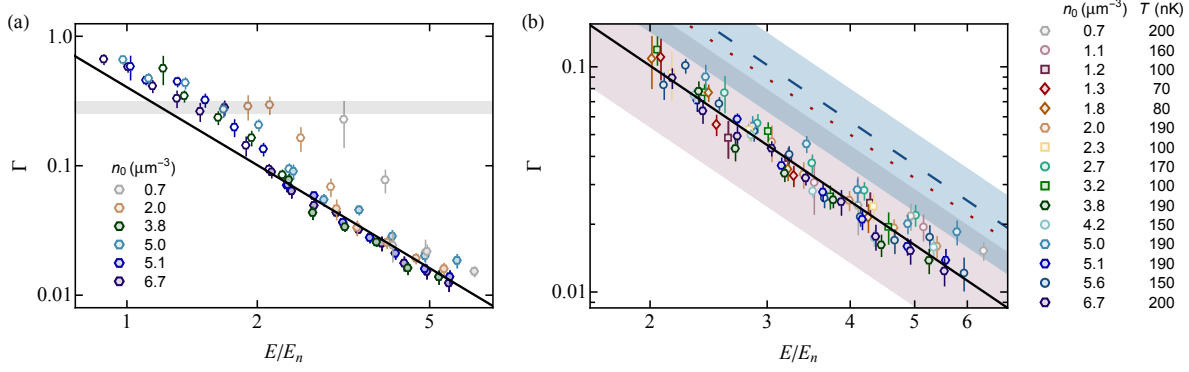


Fig. 7.17 Loss dynamics of thermal Bose gases quenched to unitarity. (a) Dimensionless loss rate Γ versus E/E_n for data with varying n_0 but essentially constant initial $T \approx 200$ nK. The solid line shows the expected result for three-body recombination in a thermal unitary gas $\Gamma \propto (E_n/E)^2$, in excellent agreement with the long-time data [$t_{\text{hold}} > 2\sqrt{t_{n_0}t_\lambda}$, filled symbols]. At early times [$t_{\text{hold}} < 2\sqrt{t_{n_0}t_\lambda}$, open symbols], we observe enhanced three-body loss compared to the long-time extrapolation, and a peculiar dependence on n_0 , with the lowest phase-space density gases showing the most dramatic deviations from the long-time behavior. (b) Dimensionless loss rate Γ versus E/E_n , focusing only on long times ($t_{\text{hold}} > 2\sqrt{t_{n_0}t_\lambda}$) after the quench when the gas is essentially in equilibrium. Our data is described well by $\Gamma \propto (E_n/E)^2$ [solid line]. The dotted line corresponds to our degenerate gas result from Fig. 7.7, and while the absolute values differ, the two measurements are in agreement taking into account systematic uncertainties in box volume; the red shaded region depicts a $\pm 10\%$ uncertainty in the linear box size. The dashed line shows the previously measured loss rate from [321], and the blue shaded region its systematic uncertainty.

to facilitate comparison with our degenerate gas data, where we recall that $\zeta_3 = (1 - e^{-4\eta^*})$ and η^* is the Efimov width parameter (see Section 7.1.2).

In Fig. 7.17(a) we plot Γ versus E/E_n on log-log scale comparing data series with approximately constant $T \approx 0.2$ μK but varying n_0 , at all times after the quench. At long times when the gas has reached an equilibrium state $t_{\text{hold}} > 2\sqrt{t_{n_0}t_\lambda}$ (filled symbols) we observe excellent agreement between the data which follow the expected $\Gamma \propto (E_n/E)^{-2}$ scaling expected for three-body recombination heating of a thermal-unitary Bose gas. At early times ($t_{\text{hold}} < 2\sqrt{t_{n_0}t_\lambda}$, open symbols) we observe somewhat enhanced losses, with a rather peculiar feature that low phase-space density data deviate most dramatically. We currently do not understand the reason for this behavior, but it could be an indication for Efimov physics breaking universality.

In Fig. 7.17(b) we turn our attention exclusively to the long-time behavior ($t_{\text{hold}} > 2\sqrt{t_{n_0}t_\lambda}$), and plot the extracted Γ versus E/E_n for all our 15 data series (see legend). We find that this collapses all our data onto a single universal curve, in agreement with the anticipated scaling law $\Gamma \propto (E_n/E)^2$. The solid line shows the best fit value to the data, which would suggest that $\zeta_3 \approx 0.13$, and a remarkably low corresponding $\eta^* \approx 0.03$. However, our $\sim \pm 10\%$ systematic uncertainties in the linear box dimension lead to relatively large systematic uncertainties in ζ_3 (red band). Our measurement is consistent with our previous result for initially degenerate gases that have heated to become thermal (dotted line, see Section 7.2), which feature similar systematic uncertainties. Overall, our measurements are in good agreement with previous

measurement of the thermal unitarity-limited loss rate coefficient ζ_3 for our ^{39}K state, which found $\eta^* = 0.09(4)$ [321] (dashed line, and corresponding blue shaded region).

7.4 Conclusion

In conclusion, we have performed a detailed study of both degenerate and thermal Bose gases quenched to unitarity. Our experiments establish a comprehensive view of the prethermal dynamics and thermodynamics at both low and high temperatures, providing benchmarks for the theory, and uncovering new conceptual puzzles. They reveal remarkably robust universal behavior, which would be interesting to further test by performing the same quench experiments using a far-from-equilibrium initial state, such as a turbulent gas.

Focusing particularly on the degenerate unitary Bose gas (where our understanding is still in its infancy), our experiments unveiled three key facts that make further exploration of this system promising:

1. The post-quench dynamics reveal that the gas, even though not in true thermal equilibrium, does attain a well-defined quasi-equilibrium (prethermal) state.
2. The quench-induced correlation energy is on the order of E_n , indicating that this is a strongly-correlated state.
3. The prethermal unitary gas has a non-zero condensed fraction, of about 20%, suggesting that it may be a novel kind of superfluid.

The reason that such a superfluid state may be truly unique is that Efimov physics is thought to play a fundamental role in the gas's behavior. Experiments using unitary thermal Bose gases have recently revealed few-body signatures of such novel three-body correlations [65]. A major experimental goal is finding out whether these states also have a profound impact on the many-body state at low temperature, where theorists have predicted the formation of a molecular superfluid state consisting of Efimov trimers [319]. In the future we hope to devise spectroscopic and interferometric measurements that reveal and probe this exciting new state of matter.

8 Outlook

Libiamo, libiamo ne'lieti calici

La Traviata

- Giuseppe Verdi -

Throughout our four experimental chapters we delved into fundamental quantum many-body physics, exploring interacting Bose gases both in and out of equilibrium. Our experiments operate at the interface of theory and experiment, providing invaluable input for theoretical discourse, in the true spirit of quantum simulation. We have reaped the benefits of our quasi-uniform optical box potential as well as our ability to precisely control the interparticle interactions. Having already provided detailed summaries of the experiments and our more immediate future goals within each chapter, here we take a step back and consider a few possible future research avenues, which leverage the key advantages of our experimental platform.

Critical dynamics. It would be interesting to investigate how interactions affect the critical behavior near the (second-order) Bose–Einstein condensation phase transition. In general, close to such a phase transition the details of the short-range physics become unimportant and all systems can be classified into just a few categories known as universality classes, according to their generic properties such as symmetries, dimensionality, and type of interaction [387]. This was previously studied in our group using ^{87}Rb in a box [186] (see also [388]), and alongside two other experiments [23,389] comprehensively explored and validated the Kibble-Zurek mechanism [390,391], obtaining unprecedented access to the critical exponents of the BEC phase transition [392]. We intend on extending these experiments, making use of our readily tuneable interaction strength. A particularly intriguing issue is that the ideal and interacting Bose gas are in different universality classes. Experimentally, we are able to continuously tune the interaction strength from interacting to non-interacting, raising the question: can one actually change the universality class of a system, and if so, how does this change occur?

Critical temperature shift. In a homogeneous Bose gas, quantum correlations close to the critical point are believed to aid condensation. While mostly accepted today, this theoretical consensus emerged after an over 50-year-long debate (see *e.g.* [393–396]), following the pioneering work of Lee and Yang [43, 397]. The beyond-mean-field contribution has been observed indirectly in harmonically trapped Bose gases [398], but a direct experimental observation remains absent. Our experimental platform offers a promising setting to observe this interaction-induced shift directly, which is expected to scale as

$$\frac{\Delta T_c}{T_c^0} \approx 1.8 \frac{a}{\lambda}. \quad (8.1)$$

Observing such (typically few %) shifts will require high-precision differential measurements and perhaps even improvements to the uniformity of our quasi-uniform potential (if the relevant quantity for comparison is the shift ΔT_c , rather than T_c itself).

Space-borne homogeneous Bose–Einstein condensates with tuneable interactions. A major limitation in our experiments is the need to compensate the gravitational force to ensure a homogeneous trapping potential. A natural (albeit technically non-trivial) solution to this is to perform the experiments in outer space, which enjoys a low-gravity environment. The first BEC was recently created in space [399], with its sights on precision interferometry. Letting our imagination flow, here we outline a few particularly exciting prospects for using our experimental platform in such a low-gravity environment (entirely neglecting technical challenges). It would significantly relax the inherent ‘size-limit’ of our boxes (to ensure sample homogeneity). This would in turn allow for vast experimentally accessible density ranges (in particular towards lower densities). Such low densities would be invaluable in reducing three-body recombination compared to the effect of beyond-mean-field correlations (recall Chapter 6). To name a few particularly exciting prospects, it would be a remarkable setting for studying quantum turbulence, spin mixtures, and the unitary regime.

A Cross-calibration of the zero-crossing of a

The measurements in Section 5.3.1 used the collapse of a Bose–Einstein condensate to measure $a(B_0)$, the zero crossing of the Feshbach resonance at $B_\infty = 402.70(3)$ G [65] in the ^{39}K $|1, 1\rangle$ state. To measure B_0 , we extrapolated the critical point for collapse to the $1/N \rightarrow 0$ limit, obtaining $B_0 = 350.45(3)$ G, where we calibrated the absolute field strength using rf-spectroscopy. This result was found to be in good agreement with previous measurements [83, 243, 244], and corresponds to a resonance width $\Delta = -52.25(4)$ G.

Here we present an independent measurement of the zero crossing using the evaporation of a thermal Bose gas. We initially prepare an equilibrium thermal cloud of $N \approx 1 \times 10^5$ atoms at a temperature of ≈ 200 nK at $\approx 200 a_0$. We then ramp the scattering length to a final value a over 200 ms before lowering the trap depth by a factor of ≈ 6 in 3 s and subsequently waiting for an additional 27 s. We finally image the cloud after 30 ms ToF expansion. In Fig. A.1 we plot the cloud’s energy per particle E versus a , where we assume our previous calibration of the Feshbach resonance to convert to a . A clear symmetric peak in E is observed, which arises from the failure of the gas to thermalize during evaporation as scattering events become too infrequent. The peak is centered at $-0.05(8) a_0$, thus cross-validating our previous measurement.

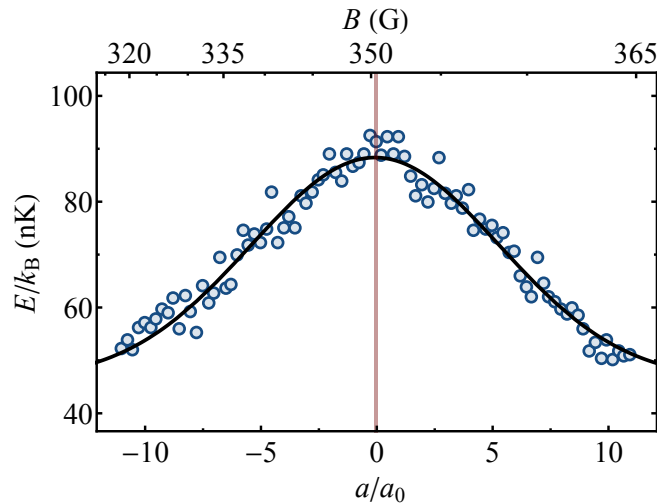


Fig. A.1 Cross-calibration of the zero crossing of a in the lowest hyperfine state. We plot the energy per particle of a thermal cloud after evaporation at a variable scattering length a (see text for details). A clear peak is observed around $a \approx 0$ as scattering events become too rare for the gas to thermalize. The solid line is a gaussian fit to the data, which gives the center position $-0.05(8) a_0$ (red vertical band), consistent with zero and thus cross-validating the previous independent calibration using the collapse of a BEC (see Section 5.3.1).

B Atom number control & stability

The data supporting our results typically consist of tens of thousands of experimental repetitions spread over months. Hence, a particularly important aspect is the control and stability of the initial atom number N_0 in our experiments, which we provide benchmarks for below.

To reduce the otherwise maximal achievable N_0 [which varies between $(2 - 3) \times 10^5$ depending on how well previous cooling/preparation steps work] we use three-body losses at the end of evaporation in the ODT (before loading into the box). Experimentally, we vary the B field (and hence a) at the end of evaporation using the control voltage V_{FeshODT} to vary N_0 [see Fig. B.1(a)]. The exact value of V_{FeshODT} needed to produce the same average N_0 , does vary slightly from day to day (as previous cooling steps may be more or less efficient), but this is readily adjusted for by tweaking V_{FeshODT} .

In Fig. B.1(b) we plot N_0 as a function of time during continuous operation on three separate days¹, intending to achieve the same $N_0 \approx 9.8 \times 10^4$. While the repetition rate here was 31.7 s, we only sample N_0 twice every 98 repetitions (0.86 hours)². We see only minimal drifts in N_0 over time, and averaging gives $\{9.6, 9.8, 9.8\} \times 10^4$ (for the three series), with a standard deviation of 0.3×10^4 ($\approx 3\%$). We are typically able to continuously run for up to ~ 50 hours before we need to replenish our MOT using the getters (though this varies based on the desired N_0 ; lower/higher N_0 are stable for longer/shorter durations).

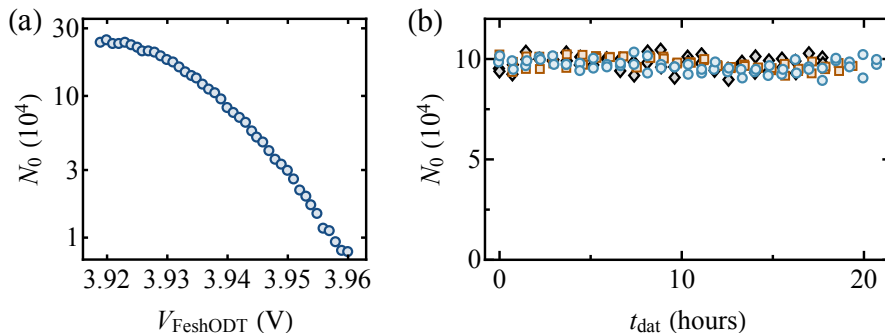


Fig. B.1 Atom number control and stability. (a) Quasi-pure homogeneous BEC atom number N_0 versus control voltage V_{FeshODT} , which sets a at the end of evaporation (in the ODT). (b) N_0 as a function of time during continuous operation (N_0 is sampled only in a subset of the data series which started at $t_{\text{dat}} = 0$, see text).

¹We restrict ourselves to three for visual clarity.

²These data correspond to a subset of those in which we explore the unitary regime (see Chapter 7). Out of the full data series, consisting of ~ 2000 images each, we have removed $\lesssim 0.5\%$ in post-selection, corresponding primarily to blank images (where it is clear that one of the preparation steps was erroneous).

C Inverse-Abel transform

We use an inverse-Abel transform to reconstruct the three-dimensional momentum distribution \tilde{n}_k from the line-of-sight integrated density profile n_{2D} that our absorption images provide. In the cases where the distribution is spherically symmetric (as satisfied for our uses), we can consider the azimuthally averaged $\tilde{n}_{2D}(\bar{k}) = F(\bar{k})$ without the loss of information. Formally, for a function $f(k)$, which drops to zero faster than $1/k$, the inverse-Abel transform is

$$f(k) = -\frac{1}{\pi} \int_k^\infty \frac{dF}{d\bar{k}} \frac{d\bar{k}}{\sqrt{\bar{k}^2 - k^2}}. \quad (\text{C.1})$$

We implement this procedure numerically, converting the integral to a sum (as the measured $F(\bar{k})$ is discretized, with $\bar{k}_i \in \{\bar{k}_1, \bar{k}_2, \dots, \bar{k}_{m-1}, \bar{k}_m\}$), and numerically differentiating $F(\bar{k})$. We also separate out the first term in the sum (at k) and analytically approximate its contribution to tame the otherwise potentially divergent behavior (in the presence of statistical noise).

D Field control & stability

Here we give an overview of our field stability and control, with particular emphasis on our field quenches into the unitary regime (relevant for Chapter 7).

D.1 Mains oscillation

The coils used to create the magnetic field that the atoms experience (see Fig. 3.2) are driven by power-supplies connected to the three-phase 50 Hz alternating-current mains. This unfortunately feeds into the fields that they produce, and leads to a modulation of B as a function of time (with 20 ms overall period)¹. The variation in field is of order 100 mG, which is significantly larger than other technical limitations [*e.g.* typical field drifts over the course of a day of order ~ 10 mG, or the variation across the cloud from the field gradient 6.855 G/cm used to compensate gravity (corresponding to ≈ 34 mG across 50 μm)].

While typically negligible at low a [where (i) the percentage modulation in a is small, and (ii) the cloud's intrinsic timescales are much longer so that this averages out], it is a major issue upon approaching the Feshbach resonance as well as for field-sensitive spectroscopy at all a ².

As a starting point for tackling this problem, we externally trigger on the mains cycle, which synchronizes our experimental clock to it (by waiting for it in the sequence). This solves the main aspect of the spectroscopy problem, as it hampers the shot-to-shot field variations arising from the oscillation over the course of the short ($\lesssim 100$ μs) pulses. We can now map out the oscillation in detail, by varying the time t_{trig} following the trigger and performing high-resolution rf-spectroscopy to measure B (see Section 3.2.3). In Fig. D.1 we plot B , normalized by its average over the full range of data, revealing a striking oscillation. We fit the data with a function of the form

$$\sum_{j=1}^{10} c_j \sin(2\pi \nu_0 j t_{\text{trig}} + \phi_j), \quad (\text{D.1})$$

with $\nu_0 = 50$ Hz and where c_j and ϕ_j are fitting parameters. This captures the data excellently, confirming the higher-multiple-of- ν_0 frequency components in the oscillation (it is also

¹A solution to this would be to run the coils on batteries, which we are contemplating as an upgrade.

²Two prime examples are rf-spectroscopy (see Section 3.2.3) and molecular dimer spectroscopy, where the binding energy $E_b \approx -\hbar^2/(ma^2)$ (see *e.g.* [365]).

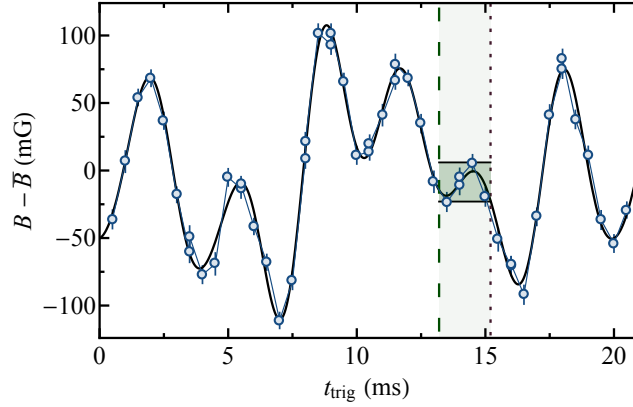


Fig. D.1 Mains oscillation. We plot the measured field variation (B around its mean \bar{B}) as a function of time t_{trig} following an external trigger to synchronize with the mains cycle (see text). We identify a 2 ms window following $t_{\text{trig}} = 13.2$ ms (dashed line), over which the field changes by $\lesssim 30$ mG. Field-sensitive experiments, in particular those quenching into the unitary regime (see Chapter 7), are always performed in this region. For experiments that are longer, we inadvertently sample the oscillation.

consistent with a Fourier analysis). The multiple-frequency components most likely arise due to coupling between our different power-supplies used to control B , but the exact form is not important here. We identify a 2 ms window following $t_{\text{trig}} = 13.2$ ms where the field changes by $\lesssim 30$ mG. We use this trigger at $t_{\text{trig}} = 13.2$ ms in all experiments that do not inevitably average over this oscillation [*i.e.* where the critically sensitive part of the experiment occurs in $\ll 20$ ms]³.

D.2 Dynamical field control

Throughout this thesis we rely on dynamical control of the magnetic field, and consequently *a*. The response time of the Feshbach coils (in conjunction with the entourage of coils striving to maintain gravity compensation, from here on collectively referred to as primary coils) is limited to a few milliseconds, but is still typically suitable for our experiments. However, for our experiments at unitarity, this is far too slow, and we instead rely on a set of auxiliary ‘fast’ coils to perform rapid field quenches (on μs timescales). In the following we first characterize the response time of our slower primary field ramps, before detailing and benchmarking our quenches to unitarity.

³This curve was measured continuously over a ≈ 12 hour period; each point corresponds to the center frequency of a 31-point rf-spectrum, and the data were taken in randomized order). It therefore also acts as a measure of our field stability, which is typically better than ± 10 mG over the course of a day (weekends and nights are best), and a long warm-up period (> 3 hours) is typically necessary. We have also re-measured this curve several times (months apart) and never observed a statistically significant difference.

D.2.1 Primary field response time

A prevalent situation in which we wish to push the primary field response time to the limit is for turning off interactions during ToF⁴. Such primary coil ramps are also at the heart of our quench experiments exploring collapse dynamics (see Chapter 5).

In Fig. D.2 we plot B (measured using rf-spectroscopy) following a quench (initiated at $t = 0$) using our primary coils. The example we provide corresponds to a typical measurement in which we wish to rapidly turn off the interactions for ToF. The blue circles depict the result if we simply dial in an instantaneous quench (setting the control voltage V_c to its final value, see blue line in inset). We obtain a slight improvement in the response time by programming in an ‘overshoot’ (red circles, see also inset). The magnitude of such controlled field quenches (here rather large at ≈ 50 G) does not significantly affect the response time, though we do achieve significantly faster response times when entirely turning off the coils ($\lesssim 1$ ms).

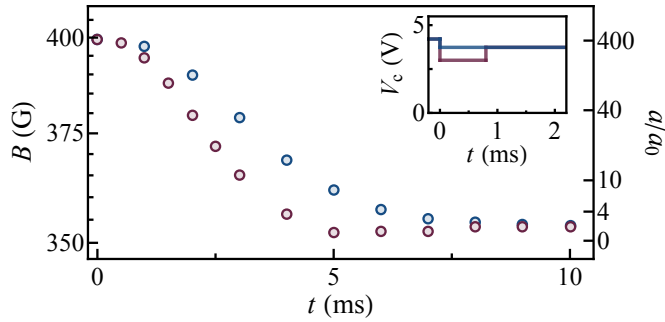


Fig. D.2 Field response following a quench using our primary coils. The quench is initiated at $t = 0$ and the field is measured using rf-spectroscopy as a function of t for two quench protocols depicted in the inset and described in the text.

D.2.2 Quenches to unitarity

To reach the unitary regime we use a set of strategically placed auxiliary coils (a.k.a. ‘fast coils’) that avoid significant inductive coupling to the Feshbach coils, thus minimizing eddy currents and allowing for field switching on μs timescales. The auxiliary coils are powered by a Elektroautomatik PS9360-30 1U supply, and for switching we use an H-bridge circuit (see Fig. D.3), which was designed, built, and tested by Jake Glidden [86]; here we only summarize key features. Using the H-bridge we can isolate the coil from the supply for switch-off, so that the energy stored in the magnetic field can be dissipated over the the sum of the auxiliary coil’s internal resistance and R_2 . The on/off configurations of the H-bridge form a simple RL circuit, for which we expect exponential transient behavior, characterized by a rise time τ_{in} and a fall

⁴This for example allows for more accurate measurements of the momentum distribution by avoiding contamination from the conversion of interaction to kinetic energy in ToF. Note that we can also achieve this more rapidly ($\approx 60 \mu\text{s}$) using an rf spin-flip to $|1, 0\rangle$, though this is not always convenient or possible.

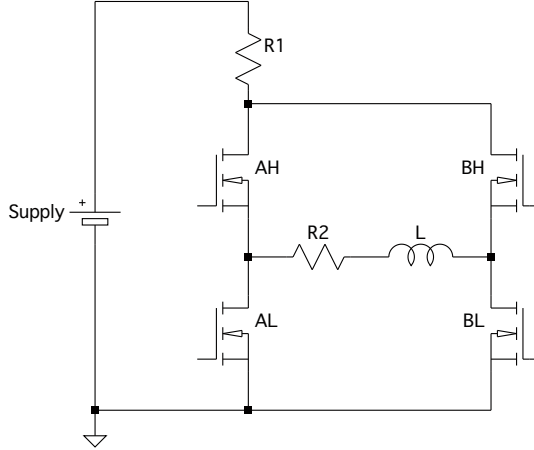


Fig. D.3 Schematic of the H-bridge circuit used for rapid field switching. We highlight only the core components of the circuit, which are the power supply, two resistors (R_1 and R_2), four n -channel IXFN48N50 MOSFETS (denoted AH, AL, BH, and BL), and our set of auxiliary coils (denoted L). The circuit is driven using a pair of half-bridge FAN7380 drivers; figure from [86], where additional details are available.

time τ_Q . Moreover, keeping the sum $R_{\text{tot}} = R_1 + R_2$ fixed allows us to fix τ_{in} while varying τ_Q .

The field probes that we currently have access to do not allow for a detailed characterization of the response times⁵, and instead we characterize the ramp speeds using the current in coil. We however do measure the field using rf-spectroscopy at unitarity (once it has settled)⁶.

As exemplified in Fig. D.4 (for two different initial ramp-out rates $\mathcal{R} = \Delta B/\tau_Q$), the measured current I_q shows an exponential rise/fall as a function of t (we show examples of a typical quench into the unitary regime with $t_{\text{hold}} = 20 \mu\text{s}$)⁷. The two different τ_Q are achieved using a fixed $R_{\text{tot}} = 10 \Omega$, using either $R_2 = R_{\text{tot}}$ or $R_2 = 0$. This gives access to values of τ_Q in the range (1-10) μs ; Table D.1 summarizes the measured τ_Q for different combinations of R_1 and R_2 .

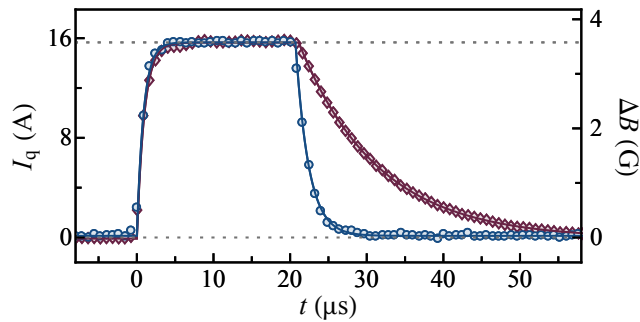


Fig. D.4 Current response of the fast coils used for quenches to unitarity. Here we use an on-resonance hold time $t_{\text{hold}} = 20 \mu\text{s}$, and calibrate the field jump magnitude ΔB using rf-spectroscopy at unitarity (the conversion as a function of time assumes proportionality with I_q).

⁵We intend on implementing two-photon Raman spectroscopy between $|1, 1\rangle$ and $|1, 0\rangle$, in order to both provide a faster field probe and allow for rapid spin-flips (competitive with μs time scales).

⁶For this purpose we typically work with low densities ($\approx 0.3 \mu\text{m}^{-3}$) to mitigate any risk of significant potential rf-resonance shifts of order E_n/\hbar .

⁷The low duty cycle ($\lesssim 10^{-4}$) ensures that the coils do not burn; we also include a fuse in the circuit to avoid disasters (it works).

Table D.1: Resulting τ_Q for different combinations of R_1 and R_2 , with $R_{\text{tot}} = 10 \Omega$ to maintain $\tau_{\text{in}} \approx 1 \mu\text{s}$. The uncertainty in τ_Q is $\approx 0.2 \mu\text{s}$.

$R_1 (\Omega)$	$R_2 (\Omega)$	$\tau_Q (\mu\text{s})$
10.0	0.0	10.2
9.0	1.0	4.5
7.4	2.6	3.0
6.6	3.4	2.3
0.0	10.0	1.2

We use rf-spectroscopy to calibrate the field at unitarity, an example of which is shown in Fig. D.5 as a function of t_{hold} (using a $30 \mu\text{s}$ rf pulse). We see that within the experimentally accessible range of times⁸ the field is essentially constant at B_∞ (within its uncertainty).

For our field calibration at unitarity we measure the field at early times (in the first $50 \mu\text{s}$) by performing rf-spectroscopy at unitarity with low-density samples. While our primary coils are used to set the field before the quench, we do slightly tweak ΔB (by up to $\approx 30 \text{ mG}$) for final adjustments to ensure we always start within $\delta B \approx 20 \text{ mG}$ of B_∞ before starting long data series. We always measure the field again after the run has finished (and occasionally also in-between) and retain only those data where subsequent field measurements lie within $\delta B < 40 \text{ mG}$ of B_∞ .

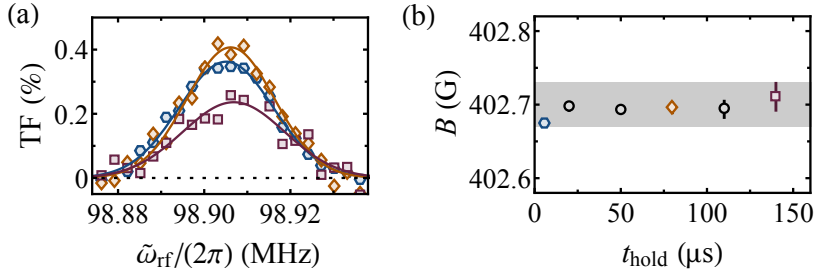


Fig. D.5 Field stability at unitarity. (a) Radio-frequency spectra showing the transferred fraction of clouds at various on-resonance t_{hold} , using a $30 \mu\text{s}$ rf pulse. (b) Measured field as a function of t_{hold} at unitarity, confirming that the field is constant to within 30 mG over $> 150 \mu\text{s}$, the most critical time frame in our experiments.

⁸We cannot currently accurately measure much long times as the clouds decay and heat significantly, diminishing our signal which relies on Stern–Gerlach separation of the spin components. State-selective imaging would improve this (though we have no reason to expect any significant changes for $t_{\text{hold}} < 2 \text{ ms}$).

Bibliography

- [1] P. W. Anderson, 'More Is Different', *Science* **177**, 393 (1972).
- [2] M. Eigen, *From Strange Simplicity to Complex Familiarity*, Oxford University Press (2013).
- [3] M. H. Anderson, J. R. Ensher, M. R. Matthews, C. E. Wieman, and E. A. Cornell, 'Observation of Bose–Einstein Condensation in a Dilute Atomic Vapor', *Science* **269**, 198 (1995).
- [4] K. B. Davis, M. O. Mewes, M. R. Andrews, N. J. van Druten, D. S. Durfee, D. M. Kurn, and W. Ketterle, 'Bose-Einstein Condensation in a Gas of Sodium Atoms', *Phys. Rev. Lett.* **75**, 3969 (1995).
- [5] C. A. Regal, M. Greiner, and D. S. Jin, 'Observation of Resonance Condensation of Fermionic Atom Pairs', *Phys. Rev. Lett.* **92**, 040403 (2004).
- [6] R. P. Feynman, 'Simulating physics with computers', *Int. J. Theor. Phys.* **21**, 467 (1982).
- [7] C. Chin, R. Grimm, P. Julienne, and E. Tiesinga, 'Feshbach resonances in ultracold gases', *Rev. Mod. Phys.* **82**, 1225 (2010).
- [8] C. Pethick and H. Smith, *Bose–Einstein Condensation in Dilute Gases*, Cambridge University Press (2002).
- [9] I. Bloch, 'Ultracold quantum gases in optical lattices', *Nat. Phys.* **1**, 23 (2005).
- [10] I. Bloch, J. Dalibard, and W. Zwerger, 'Many-body physics with ultracold gases', *Rev. Mod. Phys.* **80**, 885 (2008).
- [11] M. Inguscio, W. Ketterle, and C. Salomon (eds.), *Ultracold Fermi Gases, Proceedings of the International School of Physics "Enrico Fermi"*, Course CLXIV (2007).
- [12] W. Zwerger (ed.), *BCS-BEC Crossover and the Unitary Fermi Gas*, Springer (2011).
- [13] J. Dalibard, F. Gerbier, G. Juzeliūnas, and P. Öhberg, 'Colloquium: Artificial gauge potentials for neutral atoms', *Rev. Mod. Phys.* **83**, 1523 (2011).
- [14] I. Bloch, J. Dalibard, and S. Nascimbène, 'Quantum simulations with ultracold quantum gases', *Nat. Phys.* **8**, 267 (2012).
- [15] D. M. Stamper-Kurn and M. Ueda, 'Spinor Bose gases: Symmetries, magnetism, and quantum dynamics', *Rev. Mod. Phys.* **85**, 1191 (2013).
- [16] M. W. Zwierlein, 'Superfluidity in ultracold atomic Fermi gases', in 'Novel Superfluids: Volume 2', (edited by K.-H. Bennemann and J. B. Ketterson), Oxford University Press (2014).
- [17] L. Pitaevskii and S. Stringari, *Bose–Einstein condensation and superfluidity*, Oxford University Press (2016).
- [18] F. Chevy and C. Salomon, 'Strongly correlated Bose gases', *J. Phys. B* **49**, 192001 (2016).
- [19] N. Proukakis, D. Snoke, and P. Littlewood (eds.), *Universal Themes of Bose–Einstein Condensation*, Cambridge University Press (2017).

- [20] N. R. Cooper, J. Dalibard, and I. B. Spielman, ‘*Topological bands for ultracold atoms*’, *Rev. Mod. Phys.* **91**, 015005 (2019).
- [21] A. L. Gaunt, T. F. Schmidutz, I. Gotlibovych, R. P. Smith, and Z. Hadzibabic, ‘*Bose–Einstein Condensation of Atoms in a Uniform Potential*’, *Phys. Rev. Lett.* **110**, 200406 (2013).
- [22] C. Eigen, ‘*Realization of a Homogeneous Bose Gas with Tunable Interactions*’, Master’s thesis, University of Cambridge (2015).
- [23] L. Chomaz, L. Corman, T. Bienaimé, R. Desbuquois, C. Weitenberg, S. Nascimbène, J. Beugnon, and J. Dalibard, ‘*Emergence of coherence via transverse condensation in a uniform quasi-two-dimensional Bose gas*’, *Nat. Commun.* **6**, 6162 (2015).
- [24] B. Mukherjee, Z. Yan, P. B. Patel, Z. Hadzibabic, T. Yefsah, J. Struck, and M. W. Zwierlein, ‘*Homogeneous Atomic Fermi Gases*’, *Phys. Rev. Lett.* **118**, 123401 (2017).
- [25] K. Hueck, N. Luick, L. Sobirey, J. Siegl, T. Lompe, and H. Moritz, ‘*Two-Dimensional Homogeneous Fermi Gases*’, *Phys. Rev. Lett.* **120**, 060402 (2018).
- [26] C. Eigen, A. L. Gaunt, A. Suleymanzade, N. Navon, Z. Hadzibabic, and R. P. Smith, ‘*Observation of Weak Collapse in a Bose–Einstein Condensate*’, *Phys. Rev. X* **6**, 041058 (2016).
- [27] N. Navon, C. Eigen, J. Zhang, R. Lopes, A. L. Gaunt, K. Fujimoto, M. Tsubota, R. P. Smith, and Z. Hadzibabic, ‘*Synthetic dissipation and cascade fluxes in a turbulent quantum gas*’, *Science* **366**, 382 (2019).
- [28] R. Lopes, C. Eigen, A. Barker, K. G. H. Viebahn, M. Robert-de Saint-Vincent, N. Navon, Z. Hadzibabic, and R. P. Smith, ‘*Quasiparticle Energy in a Strongly Interacting Homogeneous Bose–Einstein Condensate*’, *Phys. Rev. Lett.* **118**, 210401 (2017).
- [29] R. Lopes, C. Eigen, N. Navon, D. Clément, R. P. Smith, and Z. Hadzibabic, ‘*Quantum Depletion of a Homogeneous Bose–Einstein Condensate*’, *Phys. Rev. Lett.* **119**, 190404 (2017).
- [30] C. Eigen, J. A. P. Glidden, R. Lopes, N. Navon, Z. Hadzibabic, and R. P. Smith, ‘*Universal Scaling Laws in the Dynamics of a Homogeneous Unitary Bose Gas*’, *Phys. Rev. Lett.* **119**, 250404 (2017).
- [31] C. Eigen, J. A. P. Glidden, R. Lopes, E. A. Cornell, R. P. Smith, and Z. Hadzibabic, ‘*Universal prethermal dynamics of Bose gases quenched to unitarity*’, *Nature* **563**, 221 (2018).
- [32] C. J. Foot, *Atomic Physics*, Oxford University Press (2005).
- [33] M. Zaccanti, B. Deissler, C. D’Errico, M. Fattori, M. Jona-Lasinio, S. Müller, G. Roati, M. Inguscio, and G. Modugno, ‘*Observation of an Efimov spectrum in an atomic system*’, *Nat. Phys.* **5**, 586 (2009).
- [34] V. Efimov, ‘*Energy levels arising from resonant two-body forces in a three-body system*’, *Phys. Lett. B* **33**, 563 (1970).
- [35] E. Braaten and H.-W. Hammer, ‘*Efimov physics in cold atoms*’, *Ann. Phys.* **322**, 120 (2007).
- [36] F. Werner and Y. Castin, ‘*General relations for quantum gases in two and three dimensions. II. Bosons and mixtures*’, *Phys. Rev. A* **86**, 053633 (2012).
- [37] J. W. Gibbs, *Elementary principles in statistical mechanics*, Yale University Press (1902).
- [38] S. N. Bose, ‘*Plancks Gesetz und Lichtquantenhypothese*’, *Z. Phys.* **26**, 178 (1924).

- [39] A. Einstein, 'Zur Quantentheorie des idealen Gases', *Sitzungsberichte der Preussischen Akademie der Wissenschaften* **3**, 18 (1925).
- [40] J. R. Taylor, *Scattering Theory*, John Wiley & Sons (1972).
- [41] S. J. Garratt, C. Eigen, J. Zhang, P. Turzák, R. Lopes, R. P. Smith, Z. Hadzibabic, and N. Navon, 'From single-particle excitations to sound waves in a box-trapped atomic Bose-Einstein condensate', *Phys. Rev. A* **99**, 021601 (2019).
- [42] N. N. Bogoliubov, 'On the theory of superfluidity', *J. Phys. (USSR)* **11**, 23 (1947).
- [43] T. D. Lee and C. N. Yang, 'Many-Body Problem in Quantum Mechanics and Quantum Statistical Mechanics', *Phys. Rev.* **105**, 1119 (1957).
- [44] T. D. Lee, K. Huang, and C. N. Yang, 'Eigenvalues and Eigenfunctions of a Bose System of Hard Spheres and Its Low-Temperature Properties', *Phys. Rev.* **106**, 1135 (1957).
- [45] N. Navon, S. Nascimbène, F. Chevy, and C. Salomon, 'The Equation of State of a Low-Temperature Fermi Gas with Tunable Interactions', *Science* **328**, 729 (2010).
- [46] N. Navon, S. Piatecki, K. Günter, B. Rem, T. C. Nguyen, F. Chevy, W. Krauth, and C. Salomon, 'Dynamics and Thermodynamics of the Low-Temperature Strongly Interacting Bose Gas', *Phys. Rev. Lett.* **107**, 135301 (2011).
- [47] S. Tan, 'Energetics of a strongly correlated Fermi gas', *Ann. Phys.* **323**, 2952 (2008).
- [48] S. Tan, 'Large momentum part of a strongly correlated Fermi gas', *Ann. Phys.* **323**, 2971 (2008).
- [49] S. Tan, 'Generalized virial theorem and pressure relation for a strongly correlated Fermi gas', *Ann. Phys.* **323**, 2987 (2008).
- [50] E. Braaten and L. Platter, 'Exact Relations for a Strongly Interacting Fermi Gas from the Operator Product Expansion', *Phys. Rev. Lett.* **100**, 205301 (2008).
- [51] E. Braaten, D. Kang, and L. Platter, 'Universal relations for a strongly interacting Fermi gas near a Feshbach resonance', *Phys. Rev. A* **78**, 053606 (2008).
- [52] S. Zhang and A. J. Leggett, 'Universal properties of the ultracold Fermi gas', *Phys. Rev. A* **79**, 023601 (2009).
- [53] R. Haussmann, M. Punk, and W. Zwerger, 'Spectral functions and rf response of ultracold fermionic atoms', *Phys. Rev. A* **80**, 063612 (2009).
- [54] F. Werner and Y. Castin, 'General relations for quantum gases in two and three dimensions: Two-component fermions', *Phys. Rev. A* **86**, 013626 (2012).
- [55] E. D. Kuhnle, H. Hu, X.-J. Liu, P. Dyke, M. Mark, P. D. Drummond, P. Hannaford, and C. J. Vale, 'Universal Behavior of Pair Correlations in a Strongly Interacting Fermi Gas', *Phys. Rev. Lett.* **105**, 070402 (2010).
- [56] J. T. Stewart, J. P. Gaebler, T. E. Drake, and D. S. Jin, 'Verification of Universal Relations in a Strongly Interacting Fermi Gas', *Phys. Rev. Lett.* **104**, 235301 (2010).
- [57] S. Nascimbène, N. Navon, K. J. Jiang, F. Chevy, and C. Salomon, 'Exploring the thermodynamics of a universal Fermi gas', *Nature* **463**, 1057 (2010).
- [58] Y. Sagi, T. E. Drake, R. Paudel, R. Chapurin, and D. S. Jin, 'Breakdown of the Fermi Liquid Description for Strongly Interacting Fermions', *Phys. Rev. Lett.* **114**, 075301 (2015).

- [59] S. Laurent, M. Pierce, M. Delehay, T. Yefsah, F. Chevy, and C. Salomon, 'Connecting Few-Body Inelastic Decay to Quantum Correlations in a Many-Body System: A Weakly Coupled Impurity in a Resonant Fermi Gas', *Phys. Rev. Lett.* **118**, 103403 (2017).
- [60] C. Carcy, S. Hoinka, M. G. Lingham, P. Dyke, C. C. N. Kuhn, H. Hu, and C. J. Vale, 'Contact and Sum Rules in a Near-Uniform Fermi Gas at Unitarity', *Phys. Rev. Lett.* **122**, 203401 (2019).
- [61] B. Mukherjee, P. B. Patel, Z. Yan, R. J. Fletcher, J. Struck, and M. W. Zwierlein, 'Spectral Response and Contact of the Unitary Fermi Gas', *Phys. Rev. Lett.* **122**, 203402 (2019).
- [62] R. Combescot, F. Alzetto, and X. Leyronas, 'Particle distribution tail and related energy formula', *Phys. Rev. A* **79**, 053640 (2009).
- [63] E. Braaten, D. Kang, and L. Platter, 'Universal Relations for Identical Bosons from Three-Body Physics', *Phys. Rev. Lett.* **106**, 153005 (2011).
- [64] R. J. Wild, P. Makotyn, J. M. Pino, E. A. Cornell, and D. S. Jin, 'Measurements of Tan's Contact in an Atomic Bose-Einstein Condensate', *Phys. Rev. Lett.* **108**, 145305 (2012).
- [65] R. J. Fletcher, R. Lopes, J. Man, N. Navon, R. P. Smith, M. W. Zwierlein, and Z. Hadzibabic, 'Two- and three-body contacts in the unitary Bose gas', *Science* **355**, 377 (2017).
- [66] T. Kraemer, M. Mark, P. Waldburger, J. G. Danzl, C. Chin, B. Engeser, A. D. Lange, K. Pilch, A. Jaakkola, H.-C. Nägerl, and R. Grimm, 'Evidence for Efimov quantum states in an ultracold gas of caesium atoms', *Nature* **440**, 315 (2006).
- [67] R. L. D. Campbell, R. P. Smith, N. Tammuz, S. Beattie, S. Moulder, and Z. Hadzibabic, 'Efficient production of large ^{39}K Bose-Einstein condensates', *Phys. Rev. A* **82**, 063611 (2010).
- [68] N. Tammuz, 'Thermodynamics of ultracold ^{39}K atomic Bose gases with tuneable interactions', Ph.D. thesis, University of Cambridge (2011).
- [69] R. L. D. Campbell, 'Thermodynamic properties of a Bose gas with tuneable interactions', Ph.D. thesis, University of Cambridge (2011).
- [70] S. Moulder, 'Persistent Currents in Bose-Einstein Condensates', Ph.D. thesis, University of Cambridge (2013).
- [71] A. L. Gaunt, 'Degenerate Bose Gases: Tuning Interactions & Geometry', Ph.D. thesis, University of Cambridge (2014).
- [72] A. Suleymanzade, 'Ultracold atoms experiment for trapping ^{39}K in an optical box trap', Master's thesis, University of Cambridge (2014).
- [73] I. Gotlibovych, T. F. Schmidutz, S. Moulder, R. L. D. Campbell, N. Tammuz, R. J. Fletcher, A. L. Gaunt, S. Beattie, R. P. Smith, and Z. Hadzibabic, 'A compact single-chamber apparatus for Bose-Einstein condensation of ^{87}Rb ', arXiv:1212.4108 (2012).
- [74] I. Gotlibovych, 'Degenerate Bose Gases in a Uniform Potential', Ph.D. thesis, University of Cambridge (2014).
- [75] T. F. Schmidutz, 'Studies of a Homogeneous Bose Gas', Ph.D. thesis, University of Cambridge (2014).
- [76] D. Nath, R. K. Easwaran, G. Rajalakshmi, and C. S. Unnikrishnan, 'Quantum-interference-enhanced deep sub-Doppler cooling of ^{39}K atoms in gray molasses', *Phys. Rev. A* **88**, 053407 (2013).

- [77] G. Salomon, L. Fouché, P. Wang, A. Aspect, P. Bouyer, and T. Bourdel, ‘*Gray-molasses cooling of ^{39}K to a high phase-space density*’, EPL (Europhysics Letters) **104**, 63002 (2013).
- [78] G. Salomon, L. Fouché, S. Lepoutre, A. Aspect, and T. Bourdel, ‘*All-optical cooling of ^{39}K to Bose–Einstein condensation*’, Phys. Rev. A **90**, 033405 (2014).
- [79] L. Landau, ‘*On the theory of transfer of energy at collisions II.*’, Phys. Z. Sowjetunion **2**, 46 (1932).
- [80] C. Zener and R. H. Fowler, ‘*Non-adiabatic crossing of energy levels*’, Proc. R. Soc. Lond. A **137**, 696 (1932).
- [81] R. W. Bowman, A. J. Wright, and M. J. Padgett, ‘*An SLM-based Shack–Hartmann wavefront sensor for aberration correction in optical tweezers*’, J. Opt. **12**, 124004 (2010).
- [82] B. C. Platt and R. Shack, ‘*History and principles of Shack–Hartmann wavefront sensing*’, J. Refract. Surg. **17**, 573 (2001).
- [83] C. D’Errico, M. Zaccanti, M. Fattori, G. Roati, M. Inguscio, G. Modugno, and A. Simoni, ‘*Feshbach resonances in ultracold ^{39}K* ’, New J. Phys. **9**, 223 (2007).
- [84] M. Lysebo and L. Veseth, ‘*Feshbach resonances and transition rates for cold homonuclear collisions between ^{39}K and ^{41}K atoms*’, Phys. Rev. A **81**, 032702 (2010).
- [85] T. L. Nicholson, S. Blatt, B. J. Bloom, J. R. Williams, J. W. Thomsen, J. Ye, and P. S. Julienne, ‘*Optical Feshbach resonances: Field-dressed theory and comparison with experiments*’, Phys. Rev. A **92**, 022709 (2015).
- [86] J. A. P. Glidden, ‘*In preparation*’, Ph.D. thesis, University of Cambridge (2020).
- [87] I. Gotlibovych, T. F. Schmidutz, A. L. Gaunt, N. Navon, R. P. Smith, and Z. Hadzibabic, ‘*Observing properties of an interacting homogeneous Bose–Einstein condensate: Heisenberg-limited momentum spread, interaction energy, and free-expansion dynamics*’, Phys. Rev. A **89**, 061604 (2014).
- [88] R. Saint-Jalm, P. C. M. Castilho, E. Le Cerf, B. Bakkali-Hassani, J.-L. Ville, S. Nascimbene, J. Beugnon, and J. Dalibard, ‘*Dynamical Symmetry and Breathers in a Two-Dimensional Bose Gas*’, Phys. Rev. X **9**, 021035 (2019).
- [89] G. Breit and I. I. Rabi, ‘*Measurement of Nuclear Spin*’, Phys. Rev. **38**, 2082 (1931).
- [90] R. J. Fletcher, J. Man, R. Lopes, P. Christodoulou, J. Schmitt, M. Sohmen, N. Navon, R. P. Smith, and Z. Hadzibabic, ‘*Elliptic flow in a strongly interacting normal Bose gas*’, Phys. Rev. A **98**, 011601 (2018).
- [91] A. Barker, ‘*Spectroscopic Studies of a Homogeneous Bose–Einstein*’, Master’s thesis, University of Cambridge (2016).
- [92] W. Gerlach and O. Stern, ‘*Der experimentelle Nachweis der Richtungsquantelung im Magnetfeld*’, Z. Phys. **9**, 349 (1922).
- [93] M. Kozuma, L. Deng, E. W. Hagley, J. Wen, R. Lutwak, K. Helmerson, S. L. Rolston, and W. D. Phillips, ‘*Coherent splitting of Bose–Einstein condensed atoms with optically induced Bragg diffraction*’, Phys. Rev. Lett. **82**, 871 (1999).
- [94] J. Stenger, S. Inouye, A. P. Chikkatur, D. M. Stamper-Kurn, D. E. Pritchard, and W. Ketterle, ‘*Bragg Spectroscopy of a Bose–Einstein Condensate*’, Phys. Rev. Lett. **82**, 4569 (1999).

- [95] W. L. Bragg, *'The Specular Reflection of X-rays.'*, Nature **90**, 410 (1912).
- [96] W. Bragg, *'The diffraction of short electromagnetic waves by a crystal'*, Proceedings of the Cambridge Philosophical Society **17**, 43 (1913).
- [97] K. G. H. Viebahn, *'Bragg Spectroscopy of an Interacting Bose–Einstein Condensate'*, Master's thesis, University of Cambridge and LMU Munich (2015).
- [98] L. F. Richardson, *Weather prediction by numerical process*, Cambridge University Press (1922).
- [99] D. A. McDonald, *'Occurrence of turbulent flow in the rabbit aorta'*, J. Physiol. **118**, 340 (1952).
- [100] O. M. Phillips, *'Spectral and statistical properties of the equilibrium range in wind-generated gravity waves'*, J. Fluid Mech. **156**, 505 (1985).
- [101] P. A. Hwang, D. W. Wang, E. J. Walsh, W. B. Krabill, and R. N. Swift, *'Airborne Measurements of the Wavenumber Spectra of Ocean Surface Waves. Part I: Spectral Slope and Dimensionless Spectral Coefficient'*, J. Phys. Oceanogr. **30**, 2753 (2000).
- [102] M. Y. Brazhnikov, G. V. Kolmakov, A. A. Levchenko, and L. P. Mezhov-Deglin, *'Observation of capillary turbulence on the water surface in a wide range of frequencies'*, Europhysics Letters (EPL) **58**, 510 (2002).
- [103] S. Lukaschuk, S. Nazarenko, S. McLelland, and P. Denissenko, *'Gravity Wave Turbulence in Wave Tanks: Space and Time Statistics'*, Phys. Rev. Lett. **103**, 044501 (2009).
- [104] P. Cobelli, A. Prasadka, P. Petitjeans, G. Lagubeau, V. Pagneux, and A. Maurel, *'Different Regimes for Water Wave Turbulence'*, Phys. Rev. Lett. **107**, 214503 (2011).
- [105] E. R. Reiter, *'The Nature of Clear Air Turbulence: A Review'*, in *'Clear Air Turbulence and Its Detection'*, (edited by Y.-H. Pao and A. Goldberg), Springer US (1969).
- [106] S. Dyachenko, A. Newell, A. Pushkarev, and V. Zakharov, *'Optical turbulence: weak turbulence, condensates and collapsing filaments in the nonlinear Schrödinger equation'*, Physica D **57**, 96 (1992).
- [107] M. Mlejnek, M. Kolesik, J. V. Moloney, and E. M. Wright, *'Optically Turbulent Femtosecond Light Guide in Air'*, Phys. Rev. Lett. **83**, 2938 (1999).
- [108] L. Bergé, S. Skupin, F. Lederer, G. Méjean, J. Yu, J. Kasparian, E. Salmon, J. P. Wolf, M. Rodriguez, L. Wöste, R. Bourayou, and R. Sauerbrey, *'Multiple Filamentation of Terawatt Laser Pulses in Air'*, Phys. Rev. Lett. **92**, 225002 (2004).
- [109] U. Bortolozzo, J. Laurie, S. Nazarenko, and S. Residori, *'Optical wave turbulence and the condensation of light'*, J. Opt. Soc. Am. B **26**, 2280 (2009).
- [110] P. Mösta, C. D. Ott, D. Radice, L. F. Roberts, E. Schnetter, and R. Haas, *'A large-scale dynamo and magnetoturbulence in rapidly rotating core-collapse supernovae'*, Nature **528**, 376 (2015).
- [111] G. S. Bisnovatyi-Kogan and S. A. Silich, *'Shock-wave propagation in the nonuniform interstellar medium'*, Rev. Mod. Phys. **67**, 661 (1995).
- [112] L. Sorriso-Valvo, R. Marino, V. Carbone, A. Noullez, F. Lepreti, P. Veltri, R. Bruno, B. Bavassano, and E. Pietropaolo, *'Observation of inertial energy cascade in interplanetary space plasma'*, Phys. Rev. Lett. **99**, 115001 (2007).

- [113] P. A. Davidson, *Turbulence: An Introduction for Scientists and Engineers*, Oxford University Press (2015).
- [114] L. da Vinci, '*Sheet of Studies of Water Flowing past Obstacles [Pen and ink over red chalk]*', Windsor Castle, Royal Library (RL 12660r) (c. 1508-1510).
- [115] O. Reynolds, '*An experimental investigation of the circumstances which determine whether the motion of water shall be direct or sinuous, and of the law of resistance in parallel channels.*', Proc. Roy. Soc. London **35**, 84 (1883).
- [116] A. N. Kolmogorov, '*The local structure of turbulence in incompressible viscous fluid for very large Reynolds numbers*', Dokl. Akad. Nauk SSSR **30**, 299 (1941).
- [117] A. Obukhov, '*On the distribution of energy in the spectrum of turbulent flow*', Dokl. Akad. Nauk SSSR **32**, 22 (1941).
- [118] U. Frisch, *Turbulence: the legacy of A.N. Kolmogorov*, Cambridge University Press (1995).
- [119] R. H. Kraichnan, '*Inertial Ranges in Two-dimensional Turbulence*', The Physics of Fluids **10**, 1417 (1967).
- [120] R. H. Kraichnan and D. Montgomery, '*Two-dimensional turbulence*', Rep. Prog. Phys. **43**, 547 (1980).
- [121] H. Kellay and W. I. Goldberg, '*Two-dimensional turbulence: a review of some recent experiments*', Rep. Prog. Phys. **65**, 845 (2002).
- [122] G. Boffetta and R. E. Ecke, '*Two-Dimensional Turbulence*', Annu. Rev. Fluid Mech **44**, 427 (2012).
- [123] H. L. Grant, R. W. Stewart, and A. Moilliet, '*Turbulence spectra from a tidal channel*', J. Fluid Mech. **12**, 241 (1962).
- [124] O. Alexandrova, J. Saur, C. Lacombe, A. Mangeney, J. Mitchell, S. J. Schwartz, and P. Robert, '*Universality of solar-wind turbulent spectrum from MHD to electron scales*', Phys. Rev. Lett. **103**, 165003 (2009).
- [125] J. Maurer and P. Tabeling, '*Local investigation of superfluid turbulence*', Europhys. Lett. **43**, 29 (1998).
- [126] A. Chepurnov, B. Burkhart, A. Lazarian, and S. Stanimirovic, '*The Turbulence Velocity Power Spectrum of Neutral Hydrogen in the Small Magellanic Cloud*', Astro. J. **810**, 33 (2015).
- [127] S. Ghashghaie, W. Breymann, J. Peinke, P. Talkner, and Y. Dodge, '*Turbulent cascades in foreign exchange markets*', Nature **381**, 767 (1996).
- [128] A. Sheremet, Y. Qin, J. P. Kennedy, Y. Zhou, and A. P. Maurer, '*Wave Turbulence and Energy Cascade in the Hippocampus*', Frontiers in Systems Neuroscience **12**, 62 (2019).
- [129] M. S. Uberoi, '*Energy transfer in isotropic turbulence*', The Physics of Fluids **6**, 1048 (1963).
- [130] M. Miyake, M. Donelan, and Y. Mitsuta, '*Airborne measurement of turbulent fluxes*', J. Geophys. Res. **75**, 4506 (1970).
- [131] W. D. McComb, *Homogeneous, isotropic turbulence: phenomenology, renormalization and statistical closures*, Oxford University Press (2014).
- [132] L. Deike, M. Berhanu, and E. Falcon, '*Energy flux measurement from the dissipated energy in capillary wave turbulence*', Phys. Rev. E **89**, 023003 (2014).

- [133] B. V. Svistunov, '*Superfluid turbulence in the low-temperature limit*', Phys. Rev. B **52**, 3647 (1995).
- [134] C. Nore, M. Abid, and M. E. Brachet, '*Kolmogorov Turbulence in Low-Temperature Superflows*', Phys. Rev. Lett. **78**, 3896 (1997).
- [135] E. Fonda, D. P. Meichle, N. T. Ouellette, S. Hormoz, and D. P. Lathrop, '*Direct observation of Kelvin waves excited by quantized vortex reconnection*', Proc. Natl. Acad. Sci. **111**, 4707 (2014).
- [136] G. P. Bewley, M. S. Paoletti, K. R. Sreenivasan, and D. P. Lathrop, '*Characterization of reconnecting vortices in superfluid helium*', Proc. Natl. Acad. Sci. **105**, 13707 (2008).
- [137] M. Paoletti, M. E. Fisher, and D. Lathrop, '*Reconnection dynamics for quantized vortices*', Physica D: Nonlinear Phenomena **239**, 1367 (2010).
- [138] W. F. Vinen, '*Decay of superfluid turbulence at a very low temperature: The radiation of sound from a Kelvin wave on a quantized vortex*', Phys. Rev. B **64**, 134520 (2001).
- [139] M. Leadbeater, T. Winiecki, D. C. Samuels, C. F. Barenghi, and C. S. Adams, '*Sound Emission due to Superfluid Vortex Reconnections*', Phys. Rev. Lett. **86**, 1410 (2001).
- [140] W. F. Vinen and J. J. Niemela, '*Quantum Turbulence*', J. Low Temp. Phys. **128**, 167 (2002).
- [141] L. Skrbek, '*Quantum turbulence*', J. Phys.: Conf. Ser. **318**, 012004 (2011).
- [142] M. S. Paoletti and D. P. Lathrop, '*Quantum turbulence*', Annu. Rev. Condens. Matter Phys. **2**, 213 (2011).
- [143] L. Skrbek and K. R. Sreenivasan, '*Developed quantum turbulence and its decay*', Phys. Fluids **24**, 011301 (2012).
- [144] C. F. Barenghi, L. Skrbek, and K. R. Sreenivasan, '*Introduction to quantum turbulence*', Proc. Natl. Acad. Sci. **111**, 4647 (2014).
- [145] L. Onsager, '*Statistical hydrodynamics*', Il Nuovo Cimento **6**, 279 (1949).
- [146] R. P. Feynman, '*Application of quantum mechanics to liquid helium*', in '*Progress in Low Temperature Physics*', (edited by C. J. Gorter), North-Holland Publishing Co. (1955).
- [147] P. M. Chesler, H. Liu, and A. Adams, '*Holographic vortex liquids and superfluid turbulence*', Science **341**, 368 (2013).
- [148] P. M. Walmsley and A. I. Golov, '*Quantum and Quasiclassical Types of Superfluid Turbulence*', Phys. Rev. Lett. **100**, 245301 (2008).
- [149] J. Salort, C. Baudet, B. Castaing, B. Chabaud, F. Daviaud, T. Didelot, P. Diribarne, B. Dubrulle, Y. Gagne, F. Gauthier, A. Girard, B. Hébral, B. Rousset, P. Thibault, and P.-E. Roche, '*Turbulent velocity spectra in superfluid flows*', Phys. Fluids **22**, 125102 (2010).
- [150] D. Bradley, S. Fisher, A. Guénault, R. Haley, G. Pickett, D. Potts, and V. Tsepelin, '*Direct measurement of the energy dissipated by quantum turbulence*', Nat. Phys. **7**, 473 (2011).
- [151] A. N. Ganshin, V. B. Efimov, G. V. Kolmakov, L. P. Mezhov-Deglin, and P. V. E. McClintock, '*Observation of an inverse energy cascade in developed acoustic turbulence in superfluid helium*', Phys. Rev. Lett. **101**, 065303 (2008).

- [152] L. V. Abdurakhimov, M. Y. Brazhnikov, A. A. Levchenko, I. Remizov, and S. Filatov, 'Turbulent capillary cascade near the edge of the inertial range on the surface of a quantum liquid', *JETP Lett.* **95**, 670 (2012).
- [153] G. V. Kolmakov, P. V. E. McClintock, and S. V. Nazarenko, 'Wave turbulence in quantum fluids', *Proc. Natl. Acad. Sci.* **111**, 4727 (2014).
- [154] G. P. Bewley, D. P. Lathrop, and K. R. Sreenivasan, 'Visualization of quantized vortices', *Nature* **441**, 588 (2006).
- [155] S. Babuin, M. Stammeier, E. Varga, M. Rotter, and L. Skrbek, 'Quantum turbulence of bellows-driven ^4He superflow: Steady state', *Phys. Rev. B* **86**, 134515 (2012).
- [156] E. A. L. Henn, J. A. Seman, G. Roati, K. M. F. Magalhães, and V. S. Bagnato, 'Emergence of Turbulence in an Oscillating Bose–Einstein Condensate', *Phys. Rev. Lett.* **103**, 045301 (2009).
- [157] T. W. Neely, A. S. Bradley, E. C. Samson, S. J. Rooney, E. M. Wright, K. J. H. Law, R. Carretero-González, P. G. Kevrekidis, M. J. Davis, and B. P. Anderson, 'Characteristics of Two-Dimensional Quantum Turbulence in a Compressible Superfluid', *Phys. Rev. Lett.* **111**, 235301 (2013).
- [158] W. J. Kwon, G. Moon, J. Choi, S. W. Seo, and Y. Shin, 'Relaxation of superfluid turbulence in highly oblate Bose–Einstein condensates', *Phys. Rev. A* **90**, 063627 (2014).
- [159] A. J. Allen, N. G. Parker, N. P. Proukakis, and C. F. Barenghi, 'Quantum turbulence in atomic Bose–Einstein condensates', *Journal of Physics: Conference Series* **544**, 012023 (2014).
- [160] A. C. White, B. P. Anderson, and V. S. Bagnato, 'Vortices and turbulence in trapped atomic condensates', *Proc. Natl. Acad. Sci.* **111**, 4719 (2014).
- [161] M. C. Tsatsos, P. E. Tavares, A. Cidrim, A. R. Fritsch, M. A. Caracanhas, F. E. A. dos Santos, C. F. Barenghi, and V. S. Bagnato, 'Quantum turbulence in trapped atomic Bose–Einstein condensates', *Phys. Rep.* **622**, 1 (2016).
- [162] N. Navon, A. L. Gaunt, R. P. Smith, and Z. Hadzibabic, 'Emergence of a turbulent cascade in a quantum gas', *Nature* **539**, 72 (2016).
- [163] W. J. Kwon, J. H. Kim, S. W. Seo, and Y.-i. Shin, 'Observation of von Karman vortex street in an atomic superfluid gas', *Phys. Rev. Lett.* **117**, 245301 (2016).
- [164] S. W. Seo, B. Ko, J. H. Kim, and Y. Shin, 'Observation of vortex-antivortex pairing in decaying 2D turbulence of a superfluid gas', *Sci. Rep.* **7**, 4587 (2017).
- [165] M. E. Mossman, M. A. Hofer, K. Julien, P. G. Kevrekidis, and P. Engels, 'Dissipative shock waves generated by a quantum-mechanical piston', *Nat. Commun.* **9**, 4665 (2018).
- [166] S. P. Johnstone, A. J. Groszek, P. T. Starkey, C. J. Billington, T. P. Simula, and K. Helmerson, 'Evolution of large-scale flow from turbulence in a two-dimensional superfluid', *Science* **364**, 1267 (2019).
- [167] G. Gauthier, M. T. Reeves, X. Yu, A. S. Bradley, M. A. Baker, T. A. Bell, H. Rubinsztein-Dunlop, M. J. Davis, and T. W. Neely, 'Giant vortex clusters in a two-dimensional quantum fluid', *Science* **364**, 1264 (2019).
- [168] L. Madeira, M. Caracanhas, F. d. Santos, and V. Bagnato, 'Quantum Turbulence in Quantum Gases', *Annu. Rev. Condens. Matter Phys.* **11**, arXiv:1903.12215 (2020).

- [169] V. E. Zakharov, V. S. L'Vov, and G. Falkovich, *Kolmogorov spectra of turbulence*, Springer Berlin (1992).
- [170] N. G. Berloff and B. V. Svistunov, 'Scenario of strongly nonequilibrated Bose–Einstein condensation', *Phys. Rev. A* **66**, 013603 (2002).
- [171] M. Kobayashi and M. Tsubota, 'Kolmogorov spectrum of superfluid turbulence: Numerical analysis of the Gross–Pitaevskii equation with a small-scale dissipation', *Phys. Rev. Lett.* **94**, 065302 (2005).
- [172] D. Proment, S. Nazarenko, and M. Onorato, 'Quantum turbulence cascades in the Gross–Pitaevskii model', *Phys. Rev. A* **80**, 051603 (2009).
- [173] M. T. Reeves, T. P. Billam, B. P. Anderson, and A. S. Bradley, 'Inverse energy cascade in forced two-dimensional quantum turbulence', *Phys. Rev. Lett.* **110**, 104501 (2013).
- [174] G. E. Falkovich and I. V. Ryzhenkova, 'Kolmogorov spectra of Langmuir and optical turbulence', *Physics of Fluids B: Plasma Physics* **4**, 594 (1992).
- [175] L. Biferale and I. Procaccia, 'Anisotropy in turbulent flows and in turbulent transport', *Phys. Rep.* **414**, 43 (2005).
- [176] I. Chantesana, A. P. n. Orioli, and T. Gasenzer, 'Kinetic theory of nonthermal fixed points in a Bose gas', *Phys. Rev. A* **99**, 043620 (2019).
- [177] O. Cadot, Y. Couder, A. Daerr, S. Douady, and A. Tsinober, 'Energy injection in closed turbulent flows: Stirring through boundary layers versus inertial stirring', *Phys. Rev. E* **56**, 427 (1997).
- [178] J. C. Vassilicos, 'Dissipation in Turbulent Flows', *Annu. Rev. Fluid Mech.* **47**, 95 (2015).
- [179] B. V. Svistunov, 'Highly nonequilibrium Bose condensation in a weakly interacting gas', *J. Moscow Phys. Soc.* **1**, 373 (1991).
- [180] D. V. Semikoz and I. I. Tkachev, 'Kinetics of Bose Condensation', *Phys. Rev. Lett.* **74**, 3093 (1995).
- [181] D. V. Semikoz and I. I. Tkachev, 'Condensation of bosons in the kinetic regime', *Phys. Rev. D* **55**, 489 (1997).
- [182] G. I. Taylor, 'Production and dissipation of vorticity in a turbulent fluid', *Proc. R. Soc. A* **164**, 15 (1938).
- [183] S. Nazarenko, *Wave turbulence*, Springer (2011).
- [184] M. Prüfer, P. Kunkel, H. Strobel, S. Lannig, D. Linnemann, C.-M. Schmied, J. Berges, T. Gasenzer, and M. K. Oberthaler, 'Observation of universal dynamics in a spinor Bose gas far from equilibrium', *Nature* **563**, 217 (2018).
- [185] S. Erne, R. Bücke, T. Gasenzer, J. Berges, and J. Schmiedmayer, 'Universal dynamics in an isolated one-dimensional Bose gas far from equilibrium', *Nature* **563**, 225 (2018).
- [186] N. Navon, A. L. Gaunt, R. P. Smith, and Z. Hadzibabic, 'Critical dynamics of spontaneous symmetry breaking in a homogeneous Bose gas', *Science* **347**, 167 (2015).
- [187] A. W. Baggaley, L. K. Sherwin, C. F. Barenghi, and Y. A. Sergeev, 'Thermally and mechanically driven quantum turbulence in helium II', *Phys. Rev. B* **86**, 104501 (2012).

- [188] K. Damle, S. N. Majumdar, and S. Sachdev, '*Phase ordering kinetics of the Bose gas*', Phys. Rev. A **54**, 5037 (1996).
- [189] A. Davey and K. Stewartson, '*On Three-Dimensional Packets of Surface Waves*', Proc. R. Soc. Lond. A **338**, 101 (1974).
- [190] C. Sulem and P.-L. Sulem, *The Nonlinear Schrödinger Equation, Self-Focusing and Wave Collapse*, Springer-Verlag New York (1999).
- [191] R. Y. Chiao, E. Garmire, and C. H. Townes, '*Self-Trapping of Optical Beams*', Phys. Rev. Lett. **13**, 479 (1964).
- [192] P. L. Kelley, '*Self-Focusing of Optical Beams*', Phys. Rev. Lett. **15**, 1005 (1965).
- [193] G. Fibich, *The Nonlinear Schrödinger Equation*, Spinger International Publishing Switzerland (2015).
- [194] V. E. Zakharov, '*Collapse of Langmuir Waves*', Sov. Phys. JETP **35**, 908 (1972).
- [195] H. C. Kim, R. L. Stenzel, and A. Y. Wong, '*Development of "Cavitons" and Trapping of rf Field*', Phys. Rev. Lett. **33**, 886 (1974).
- [196] D. A. Gurnett, J. E. Maggs, D. L. Gallagher, W. S. Kurth, and F. L. Scarf, '*Parametric interaction and spatial collapse of beam-driven Langmuir waves in the solar wind*', Journal of Geophysical Research: Space Physics **86**, 8833 (1981).
- [197] A. Y. Wong and P. Y. Cheung, '*Three-Dimensional Self-Collapse of Langmuir Waves*', Phys. Rev. Lett. **52**, 1222 (1984).
- [198] P. Y. Cheung and A. Y. Wong, '*Periodic Collapse and Long-Time Evolution of Strong Langmuir Turbulence*', Phys. Rev. Lett. **55**, 1880 (1985).
- [199] G. Thejappa, R. J. MacDowall, M. Bergamo, and K. Papadopoulos, '*Evidence for the oscillating two stream instability and spatial collapse of Langmuir waves in a solar type III radio burst*', Astrophys. J. **747**, L1 (2012).
- [200] R. A. Helliwell, '*Low-frequency waves in the magnetosphere*', Rev. Geophys. **7**, 281 (1969).
- [201] M. Houbiers and H. T. C. Stoof, '*Stability of Bose condensed atomic ${}^7\text{Li}$* ', Phys. Rev. A **54**, 5055 (1996).
- [202] S. L. Shapiro and S. A. Teukolsky, *Black Holes, White Dwarfs, and Neutron Stars*, Wiley-VCH Verlag GmbH (2007).
- [203] O. Budneva, V. Zakharov, and V. Synakh, '*Certain Models for Wave Collapse*', Sov. J. Plasma Phys. **1**, 335 (1975).
- [204] V. E. Zakharov and E. A. Kuznetsov, '*A quasi-classical theory for a three-dimensional wave collapse*', Sov. Phys. JETP **64**, 773 (1986).
- [205] V. E. Zakharov and E. A. Kuznetsov, '*Solitons and collapses: two evolution scenarios of nonlinear wave systems*', PHYS-USP **55**, 535 (2012).
- [206] C. A. Sackett, J. M. Gerton, M. Welling, and R. G. Hulet, '*Measurement of Collective Collapse in a Bose-Einstein Condensate with Attractive Interactions*', Phys. Rev. Lett. **82**, 876 (1999).
- [207] J. M. Gerton, D. Strekalov, I. Prodan, and R. G. Hulet, '*Direct observation of growth and collapse of a Bose-Einstein condensate with attractive interactions*', Nature **408**, 692 (2000).

- [208] J. L. Roberts, N. R. Claussen, S. L. Cornish, E. A. Donley, E. A. Cornell, and C. E. Wieman, ‘Controlled Collapse of a Bose–Einstein Condensate’, *Phys. Rev. Lett.* **86**, 4211 (2001).
- [209] E. A. Donley, N. R. Claussen, S. L. Cornish, J. L. Roberts, E. A. Cornell, and C. E. Wieman, ‘Dynamics of collapsing and exploding Bose–Einstein condensates’, *Nature* **412**, 295 (2001).
- [210] S. L. Cornish, S. T. Thompson, and C. E. Wieman, ‘Formation of Bright Matter-Wave Solitons during the Collapse of Attractive Bose–Einstein Condensates’, *Phys. Rev. Lett.* **96**, 170401 (2006).
- [211] P. A. Altin, G. R. Dennis, G. D. McDonald, D. Döring, J. E. Debs, J. D. Close, C. M. Savage, and N. P. Robins, ‘Collapse and three-body loss in a ^{85}Rb Bose–Einstein condensate’, *Phys. Rev. A* **84**, 033632 (2011).
- [212] R. L. Compton, Y.-J. Lin, K. Jiménez-García, J. V. Porto, and I. B. Spielman, ‘Dynamically slowed collapse of a Bose–Einstein condensate with attractive interactions’, *Phys. Rev. A* **86**, 063601 (2012).
- [213] P. A. Ruprecht, M. J. Holland, K. Burnett, and M. Edwards, ‘Time-dependent solution of the nonlinear Schrödinger equation for Bose-condensed trapped neutral atoms’, *Phys. Rev. A* **51**, 4704 (1995).
- [214] L. Santos and G. V. Shlyapnikov, ‘Collapse dynamics of trapped Bose–Einstein condensates’, *Phys. Rev. A* **66**, 011602 (2002).
- [215] H. Saito and M. Ueda, ‘Mean-field analysis of collapsing and exploding Bose–Einstein condensates’, *Phys. Rev. A* **65**, 033624 (2002).
- [216] S. K. Adhikari, ‘Dynamics of collapsing and exploding Bose–Einstein condensate’, *Phys. Lett. A* **296**, 145 (2002).
- [217] C. M. Savage, N. P. Robins, and J. J. Hope, ‘Bose–Einstein condensate collapse: A comparison between theory and experiment’, *Phys. Rev. A* **67**, 014304 (2003).
- [218] S. Métens, G. Dewel, and P. Borckmans, ‘Nonadiabatic effects in the dynamics of collapsing Bose–Einstein condensates’, *Phys. Rev. A* **68**, 045601 (2003).
- [219] L. D. Carr and J. Brand, ‘Spontaneous Soliton Formation and Modulational Instability in Bose–Einstein Condensates’, *Phys. Rev. Lett.* **92**, 040401 (2004).
- [220] S. Wüster, J. J. Hope, and C. M. Savage, ‘Collapsing Bose–Einstein condensates beyond the Gross–Pitaevskii approximation’, *Phys. Rev. A* **71**, 033604 (2005).
- [221] J. K. Chin, J. M. Vogels, and W. Ketterle, ‘Amplification of Local Instabilities in a Bose–Einstein Condensate with Attractive Interactions’, *Phys. Rev. Lett.* **90**, 160405 (2003).
- [222] G. Modugno, G. Roati, F. Riboli, F. Ferlaino, R. J. Brecha, and M. Inguscio, ‘Collapse of a Degenerate Fermi Gas’, *Science* **297**, 2240 (2002).
- [223] C. Ospelkaus, S. Ospelkaus, K. Sengstock, and K. Bongs, ‘Interaction-Driven Dynamics of ^{40}K - ^{87}Rb Fermion-Boson Gas Mixtures in the Large-Particle-Number Limit’, *Phys. Rev. Lett.* **96**, 020401 (2006).
- [224] B. J. DeSalvo, K. Patel, G. Cai, and C. Chin, ‘Observation of fermion-mediated interactions between bosonic atoms’, *Nature* **568**, 61 (2019).
- [225] T. Koch, T. Lahaye, J. Metz, B. Fröhlich, A. Griesmaier, and T. Pfau, ‘Stabilizing a purely dipolar quantum gas against collapse’, *Nat. Phys.* **4**, 218 (2008).

- [226] T. Lahaye, J. Metz, B. Fröhlich, T. Koch, M. Meister, A. Griesmaier, T. Pfau, H. Saito, Y. Kawaguchi, and M. Ueda, '*d-Wave Collapse and Explosion of a Dipolar Bose–Einstein Condensate*', Phys. Rev. Lett. **101**, 080401 (2008).
- [227] K. Aikawa, A. Frisch, M. Mark, S. Baier, A. Rietzler, R. Grimm, and F. Ferlaino, '*Bose–Einstein Condensation of Erbium*', Phys. Rev. Lett. **108**, 210401 (2012).
- [228] H. Kadau, M. Schmitt, M. Wenzel, C. Wink, T. Maier, I. Ferrier-Barbut, and T. Pfau, '*Observing the Rosensweig instability of a quantum ferrofluid*', Nature **530**, 194 (2016).
- [229] I. Ferrier-Barbut, H. Kadau, M. Schmitt, M. Wenzel, and T. Pfau, '*Observation of Quantum Droplets in a Strongly Dipolar Bose Gas*', Phys. Rev. Lett. **116**, 215301 (2016).
- [230] L. Chomaz, S. Baier, D. Petter, M. J. Mark, F. Wächtler, L. Santos, and F. Ferlaino, '*Quantum-Fluctuation-Driven Crossover from a Dilute Bose–Einstein Condensate to a Macrodroplet in a Dipolar Quantum Fluid*', Phys. Rev. X **6**, 041039 (2016).
- [231] L. Tanzi, E. Lucioni, F. Famà, J. Catani, A. Fioretti, C. Gabbanini, R. N. Bisset, L. Santos, and G. Modugno, '*Observation of a Dipolar Quantum Gas with Metastable Supersolid Properties*', Phys. Rev. Lett. **122**, 130405 (2019).
- [232] F. Böttcher, J.-N. Schmidt, M. Wenzel, J. Hertkorn, M. Guo, T. Langen, and T. Pfau, '*Transient Supersolid Properties in an Array of Dipolar Quantum Droplets*', Phys. Rev. X **9**, 011051 (2019).
- [233] L. Chomaz, D. Petter, P. Ilzhöfer, G. Natale, A. Trautmann, C. Politi, G. Durastante, R. M. W. van Bijnen, A. Patscheider, M. Sohmen, M. J. Mark, and F. Ferlaino, '*Long-Lived and Transient Supersolid Behaviors in Dipolar Quantum Gases*', Phys. Rev. X **9**, 021012 (2019).
- [234] D. S. Petrov, '*Quantum Mechanical Stabilization of a Collapsing Bose-Bose Mixture*', Phys. Rev. Lett. **115**, 155302 (2015).
- [235] P. Cheiney, C. R. Cabrera, J. Sanz, B. Naylor, L. Tanzi, and L. Tarruell, '*Bright Soliton to Quantum Droplet Transition in a Mixture of Bose–Einstein Condensates*', Phys. Rev. Lett. **120**, 135301 (2018).
- [236] C. R. Cabrera, L. Tanzi, J. Sanz, B. Naylor, P. Thomas, P. Cheiney, and L. Tarruell, '*Quantum liquid droplets in a mixture of Bose–Einstein condensates*', Science **359**, 301 (2018).
- [237] G. Semeghini, G. Ferioli, L. Masi, C. Mazzinghi, L. Wolswijk, F. Minardi, M. Modugno, G. Modugno, M. Inguscio, and M. Fattori, '*Self-Bound Quantum Droplets of Atomic Mixtures in Free Space*', Phys. Rev. Lett. **120**, 235301 (2018).
- [238] V. E. Zakharov and L. N. Shur, '*Self-similar regimes of wave collapse*', Sov. Phys. JETP **54** (1981).
- [239] G. D. Doolen, D. F. DuBois, and H. A. Rose, '*Nucleation of cavitons in strong Langmuir turbulence*', Phys. Rev. Lett. **54**, 804 (1985).
- [240] S. V. Vlasov, L. I. Piskunova, and V. I. Talanov, '*Three-dimensional wave collapse in the non-linear Schrödinger equation model*', Nonlinear and Turbulent Processes in Physics **2**, 210 (1988).
- [241] Z. Shotan, O. Machtey, S. Kokkelmans, and L. Khaykovich, '*Three-Body Recombination at Vanishing Scattering Lengths in an Ultracold Bose Gas*', Phys. Rev. Lett. **113**, 053202 (2014).
- [242] S. Lepoutre, L. Fouché, A. Boissé, G. Berthet, G. Salomon, A. Aspect, and T. Bourdel, '*Production of strongly bound ^{39}K bright solitons*', Phys. Rev. A **94**, 053626 (2016).

- [243] M. Fattori, C. D'Errico, G. Roati, M. Zaccanti, M. Jona-Lasinio, M. Modugno, M. Inguscio, and G. Modugno, '*Atom Interferometry with a Weakly Interacting Bose–Einstein Condensate*', Phys. Rev. Lett. **100**, 080405 (2008).
- [244] M. Fattori, G. Roati, B. Deissler, C. D'Errico, M. Zaccanti, M. Jona-Lasinio, L. Santos, M. Inguscio, and G. Modugno, '*Magnetic Dipolar Interaction in a Bose–Einstein Condensate Atomic Interferometer*', Phys. Rev. Lett. **101**, 190405 (2008).
- [245] Y. Kagan, A. E. Muryshev, and G. V. Shlyapnikov, '*Collapse and Bose–Einstein condensation in a trapped Bose gas with negative scattering length*', Phys. Rev. Lett. **81**, 933 (1998).
- [246] L. Bergé and J. Jull Rasmussen, '*Collapsing dynamics of attractive Bose–Einstein condensates*', Phys. Lett. A **304**, 136 (2002).
- [247] V. M. Malkin, '*Bi-self-similar wave collapse*', JETP Lett. **48**, 653 (1988).
- [248] S. N. Vlasov, L. V. Piskunova, and V. I. Talanov, '*Three-dimensional wave collapse in a model of the nonlinear Schrödinger equation*', Sov. Phys. JETP **68**, 1125 (1989).
- [249] V. E. Zakharov, N. E. Kosmatov, and V. F. Shvets, '*Ultrastrong wave collapse*', Sov. Phys. JETP **49**, 492 (1989).
- [250] H. Saito and M. Ueda, '*Intermittent Implosion and Pattern Formation of Trapped Bose–Einstein Condensates with an Attractive Interaction*', Phys. Rev. Lett. **86**, 1406 (2001).
- [251] H. Saito and M. Ueda, '*Power laws and collapsing dynamics of a trapped Bose–Einstein condensate with attractive interactions*', Phys. Rev. A **63**, 043601 (2001).
- [252] R. Meppelink, R. A. Rozendaal, S. B. Koller, J. M. Vogels, and P. van der Straten, '*Thermodynamics of Bose–Einstein-condensed clouds using phase-contrast imaging*', Phys. Rev. A **81**, 053632 (2010).
- [253] F. Merle, '*On uniqueness and continuation properties after blow-up time of self-similar solutions of nonlinear Schrödinger equation with critical exponent and critical mass*', Commun. Pure Appl. Math. **45**, 203 (1992).
- [254] P. A. Robinson, '*Nonlinear wave collapse and strong turbulence*', Rev. Mod. Phys. **69**, 507 (1997).
- [255] B. Shim, S. E. Schrauth, A. L. Gaeta, M. Klein, and G. Fibich, '*Loss of Phase of Collapsing Beams*', Phys. Rev. Lett. **108**, 043902 (2012).
- [256] P. Kapitza, '*Viscosity of liquid helium below the λ -point*', Nature **141**, 74 (1938).
- [257] J. F. Allen and A. D. Misener, '*Flow of liquid helium II*', Nature **141**, 75 (1938).
- [258] J. F. Allen and H. Jones, '*New Phenomena Connected with Heat Flow in Helium II*', Nature **141**, 243 (1938).
- [259] F. London, '*On the Bose–Einstein Condensation*', Phys. Rev. **54**, 947 (1938).
- [260] L. Tisza, '*The Theory of Liquid Helium*', Phys. Rev. **72**, 838 (1947).
- [261] L. D. Landau, '*The theory of superfluidity of helium II*', J. Phys. (USSR) **5**, 71 (1941).
- [262] S. T. Beliaev, '*Energy-spectrum of a non-ideal Bose gas*', Sov. Phys. JETP **34**, 299 (1958).
- [263] N. M. Hugenholtz and D. Pines, '*Ground-State Energy and Excitation Spectrum of a System of Interacting Bosons*', Phys. Rev. **116**, 489 (1959).

- [264] A. Miller, D. Pines, and P. Nozières, '*Elementary Excitations in Liquid Helium*', Phys. Rev. **127**, 1452 (1962).
- [265] P. Nozières and D. Pines, *The Theory of Quantum Liquids*, Westview Press (1990).
- [266] H. R. Glyde, '*Excitations in the quantum liquid ^4He : A review*', Rep. Prog. Phys. **81**, 014501 (2017).
- [267] F. Dalfovo, S. Giorgini, L. P. Pitaevskii, and S. Stringari, '*Theory of Bose–Einstein condensation in trapped gases*', Rev. Mod. Phys. **71**, 463 (1999).
- [268] R. Ozeri, N. Katz, J. Steinhauer, and N. Davidson, '*Colloquium: Bulk Bogoliubov excitations in a Bose–Einstein condensate*', Rev. Mod. Phys. **77**, 187 (2005).
- [269] S. B. Papp, J. M. Pino, R. J. Wild, S. Ronen, C. E. Wieman, D. S. Jin, and E. A. Cornell, '*Bragg Spectroscopy of a Strongly Interacting ^{85}Rb Bose–Einstein Condensate*', Phys. Rev. Lett. **101**, 135301 (2008).
- [270] P. Makotyn, C. E. Klauss, D. L. Goldberger, E. A. Cornell, and D. S. Jin, '*Universal dynamics of a degenerate unitary Bose gas*', Nat. Phys. **10**, 116 (2014).
- [271] C. E. Klauss, X. Xie, C. Lopez-Abadia, J. P. D’Incao, Z. Hadzibabic, D. S. Jin, and E. A. Cornell, '*Observation of Efimov Molecules Created from a Resonantly Interacting Bose Gas*', Phys. Rev. Lett. **119**, 143401 (2017).
- [272] A. J. Leggett, *Quantum Liquids*, Oxford University Press (2006).
- [273] H. R. Glyde, S. O. Diallo, R. T. Azuah, O. Kirichek, and J. W. Taylor, '*Atomic momentum distribution and Bose-Einstein condensation in liquid ^4He under pressure*', Phys. Rev. B **84**, 184506 (2011).
- [274] S. Giorgini, J. Boronat, and J. Casulleras, '*Ground state of a homogeneous Bose gas: A diffusion Monte Carlo calculation*', Phys. Rev. A **60**, 5129 (1999).
- [275] K. Xu, Y. Liu, D. Miller, J. Chin, W. Setiawan, and W. Ketterle, '*Observation of Strong Quantum Depletion in a Gaseous Bose–Einstein Condensate*', Phys. Rev. Lett. **96**, 180405 (2006).
- [276] M. Greiner, M. O. Mandel, T. Esslinger, T. Hänsch, and I. Bloch, '*Quantum Phase Transition from a Superfluid to a Mott Insulator in a Gas of Ultracold Atoms*', Nature **415**, 39 (2002).
- [277] M. Köhl, T. Stöferle, H. Moritz, C. Schori, and T. Esslinger, '*1D Bose gases in an optical lattice*', Appl. Phys. B **79**, 1009 (2004).
- [278] R. Chang, Q. Bouton, H. Cayla, C. Qu, A. Aspect, C. I. Westbrook, and D. Clément, '*Momentum-Resolved Observation of Thermal and Quantum Depletion in a Bose Gas*', Phys. Rev. Lett. **117**, 235303 (2016).
- [279] C. Qu, L. P. Pitaevskii, and S. Stringari, '*Expansion of harmonically trapped interacting particles and time dependence of the contact*', Phys. Rev. A **94**, 063635 (2016).
- [280] J. Kasprzak, M. Richard, S. Kundermann, A. Baas, P. Jeambrun, J. M. J. Keeling, F. M. Marchetti, M. H. Szymanska, R. Andre, J. L. Staehli, V. Savona, P. B. Littlewood, B. Deveaud, and L. S. Dang, '*Bose–Einstein condensation of exciton polaritons*', Nature **443**, 409 (2006).
- [281] M. Pieczarka, E. Estrecho, M. Boozarjmehr, O. Bleu, M. Steger, K. West, L. N. Pfeiffer, D. W. Snoke, J. Levinsen, M. M. Parish, A. G. Truscott, and E. A. Ostrovskaya, '*Observation of quantum depletion in a nonequilibrium exciton-polariton condensate*', arXiv:1905.10511 (2019).

- [282] F. Gerbier, J. H. Thywissen, S. Richard, M. Hugbart, P. Bouyer, and A. Aspect, '*Critical Temperature of a Trapped, Weakly Interacting Bose Gas*', Phys. Rev. Lett. **92**, 030405 (2004).
- [283] G. I. Martone, P.-E. Larré, A. Fabbri, and N. Pavloff, '*Momentum distribution and coherence of a weakly interacting Bose gas after a quench*', Phys. Rev. A **98**, 063617 (2018).
- [284] D. M. Stamper-Kurn, A. P. Chikkatur, A. Görlitz, S. Inouye, S. Gupta, D. E. Pritchard, and W. Ketterle, '*Excitation of phonons in a Bose–Einstein condensate by light scattering*', Phys. Rev. Lett. **83**, 2876 (1999).
- [285] J. Steinhauer, R. Ozeri, N. Katz, and N. Davidson, '*Excitation spectrum of a Bose–Einstein condensate*', Phys. Phys. Lett. **88**, 120407 (2002).
- [286] S. Hoinka, M. Lingham, K. Fenech, H. Hu, C. J. Vale, J. E. Drut, and S. Gandolfi, '*Precise Determination of the Structure Factor and Contact in a Unitary Fermi Gas*', Phys. Rev. Lett. **110**, 055305 (2013).
- [287] J. L. Yarnell, G. P. Arnold, P. J. Bendt, and E. C. Kerr, '*Excitations in Liquid Helium: Neutron Scattering Measurements*', Phys. Rev. **113**, 1379 (1959).
- [288] D. G. Henshaw and A. D. B. Woods, '*Modes of Atomic Motions in Liquid Helium by Inelastic Scattering of Neutrons*', Phys. Rev. **121**, 1266 (1961).
- [289] G. Careri, '*Chapter II Helium Ions in Liquid Helium II*', in '*Progress in Low Temperature Physics: Volume 3*', (edited by C. Gorter), Elsevier (1961).
- [290] S. Ronen, '*The dispersion relation of a Bose gas in the intermediate- and high-momentum regimes*', J. Phys. B: At. Mol. Opt. Phys. **42**, 055301 (2009).
- [291] J. J. Kinnunen and M. J. Holland, '*Bragg spectroscopy of a strongly interacting Bose–Einstein condensate*', New J. Phys. **11**, 013030 (2009).
- [292] R. Sarjonen, M. Saarela, and F. Mazzanti, '*The Effective Two-Particle Interaction of Cold Atoms as Derived from Bragg Scattering*', J. Low Temp. Phys. **169**, 400 (2012).
- [293] C. E. Sahlberg, R. J. Ballagh, and C. W. Gardiner, '*Dynamic effects of a Feshbach resonance on Bragg scattering from a Bose–Einstein condensate*', Phys. Rev. A **87**, 043621 (2013).
- [294] J. Hofmann and W. Zwerger, '*Deep Inelastic Scattering on Ultracold Gases*', Phys. Rev. X **7**, 011022 (2017).
- [295] I. Shammass, S. Rinott, A. Berkovitz, R. Schley, and J. Steinhauer, '*Phonon Dispersion Relation of an Atomic Bose–Einstein Condensate*', Phys. Rev. Lett. **109**, 195301 (2012).
- [296] D. Petter, G. Natale, R. M. W. van Bijnen, A. Patscheider, M. J. Mark, L. Chomaz, and F. Ferlaino, '*Probing the Roton Excitation Spectrum of a Stable Dipolar Bose Gas*', Phys. Rev. Lett. **122**, 183401 (2019).
- [297] R. Rota, F. Tramonto, D. E. Galli, and S. Giorgini, '*Quantum Monte Carlo study of the dynamic structure factor in the gas and crystal phase of hard-sphere bosons*', Phys. Rev. B **88**, 214505 (2013).
- [298] R. P. Feynman, '*Atomic Theory of the Two-Fluid Model of Liquid Helium*', Phys. Rev. **94**, 262 (1954).
- [299] R. P. Feynman and M. Cohen, '*Energy Spectrum of the Excitations in Liquid Helium*', Phys. Rev. **102**, 1189 (1956).

- [300] J. Steinhauer, R. Ozeri, N. Katz, and N. Davidson, 'Peak in the static structure factor of a Bose–Einstein condensate', *Phys. Rev. A* **72**, 023608 (2005).
- [301] L. H. Dogra, J. A. P. Glidden, T. A. Hilker, C. Eigen, E. A. Cornell, R. P. Smith, and Z. Hadzibabic, 'Can Three-Body Recombination Purify a Quantum Gas?', *Phys. Rev. Lett.* **123**, 020405 (2019).
- [302] T. Weber, J. Herbig, M. Mark, H.-C. Nägerl, and R. Grimm, 'Three-Body Recombination at Large Scattering Lengths in an Ultracold Atomic Gas', *Phys. Rev. Lett.* **91**, 123201 (2003).
- [303] N. Katz, J. Steinhauer, R. Ozeri, and N. Davidson, 'Beliaev Damping of Quasiparticles in a Bose–Einstein Condensate', *Phys. Rev. Lett.* **89**, 220401 (2002).
- [304] N. Katz, E. Rowen, R. Ozeri, and N. Davidson, 'Collisional Decay of a Strongly Driven Bose–Einstein Condensate', *Phys. Rev. Lett.* **95**, 220403 (2005).
- [305] E. Braaten and A. Nieto, 'Quantum corrections to the energy density of a homogeneous Bose gas', *Eur. Phys. J. B* **11**, 143 (1999).
- [306] E. Braaten, H.-W. Hammer, and T. Mehen, 'Dilute Bose–Einstein Condensate with Large Scattering Length', *Phys. Rev. Lett.* **88**, 040401 (2002).
- [307] R. Rota, F. Tramonto, D. E. Galli, and S. Giorgini, 'Many-body Bose systems and the hard-sphere model: dynamic properties from the weak to the strong interaction regime', *J. Phys.: Conf. Ser.* **529**, 012022 (2014).
- [308] L. W. Clark, A. Gaj, L. Feng, and C. Chin, 'Collective emission of matter-wave jets from driven Bose–Einstein condensates', *Nature* **551**, 356 (2017).
- [309] J. C. Jaskula, G. B. Partridge, M. Bonneau, R. Lopes, J. Ruaudel, D. Boiron, and C. I. Westbrook, 'Acoustic Analog to the Dynamical Casimir Effect in a Bose–Einstein Condensate', *Phys. Rev. Lett.* **109**, 220401 (2012).
- [310] S. Cowell, H. Heiselberg, I. E. Mazets, J. Morales, V. R. Pandharipande, and C. J. Pethick, 'Cold Bose Gases with Large Scattering Lengths', *Phys. Rev. Lett.* **88**, 210403 (2002).
- [311] T.-L. Ho, 'Universal Thermodynamics of Degenerate Quantum Gases in the Unitarity Limit', *Phys. Rev. Lett.* **92**, 090402 (2004).
- [312] M. W. Zwierlein, C. A. Stan, C. H. Schunck, S. M. F. Raupach, A. J. Kerman, and W. Ketterle, 'Condensation of Pairs of Fermionic Atoms near a Feshbach Resonance', *Phys. Rev. Lett.* **92**, 120403 (2004).
- [313] C. Chin, M. Bartenstein, A. Altmeyer, S. Riedl, S. Jochim, J. Hecker-Denschlag, and R. Grimm, 'Observation of the Pairing Gap in a Strongly Interacting Fermi Gas', *Science* **305**, 1128 (2004).
- [314] T. Bourdel, L. Khaykovich, M. E. Cubizolles, J. Zhang, F. Chevy, M. Teichmann, L. Tarruell, M. F. K. S. J. H, and C. Salomon, 'Experimental Study of the BEC-BCS Crossover Region in Lithium 6', *Phys. Rev. Lett.* **93**, 050401 (2004).
- [315] J. Kinast, S. L. Hemmer, M. E. Gehm, A. Turlapov, and J. E. thomas, 'Evidence for Superfluidity in a Resonantly Interacting Fermi Gas', *Phys. Rev. Lett.* **92**, 150402 (2004).
- [316] M. W. Zwierlein, J. R. Abo-Shaer, A. Schirotzek, C. H. Schunck, and W. Ketterle, 'Vortices and superfluidity in a strongly interacting Fermi gas', *Nature* **435**, 1047 (2005).

- [317] L. Radzihovsky, J. Park, and P. B. Weichman, 'Superfluid Transitions in Bosonic Atom-Molecule Mixtures near a Feshbach Resonance', *Phys. Rev. Lett.* **92**, 160402 (2004).
- [318] M. W. J. Romans, R. A. Duine, S. Sachdev, and H. T. C. Stoof, 'Quantum Phase Transition in an Atomic Bose Gas with a Feshbach Resonance', *Phys. Rev. Lett.* **93**, 020405 (2004).
- [319] S. Piatecki and W. Krauth, 'Efimov-driven phase transitions of the unitary Bose gas', *Nat. Commun.* **5**, 3503 (2014).
- [320] B. S. Rem, A. T. Grier, I. Ferrier-Barbut, U. Eismann, T. Langen, N. Navon, L. Khaykovich, F. Werner, D. S. Petrov, F. Chevy, and C. Salomon, 'Lifetime of the Bose Gas with Resonant Interactions', *Phys. Rev. Lett.* **110**, 163202 (2013).
- [321] R. J. Fletcher, A. L. Gaunt, N. Navon, R. P. Smith, and Z. Hadzibabic, 'Stability of a Unitary Bose Gas', *Phys. Rev. Lett.* **111**, 125303 (2013).
- [322] U. Eismann, L. Khaykovich, S. Laurent, I. Ferrier-Barbut, B. S. Rem, A. T. Grier, M. Delehaye, F. Chevy, C. Salomon, L.-C. Ha, and C. Chin, 'Universal Loss Dynamics in a Unitary Bose Gas', *Phys. Rev. X* **6**, 021025 (2016).
- [323] Y.-L. Lee and Y.-W. Lee, 'Universality and stability for a dilute Bose gas with a Feshbach resonance', *Phys. Rev. A* **81**, 063613 (2010).
- [324] J. M. Diederix, T. C. F. van Heijst, and H. T. C. Stoof, 'Ground state of a resonantly interacting Bose gas', *Phys. Rev. A* **84**, 033618 (2011).
- [325] D. Borzov, M. S. Mashayekhi, S. Zhang, J.-L. Song, and F. Zhou, 'Three-dimensional Bose gas near a Feshbach resonance', *Phys. Rev. A* **85**, 023620 (2012).
- [326] W. Li and T.-L. Ho, 'Bose Gases near Unitarity', *Phys. Rev. Lett.* **108**, 195301 (2012).
- [327] X. Yin and L. Radzihovsky, 'Quench dynamics of a strongly interacting resonant Bose gas', *Phys. Rev. A* **88**, 063611 (2013).
- [328] A. G. Sykes, J. P. Corson, J. P. D'Incao, A. P. Koller, C. H. Greene, A. M. Rey, K. R. A. Hazzard, and J. L. Bohn, 'Quenching to unitarity: Quantum dynamics in a three-dimensional Bose gas', *Phys. Rev. A* **89**, 021601 (2014).
- [329] S.-J. Jiang, W.-M. Liu, G. W. Semenoff, and F. Zhou, 'Universal Bose gases near resonance: A rigorous solution', *Phys. Rev. A* **89**, 033614 (2014).
- [330] A. Rançon and K. Levin, 'Equilibrating dynamics in quenched Bose gases: Characterizing multiple time regimes', *Phys. Rev. A* **90**, 021602 (2014).
- [331] S. Laurent, X. Leyronas, and F. Chevy, 'Momentum Distribution of a Dilute Unitary Bose Gas with Three-Body Losses', *Phys. Rev. Lett.* **113**, 220601 (2014).
- [332] M. Rossi, L. Salasnich, F. Ancilotto, and F. Toigo, 'Monte Carlo simulations of the unitary Bose gas', *Phys. Rev. A* **89**, 041602 (2014).
- [333] D. H. Smith, E. Braaten, D. Kang, and L. Platter, 'Two-Body and Three-Body Contacts for Identical Bosons near Unitarity', *Phys. Rev. Lett.* **112**, 110402 (2014).
- [334] H. T. C. Stoof and J. J. R. M. van Heugten, 'Resummation of Infrared Divergencies in the Theory of Atomic Bose Gases', *J. Low Temp. Phys.* **174**, 159 (2014).
- [335] B. Kain and H. Y. Ling, 'Nonequilibrium states of a quenched Bose gas', *Phys. Rev. A* **90**, 063626 (2014).

- [336] M. Barth and J. Hofmann, ‘*Efimov correlations in strongly interacting Bose gases*’, *Phys. Rev. A* **92**, 062716 (2015).
- [337] J. P. Corson and J. L. Bohn, ‘*Bound-state signatures in quenched Bose–Einstein condensates*’, *Phys. Rev. A* **91**, 013616 (2015).
- [338] M. Kira, ‘*Coherent quantum depletion of an interacting atom condensate*’, *Nat. Commun.* **6**, 6624 (2015).
- [339] F. Ancilotto, M. Rossi, L. Salasnich, and F. Toigo, ‘*Quenched Dynamics of the Momentum Distribution of the Unitary Bose Gas*’, *Few-Body Syst.* **56**, 801 (2015).
- [340] S.-J. Jiang, J. Maki, and F. Zhou, ‘*Long-lived universal resonant Bose gases*’, *Phys. Rev. A* **93**, 043605 (2016).
- [341] T. Comparin and W. Krauth, ‘*Momentum Distribution in the Unitary Bose Gas from First Principles*’, *Phys. Rev. Lett.* **117**, 225301 (2016).
- [342] X. Yin and L. Radzihovsky, ‘*Postquench dynamics and prethermalization in a resonant Bose gas*’, *Phys. Rev. A* **93**, 033653 (2016).
- [343] Y. Ding and C. H. Greene, ‘*Renormalized contact interaction in degenerate unitary Bose gases*’, *Phys. Rev. A* **95**, 053602 (2017).
- [344] J. Carlson, S. Gandolfi, U. van Kolck, and S. A. Vitiello, ‘*Ground-State Properties of Unitary Bosons: From Clusters to Matter*’, *Phys. Rev. Lett.* **119**, 223002 (2017).
- [345] M. W. C. Sze, A. G. Sykes, D. Blume, and J. L. Bohn, ‘*Hyperspherical lowest-order constrained-variational approximation to resonant Bose–Einstein condensates*’, *Phys. Rev. A* **97**, 033608 (2018).
- [346] V. E. Colussi, J. P. Corson, and J. P. D’Incao, ‘*Dynamics of Three-Body Correlations in Quenched Unitary Bose Gases*’, *Phys. Rev. Lett.* **120**, 100401 (2018).
- [347] V. E. Colussi, S. Musolino, and S. J. J. M. F. Kokkelmans, ‘*Dynamical formation of the unitary Bose gas*’, *Phys. Rev. A* **98**, 051601 (2018).
- [348] J. P. D’Incao, ‘*Few-body physics in resonantly interacting ultracold quantum gases*’, *J. Phys. B* **51**, 043001 (2018).
- [349] V. E. Colussi, B. E. van Zwol, J. P. D’Incao, and S. J. J. M. F. Kokkelmans, ‘*Bunching, clustering, and the buildup of few-body correlations in a quenched unitary Bose gas*’, *Phys. Rev. A* **99**, 043604 (2019).
- [350] E. J. Halperin, M. W. C. Sze, J. P. Corson, and J. L. Bohn, ‘*Stable production of a strongly interacting Bose–Einstein condensate via mode matching*’, *Phys. Rev. A* **100**, 013608 (2019).
- [351] M. W. C. Sze and J. L. Bohn, ‘*Two-step production of resonant Bose–Einstein condensates*’, *Phys. Rev. A* **99**, 033606 (2019).
- [352] C. Gao, M. Sun, P. Zhang, and H. Zhai, ‘*Universal Dynamics of a Degenerate Bose Gas Quenched to Unitarity*’, arXiv:1812.06709 (2018).
- [353] S. Musolino, V. E. Colussi, and S. J. J. M. F. Kokkelmans, ‘*Pair formation in quenched unitary Bose gases*’, *Phys. Rev. A* **100**, 013612 (2019).
- [354] A. Muñoz de las Heras, M. M. Parish, and F. M. Marchetti, ‘*Early-time dynamics of Bose gases quenched into the strongly interacting regime*’, *Phys. Rev. A* **99**, 023623 (2019).

- [355] J. Berges, S. Borsányi, and C. Wetterich, ‘Prethermalization’, *Phys. Rev. Lett.* **93**, 142002 (2004).
- [356] N. Nessi, A. Iucci, and M. A. Cazalilla, ‘Quantum Quench and Prethermalization Dynamics in a Two-Dimensional Fermi Gas with Long-Range Interactions’, *Phys. Rev. Lett.* **113**, 210402 (2014).
- [357] A. Piñeiro Orioli, K. Boguslavski, and J. Berges, ‘Universal self-similar dynamics of relativistic and nonrelativistic field theories near nonthermal fixed points’, *Phys. Rev. D* **92**, 025041 (2015).
- [358] C.-M. Schmied, A. N. Mikheev, and T. Gasenzer, ‘Prescaling in a Far-from-Equilibrium Bose Gas’, *Phys. Rev. Lett.* **122**, 170404 (2019).
- [359] N. Gross, Z. Shotan, S. Kokkelmans, and L. Khaykovich, ‘Nuclear-Spin-Independent Short-Range Three-Body Physics in Ultracold Atoms’, *Phys. Rev. Lett.* **105**, 103203 (2010).
- [360] F. Ferlaino, A. Zenesini, M. Berninger, B. Huang, H. C. Nägerl, and R. Grimm, ‘Efimov Resonances in Ultracold Quantum Gases’, *Few-Body Syst.* **51**, 113 (2011).
- [361] O. Machtey, Z. Shotan, N. Gross, and L. Khaykovich, ‘Association of Efimov Trimers from a Three-Atom Continuum’, *Phys. Rev. Lett.* **108**, 210406 (2012).
- [362] S. Roy, M. Landini, A. Trenkwalder, G. Semeghini, G. Spagnolli, A. Simoni, M. Fattori, M. Inguscio, and G. Modugno, ‘Test of the Universality of the Three-Body Efimov Parameter at Narrow Feshbach Resonances’, *Phys. Rev. Lett.* **111**, 053202 (2013).
- [363] P. Naidon and S. Endo, ‘Efimov physics: a review’, *Rep. Prog. Phys.* **80**, 056001 (2017).
- [364] Y. Yudkin, R. Elbaz, P. Giannakeas, C. H. Greene, and L. Khaykovich, ‘Coherent Superposition of Feshbach Dimers and Efimov Trimers’, *Phys. Rev. Lett.* **122**, 200402 (2019).
- [365] R. Chapurin, X. Xie, M. J. Van de Graaff, J. S. Popowski, J. P. D’Incao, P. S. Julienne, J. Ye, and E. A. Cornell, ‘A Precision Test of the Limits to Universality in Few-Body Physics’, arXiv:1907.00729 (2019).
- [366] J. P. D’Incao, J. Wang, and V. E. Colussi, ‘Efimov Physics in Quenched Unitary Bose Gases’, *Phys. Rev. Lett.* **121**, 023401 (2018).
- [367] J.-L. Song and F. Zhou, ‘Ground State Properties of Cold Bosonic Atoms at Large Scattering Lengths’, *Phys. Rev. Lett.* **103**, 025302 (2009).
- [368] F. Zhou and M. S. Mashayekhi, ‘Bose gases near resonance: Renormalized interactions in a condensate’, *Ann. Phys.* **328**, 83 (2013).
- [369] T. F. Schmidutz, I. Gotlibovych, A. L. Gaunt, R. P. Smith, N. Navon, and Z. Hadzibabic, ‘Quantum Joule–Thomson Effect in a Saturated Homogeneous Bose Gas’, *Phys. Rev. Lett.* **112**, 040403 (2014).
- [370] Y. Kagan, B. V. Svistunov, and G. V. Shlyapnikov, ‘Effect of Bose condensation on inelastic processes in gases’, *JETP Lett.* **642**, 209 (1985).
- [371] E. A. Burt, R. W. Ghrist, C. J. Myatt, M. J. Holland, E. A. Cornell, and C. E. Wieman, ‘Coherence, Correlations, and Collisions: What One Learns About Bose–Einstein Condensates from Their Decay’, *Phys. Rev. Lett.* **79**, 337 (1997).
- [372] J. Söding, D. Guéry-Odelin, P. Desbiolles, F. Chevy, H. Inamori, and J. Dalibard, ‘Three-body decay of a rubidium Bose–Einstein condensate’, *Appl. Phys. B* **69**, 257 (1999).

- [373] E. Haller, M. Rabie, M. J. Mark, J. G. Danzl, R. Hart, K. Lauber, G. Pupillo, and H.-C. Nägerl, '*Three-Body Correlation Functions and Recombination Rates for Bosons in Three Dimensions and One Dimension*', Phys. Rev. Lett. **107**, 230404 (2011).
- [374] P. O. Fedichev, M. W. Reynold, and G. V. Shlyapnikov, '*Three-Body Recombination of Ultracold Atoms to a Weakly Bound s Level*', Phys. Rev. Lett. **77**, 2921 (1996).
- [375] M. Thøgersen, D. V. Fedorov, and A. S. Jensen, '*N-body Efimov states of trapped bosons*', EPL (Europhysics Letters) **83**, 30012 (2008).
- [376] N. P. Mehta, S. T. Rittenhouse, J. P. D'Incao, J. von Stecher, and C. H. Greene, '*General Theoretical Description of N-Body Recombination*', Phys. Rev. Lett. **103**, 153201 (2009).
- [377] C. H. Greene, B. Esry, and H. Suno, '*A revised formula for 3-body recombination that cannot exceed the unitarity limit*', Nucl. Phys. A **737**, 119 (2004).
- [378] J. P. D'Incao, H. Suno, and B. D. Esry, '*Limits on Universality in Ultracold Three-Boson Recombination*', Phys. Rev. Lett. **93**, 123201 (2004).
- [379] B. S. Rem, '*The Road to the Unitary Bose Gas*', Ph.D. thesis, Ecole Normale Supérieure de Paris (2013).
- [380] C. E. Klauss, '*Resonantly Interacting Degenerate Bose Gas Oddities*', Ph.D. thesis, University of Colorado at Boulder (2018).
- [381] E. Altman and A. Vishwanath, '*Dynamic Projection on Feshbach Molecules: A Probe of Pairing and Phase Fluctuations*', Phys. Rev. Lett. **95**, 110404 (2005).
- [382] C. A. Regal, C. Ticknor, J. L. Bohn, and D. S. Jin, '*Creation of ultracold molecules from a Fermi gas of atoms*', Nature **424**, 47 (2003).
- [383] E. Hodby, S. T. Thompson, C. A. Regal, M. Greiner, A. C. Wilson, D. S. Jin, E. A. Cornell, and C. E. Wieman, '*Production Efficiency of Ultracold Feshbach Molecules in Bosonic and Fermionic Systems*', Phys. Rev. Lett. **94**, 120402 (2005).
- [384] E. A. Donley, N. R. Claussen, S. T. Thompson, and C. E. Wieman, '*Atom-molecule coherence in a Bose-Einstein condensate*', Nature **417**, 529 (2002).
- [385] S. S. Natu and E. J. Mueller, '*Dynamics of correlations in a dilute Bose gas following an interaction quench*', Phys. Rev. A **87**, 053607 (2013).
- [386] P. M. A. Mestrom, J. Wang, C. H. Greene, and J. P. D'Incao, '*Efimov - van der Waals universality for ultracold atoms with positive scattering lengths*', Phys. Rev. A **95**, 032707 (2017).
- [387] M. Kardar, *Statistical Physics of Fields*, Cambridge University Press (2007).
- [388] J. Beugnon and N. Navon, '*Exploring the Kibble-Zurek mechanism with homogeneous Bose gases*', J. Phys. B: At. Mol. Opt. Phys. **50**, 022002 (2017).
- [389] L. Corman, L. Chomaz, T. Bienaimé, R. Desbuquois, C. Weitenberg, S. Nascimbène, J. Dalibard, and J. Beugnon, '*Quench-Induced Supercurrents in an Annular Bose Gas*', Phys. Rev. Lett. **113**, 135302 (2014).
- [390] T. W. B. Kibble, '*Topology of cosmic domains and strings*', J. Phys. A **9**, 1387 (1976).
- [391] W. H. Zurek, '*Cosmological experiments in superfluid helium?*', Nature **317**, 505 (1985).
- [392] P. C. Hohenberg and B. I. Halperin, '*Theory of dynamic critical phenomena*', Rev. Mod. Phys. **49**, 435 (1977).

- [393] G. Baym, J.-P. Blaizot, M. Holzmann, F. Laloë, and D. Vautherin, '*Bose–Einstein transition in a dilute interacting gas*', *Eur. Phys. J. B* **24**, 107 (2001).
- [394] M. Holzmann, J. N. Fuchs, G. Baym, J. P. Blaizot, and F. Laloë, '*Bose–Einstein transition temperature in a dilute repulsive gas*', *Comptes Rendus Physique* **5**, 21 (2004).
- [395] J. O. Andersen, '*Theory of the weakly interacting Bose gas*', *Rev. Mod. Phys.* **76**, 599 (2004).
- [396] R. P. Smith, '*Effects of Interactions on Bose–Einstein Condensation*', in '*Universal Themes of Bose–Einstein Condensation*', (edited by N. Proukakis, D. Snoke, and P. Littlewood), Cambridge University Press (2017).
- [397] T. D. Lee and C. N. Yang, '*Low-Temperature Behavior of a Dilute Bose System of Hard Spheres. I. Equilibrium Properties*', *Phys. Rev.* **112**, 1419 (1958).
- [398] R. P. Smith, R. L. D. Campbell, N. Tammuz, and Z. Hadzibabic, '*Effects of Interactions on the Critical Temperature of a Trapped Bose Gas*', *Phys. Rev. Lett.* **106**, 250403 (2011).
- [399] D. Becker, M. D. Lachmann, S. T. Seidel, H. Ahlers, A. N. Dinkelaker, J. Grosse, O. Hellmig, H. Müntinga, V. Schkolnik, T. Wendrich, A. Wenzlawski, B. Weps, R. Corgier, T. Franz, N. Gaaloul, W. Herr, D. Lüdtke, M. Popp, S. Amri, H. Duncker, M. Erbe, A. Kohfeldt, A. Kubelka-Lange, C. Braxmaier, E. Charron, W. Ertmer, M. Krutzik, C. Lämmerzahl, A. Peters, W. P. Schleich, K. Sengstock, R. Walser, A. Wicht, P. Windpassinger, and E. M. Rasel, '*Space-borne Bose–Einstein condensation for precision interferometry*', *Nature* **562**, 391 (2018).